Experimental and Numerical Hydrodynamic Analysis of a Novel Tidal Turbine, the Hydro-Spinna

Roslynna Rosli

Submitted for the degree of Doctor of Philosophy

January 2018

School of Engineering

Faculty of Science, Agriculture and Engineering

Newcastle University

Newcastle upon Tyne, UK

Abstract

Energy security, economic growth and mitigation of climate change have been driving factors in the development and deployment of renewable energy technologies. Tidal power is one such technology and includes both tidal barrages and grid connected marine current turbines although among the latter grouping, devices have yet to go beyond the prototype phase.

A novel horizontal marine current turbine, *"The Hydro-Spinna",* is introduced in this thesis. The basic geometry of the turbine is defined by some key parameters and their influences on the operation of the device are studied using numerical and experimental methods. Firstly, the performance of the Hydro-Spinna at different pitch to diameter ratio (*P/D*) was investigated using a numerical model. It was found that a turbine with low *P/D* performed better than one with a higher value, with a maximum Power Coefficient (C_P) of 0.32 at optimal Tip Speed Ratio (*TSR*) of 2.25. The power characteristic of the turbine was further investigated with different blade profiles where there was little variation in power generated, indicating that the *P/D* is a more significant turbine parameter than the blade profile for this particular turbine. Experimental investigations conducted in a towing tank indicated that the turbine can operate with little dependency on the immersion depth. It was also determined that the Hydro-Spinna was able to operate at a half-submerged condition i.e. with half the turbine above the water surface.

Finally, the cavitation and Underwater Radiated Noise (URN) characteristics of the Hydro-Spinna turbine were measured in a cavitation tunnel and analysed; the Hydro-Spinna was generally found to operate cavitation free and even in extreme conditions, only tip vortex cavitation was observed. The model scale URN levels measured was scaled up the full-scale and the data compared to a representative reference level recommended by ICES for fisheries research. In normal operating conditions for the turbine, the URN was predicted to be below the acceptable threshold level.

Acknowledgements

"Sunrise offered a very beautiful spectacle; the water was quite unruffled, but the motion communicated by the tides was so great that, although there was not a breath of air stirring, the sea heaved slowly with a grand and majestic motion"

George Grey

الحَمْد لله

Praise and gratitude be to Allah SAW for His blessings, for everything that is bestowed and for everything that is taken. For the trying moments to make me stronger.

Sincere thanks to my supervisor, Dr Rose Norman, for her constructive guidance through this long and winding journey. I'm equally grateful to my second supervisor, Professor Mehmet Atlar, for always pushing me to do my best. I would also like to thanks the Marine Technology staff, particularly the guys down at the lab for their assistance throughout my study.

It had been a very eventful PhD for me, to be diagnosed with Multiple Sclerosis after a year on this journey was far from ideal. Through the struggle and the hardship, I found two friends for life, the amazing South East Asian girls, Vita Rumanti Kurniawati and Serena Lim Shiou Yuan for always, always being there to take care of me and cheer me up. I would like to thank my colleagues for their friendship and endless support, my tidal buddy Weichao Shi, Batuhan Aktas, Serkan Turkmen, Emmanuel Irimagha, Ayman Badawy, Alaa Balkees, Maria Syrigou, Maria Prodromou and last but not least Yanti Puasa for bringing a little taste of Brunei in Newcastle. Special mention goes to Carol Richards and the nurses of Ward 15, RVI and Lizzie Vinnicombe of the Students Wellbeing office for keeping my health in check.

I'm forever indebted to the support of my family, especially my mum, for her love and sacrifice. For jumping on a plane the minute she learnt about my illness and for keeping up with me through my lowest moments. To my siblings, thank you for the prayers and love. To my pillar of strength, my nephews and nieces, for making life enjoyable that there are so many reasons to be happy. I'm forever grateful and blessed. For you, a thousand times over. I love you so much.

List of Publications

1. Rosli, R., Norman, R., Atlar, M. (2016): **Experimental investigations of the Hydro-Spinna turbine performance**. Renewable Energy. Volume 99 pp 1227 – 1234.

Conferences Attended

1. Rosli, R., Norman, R., Atlar, M. (2014): **Computational Investigation using a simple RANS model on the performance of a novel marine turbine: Hydro-Spinna**. GRAND Renewable Energy Conference together with the 2nd Asia Wave and Tidal Energy Conference. Tokyo, Japan. 27th July – 1st August.

2. Rosli, R., Shi, W., Norman, R., Atlar, M. (2015): **Cavitation tunnel investigation on the performance, cavitation and noise generation of marine current turbine: Hydro-Spinna**. The 4th International Conference on Advanced Model Measurement Technologies for the Maritime Industry. Istanbul, Turkey. 28th – 30th September.

Table of Contents

List of Figures

List of Tables

Nomenclature

Ω	Angular speed
p	Apparent order of accuracy
e_a^{21}	Approximate relative error (fine grid)
e_a^{32}	Approximate relative error (coarse grid)
A	Area of turbine
β	Blade pitch angle
σ	Cavitation number
σ_{FS}	Cavitation number (Full-Scale)
C	Chord length
C_P	Coefficient of power
C_Q	Coefficient of Torque
C_T	Coefficient of Thrust
ρ	Density
∇	Del operator
D	Diameter
μ_t	Eddy viscosity
Δf	Frequency Bandwidth
h	Grid size
g	Gravitational acceleration
H_M	Height of mercury
H_I	Immersion depth
δ_{ij}	Kronecker delta

P_L	Local pressure
k	Mean kinetic energy
N	Number of cells
GCI_{fine}^{32}	Coarse-grid convergence index
GCI_{fine}^{21}	Fine-grid convergence index
a	Radius/Scaling factor
ε	Rate of dissipation
r	Reference distance
r_{ab}	Refinement factor for GCI
W	Relative velocity
f_b	Resultant body force
n	Rotational speed
ϕ	Solution for grid
SPL	Sound Pressure Level in 1 Hz band relative to 1µPa at 1m
SPL_{N}	Sound Pressure Level (Nett)
TSR	Tip Speed Ratio
SPL_{T}	Total Sound Pressure Level (Total)
SPL_1	Sound Pressure Level in 1 Hz band relative to 1µPa
SPL_{M}	Sound Pressure Level in 1/3 Octave band relative to 1µPa
S	Strain
τ	Stress
θ	Swept angle
T	Thrust
Q	Torque
SPL_{T}	Total Sound Pressure Level

ω	Turbulent frequency
P_O	Undisturbed upstream pressure
U_O	Upstream velocity
P_V	Vapour pressure
V	Velocity
ΔV	Volume
U_W	Wake velocity

CHAPTER 1. INTRODUCTION

1.1 General Remarks

This chapter introduces the significance of renewable energy particularly tidal energy development in today's global energy consumption in Section 1.2. Section 1.3 identifies the research gap while Section 1.4 states the aim and objectives of this research. An overview of this thesis is provided in 1.5.

1.2 Energy use and concerns

The 2015 United Nations Conference on Climate Change, that took place in Paris, acknowledged that the world is in an environmental crisis and called for immediate action to remedy the situation. Climate change is real; hundreds of years of human activities, dating to the industrial revolution is steadily increasing earth's atmospheric temperature and inducing extreme weather conditions. Fossil fuels became the key ingredient driving forward the world's industrialisation and modernisation. Energy is a necessity, and the desire for a better livelihood and standard of living required more energy to be generated and consumed. The burning of fossil fuels for this purpose emitted greenhouse gases such as carbon dioxide that are now trapped in the earth's atmosphere. These gases increase the earth's temperature causing global warming, triggering unstable weather systems and putting our habitat in jeopardy.

In Paris, countries declared their commitment to a climate agreement of energy usage that will meet a maximum target temperature rise of 2^{o}C with recommended level of 1.5^{o}C since the industrial revolution (Climate Vulnerable Forum, 2015; United Nations, 2016; United Nations, 2017) instead of the current energy trend that will see a critical rise of 3^{o}C, a catastrophic level according to scientists (Spratt, 2010). The climate change commitment also requires countries to be carbon neutral by the final half of the century, hence expecting carbon emissions to peak in the foreseeable future. On top of that, the global fossil fuel reserves, including coal, are expected to peak by 2030 (Moriarty and Honnery, 2012). Pre the Paris

agreement, the global energy demand was expected to increase by 56% in the next three decades mainly contributed from the two rapidly growing economies of China and India (Zhou, 2013).

In the EIA (2017a) report, with the current policies and regulations in place, the energy related carbon dioxide emissions are projected to increase by 34% by 2040 which would contribute to more global warming. In other findings by the Renewable Energy Policy Network for the 21st Century, 2016 was the third year in a row where the carbon dioxide level remained stable even with the 3% increase in the global economy (REN21, 2017a). Even with the encouraging development towards tackling climate change and the growing transition to a sustainable energy production presented in Figure 1.1, it is still believed that with the current pledges from the Paris agreement the world will still see the 2°C threshold passed which calls for more commitment and efforts from the stakeholders.

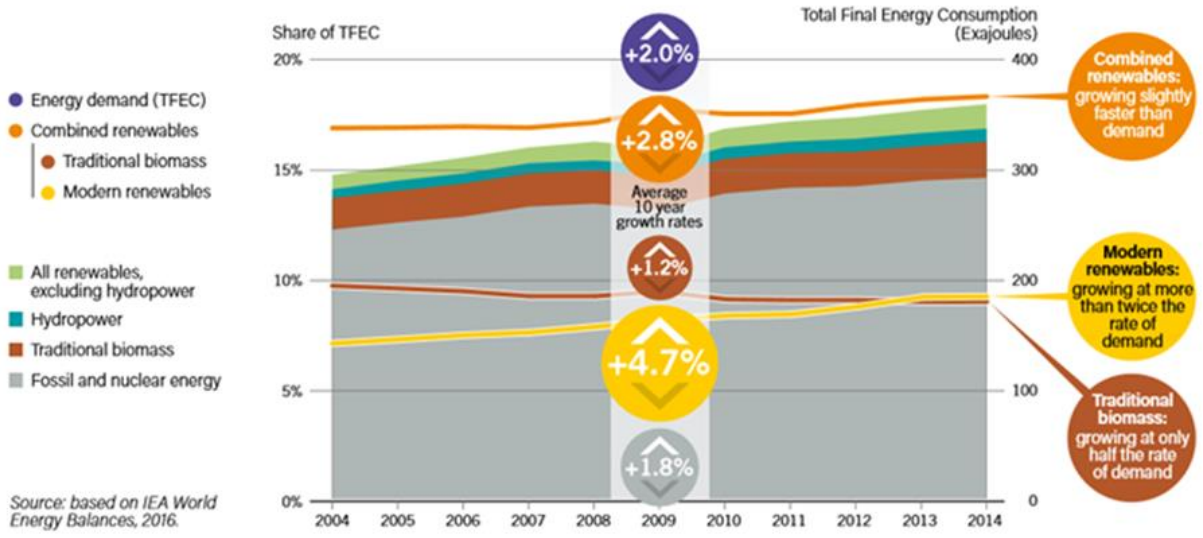

Figure 1.1 Share of renewable energy generation in the Total Final Energy Consumption (TFEC), from 2004 to 2014 (REN21, 2017a)

Global oil has been in overproduction recently and the demand had been low, causing oil prices to fall to plunge to USD29 per barrel (Reuters, 2016; Klann, 2017). Reduced demand because of weakened economies and more energy efficient technologies are two reasons for the fall. With the lure of cheap oil prices and established fossil fuel energy generation, this may divert stakeholder's priorities from looking into newer technologies including further

investment in renewable energy technologies. However, the Paris agreement stands and countries are committed to achieving their energy and climate change targets.

Renewable energy is widely recognised as an alternative to fossil fuel energy generation that is sustainable and less environmentally invasive. However, the general reliance on fossil fuel energy generation has dominated the progress in renewable energy development in the overall energy hierarchy. It is estimated that 13 – 17% of the world's energy supply is generated from renewable energy resources and the number is expected to grow with ongoing research and development in renewable energy system and technologies, (Gross *et al.*, 2003; Teske *et al.*, 2010). In more recent data, renewable energy generation was found to have increased by up to 9% in the year from 1856 GW to 2017 GW by 2016 (REN21, 2017b). Moreover, in 2016, the renewable energy sector contributed 62% of the new energy generation capacity globally.

Nuclear energy is seen as another alternative source of energy that can meet the climate change challenge having contributed up to 371.8 GW which corresponds to about 12.3% of the global energy supply at the end of 2011 and beginning of 2012 (Rogner, 2013). However, the issue of safety and radioactive waste remains a concern where the accident in the 2011 Japan earthquake has slowed down the progress of nuclear energy development all around the world and has further diminished the public's trust. Nonetheless, in 2015 the global energy supply from nuclear power increased to 382.9 GW with the addition of 10 new reactors, giving a total number of operational reactors of 441 (IAEA, 2015). This indicated an increase in nuclear power generation of up to 2.89% from 2012 to 2015. Renewable energy generation has grown by 9% in a year in the period from 2015 to 2016, as reported earlier, indicating a more progressive development. The U.S Energy Information Administration recently reported that the country's renewable energy electricity generation has surpassed that of the nuclear production in March and April 2017, which reflects the growth in renewable energy, although it could also be due to maintenance and refuelling schedules in the nuclear plants shown in Figure 1.2 (EIA, 2017b).

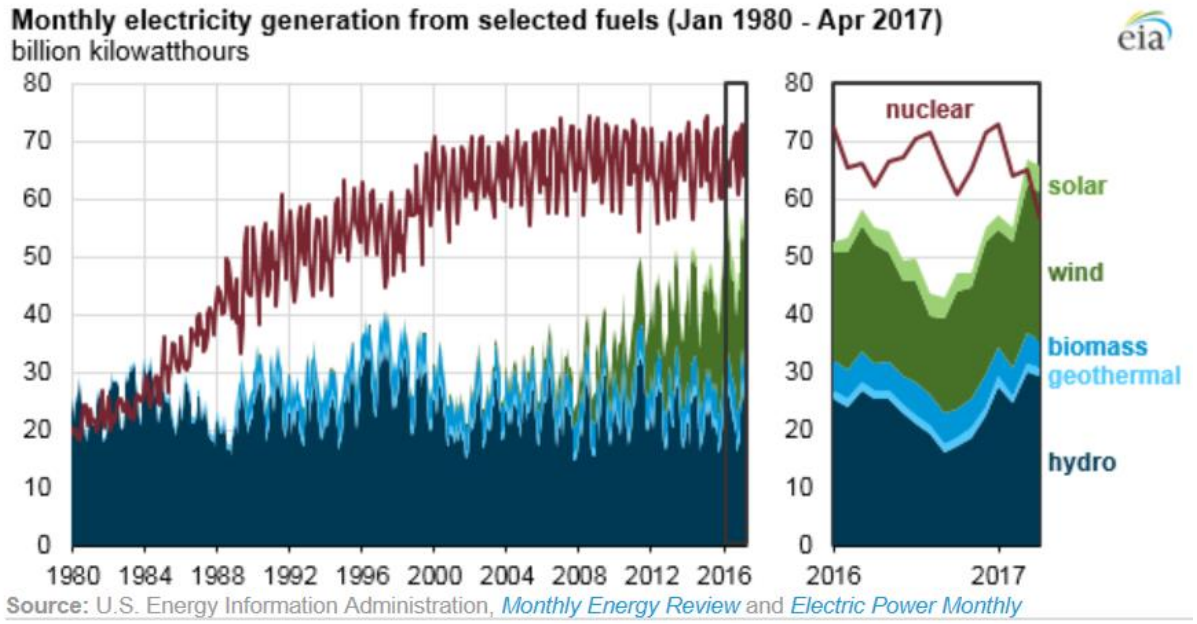

Figure 1.2 USA's monthly generation seen renewable energy surpassing nuclear power generation in March and April 2017 (EIA, 2017b)

The global energy supply has the potential to be met by energy generation from renewable resources alone. Renewable energy resources are defined as the energy primarily generated by the sun. The most obvious form of renewable energy is solar power, where it is used for both heating and cooling spaces as well as generating electricity by means of photovoltaic cells. Wind energy, another established source is growing rapidly, where in the UK alone, wind saw a 13% increase in generation from 2013 to 2014 (DUKES, 2015).

One would have thought that, as long as the planet is inhabitable, renewable energy resources would always be available. Climate change suggests renewable energy as a possible solution, however, climate change itself has an impact on the renewable energy resources. The intermittent nature of renewable energy resources, at its best, is already a constraint. The impact of climate change will not only restrict the availability of these resources but also their quality. Obvious effects will be on solar, hydro, biomass, wind and wave as these resources rely heavily on the global climate and weather patterns (Moriarty and Honnery, 2011). Nonetheless, what needs to be realised from the Paris agreement is that the environmental factor calls for desperate action for the world to be independent from fossil fuel energy generation.

Besides established renewable energy generation, such as solar and wind energy, tidal energy has the potential to contribute significantly to a global energy solution as 71% of Earth's surface is covered in water. The worldwide potential for tidal energy resources was estimated to be 1.5 times the current world energy usage in 2006 (Ferro, 2006). The wave energy potential in the UK is greater than that of tidal (Westwood, 2007) however, wave energy conversion devices are subjected to a harsher environment in addition to the unpredictability of wave generation. The global tidal energy potential is estimated to generate 500 to 1000 TWh/year, where the United Kingdom, strategically located between the Atlantic Ocean and the North Sea, has potential production of 50.2 TWh/year (Pelc and Fujita, 2002).

The UK is understood to contribute to 27% of tidal energy development globally (DIT UK, 2014). Half of Europe's tidal energy resources was estimated to be possessed by the UK alone where the potential resource of 25 to 30 GW could meet 12% of the country's electricity demand (DBEIS UK, 2013). In the Renewable Energy roadmap published by the Department of Energy and Climate Change UK, the 4 MW wave and tidal capacity currently generating are projected to increase to up to 300 MW by 2020 (DECC UK, 2013). Globally, tidal energy had contributed up to 536 MW by the end of 2016 (REN21, 2017b).

Tides are the rise and fall of earth's water, within a constant period of time due to the periodic movement of the moon around earth. Tide generation is highly predictable as it is produced by the gravitational pull of the moon, hence tidal energy is predictable too. With its predictable nature, it is easier to deploy tidal energy conversion devices specific to the resources available at a location. Moreover, unlike other renewable energy resources, tidal energy can deliver electricity for base power by installing various identical farms with fixed offset flow period (Lago *et al.*, 2010). As tidal energy offers a more predictable energy generation, the arrangement of energy supply to grid power can be better managed.

Renewable energy resources including tidal energy are scattered and geographically dependent and, unlike fossil fuels, the resources are not transferrable. When identifying tidal site potential, researchers need to consider both the overall energy potential possessed in the free stream flow as well as the amount of energy that can realistically be extracted from the flow (Ng *et al.*, 2013). High potential sites are often very remote. They are usually located in deeper water, in the harsh sea environment away from civilisation, meaning that the total tidal energy potential is unlikely be entirely realised. In the literature, the only site assessments are

for tidal channels in which the deployment of tidal turbine fences have the potential of achieving a higher than the Betz Limit power coefficient due to restriction of the flow in the channel (Garrett and Cummins, 2007; Garrett and Cummins, 2008; Vennell, 2012a; Vennell, 2013). Although the assessment of tidal site potential for the open sea has not been found in the literature, it is understood that, due to the unrestricted dimensions of the tidal site, the power potential of the site is only dependent on the efficiency of the overall hydrodynamic performance of the turbines.

The UK and Europe are the major leaders in the research and development of marine energy. It is only fitting as the region is strategically gifted with vast marine resources ready to be exploited. The UK, for example, is the home of the established European Marine Energy Centre, EMEC, responsible for the development and deployment of scaled and prototype wave and tidal energy devices (EMEC, 2013). The centre, located in the Orkney Islands in Scotland is the nucleus for the development of wave and tidal energy systems with various prototype energy conversion devices being tested in open water conditions. The site has remarkable wave and tidal energy resources with average wave height of 2.5 m and tidal current velocity of 3.7 m/s (EMEC, 2013). Most tidal current turbines tested at EMEC employ the conventional horizontal axis tidal turbine design that is similar to the established design in wind energy. Due to the reliable performance of horizontal axis wind turbines; the design is generally replicated for tidal energy since both wind and tidal currents are fluids and obey the same fundamental law albeit with a few differences.

1.3 Research gap and contributions

As tidal current energy technology is relatively new, it offers interesting range of design concepts and energy conversion principles and has not settled on a standard design unlike the wind turbine. With the variety of tidal energy converter designs, there is a need for an appropriate research and development (R&D) to exploit their true potential. Inspired by the recent global tidal activities and those in the UK in particular, a novel horizontal axis tidal turbine, which is named *"The Hydro-Spinna"* has been explored and further developed at Newcastle University presenting a unique design. As introduced by its originator, Mr Mike Gilbert based on observations with various wind spinning devices, the blades of the turbine have a cardioidal shape that twist around a common axis like a helix (Lin, 2009; Wen, 2011).

At present, there are no other devices similar to the Hydro-Spinna being developed. With the unique design presented by the Hydro-Spinna turbine, there is a need to explore its true potential and capabilities as a marine current turbine, since its initial observations had only been in wind ornament application. In order to assess its hydrodynamic potential, the scientific approach at this stage may require model testing and numerical investigations to determine its power performance as well as other hydrodynamic performance characteristics such as cavitation and noise measurements.

Based on the initial observation of its design ability to rotate in low wind speed, the Hydro-Spinna is believed to be able to operate in low flow velocity environment. There is a potential for the Hydro-Spinna to be deployed in low flow velocity sites such as river applications. Additionally, with river applications, water depth is a factor one needs to consider, therefore it is essential to evaluate the Hydro-Spinna performance at different immersion depth as well. Most marine turbines are deployed in a high tidal potential site such as that in the EMEC location in Orkney, Scotland. Figure 1.3 presents the potential tidal locations all around the world. Hence, if the Hydro-Spinna is proven to be able to operate at low velocity and low water depth application, it may be able to offer a diverse application where majority of marine current turbines at present are deployed in high flow velocity site.

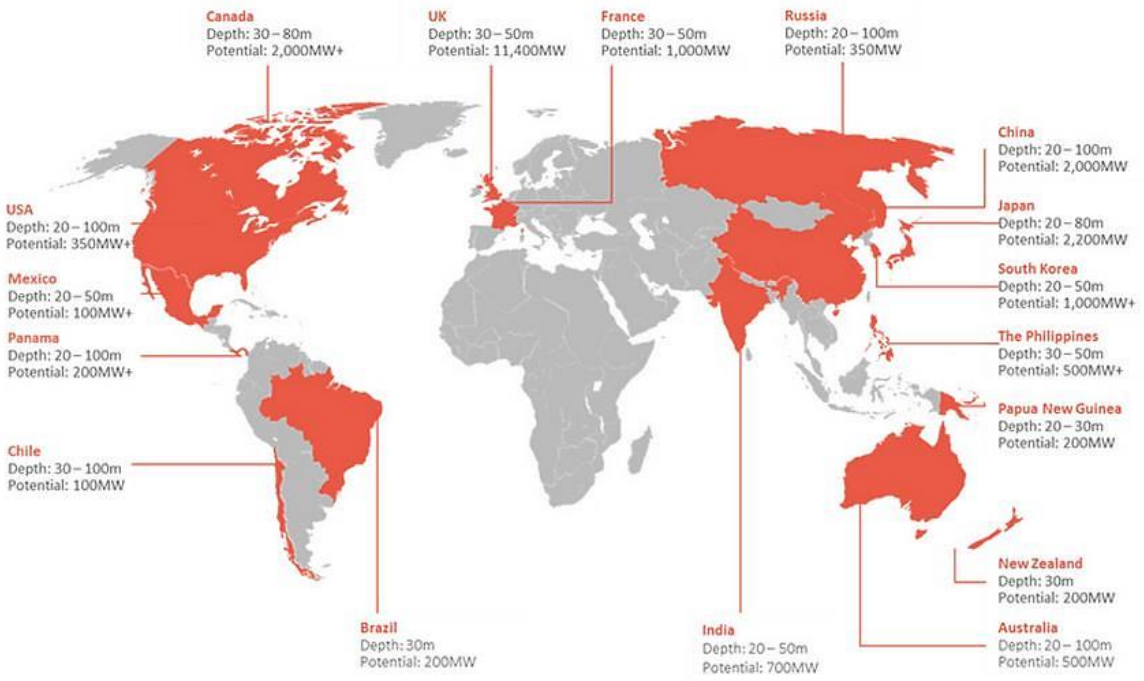

Figure 1.3 Countries of prospective tidal sites with water depth and potential capacity stated (Tidal Energy Today, 2015)

1.4 Aims and objectives

The research presented in this thesis aims to explore the potential of an innovative Horizontal Axis Tidal Turbine (HATT) design, the Hydro-Spinna, and further develop it as an efficient energy conversion device. The specific research objectives are as follows: (1) to define the turbine geometry and concept, (2) to conduct experimental investigations and produce validated numerical models (3) to investigate the variation in performance of the Hydro-Spinna with turbine parameters, specifically with different pitch length to diameter ratio (P/D), (4) to investigate the turbine performance with free-surface interaction, (5) to investigate the turbine performance in terms of Underwater Radiated Noise, (6) to investigate the cavitation behaviour of the Hydro-Spinna, and (7) to investigate the influence of different blade profiles on the turbine performance.

1.5 Thesis outline

Chapter 1 – Introduction

Chapter 1 provides an introduction to the potential and contribution of renewable energy, and specifically tidal energy, to the energy supply worldwide. It also looks into the potential contribution and deployment of the novel turbine presented in thesis. The chapter presents the main aim and objectives of the thesis as well as the outline and brief summary of individual chapters.

Chapter 2 – Literature Review

A literature review is presented in Chapter 2 to identify methodologies and approaches to be taken for this thesis. The general theory and progress of tidal energy are discussed along with the diversity in tidal energy converters that can be found either in concept designs or actual sea deployment. Their performances and contributing factors are also discussed in this chapter. In addition, resultant issues such as cavitation and increased noise level are also considered.

Chapter 3 – Novel Marine Current Turbine: Hydro-Spinna

The novel marine turbine, the Hydro-Spinna is introduced in Chapter 3. The basic design concept is discussed where key turbine parameters are introduced. Three designs have been considered since the introduction of the concept design by the turbine creator, Mr Mike Gilbert. All three concepts and their performance as investigated by previous researchers are discussed.

Chapter 4 – Numerical Investigation of the Turbine *P/D* Parameter

Chapter 4 investigates perhaps the most important design parameter of a turbo-machinery, the pitch to diameter ratio (P/D) for the Hydro-Spinna turbine and its consequences on the turbine performance. The aim of this numerical investigation was to assess the most favourable P/D parameter over a practical range selected for this turbine from the hydrodynamic performance efficiency point of view. The numerical model and physics used in this

investigation and in the rest of the numerical investigations involved in this thesis are described in this chapter.

Chapter 5 – Free Surface Interaction with the Hydro-Spinna Performance

The first part of Chapter 5 explores the effect of varying depths of submergence of the horizontal shaft axis of the Hydro-Spinna on the turbine performance through detailed experimental investigation in the towing tank of Newcastle University. The test facilities and set up are described and the findings are presented. The second part of the chapter reports the same investigation but using numerical modelling by employing the Reynolds Average Navier-Stokes (RANS) equations in combination with a commercial Computational Fluid Dynamics (CFD) software package. The experimental and numerical results were compared in order to validate the numerical model. The numerical model was further used to analyse the wake behaviour of the turbine with the boundary proximities at different shaft immersion depths.

Chapter 6 – Performance of the Hydro-Spinna HS280 Turbine

Chapter 6 involves the hydrodynamic performance evaluation of the optimized 280 mm diameter Hydro-Spinna turbine (HS280) from the efficiency (power coefficient), cavitation and URN point of view in the Emerson Cavitation Tunnel of Newcastle University. The facilities and experimental set up are presented and the investigation was used to validate the numerical performance prediction performed by a previous researcher using Blade Element Momentum Theory (Wen, 2011). URN levels were measured and cavitation observation carried out and based on these findings, further noise and cavitation observation analysis are carried out in the next chapter. A numerical model using Large Eddy Simulations (LES) was developed and the results compared to the experimental data. The numerical model was further used to investigate the variation of power performance with different blade profiles.

Chapter 7 – Cavitation and Radiated Noise Level of Hydro-Spinna Turbine

The purpose of Chapter 7 is to analyse the measured URN levels in the previous chapter with a specific emphasis on the cavitation observations. In the same chapter the model scale

URN levels were extrapolated to a full-scale turbine with three representatives but different turbine diameters to evaluate the URN in full-scale against some useful URN criterion available in terms of Sound Pressure Levels (SPL).

Chapter 8 – Conclusion and Recommendations for Future Work

This chapter concludes the thesis and the design and hydrodynamic characteristics of the Hydro-Spinna turbine. This is followed by recommendations for future work for further development and real sea deployment of the turbine.

CHAPTER 2. LITERATURE REVIEW

2.1 Tidal Energy

Unlike other renewable energy resources, tidal energy is generated by the gravitational pull of the moon. Although the sun has a small part to play in tide generation, it is safe to say that tidal energy will not be susceptible to climate change except maybe the small impact to be caused by the change in sea level globally. Tides are the rise and fall of earth's sea water, within a constant period of time due to the periodic movement of the moon around the earth. Basically, there are two distinct movements of the tides, the vertical rise and fall of water level and hence resulting horizontal flow of water and more commonly known as marine or tidal current. Marine currents are generated due to the flow of water during the process of flood and ebb tides.

The gravitational pull of the moon creates two bulges, where the oceanic water of earth is stretched towards the moon. One of these bulges is created at the location facing the moon and another is on the other side of earth, directly opposite the first bulge. The bulge facing the moon is slightly ahead of it due to the friction with the earth's surface caused by the earth rotating about its axis as illustrated in Figure 2.1. As the moon completes one revolution around earth every 27.3 days, the rise of the tide varies each day by a period of approximately one hour. The earth experiences daily diurnal and semi-diurnal tides, with periods of approximately 24.8 and 12.4 hours respectively, as it revolves around its axis.

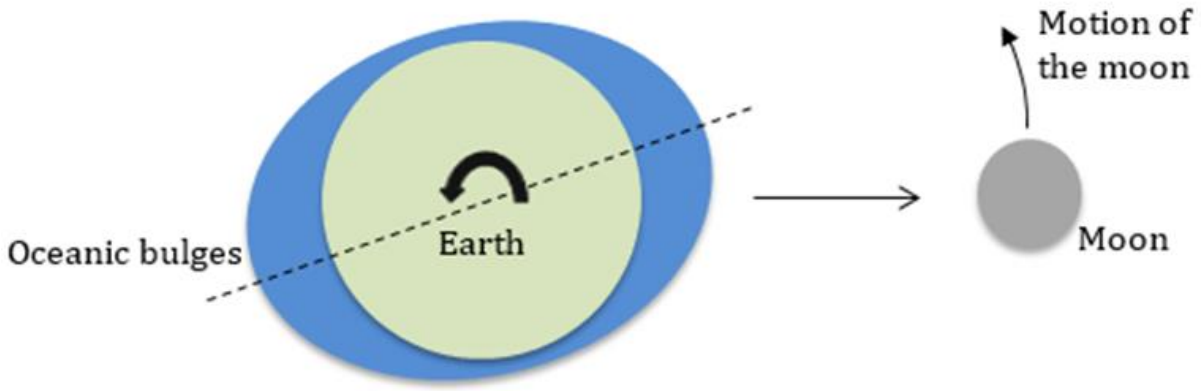

Figure 2.1 Illustration of the two oceanic bulges created by the gravitational pull of the moon

In addition to the lunar tide, the contribution of the sun's gravitational force, the solar tide, and its interaction with the gravitational pull of the moon on the earth creates spring and neap tides. When the earth, moon and the sun are in-line with each other, during new and full moon, the combined gravitational pull of both the moon and the sun on the earth is much higher than that of the gravitational pull from the moon alone creating Spring tides as illustrated in Figure 2.2. The tidal range is approximately 1.5 times of that of only the moon in a Spring tide and marine current velocities can reach up to 3.5 to 4 m/s (Aly and El-Hawary, 2011).

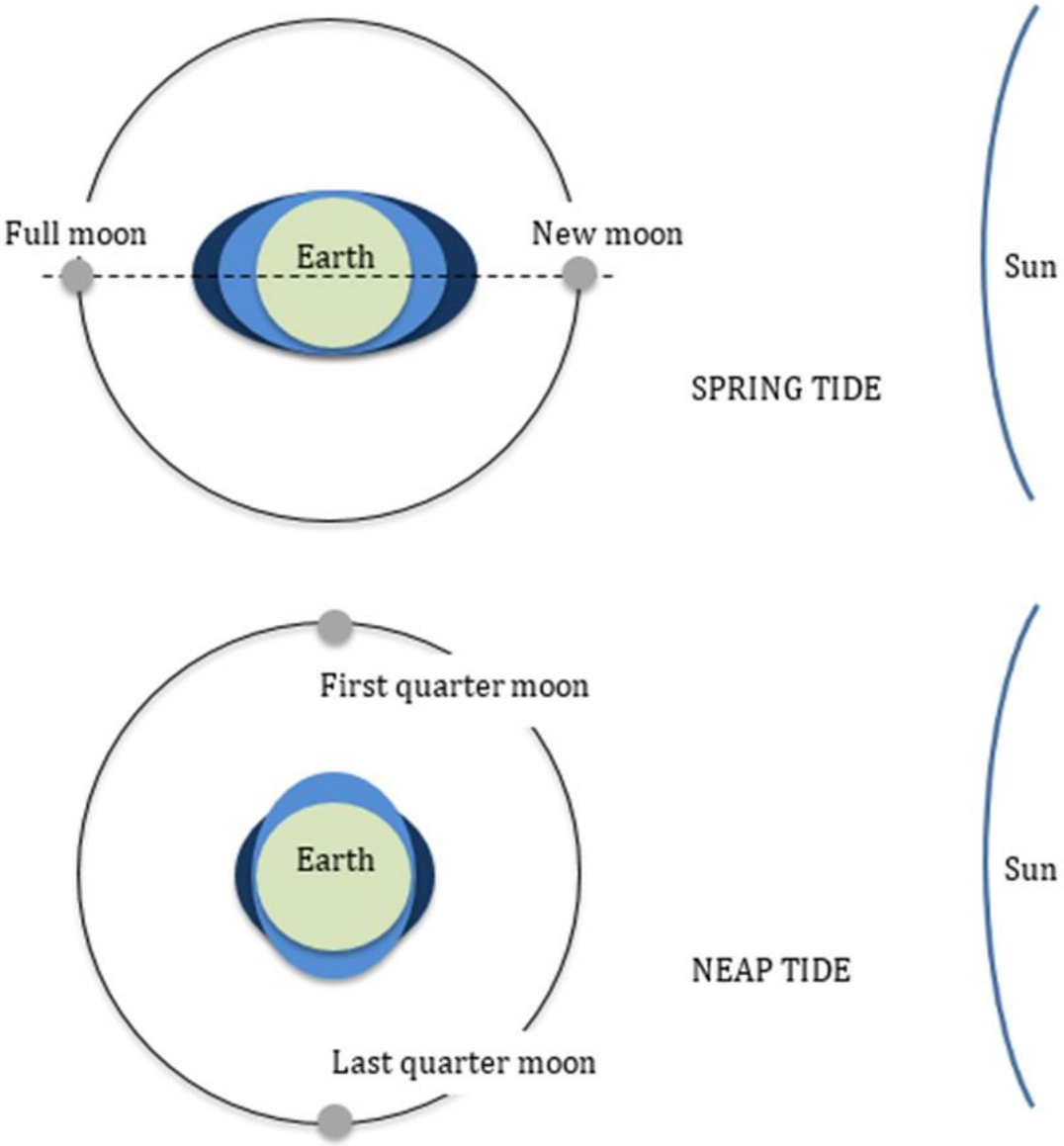

Figure 2.2 Position of the moon, earth and sun during Spring and Neap tide.

When the moon and the sun are perpendicular to each other, in relation to the earth, the gravitational pull of the tides by the moon is reduced due to the sun pulling the tides in the normal direction hence creating a Neap tide. The tidal range in this case is about half of the lunar tide alone. The Neap tide current velocity is between 2 and 2.5 m/s (Aly and El-Hawary, 2011). The Spring and Neap tides occur on an approximately 14-day cycle, half the duration of the moon's orbit around the earth.

2.2 Tidal Energy Technologies

Tidal barrages are the traditional way of harnessing the energy from the tides by utilizing the vertical rise and fall of the tides and the potential energy available. Barrages work on a similar principle to a hydropower dam except that the flow is bidirectional making it possible for both flood and ebb tides to be exploited. Similar to hydropower, the tidal turbine in a tidal barrage is a reaction turbine that operates due to the pressure head in the stream. There are five major tidal barrages in operation in world as listed in Table 2.1 although there are numerous potential sites identified. Issues contributing to the lack of development of tidal barrages include the high cost involved in the civil construction and environmental impacts (O Rourke *et al.*, 2010). The Severn barrage project for example had been deemed to be economically unfeasible, disruptive to the maritime activities, and endangering local wildlife and environment (Harvey, 2013; Binnie, 2016)

Table 2.1 Major tidal barrages in operation (O Rourke *et al.*, 2010)

Tidal barrage	**Mean range, m**	**Basin area, km^2**	**Potential mean power, MW**
La Rance, France	8.4	22	240
Annapolis, Canada	No data	No data	20
Kislaya Guba, Russia	2.4	2	2
Jangxia Creek, China	7.1	2	No data
Sihwa Lake, S. Korea	5.6	30	254

As with a hydropower plants, tidal barrages disturb the transportation of sediments, marine diversity and water quality (Baker, 1991; O Rourke *et al.*, 2010; Esteban and Leary, 2012). Further drawbacks include significant changes in water level, changes in water quality, pollution and noise. Tidal barrages can also hinder human and maritime activities and may restrict development of other renewable energy opportunities (Hooper and Austen, 2013).

However, tidal barrages do present benefits such as protection against flooding and may be useful especially in low lying and flood risk areas. The Sihwa Lake tidal power plant was constructed partly to remedy the water quality issues introduced by the construction of an embankment and man made fresh water lake for agricultural, industrial and recreational use and mainly to maintain the lake at sea level. The construction of the plant not only offered a sustainable power generation but allowed low lying areas to be reclaimed (Bae *et al.*, 2010; Cho *et al.*, 2012). In addition, the new Swansea bay tidal lagoon project was proposed to revitalise the local marine ecosystems and its dependent industries as well as creating a venue for sports and recreation (Waters and Aggidis, 2016; Tidal Lagoon Power, 2017).

A less environmentally invasive technique of extracting power from tides is by exploiting the kinetic energy available in the marine current flow. Unlike wind energy where the energy conversion devices are pretty much homogenous, the same cannot be said about tidal energy conversion devices. Being a relatively new area of research, tidal energy technologies offer an interesting range of design concepts and energy conversion principles. Marine current technologies are less invasive to the marine environment, much smaller in size and capacity than tidal barrages. Nonetheless, several marine current devices can be deployed in arrays to increase the power generation.

Even though the development of tidal energy technologies and systems is steadily advancing, it still needs to overcome a few barriers which are restricting its progress. Designers and developers need to evaluate the technical design and performance of their devices, in addition to the ease of construction, operation and maintenance. The environmental repercussions, although minor compared to those of tidal barrages, method of installation and power transmission method also need to be considered (O Rourke *et al.*, 2010). However, developers of marine current devices can use the knowledge and experience of other established marine technologies such as the oil and gas industry to simplify these processes (O'Sullivan *et al.*, 2013; Ossai *et al.*, 2014).

Marine current conversion technologies are generally categorised in three groups, namely horizontal axis tidal turbines (HATT), cross flow or vertical axis turbines and non-turbine devices (Khan *et al.*, 2009) as illustrated in the examples in Figure 2.3. The fundamentals of HATT are similar to those of the horizontal axis wind turbine where the axis of rotation is in line with the direction of marine current flow. The rotor can either be located upstream or downstream of the turbine hub in the top third of the water column away from any seabed disturbance (Marine Current Turbines, 2013; Ocean Flow Energy, 2013). Whereas seabed mounted tidal turbines exploit the tidal flow on the bottom third of the water column and pose no risk to shipping traffics (Hammerfest Strom, 2013).

Figure 2.3 (from left to right) Evopod tidal turbine, an example of a floating HATT, Stingray, harnessing energy by oscillating hydrofoil concept and Gorlov helical turbine, an example of a vertical axis turbine (Google image, 2017)

Cross flow or vertical axis turbines have their axis of rotation perpendicular to the flow and can also be at an angle with respect to the free surface. Non turbine devices, here onwards termed as non-conventional devices, have a great diversity in design concepts, including oscillating hydrofoils, flutter vane, vortex induced motion, hydro venture devices, piezoelectric, paddle wheel systems, sails and many more (Lago *et al.*, 2010). Since the devices harness the kinetic energy of the water flow regardless of whether the flow originates from tides or ocean currents, the term tidal current is hereinafter called marine current to encompass their different sources in general.

2.3 Horizontal Axis Tidal Turbines

The principles of horizontal axis tidal turbines are similar to those of horizontal axis wind turbines except that instead of wind, the working fluid is seawater. It is also worth mentioning that unlike the wind, the tidal flow is bounded by the free surface of seas and the seabed. Converging passages such as channels and estuaries further restrict the tidal flow although this results in an increase of the current velocity, therefore increasing its energy density (Bryden *et al.*, 2007). In addition, marine current turbines are smaller in dimensions than wind turbines because of the higher density of water, corresponding to greater power available to extract although they are also subjected to greater thrust which can create undesirable anchorage problems.

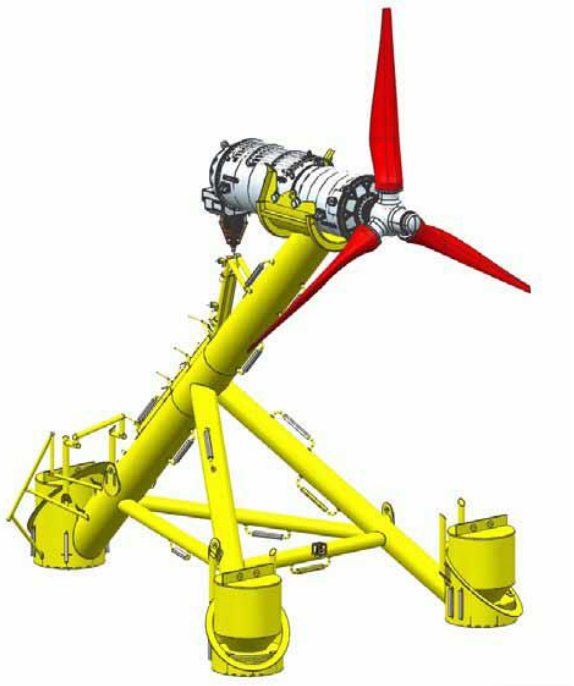

Figure 2.4 Andritz Hydro Hammerfest turbine for seabed deployment (Hammerfest Strom, 2013)

The world's first grid connected marine current turbine was designed and commissioned in 2001 by the Andritz Hydro Hammerfest Strom. This device was a fixed yaw, three bladed HATT rated at 300 kW and called the HS300. The turbine converts the energy from the tidal

stream in both directions by changing the pitch of the blades. The turbine nacelle, housing the power generation system, is mounted on a modular sub structure ballasted to the seabed, as shown in Figure 2.4. A higher capacity turbine, the 1 MW full-scale HS1000, has also been deployed at Orkney Isles as part of the EMEC demonstration project (Hammerfest Strom, 2013). Another seabed based turbine is the OpenHydro turbine which has six projects around the world, and was the first tidal turbine to be connected to the Canadian grid with the Bay of Fundy project (OpenHydro, 2016).

Another example of an HATT is the SeaGen, deployed in 2008, the first OFGEM recognized commercial tidal energy power station in the UK. The SeaGen, shown in Figure 2.5, consists of two turbine rotors mounted on either end of a fully submerged crossbeam that can be elevated up a monopole above the water level for maintenance hence reducing cost and downtime (Marine Current Turbines, 2013). Similar to Hammerfest Strom, the pitch of the turbine rotor blades can be adjusted for operation with marine current coming from both flood and ebb directions. A bigger 20 m diameter SeaGen S turbine rated at 2 MW has been developed incorporating changes and improvement from the first generation turbine deployed at Strangford Lough.

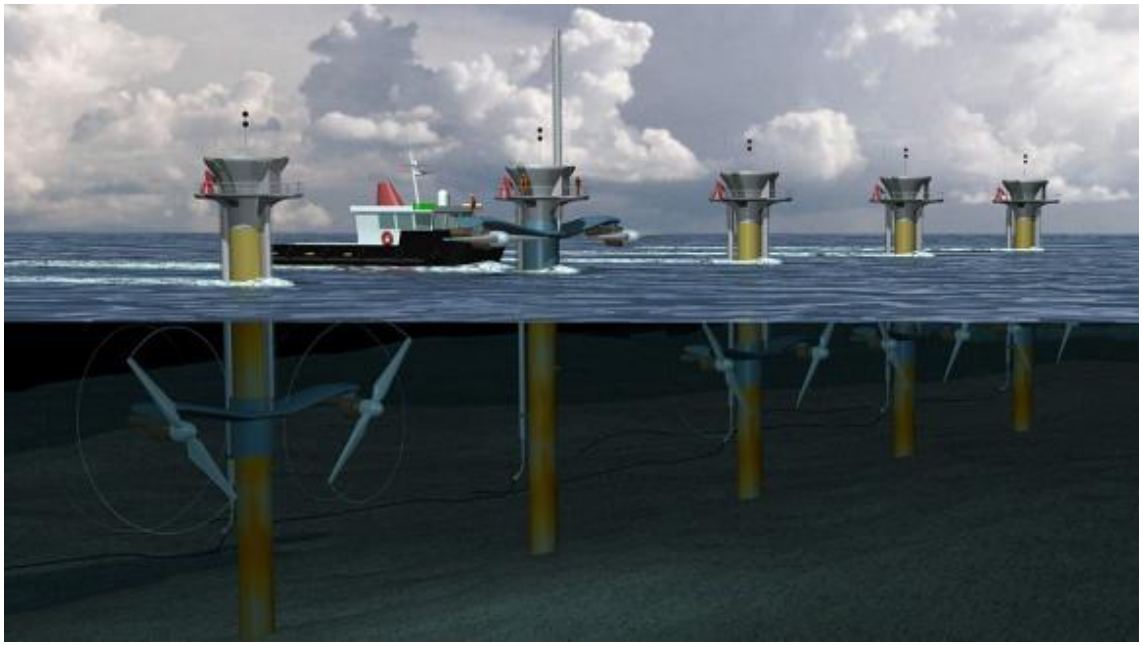

Figure 2.5 Artist impression of the SeaGen turbine (Marine Current Turbines, 2013)

The earlier mentioned turbines were based on a fixed yaw concept and anchored to fixed offshore structures (e.g. to piles or solid foundations). Evopod is another HATT design based on a floating concept and free to yaw. A 1:40th scale model of the single turbine version Evopod was tested in Newcastle University which was later on followed by the design and testing of its twin turbine version. A 1:10th scale prototype of Evopod was later commissioned and installed at Strangford Lough. The prototype had a yawing mechanism to direct the turbine into the direction of the current flow. Evopod is a unique floating turbine, consisting of three struts for stability, moored to the seabed via a catenary spread mooring system (Ocean Flow Energy, 2013). The SR2000 turbine, developed by Scotrenewables, is another floating concept which was funded under the Floating Tidal Energy Commercialisation (FloTEC). Rated at 2 MW, the world's largest tidal turbine was deployed in Orkney in October 2016 (EMEC, 2016; ScotRenewables, 2017).

2.3.1 Performance of Horizontal Axis Tidal Turbine

The hydrodynamic performance of HATT turbines may be estimated using Blade Element Momentum Theory (BEMT) which is analogous to the technique used for horizontal axis wind turbines. The basic principles of HATT turbine operation are similar to those of a horizontal axis wind turbine, with the main distinction being the different working fluid. As mentioned earlier, seawater, which is the working fluid for the marine current turbine, is much denser than air, approximately 850 times the density of air at sea level. Hence, the energy content of the seawater is greater due to its higher density that in turn results in smaller diameter rotors for marine current turbines compared to wind turbines. The hydrodynamic forces experienced by marine current turbines are also greater which requires them to be more structurally sound and robust designs. Other significant differences between the operation of marine current turbines and wind turbines include the difference in operating Reynolds Number, stall characteristics, potential occurrence of cavitation (Wang *et al.*, 2004; Bahaj *et al.*, 2007b; Wang *et al.*, 2007), blade fouling (Walker *et al.*, 2014), blade section designs (Ahmed, 2012), and the wake expansions due to the confinement of the free surface and seabed.

The designs of most existing marine current turbine blades utilise either existing airfoil specifications such as the NACA series or modified versions to suit exclusively to marine energy applications. Due to the conventional design of such turbines, they are limited to

extracting a maximum of 59% of the power available in the unconstrained marine current flow to conform to Betz Theory (Cuerva and Sanz-Andrés, 2005; Masters *et al.*, 2011). Investigations into turbine performance using experimental methods with two blade and three blade HATT were found to obtain maximum power coefficients of 0.43 and 0.46 respectively. Both studies were conducted using NACA 63-xxx series blade designs (Bahaj *et al.*, 2007b; Luznik *et al.*, 2012). Experimental investigations on a 0.7 m model and 2 m diameter full-scale HATT using S809 profiled blades were conducted with maximum power coefficients obtained of 0.30 and 0.388 respectively (Jing *et al.*, 2017). Zhou *et al.* (2017) reviewed the performance of six existing large HATT with maximum power coefficients ranging from 0.34 to 0.45 with detailed results reproduced in Table 2.2 below.

Table 2.2 Performance characteristics of large scale HATT (Zhou *et al.*, 2017)

Turbine	**Rated Power (MW)**	**Rated flow (m/s)**	**Rotor Diameter (m)**	**Estimated maximum CP**
DCNS OpenHydro	2.0	4.0	16	0.34
Atlantis AR1000	1.0	2.65	18	0.41
SeaGen S	2.0	2.4	20	0.45
Voith Hydro 1MW	1.0	2.9	16	0.41
Sabella D10	1.1	4.0	10	0.43
GE Alstrom 1MW	1.0	2.7	18	0.39

2.3.2 Boundary Proximity Effects

Marine current flows are confined by the open sea free surface as well as the seabed topography. Depending on where in the water column the HATTs are deployed, either or both boundaries would influence the current flow behaviour. Turbines are preferably to be deployed in the top third of the water column where the current velocity is the highest according to several vertical velocity boundary profile laws (European Commision, 1996; Burton *et al.*, 2011; Bahaj

et al., 2012). Floating HATT devices such as Scotrenewables and Evopod will certainly benefit from the higher velocity flow available at the top third of the water column but are prone to the free surface effect. In practice however, most of the large scale HATT currently in operation are deployed on the seabed such as the Andritz Hydro Hammerfest HS1000, Atlantis AR1500 and OpenHydro and are therefore susceptible to the seabed effects.

Turbines towards the top of the water column are more subjected to the free surface effects, whereas turbines that are close to the seabed will be more limited by the seabed boundary. In shallower water, both the free surface and seabed effects may need to be considered on the turbine performance. Similarly, turbines placed in a tidal farm will disturb the current flow seen by the other turbines as opposed to having a single turbine deployed in the same flow condition (Stallard *et al.*, 2013).

The locations where the tidal turbines are deployed also have consequences on their performance. Turbines located in a tidal channel, a narrowed passage connecting two large bodies of water, were found to produce higher performance due to the flow being constrained by the topography (Garrett and Cummins, 2007; Garrett and Cummins, 2008). Turbines positioned across a channel creating a tidal fence would each produce higher power than they would when operating as a solitary turbine. It was understood that the turbines increase the blockage ratio across the channel hence forcing a higher velocity flow to pass through the turbines (Vennell, 2012b; Vennell, 2012a; Vennell, 2013).

The presence of the free surface and the seabed alter the flow characteristic of the current by limiting the expansion of the downstream wake. In theory, the turbine extracts the energy from the current flow hence slowing it down by up to a third of the upstream velocity in the ideal condition where a maximum of 59% of the energy can be extracted. The low velocity region, called the wake region, downstream of the turbine expands in an axisymmetric manner as shown in Figure 2.6. The slower wake will mix with the faster free flow outside the stream tube and eventually the flow will recover to its upstream state.

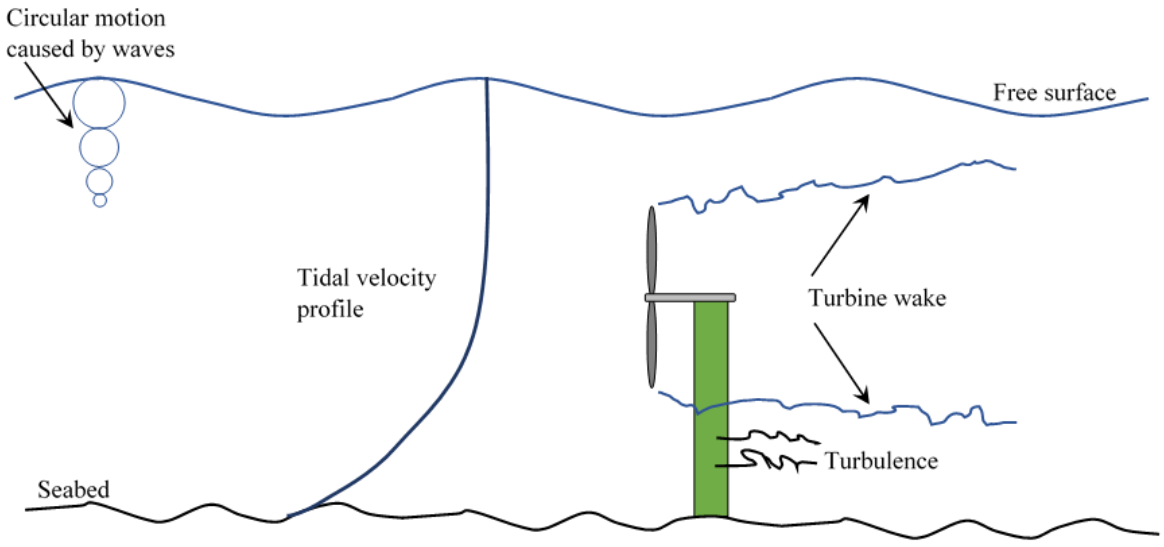

Figure 2.6 Overview of the operation of tidal current turbine and their wake characteristics with the seabed and free surface boundaries including waves

With wind turbines, the downstream wake expansion is unrestricted whereas in tidal current turbines the wake expansion is bounded by the free surface and seabed. Bahaj *et al.* (2012) and Chen and Lam (2014) carried out studies into the effect of boundary proximity on the wake structure for turbines located near the seabed. Due to the low velocity near the seabed, the wake recovers much more slowly because of the lack of higher velocity free stream flow around the wake. Turbines further from the seabed and nearer to the free surface, displayed more active mixing with a larger pressure gradient extended downstream. Moreover, the presence of the boundaries distorted the axisymmetric shape of the downstream wake region.

Investigations of marine turbine wake interactions with the flow boundaries not only encompass studies on single turbines but also the wake interactions of turbines in arrays (Pinon *et al.*, 2012; Chamorro *et al.*, 2013; Stallard *et al.*, 2013). The interactions of turbine wakes in arrays are significant in order to study the effect of the lateral boundaries created by the turbine presence. Moreover, these studies also provide an insight into the optimal lateral and longitudinal spacing of the turbine locations in the array.

2.3.3 Surface Wave

The influence of surface waves on turbine performance have also been investigated showing that the effect of the interaction of surface waves with the marine current on the turbines was insignificant with the results produced being similar with and without waves (Luznik *et al.*, 2013). The study also concluded that torque increases with the vertical velocity component of the wave and that the turbine is operational at a lower tip speed ratio in the absence of waves. Similar results was obtained at lower current velocity (Barltrop *et al.*, 2007) where the torque of the turbine increases in the presence of waves. This study also confirmed the increase in torque with an increase in wave height.

Similar to the free surface having an influence on turbine performance, the operation of turbines will undoubtedly affect the free surface. Operation of tidal turbines is understood to decrease the depth of water downstream of the turbine because of the energy extraction process. In addition, the water surface upstream of the turbine increases due to the slowing down of the flow at and downstream of the turbine (Myers and Bahaj, 2007).

2.3.4 Blockage Effects in Model Testing

In model testing, the proximity of the boundaries of the experimental facilities such as a towing tank or cavitation tunnel will induce a blockage effect where the turbine performance is improved. The increase in performance is due to an increase in the relative current velocity being accelerated by the facilities boundaries. Blockage ratio is defined as the ratio of the turbine swept area divided by the flow area and is usually given in percentage. A full experimental and numerical study on boundary proximity and blockage effects conducted by Kolekar and Banerjee (2015) found that a blockage ratio below 10% has no effect on the turbine performance. Moreover, turbine performance was shown to increase by up to 35% with a blockage ratio of 42% blockage.

A blockage correction factor can be included in the theoretical analysis as well as in experimental data analysis (Whelan *et al.*, 2009; Birjandi *et al.*, 2013) to present the data as closely as possible to the real environment where the constraint is only from the free surface and seabed . An experimental study conducted by (Bahaj *et al.*, 2007b) on the effect of free surface on turbine performance found a reduction in power and thrust as the depth of immersion

of the turbine rotor was decreased from 0.55D to 0.19D, where D is the rotor diameter, due to the limitation of the downstream area for the wake expansion to properly develop. In addition, the slowing down of the flow created a blockage to the flow that affected the turbine performance.

Turbine performance with varying yaw angles was investigated where it was found that the performance and optimum tip speed ratio of the turbine drop as yaw angle increases (Myers and Bahaj, 2006; Bahaj *et al.*, 2007b; Galloway *et al.*, 2011). Research on marine current turbines has now progressed into investigating the interaction of turbines deployed in tidal farms with different array configurations. Configurations of the turbine position take into account the spacing between turbines and wake expansion to optimise the overall performance of the tidal farm. Bai *et al.* (2013b) found that turbines arranged in a staggered manner generated more power than those arranged in rectilinear configuration. Power generation also increased with increasing longitudinal and lateral distances of the turbines from each other.

2.4 Experimental Investigations in Marine Turbine Performance

Actual investigations of marine turbine designs can be costly especially when the designs are still developing. Although some prototypes are being tested in the real marine environment (EMEC, 2013) testing of model scale turbines in controlled facilities are much easier and considerably more economical. There are several studies involving experimental investigations of marine turbines performance found in literature. Bahaj *et al.* (2007b) conducted an experimental investigation on scaled model turbine performance at different operating conditions including immersion depth and turbine yaw angles in a towing tank and cavitation tunnel. Similar performance characteristics of tidal turbine with different hydrodynamic parameters including different flow characteristics was also investigated by Maganga *et al.* (2010) at the IFREMER flume tank facility. Gaurier *et al.* (2013) also conducted a performance investigation at the same facility with different wave and current loadings.

Similar wave current loadings investigations were also performed in addition to the performance characterization with different turbine pitch angle (de Jesus Henriques *et al.*, 2014; de Jesus Henriques *et al.*, 2016). The effect of non-dimensional analysis of turbine parameters to its performance was also carried out by (Mason-Jones *et al.*, 2012).

Fernandez-Rodriguez *et al.* (2014) conducted an investigation on the thrust and drag forces on a model turbine under turbulent flow with and without waves. Work conducted by Wang *et al.* (2004) in the Emerson Cavitation Tunnel, investigated the power performance of tidal current turbines including cavitation tests with further exploration on the noise level generation and slipstream measurement (Wang *et al.*, 2007). A new blade design concept integrating humpback whale tubercles at the leading edge was also investigated in a more recent study to assess the performance of the turbine with such a design (Shi *et al.*, 2016c). Another investigation included the assessment and comparison of power performance between a 700 mm diameter model scale turbine tested in a towing tank and its 2 m full-scale counterpart tested in real sea conditions (Jing *et al.*, 2017).

2.5 Computational Fluid Dynamics in Marine Turbine Development

Alternatively, as well as in supporting roles, assessment of turbine design and turbine performance prediction using computational methods i.e. Computational Fluid Dynamics (CFD) is gaining popularity among researchers. Flow behaviour around the turbine along with the wake behaviour are among the many investigations that can be easily evaluated with CFD. Validation of computational models against experimental data are common. For example, Bahaj *et al.* (2007a) developed a computational model using GH-Tidal and SERG-Tidal software to predict the performance of a tidal turbine which was validated against experimental data. The same experimental results were also used to validate a numerical code using BEMT (Batten *et al.*, 2007; Batten *et al.*, 2008). Experimental data is not only used to validate a computational model, but it can also be used to further investigate the thrust loading on a turbine rotor as well as the wake profile (Olczak *et al.*, 2016). Bai *et al.* (2014) produced a computational simulation to assess the performance of a tidal turbine with free surface effects that was validated against experimental results.

When developing turbine designs, especially non- conventional ones, it is usually convenient for researchers to conduct CFD investigation to assess their designs such as that performed by Ashuri *et al.* (2013) with their development of a combined Darrieus and Wells turbine concept. The flow and performance analysis of an H-Darrieus turbine was also evaluated through CFD in addition to the experimental results. Other computational investigations include a performance evaluation of a new concept cross-flow design

(Gebreslassie *et al.*, 2013), a flapping foil concept (Young *et al.*, 2014), and a shrouded HATT (Sun and Kyozuka, 2012). Shi *et al.* (2016a) also utilised CFD method in combination with the experiments to be able to design and apply tubercles on the leading edges of the HATT blades to improve their hydrodynamic performance.

Investigations using computational methods also include assessment of turbine performance for single turbine deployment (Malki *et al.*, 2013), and tidal farm conditions (Antheaume *et al.*, 2008), influences of surface waves (Saruwatari *et al.*, 2013), and blockage effects on turbine design and performance (Schluntz and Willden, 2015). The effect of turbine parameters on the turbine performance and flow structure were also carried out (Asim *et al.*, 2013) as well as cavitation predictions on a turbine rotor (Silva *et al.*, 2016) using computational modelling. The comparison of the consistency of computational investigations using different hydrodynamic models has also been looked at, such as a comparison between BEMT and Reynolds-Averaged Navier Stokes (RANS) equation models (Bai *et al.*, 2013a).

The abundance of research involving computational simulation using CFD supports the reliability of such a method in tidal turbine and tidal energy investigations. In circumstances where laboratory facilities are not readily available or experiments are difficult to conduct, computational modelling offers an alternative method for a diverse range of investigations concerning tidal turbines and tidal energy in general.

2.6 Cavitation of Horizontal Axis Tidal Turbines

Cavitation is a phenomenon that is well known in the turbo machinery and marine propeller industries, and can have adverse effects on the hydrodynamic performance and structure of their rotors. Cavitation occurs when, while the ambient temperature stays constant, the fluid pressure around the turbine drops until the vapour pressure of the liquid, in this case seawater, is reached. The physics of cavitation is more complex than just the mere vaporisation of liquid. Carlton (2012) stated that cavitation involves the creation of cavities in the moving liquid where cavitation requires the presence of gas nuclei to occur.

Cavitation is a very quick process of the vaporisation and break down of gas bubbles where the shock wave generated by the collapse of the bubbles causes erosion damage to the surface of the turbine blades. The bubble collapse is the main cause of the Underwater Radiated

Noise (URN) while extensive coverage of the blades by the cavitation may also deteriorate the blade performance. Tidal turbines are susceptible to cavitation at certain operating conditions where the turbine blades may suffer from reduced lift and will also limit its operating life due to fatigue (Buckland *et al.*, 2013). Cavitation is generally defined by Cavitation Number, σ, which is derived based on the equality of the local pressure at a point of concern with the standard vapour pressure as given in Equation 2.1. The Cavitation Number describes the liquid resistance to cavitation that will take place at low pressure values which are represented by a non-dimensional pressure coefficient given by Equation 2.2.

$$\sigma = \frac{P_O - P_V}{0.5\rho W^2}$$

Equation 2.1

$$C_P = \frac{P_O - P_L}{0.5\rho W^2}$$

Equation 2.2

where P_O is the undisturbed upstream pressure of the flow, P_L is the local pressure at the point of concern, P_V is the saturated vapour pressure of the liquid, ρ is the density of the liquid and W is the relative velocity of the flow.

At the cavitation inception, the local pressure at the surface of the turbine blade has to be equal to or lower than the vapour pressure. There are different types of cavitation that occur in hydrodynamic systems such as hydraulic, body, hydrofoil, vortex, wake turbulence and jet cavitation as listed by Ross (1976). Hydraulic and jet cavitation are cavitation relating to fluid flow in pipe systems and turbulent flow in jets respectively. While body cavitation is defined as the cavitation on the surface of a submerged stationary body in a flow and wake turbulence cavitation concern with the turbulence eddies in the wake. Hydrofoil and vortex cavitation are more common in propellers and marine current turbines as their inception are both associated with the presence of lift and drag. Cavitation can also be described based on its visual

appearance and location. In marine propellers, various types of cavitation can be observed such as bubble, sheet, cloud and tip vortex cavitation (Atlar *et al.*, 2001; Kuiper, 2012; Lee *et al.*, 2014; Aktas *et al.*, 2016a).

Similar cavitation behaviours have been observed in marine current turbines however, research into turbine cavitation has been relatively limited. Wang *et al.* (2007) conducted a cavitation study on the operation of tidal turbines at three operating conditions i.e. design, pre-stall and post-stall conditions. The scaled study investigated the cavitation behaviour for a full-scale version of the turbine at a design depth of 20 m and a shallow depth of 11 m. Various forms of cavitation were observed at the three conditions: tip vortices were observed at designed and pre-stall conditions with different strengths, whereas in post-stall conditions, sheet and cloud cavitation were also observed and the cavitation was found to be more visible and stronger in the shallow depth condition. In a more recent work in the Emerson Cavitation Tunnel at Newcastle University on a tidal turbine blade comparison between a normal blade design and one with a biomimetic leading edge profile, cavitation observations were also conducted (Shi *et al.*, 2016b). Tip vortex and cloud cavitation both on the face and back side of the turbine blades were observed during the course of the investigation.

The above mentioned work on turbine cavitation observation also collected the noise generation level where there was observed to be an increase in the noise level corresponding to the presence and strength of cavitation. Another study on the performance of tidal turbines at different hydrodynamic conditions also observed various cavitation types including tip vortices, sheet, cloud and a 'horseshoe' cavitation (Bahaj *et al.*, 2007b). Based on these studies, it is clear that cavitation exists in marine current turbine operation and that there is a corresponding increase in the noise level generated. In addition to cavitation observations, various studies have also been conducted on cavitation inception prediction using numerical methods (Batten *et al.*, 2006; Batten *et al.*, 2008; Buckland *et al.*, 2013).

One of the concerns with cavitation observation and inception was that cavitation was found to occur at a lower pressure coefficient than the theoretical value indicating cavitation occurred at higher local pressure than the vapour pressure. A cavitation study on HATT blades conducted by Molland *et al.* (2004) concluded that the numerical calculation under-predicted the cavitation in the experiments. In scaled model tests, cavitation observations may not accurately reflect what would occur at full-scale due to scale effects (Ross, 1976; Bark, 1985).

Billet and Holl (1981) suggested two types of scale effects where one was concerned with the flow characteristics of the fluid such as Reynolds number while the second was to do with scale effects associates with the cavitation bubble growth process such as surface tension and cavitation nuclei which are required for cavitation inception. In laboratory facilities the presence of nuclei can be monitored via the air and oxygen content (Wang *et al.*, 2004). However, when deployed in the actual sea environment, the turbines are subjected to the free flow of seawater where there are impurities and nuclei presence is not regulated. Nonetheless, work on cavitation observations at model scale as well as cavitation inception provides an insight into the operation of marine current turbines.

2.7 Underwater Radiated Noise from Marine Current Turbines

Little is known about the environmental effect of tidal current technology especially on marine life. Marine current technology is however less intrusive than the current energy dependence of fossil fuels. Deployment of marine current turbines is an addition to the already hectic maritime activities. It is acknowledged that maritime activities such as shipping movements affect the marine life specifically with regard to the acoustic aspects (Mitson and Knudsen, 2003; Williams *et al.*, 2015). A study by Halvorsen *et al.* (2011) had also considered the impacts of tidal turbine generated URN on marine life behaviour and existence

The operation of marine propellers, as part of the growing shipping activities, is understood to emit URN which has contributed to the rise in underwater ambient noise (Frisk, 2012). In addition, the presence of cavitation will further increase the noise radiated where different forms of cavitation are understood to influence the noise level differently (Sharma *et al.*, 1990). Since the operation of marine current turbines is similar to marine propellers, it is also believed that their operations will contribute to an increase in the ambient noise level of the subsea environment.

At Newcastle University, various investigations and measurements of URN from marine propellers and turbines have been conducted, including URN level of models tested with and without cavitation (Aktas *et al.*, 2016a; Aktas *et al.*, 2016b; Shi *et al.*, 2016b). Various research projects such as the SILENV (Ships oriented Innovative soLutions to rEduce Noise and Vibrations), AQUO (Achieve QUieter Oceans) and SONIC (Supression Of underwater

Noise Induced Cavitation) have been carried out to explore the impact of URN on the marine environment. In addition, international bodies such as the International Maritime Organization (IMO) and its Marine Environmental Protection Committee (MEPC) are looking into the impact of URN from commercial shipping with the aim of regulating the activity (SONIC, 2012).

Sounds are vital to marine animals' existence. Marine animals use different pitches and frequencies to communicate, mate, navigate and hunt for food. The concern over URN from marine machinery is that it will interfere with the frequencies used by the animals to communicate which will impact their survival (Richardson *et al.*, 2013). Wenz (1972) identified five types of underwater noise which are radiated noise and four sonar categorised noises namely ambient noise, self-noise, target noise and reverberation noise. Ross (1976) also identified five similar types of noise including radiated and ambient noise whilst the other three are sonar related noise. Ambient noise is defined as the reference noise of the underwater environment when external noise sources are removed or minimised. Radiated noise on the other hand is the undesired acoustic output from man-made marine systems, including marine turbines.

A range of research on URN had been carried out including its effect on the marine environment. From investigations on the impacts of URN on marine biodiversity and their behaviours (Brownell *et al.*, 2008; Hawkins *et al.*, 2008; Spiga *et al.*, 2012) to investigations on propellers and shipping noise (Hildebrand, 2009; Williams *et al.*, 2015; Aktas *et al.*, 2016b). URN produced from pile driving noise (Thomsen *et al.*, 2012; Spiga, 2016) as well as from offshore wind turbine operations (Madsen *et al.*, 2006) has also been considered.

Undoubtedly, the increasing deployment of marine current turbines whether as prototypes or established power generation devices will only increase the URN level of the marine environment. Noise level measurements on model scaled turbines have been carried out in the Emerson Cavitation Tunnel (ECT) in Newcastle University to consider the URN profiles from marine turbines with and without cavitation (Wang *et al.*, 2004; Wang *et al.*, 2007; Shi *et al.*, 2016b). Moreover, investigations into turbulence noise generation using numerical methods have also been conducted (Lloyd *et al.*, 2011; Lloyd *et al.*, 2013; Lloyd *et al.*, 2014). The ÆMORE (Acoustic Emission technology for environmental and engineering health Monitoring of Offshore Renewable Energy) project, proposed using Acoustic Emission (AE) monitoring

to detect any impending component failures of marine turbines (Walsh *et al.*, 2015). AE monitoring is used in wind turbines to predict failures providing extensive procedures for predictive maintenance and repair. A similar approach could be implemented in marine turbine technology to monitor turbine operations to avoid the occurrence of severe failures.

Marine current turbines are designed to operate over the range of a tidal cycle. The operation of turbines produce noise over a constant period of time due to the mechanical system involved such as generator and power transmission noise as well as the induced turbulence in the flow. Occurrence of cavitation will further increase the noise level, where the amount of noise generated is the product of the average energy radiated per bubble and the rate of collapse of cavitation bubbles (Ross, 1976). Operation of marine current turbines were found to contribute to the increase in underwater noise as discovered in studies conducted by Rosli *et al.* (2015) and Shi *et al.* (2016b).

Likewise, URN will also be generated during the installation, maintenance and decommissioning stages. Studies from the wind turbines industry have shown that installation of wind farms, including pile driving, disturbed the acoustic range of marine animals causing behavioural changes (Madsen *et al.*, 2006; Bailey *et al.*, 2010). Indeed, URN generated both from turbine and non-turbine operation will interfere with the general ambient acoustic of the marine environment. As there are no studies yet performed to compare the level of URN generated both from the two process, it is difficult to evaluate their impact to the ambient noise. It was argued that even though it happen over a shorter period, URN from non-turbine operations such as pile driving for turbine supporting structures could be more harmful due to the high amount of noise generated (Bailey *et al.*, 2010). On the other hand, as URN from turbine operation could be equally detrimental as it occurs consistently over a long period of time (Bevelhimer *et al.*, 2016).

2.8 Resource assessment of potential sites

When selecting a site with suitable tidal resources, one of the ultimate factors that needs to be considered is the mean kinetic energy flux corresponding to the tidal velocity at the site (Bryden *et al.*, 2007). Additionally, the tidal range is also an important factor in resource assessment. Tidal range and tidal velocities give the potential power that can be exploited. As

tidal turbines extract the energy from the kinetic energy content in the flow, the higher the velocity, the higher the power with the potential to be extracted. It has been stated that marine current energy devices require a spring tide velocity of 2.5 m/s and water depth between 25 and 50 m (Lewis *et al.*, 2015).

In the UK, the average velocity and mean energy flux had been mapped out, although a more detailed investigation needs to be carried out once a specific site is identified. In fact, with any location in the world, once a potential site is identified, relevant data needs to be gathered to identify the resource at the site. The spatial and temporal variability of the site needs to be quantified. Resource assessment of a potential site can be conducted through direct measurements and surveys for the bathymetry (Zhang *et al.*, 2017). Bahaj (2011) suggested that due to the predictability and reliability of tidal energy resource, a month's worth data is adequate to evaluate the available energy potential. In addition, Blunden and Bahaj (2007) reviewed the methodology and justification for resource assessment specifically to maximise power generation using analytical modelling. Canada, China and Norway have produced implementation models for marine turbines which include national and regional resource assessments as well as indicating factors hindering the full potential of marine turbines from being achieved (Sangiuliano, 2017).

Tidal currents are constraint by the seabed and the free surface and hence, although the average velocity is taken for hydrodynamic calculations such as in the power and thrust performance, in reality the velocity varies with the water depth. Therefore, it is also equally important to identify the water depth both in ebb and flood, and also the bathymetry of the site. These two characteristics of the site dictate the size of the turbine to be deployed. The velocity profile is defined by power laws and the one most commonly used is the one seventh power law (European Commision, 1996) as presented in Figure 2.7. Careful consideration of the type of turbine deployed also needs to be made when conducting velocity measurement for resource assessment. For yaw oriented turbines, the turbine axis is always in line with the direction of the flow whereas for a fixed turbine, the axis of the turbine may not always be in line with the flow direction hence the variation in velocities need to be considered. El Tawil *et al.* (2017) proposed a method for energy characterization for tidal velocities to address this issue which was particularly used for a tidal site assessment in France.

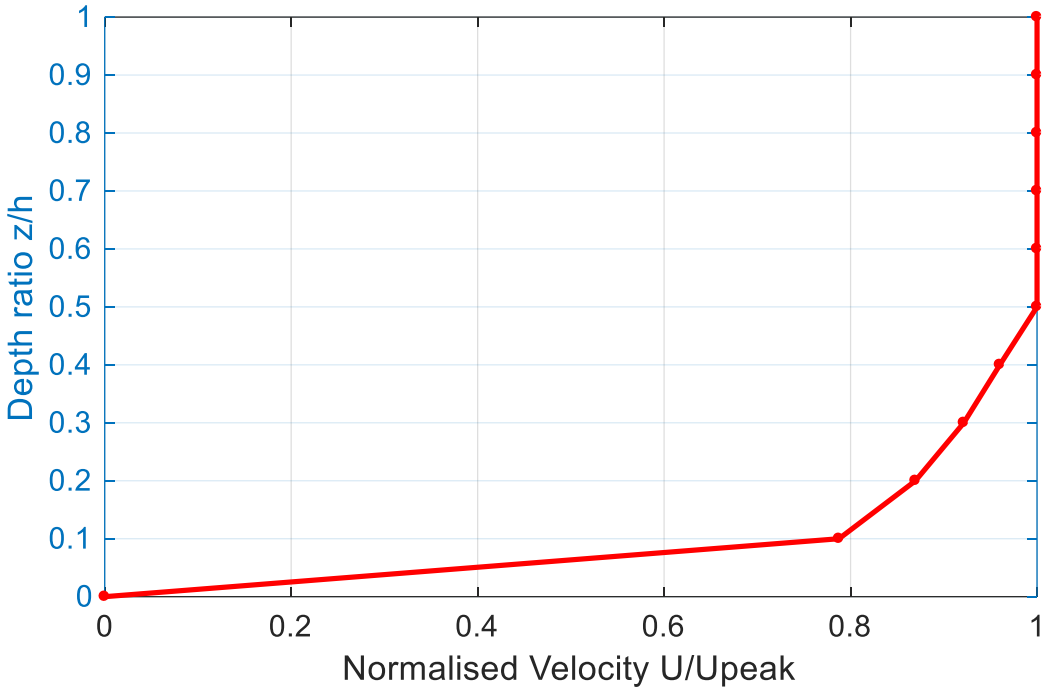

Figure 2.7 One seventh power law of velocity variation with depth

The velocity profile is an important factor in setting the dimension of the turbine to be deployed at a potential site and its clearance from the free surface and seabed. Bryden *et al.* (2007) demonstrated the calculation for the average velocity when the diameter and the location of the turbine hub in terms of the water depth were set giving a more accurate velocity rather than just using the power law profile. Marine turbines are preferably deployed in the top third of the water column to exploit the higher velocity however, most turbines in sea operations are attached to the seabed such as the OpenHydro, the Andritz Hammerfest among many (EMEC, 2013; Hammerfest Strom, 2013; Tidal Energy Ltd, 2013; OpenHydro, 2016; Atlantis Resources Corporation, 2017). There are other issues that need to be considered which inhibit marine turbine deployment in the top third. Another main concern in offshore deployment is the disturbance to established shipping activities at the site. Once the resource assessment is evaluated, the marine turbine can be optimised specifically for the site whether for lone operation or array arrangement.

Future project expansion of the tidal plant also needs to be determined at an early stage when identifying and deciding on a site. This is because turbines deployed in arrays may be

economically efficient but they interact with the environment differently than a single turbine and their impacts are also different (Myers and Bahaj, 2012). Assessment on turbine spacing and power generation capacity of an array needs to be included to ensure an optimised deployment (Myers and Bahaj, 2005; Vennell, 2012a; Bai *et al.*, 2013b; Thiébot *et al.*, 2016).

2.9 Considerations on the environmental impacts

The operation of marine turbines and their supporting structures alters the flow at the location. Besides altering the flow characteristics of the site from the energy extraction process, it was identified that the marine environment also suffers (Hammar *et al.*, 2017). It is understood that the change in flow characteristics such as velocity and direction and generation of vortices alter the transport process of suspended marine particles which may affect the benthic habitat (El-Geziry and Couch, 2009). However, a numerical model investigation involving a case study in the Pentland Firth concluded that deployment of turbines in an array has minimal impact on the sediment transfer (Fairley *et al.*, 2015) supporting the same findings by Scottish Marine Renewables SEA (2007a). Nonetheless, this might be true to of that particular location and not for other locations, therefore a thorough investigation on the environmental impacts has to be conducted once a potential site is identified and its impacts on the ecology monitored. On the ecological aspects however, Scottish Marine Renewables SEA (2007b) acknowledged the disturbance of the marine turbine operation on the local benthic ecology.

Although the deployment of marine turbines may not be as environmentally harmful as that of tidal barrages (Harvey, 2013; Hooper and Austen, 2013) the true extent of their environmental impacts are not fully understood. Hence, for full-scale and real sea deployment, turbine developers are required to obtain consents from environmental legislators that must identify and quantify the potential impacts of the turbine operation from the entire range of activities involved in the work from the construction, through operation until decommissioning of the site (Kerr, 2005). As extensively described in the Environmental Impact Assessment (EIA) directives, direct and indirect effects on different aspects such as human, marine life and water quality from a tidal project have to be identified, described and assessed (Environmental Agency, 2011). The directives detail the activities involved and their potential impacts on the water, land and air quality while also considering the ecological and human factors. Although the installation and decommissioning processes are similar in terms of their technical needs and

impacts, turbine developers are required to abide by the decommissioning regulations imposed to ensure effective recovery of the marine environment to its previous purpose (DECC UK, 2004).

2.10 Summary

Tidal energy offers an alternative source to power generation with established power contribution from tidal barrages and steady developments on numerous marine turbine prototypes and full-scale deployment. While there is limited data in the public domain with regard to the performance of full-scale turbines in operation, there is however ample literature available on model scale and numerically-based work. In this chapter, various literature was reviewed in the assessment of turbine performance with different turbine parameters and hydrodynamic conditions. The effects of other external factors such as blockage ratio and boundary proximities were also considered. Resultant phenomena from HATT operation such as cavitation and noise generation along with the application and contribution of CFD in marine energy studies were also reviewed.

The aim of this chapter is to provide an insight into various research conducted in the marine energy field where common practices in different areas investigated can be adopted to carry out the investigations on the Hydro-Spinna turbine.

CHAPTER 3. NOVEL MARINE CURRENT TURBINE: HYDRO-SPINNA

3.1 General Remarks

The objective of this chapter is to introduce the novel concept of the Hydro-Spinna turbine and the subsequent designs developed based on the ideas of the initial concept of originator, Michael Gilbert, who approached Professor Atlar of Newcastle University to explore the concept for marine turbine applications. The concept of the turbine was conceived from his passion for constructing wind spinners as garden ornaments in his private garden. Although inspired by a vertical axis wind spinning mechanism, the Hydro-Spinna turbine in this thesis is explored to be a horizontal axis tidal turbine. The initial design of the Hydro-Spinna had three simple cardioid shaped blades that spiralled around one common axis.

Three designs have been considered in the study, starting with the initial concept of the first Hydro-Spinna. The second design, a 280 mm diameter model, termed the HS280 was used for cavitation tunnel testing while the third turbine design, a 500 mm diameter model, the HS500, was used in the towing tank. The HS280, is an optimised turbine design developed by Wen (2011) in the initial stages of the Hydro-Spinna project, while the HS500 was based on the original turbine design, but is a model designed with accurate parametric values. The chapter begins with extensive explanation of the basic blade concept and geometry of the Hydro-Spinna turbine. The three Hydro-Spinna turbine designs are then discussed individually and comparison of the designs is carried out.

Section 3.2 to Section 3.4 presents the design, geometry and parameters of the Hydro-Spinna turbine. Section 3.5 presents the original turbine concept, while Section 3.6 describes the 280 mm model, HS280. Section 3.7 presents the 500 mm model, HS500, Hydro-Spinna turbine. Section 3.8 provides an overview of the three Hydro-Spinna models developed and Section 3.9 concludes this chapter.

3.2 Basic Geometry of the Hydro-Spinna Blade

The Hydro-Spinna consists of three helical blades twisting around one common axis. The blades are equally spaced from each other i.e. 120^{o} apart. The blade geometry is not circular

as in the case of a common helix. In fact, the blades follow a cardioid shaped profile, shown in Figure 3.1. The polar coordinates of a cardioid follow that of a circle except that instead of a constant radius, the radius of the cardioid varies with swept angle θ, defined in Equation 3.1. The polar coordinates of a circle and cardioid are presented in Equation 3.2 and Equation 3.3 respectively for comparison.

$$R = a(1 - \cos\theta)$$

Equation 3.1

$$x = a\cos\theta$$
$$y = a\sin\theta$$

Equation 3.2

$$x = a(1 - \cos\theta)\cos\theta$$
$$y = a(1 - \cos\theta)\sin\theta$$

Equation 3.3

where a is the radius of the circle or scaling factor for the cardioid, and $0 \ll \theta \ll 2\pi$.

Table 3.1 The variation in radius of the cardioid with scaling factor a $= 5$ for swept angle $0 \ll \theta \ll 2\pi$ against a circle with the same radius.

θ(°)	Cardioid			Circle		
	radius	**x-values**	**y-values**	**radius**	**x-values**	**y-values**
0	0	0	0	5	5	0
π/2	5.0	0	5	5	0	5
π	10.0	-10	0	5	-5	0
3π/2	5.0	0	-5	5	0	-5
2π	0	0	0	5	5	0

Table 3.1 shows the variation in radius for a cardioid and a circle for $a = 5$. The contrast of the coordinates is more noticeable in graphical form as displayed in Figure 3.1. The variation of the radius of the cardioid with the swept angle can be seen, reaching a maximum at $\theta = \pi$.

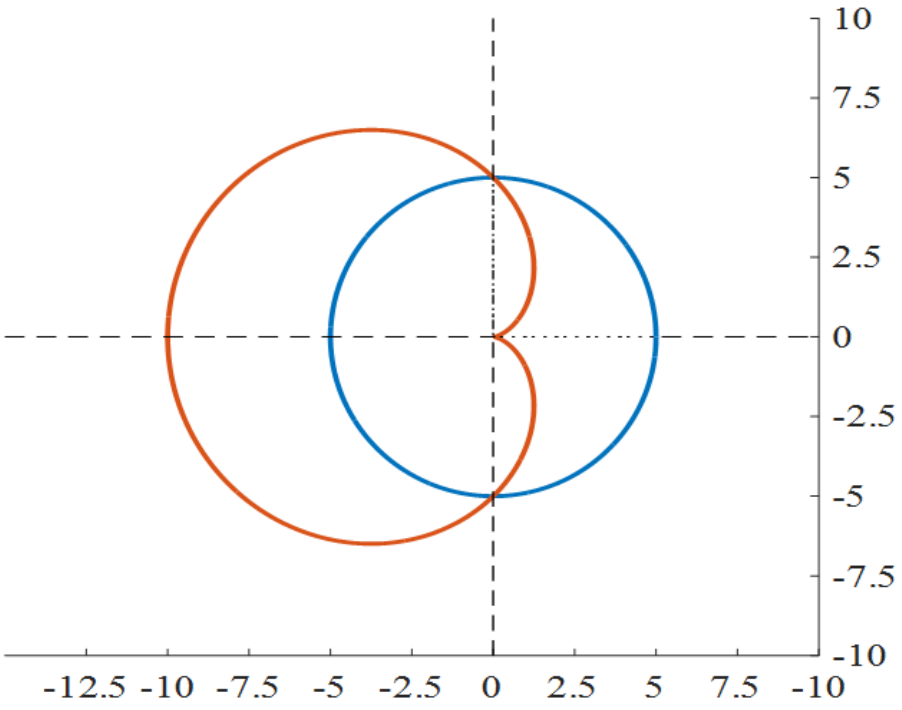

Figure 3.1 The basic cardioid geometry (red) compared to the geometry of a circle (blue) with an equivalent radius/scaling factor of 5.

3.3 Maximum Radius and Width of the Cardioid

The radius of the cardioid varies with the swept angle, according to the formula in Equation 3.1. The maximum radius of the cardioid is therefore obtained at $\theta = \pi$ where $\cos\theta = -1$. To find the angle at which the maximum width of the cardioid is located, as presented in Figure 3.2, the *y* coordinate in Equation 3.3 is differentiated. The first derivative, shown in Equation 3.4, is equated to zero to find the turning points of the curve which are found to be 0 and $\frac{2}{3}\pi$. The maximum point of the curve that gives the highest value is evaluated by using the second derivative in Equation 3.5. Hence, the maximum width of the Hydro-Spinna turbine is found at $\theta = \frac{2}{3}\pi$ as illustrated in Figure 3.2 below.

$$\frac{dy}{d\theta} = -2\cos^2\theta + \cos\theta + 1$$

Equation 3.4

$$\frac{d^2y}{d\theta^2} = 4\cos\theta\sin\theta + \sin\theta$$

Equation 3.5

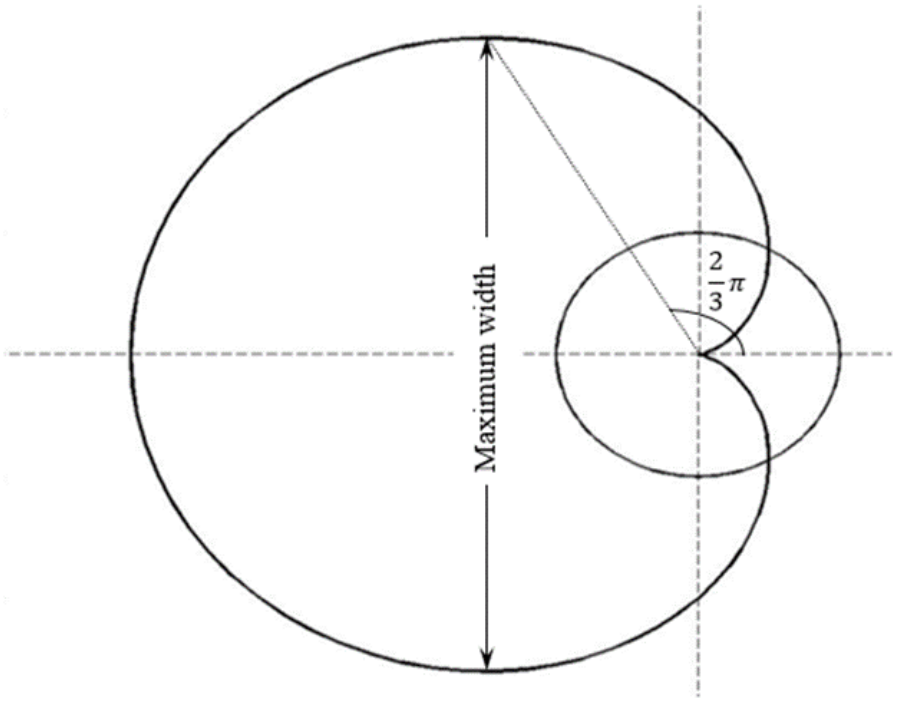

Figure 3.2 Location of the maximum width of the cardioid at a radius, $r = a(1 - \cos\theta)$ where $\theta = \frac{2}{3}\pi$ or 120°.

3.4 Turbine Parameters

For the sake of clarity, the parameters of the Hydro-Spinna are briefly defined. As with other conventional HATT, the diameter (*D*) of the turbine is simply the diameter of the turbine swept area. The chord length (*C*) of the turbine is the length of the turbine blade from the leading to the trailing edge. The pitch angle (β) is the geometric twist angle of the

blade in the direction of the fluid flow which will be elaborated more in each turbine design concept. A new turbine parameter is introduced for the Hydro-Spinna turbine which is lengthwise pitch (or pitch length) of the turbine in addition to the geometric pitch definition in terms of angle. The lengthwise pitch is defined as the extension of the turbine in the flow direction, hence the distance between the upstream and downstream end of the axis parallel to the direction of flow, as illustrated in Figure 3.3.

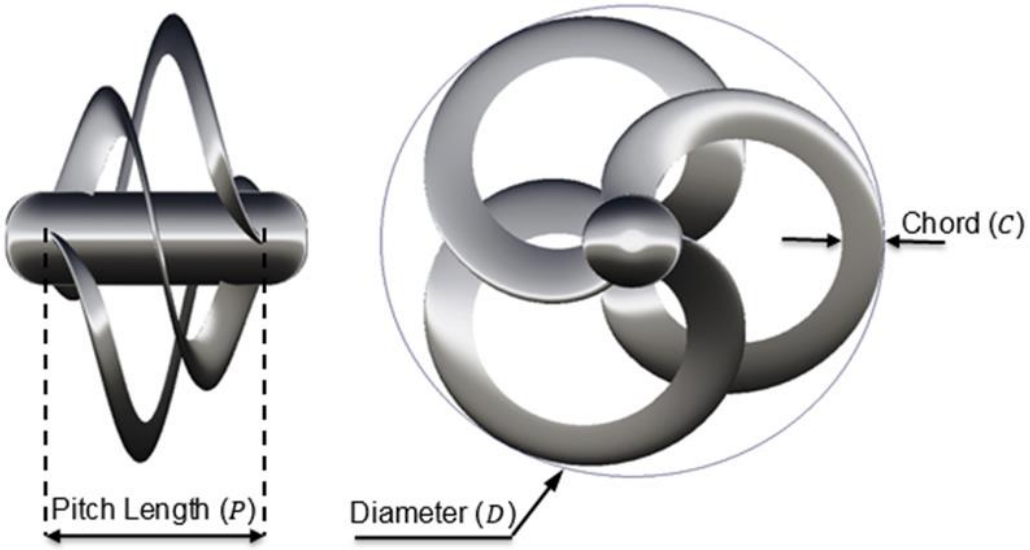

Figure 3.3 The parameters of the Hydro-Spinna turbine illustrated using the 500 mm turbine model.

3.5 Initial Concept of the First Hydro-Spinna Turbine

The initial concept of the turbine had three cardioid shaped blades mounted on a 30 mm diameter sphere at the two ends of a shaft. Each blade was cut from a 0.914 mm thick brass plate with a cardioid scaling factor of $a = 5.1$, giving a maximum radius of 140 mm. The blades were then stretched along a central shaft and mounted to the sphere at each end, as shown in Figure 3.4. The blades were mounted to the spheres at 45^o giving an approximate average blade pitch angle of 64^o. The rotor diameter is 280 mm and the blades have a constant chord length of 40 mm which was set to be 15% of the blade width according to the designer's concept. This first turbine was built with a pitch length to diameter ratio (*P/D*) of 1.

The first Hydro-Spinna turbine, shown in Figure 3.5, is truly the suggestion from the inventor where there is a lack of proper design in terms of setting the blades on the spheres

hence the blades can flex to any angle. The two subsequent designs, the HS280 and HS500, were created based on a fixed geometry and the parameters of the turbines were calculated using mathematical formulae to simplify and accurately present those parameters.

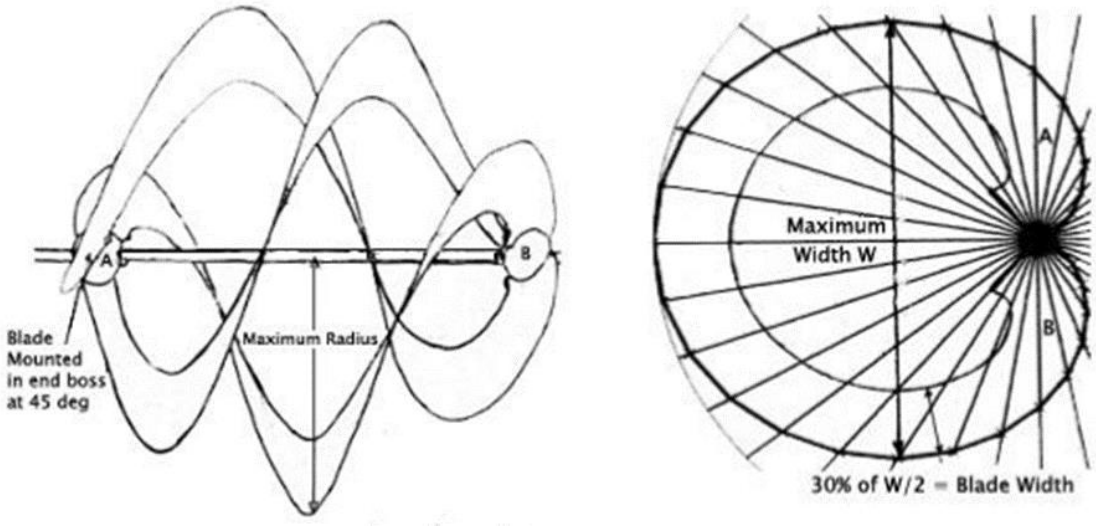

Figure 3.4 The sketch of the Hydro-Spinna design by Michael Gilbert on which the first turbine was based on (Lin, 2009).

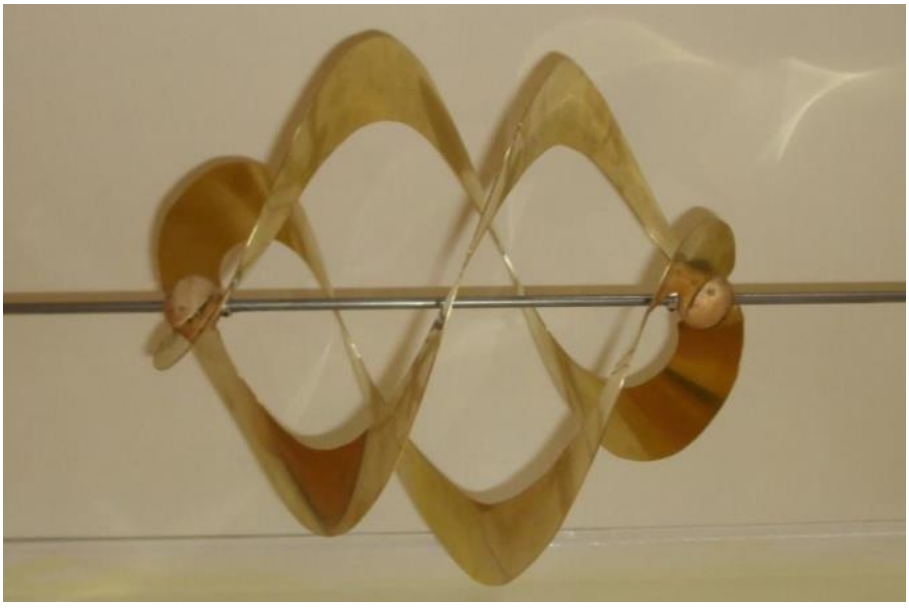

Figure 3.5 The first Hydro-Spinna turbine fabricated by Michael Gilbert and Htet Lin (Lin, 2009).

3.6 The 280 mm Diameter Turbine

The 280 mm Hydro-Spinna model, termed HS280, is a modification of the first basic Hydro-Spinna turbine described in the previous section. The HS280 possesses a circular trailing edge instead of a cardioid shape. The 280 mm was intended to optimise the Hydro-Spinna design for effective energy conversion. The design developed by Wen (2011) not only possesses a circular trailing edge, but the blade chord length and pitch angle at different radii are set by using concentric circles intersecting the blade as shown in Figure 3.6. The concentric circles cut through the turbine blade section not only to determine the chord length and blade pitch angle but also the blade cross sectional profile is set at these locations.

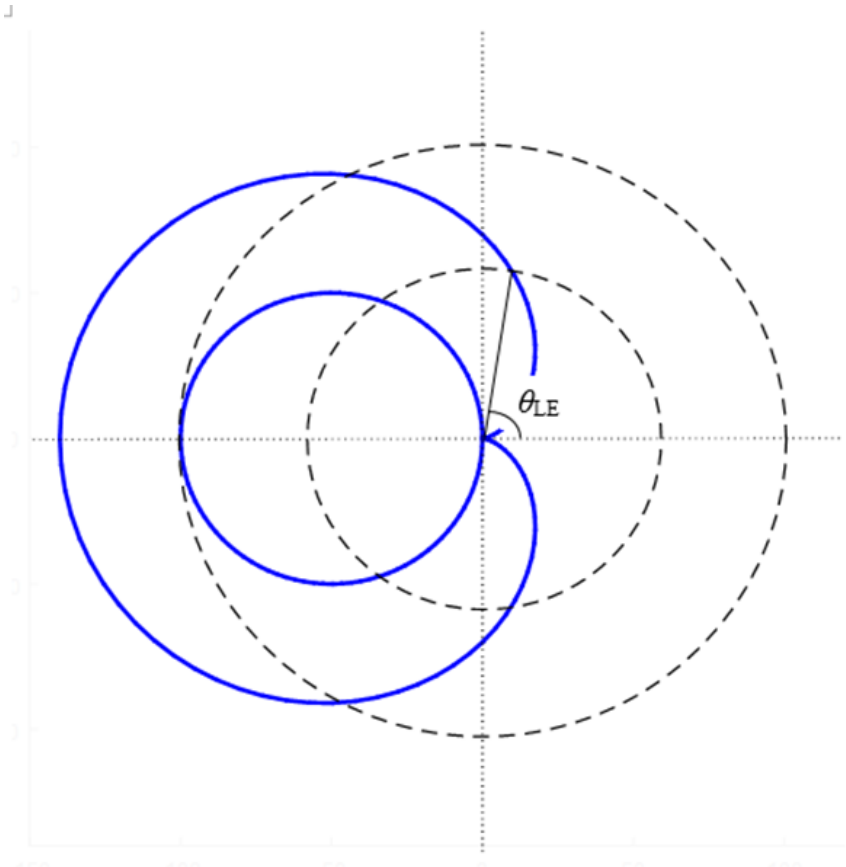

Figure 3.6 Illustration of the two concentric circles that cut through the leading and trailing edges of the turbine blade (blue) to determine the chord length and blade pitch angle with the leading edge angle also shown.

The blade pitch angle and chord length at each radius for the HS 280 model, as shown in Figure 3.7, are calculated by first calculating the leading edge angle at that section by

equating the radius of the circle and the radius of the leading cardioid at that angle which is given in Equation 3.6. Similarly, the trailing edge angle is defined in Equation 3.7. By defining the trailing edge angle, the coordinates of the circular trailing edge can be calculated.

$$\theta_{LE} = \cos^{-1}\left(\frac{1 - r_i}{a}\right)$$

Equation 3.6

$$\theta_{TE} = \pi - \theta_2$$

Equation 3.7

$$\theta_2 = \cos^{-1}\left(\frac{r_i}{2r_c}\right)$$

Equation 3.8

To this point, the HS280 is defined in two dimensions, the *x* and *y* coordinates giving the planform. The *z* coordinates of the turbine, were determined by interpolation. The swept angle was divided into *n* equal angles and the pitch length of the turbine was also divided into *n* equal distances. The *z* coordinates of the trailing edge were also interpolated by the same method. With all of the coordinates and angles of the leading and trailing edge defined, the blade pitch angle and the chord length of the HS280 blade are defined in Equation 3.9 and Equation 3.10.

$$\beta = \tan^{-1}\frac{(z_{TE} - z_{LE})}{r_i(\theta_{TE} - \theta_{LE})}$$

Equation 3.9

$$C = \frac{r_i(\theta_{TE} - \theta_{LE})}{\cos\beta}$$

Equation 3.10

where r_i is the radius of the concentric circle as shown in Figure 3.7.

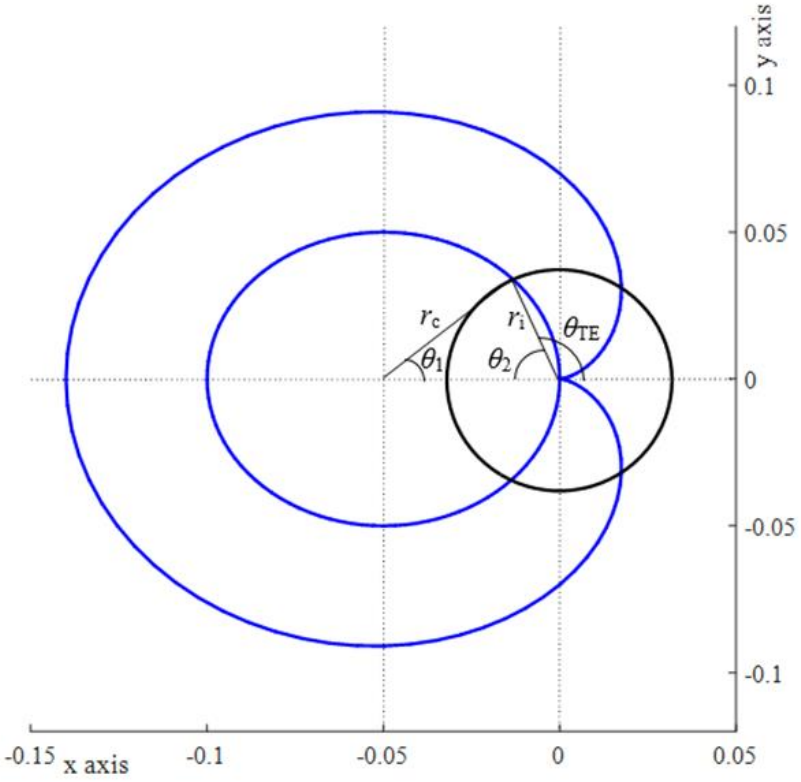

Figure 3.7 The trailing edge angle of the Hydro-Spinna as well as the associated radius and angles. The units of the axes are in metres (m).

The Hydro-Spinna blade design was further improved by using a NACA 0006 airfoil profile along the cross section of chord length of the blade. The symmetrical NACA 00xx airfoil is defined by the following Equation 3.11 below where the digit xx represents the percentage thickness to chord length of the airfoil, in this case 6%.

$$y_t = 5t\left[0.2969\sqrt{x} - 0.1260x - 0.3516x^2 + 0.2843x^3 - 0.1015x^4\right]$$

Equation 3.11

where x is the position along the chord between 0 and 1, y_t is the half thickness of the blade and t is the maximum thickness as a fraction of the chord.

The enhancement of the blade cross sectional profile from the initial flat plate profile was intended to increase the lift to drag ratio of the blade. The HS280 turbine, shown in Figure

3.8, has a leading edge with a cardioid scaling factor of 70 mm to obtain blade radius of 140 mm, the same dimension as the first turbine. The radius of the circular trailing edge is 50 mm to achieve a blade radius of 40 mm at $\theta = \pi$. The hub diameter of the HS280 turbine was set at 28 mm, 10% of the overall turbine diameter. The pitch length of the turbine is 120 mm giving a pitch to diameter ratio of 0.43.

The theoretical power performance of three different turbines of pitch length 240 mm, 210 mm and 120 mm with *P/D* ratios of 1.0, 0.75 and 0.43 respectively were assessed using Blade Element Theory. It was concluded that the turbine with the lowest *P/D* (i.e. 0.43) produces the highest performance of 0.529 at *TSR* = 2.4. The three turbines' specifications as well as the predicted power performance were presented in detail in Wen (2011). The radial, chord and pitch angle distribution of the *P/D* = 0.43 of the turbine are specified in Table 3.2 for convenience. A full description of the HS280 turbine is provided in Appendix A.

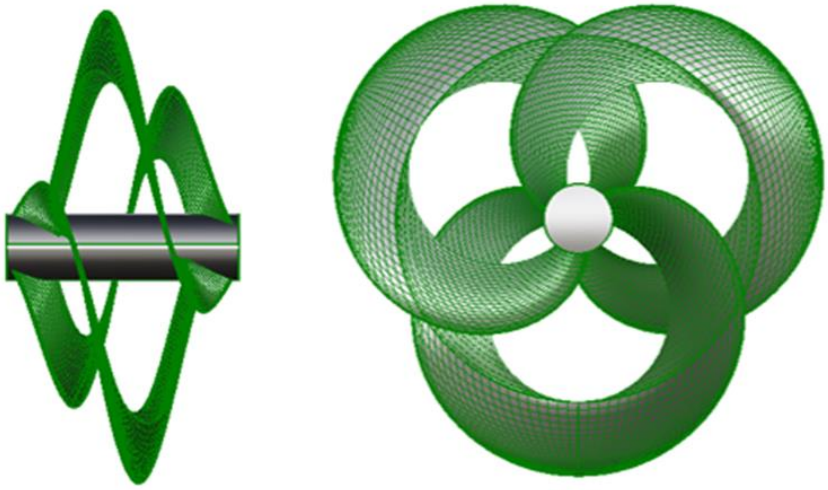

Figure 3.8 The 280 mm diameter Hydro-Spinna model with NACA 0006 blade profile.

Table 3.2 The chord length and pitch angle distribution with radius of the HS280 Hydro-Spinna model

r/R	C/R	Pitch Angle, β(°)
0.1000	0.2007	57.86
0.2064	0.2400	37.63
0.3390	0.3080	25.15
0.4860	0.3970	18.13
0.6100	0.5055	14.62
0.7143	0.8254	12.56
0.8302	0.7180	10.85
0.9128	0.5555	9.89
1.0000	0.0000	9.05

3.7 The 500 mm Diameter Turbine

The first Hydro-Spinna turbine discussed in Section 3.5, had blades with cardioid shaped leading and trailing edges with a constant blade chord length. The HS280 model meanwhile had a circular trailing edge. The 500 mm diameter model, termed HS500, is a modified design based on the first model, maintaining the original cardioid shaped leading and trailing edges. The planform of the turbine was formed by creating two concentric cardioids that act as the leading (blue) and trailing edge (red) of the turbine, as shown in Figure 3.9. The two cardioids were arranged in such way that they have a common designated centre, o.

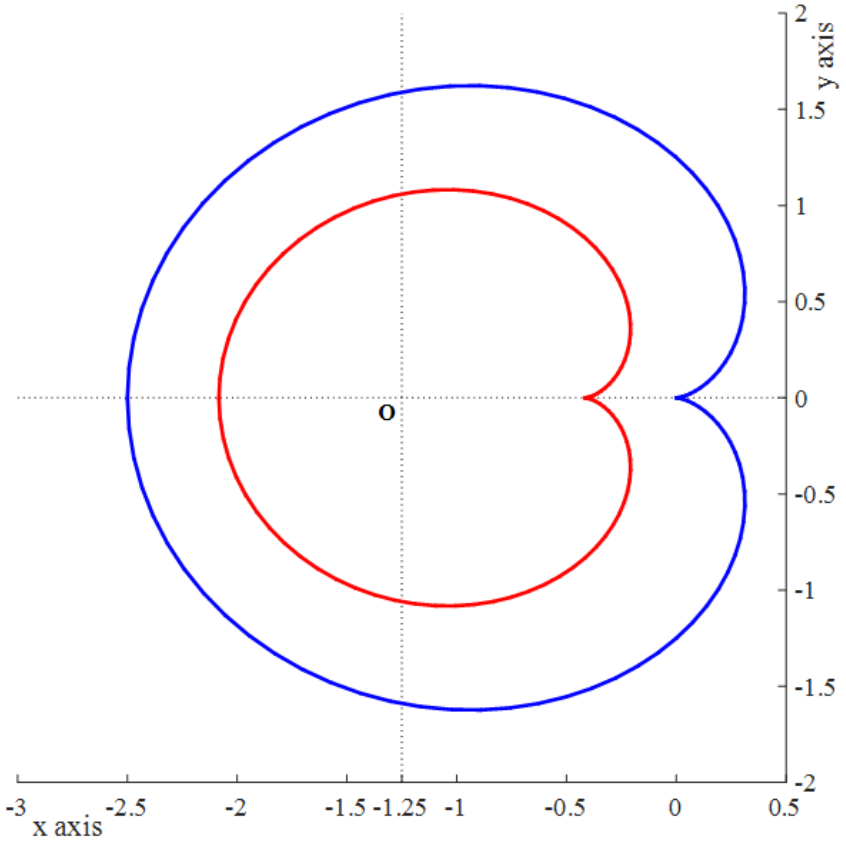

Figure 3.9 The designated centre, o, of the two cardioids.

The leading edge cardioid is 0.75 times larger than the trailing edge cardioid to give an average chord length of 15% of the maximum width. The rationale of setting up the cardioids as such, setting the designated centre, was to normalize the parameters of both cardioids to a single point, i.e. o, as well as to create the planform of the blade. Moreover, it allows the radius of the cardioid, *R*, to be redefined as well as introducing the length *L*, which is the distance between o and a point on the cardioid as shown in Figure 3.10. The new parameters are introduced to allow the chord length and blade pitch angle to be defined.

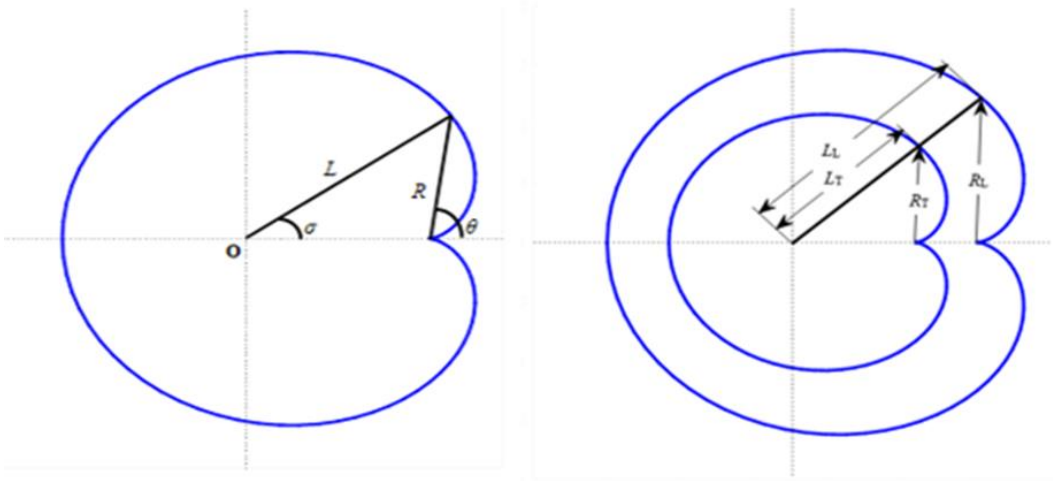

Figure 3.10 Illustration on the radiuses and lengths of the cardioids

As defined in Equation 3.1, the radius of the cardioid is dependent on the swept angle θ. The central angle, σ, and the length, L, are mathematically defined in Equation 3.12 and Equation 3.13 below.

$$\sigma = \sin^{-1}\left[\frac{(1-\cos\theta)\sin\theta}{\sqrt{2-\cos^2\theta}}\right]$$

Equation 3.12

$$L = a\sqrt{2-\cos^2\theta}$$

Equation 3.13

So far, the blade of the Hydro-Spinna is defined in two dimensional (xy) form. As the Hydro-Spinna is a helical turbine, it is three-dimensional, spiralling along the z-axis. For clarity of explanation, the two ends where the blades meet the central z-axis are defined as the upstream and downstream ends. The upstream end of the turbine will see the flow ahead of the downstream end. The lengthwise pitch of the turbine, P, for one complete helical cycle, is defined in Equation 3.14. The z-coordinate of the turbine is defined in Equation 3.15.

$$P = m \times 2\pi$$

Equation 3.14

$$z = m \times \theta$$

Equation 3.15

where *m* is a constant, that can be defined by choosing the pitch length of the turbine.

The pitch angle of the blade varies with both the radius and pitch length as it moves from the root of the blade at the upstream end to the tip of the blade at maximum radius, halfway along the *z*-axis, and spirals back to the downstream end. The pitch angle of the blade, β, at each radius is defined in Equation 3.16. The chord length of the blade, *C*, at each radius can be calculated using Pythagoras theorem in Equation 3.17.

$$\beta = \tan^{-1}\left[\frac{z_{TE} - z_{LE}}{L_{LE} - L_{TE}}\right]$$

Equation 3.16

$$C = \sqrt{(z_{TE} - z_{LE})^2 + (L_{LE} - L_{TE})^2}$$

Equation 3.17

where subscripts TE and LE represents the trailing and leading edge coordinates respectively.

A MATLAB script was created to generate the *x, y, z* offset data points and parameters of the 500 mm Hydro-Spinna turbine. The code allows turbines with different pitch to diameter ratio (*P/D*) to be easily produced such as the one displayed in Table 3.3. A full specification of the HS500 is provided in Appendix B. Figure 3.11 shows the planform and side view of the HS500 turbine presenting a cardioid shaped trailing edge.

Table 3.3 The parameters of the 500 mm Hydro-Spinna model with pitch length of 215 mm giving a turbine *P/D* of 0.43

Swept Angle, θ(°)	***r/R***	**C/R**	**Pitch Angle, β(°)**
0	0	0.2198	40.7
22.5	0.0381	0.2181	35.1
45.0	0.1465	0.2307	27.8
67.5	0.3087	0.2439	21.5
90.0	0.5000	0.2463	16.9
112.5	0.6913	0.2332	13.3
135.0	0.8535	0.2073	10.0
157.5	0.9619	0.1793	5.7
180.0	1.0000	0.1667	0

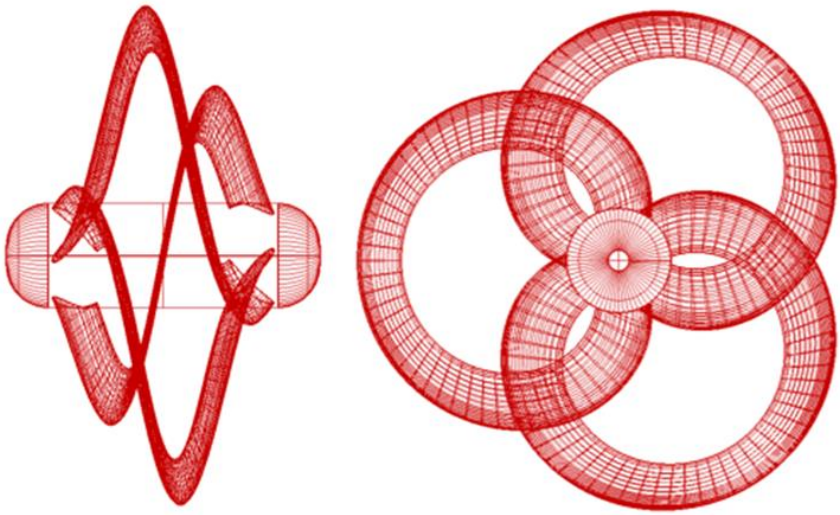

Figure 3.11 Planform and side view of the 500 mm Hydro-Spinna model.

The HS500 turbine has a hub diameter of 20% of the turbine diameter which is 100 mm for the 500 mm diameter turbine. Due to the fixed geometry of the turbine blades, the diameter was set at 20% as it was the minimum diameter for the hub to avoid the blades intersecting each

other at both ends. The cross section of the blade is a NACA 0015 profile that is defined by the previous Equation 3.11.

The HS500 was designed with a cardioidal trailing to satisfy the requirement by the turbine designer to revert to the original design concept. It was made with a thicker NACA 0015 profile which has a higher lift to drag ratio to make up for the decrease in chord length in the design. Moreover, it has a bigger diameter than the HS280 as the HS500 was intended to be tested at the Towing Tank facility.

3.8 Hydro-Spinna Models

The three Hydro-Spinna designs have been modelled and investigated in previous and the current research. Previous investigations by Lin (2009) involved determining the power performance of the Hydro-Spinna models and Wen (2011) looked at optimising the turbine blade design. Whilst the details of their work are stated in the above literature, this section summarises their work with an overview of the designs, given in Table 3.4.

Table 3.4 Overview of the Hydro-Spinna models

	First Model	**HS280**	**HS500**
Diameter (mm)	280	280	500
Blade Chord (mm)	40	varies	varies
Blade Profile	Flat Plate	NACA0006	NACA0015
Pitch Angle (°)	64 (average)	varies	varies
Pitch to Diameter Ratio	1	0.43	0.43
Leading Edge	Cardioid	Cardioid	Cardioid
Trailing Edge	Cardioid	Circular	Cardioid

The first model was tested in the Towing Tank facility in Newcastle University by Lin (2009) and in the Emerson Cavitation Tunnel (ECT) by Wen (2011). The Towing Tank

experiments covered tests between $1 \ll TSR \ll 2.5$ and produced a maximum power coefficient of $C_P = 0.26$ while the Cavitation Tunnel test gave a value of $C_P = 0.3$ over a range of $0.25 \ll TSR \ll 2.5$. For both tests, the maximum power coefficient occurred at $TSR = 1.25$.

The optimised Hydro-Spinna, HS280, was evaluated by means of the BEMT where it was predicted to produce power coefficient of $C_P = 0.529$ at $TSR = 2.4$. The HS280 was finally tested in the ECT facility and the results are presented in Chapter 6.

3.9 Summary

This chapter outlined the basic geometry of the Hydro-Spinna turbine. The key parameters of the turbine were also defined. The initial concept and two different Hydro-Spinna models were described with their specifications listed.

CHAPTER 4. NUMERICAL INVESTIGATION OF THE TURBINE *P/D* PARAMETER

4.1 General Remarks

Blade Element Momentum Theory (BEMT) is a widely used numerical method to predict theoretical thrust, torque and power of a conventional HATT. The theory, a combination of Momentum Theory and Blade Element Method is widely applied in design and analysis of wind turbines. This theory is further employed in the investigation of HATT, where the principle is the same and the only difference is the nature of fluid they are operating in. With BEMT, the turbine is assumed to be a thin actuator disc that obstructs the flow, extracting kinetic energy from the fluid and converting it to useful power (Madsen *et al.*, 2007; Buckland *et al.*, 2010; Masters *et al.*, 2011).

The Hydro-Spinna turbine is a unique design concept where one of the main parameters of the turbine is the pitch to diameter ratio (*P/D*). The performance of the optimized Hydro-Spinna, HS280, was predicted by using BEMT with a maximum power coefficient of 0.529 although further details of the calculation were not provided (Wen, 2011). However, as the Hydro-Spinna turbine extends in the axial direction making it more 'three dimensional' than conventional HATT devices, it was concluded that the theory did not accurately predict the Hydro-Spinna performance. Furthermore, the design of the Hydro-Spinna turbine, which has a portion of the blade downstream of the first portion, is more similar to that of the vertical axis tidal turbine where the double streamtube theory is more relevant. However, the prediction of power performance based on that theory was not within the scope of the research which instead focussed on an alternative investigation using Computational Fluid Dynamics (CFD).

This chapter presents the numerical analysis using CFD using Reynolds Averaged Navier Stokes (RANS) equation of the Hydro-Spinna performance with different *P/D*s. Section 4.2 looks into the different momentum models used in CFD, and Section 4.3 considers the numerical domain independency analysis to ensure convergence of the numerical results. Section 4.4 presents the Grid Convergence Index (GCI) analysis on the numerical model, Section 4.5 looks into the effect of *P/D* on the hydrodynamic efficiency performance of the

Hydro-Spinna. The findings from the numerical analysis are discussed in Section 4.6 and the summary of the chapter is presented in Section 4.7.

4.2 Computational Fluid Dynamics

A Computer Aided Engineering (CAE) software package called Star-CCM+ developed by CD-Adapco (recently taken over by SIEMENS in 2016) was used for numerical modelling in this thesis, employing the RANS equation. Other equations commonly used in computational simulations are the Large Eddy Simulation (LES) and a hybrid of the RANS and LES known as the Detached Eddy Simulation (DES). In comparison to the latter two methods, RANS is less demanding in terms of the computational time and capacity. However, RANS is a time averaged operation where the characteristic of the flow in its instantaneous fluctuations are ignored which is proven as its shortcoming. Because of this simplified approach it was understood that this method would not be able to accurately predict the unsteadiness in the flow (Breuer *et al.*, 2003).

4.2.1 Reynolds-Averaged Navier Stokes Equation

A computational domain was produced to predict the performance of the Hydro-Spinna turbine using the continuity equation and RANS equations. The Navier-Stokes equations, defined in Equation 4.1, has four unknowns, three velocities components, and a pressure component, yet it presents only three equations each for the x-y-z directions. The other equation to complete the solution to solve for the four unknowns is the continuity equation given in Equation 4.2 below. When using the Navier-Stokes equations it is assumed that the flow is incompressible with a constant density and isothermal where the viscosity of the fluid is constant too. The same assumptions apply to the continuity equation as well.

$$\frac{\partial(\rho V)}{\partial t} + \rho\left(V.\vec{\nabla}\right)V = -\vec{\nabla}.p + \mu\vec{\nabla}^2 V + f_b$$

Equation 4.1

$$\frac{\partial \rho}{\partial t} + \nabla.(\rho V) = 0$$

Equation 4.2

where ρ is the density, V is the velocity (u, v, w in the x, y, z components) and p is the pressure component respectively, μ is the viscosity, f_b is the resultant body force, and ∇ is defined as $\nabla = \frac{\partial}{\partial x} + \frac{\partial}{\partial y} + \frac{\partial}{\partial z}$

The RANS model takes the time averaged values of the turbulence fluctuations in the flow to calculate the velocities and pressure in the momentum equations. Hence, the pressure and velocity values are taken as the sum of the mean value and their fluctuating components as shown in Equation 4.3. Instead of taking the actual values of the pressure and velocities components, the averaged values are taken and by taking the time averaged values, the model disregards the instantaneous state of the flow in time hence expanding Equation 4.1 into Equation 4.4 (CD-Adapco, 2013).

$$\emptyset = \overline{\emptyset} + \emptyset'$$

Equation 4.3

$$\frac{\partial(\rho \bar{V})}{\partial t} + \rho(\bar{V}.\vec{\nabla})\bar{V} = -\vec{\nabla}.p + \mu\vec{\nabla}^2\bar{V} + \vec{\nabla}T_t + f_b$$

Equation 4.4

$$T_t = -\rho\begin{bmatrix} \overline{u'u'} & \overline{u'v'} & \overline{u'w'} \\ \overline{u'v'} & \overline{v'v'} & \overline{v'w'} \\ \overline{u'w'} & \overline{v'w'} & \overline{w'w'} \end{bmatrix} = \begin{bmatrix} \tau_{xx} & \tau_{xy} & \tau_{xz} \\ \tau_{yx} & \tau_{yy} & \tau_{yz} \\ \tau_{zx} & \tau_{zy} & \tau_{zz} \end{bmatrix}$$

Equation 4.5

where ∅ represents velocity components, pressure, or energy, $\bar{V}$ is the mean velocity and T_t is the Reynolds stress tensor.

In modelling the turbulence for the complete solution of the RANS equations, two methods can be approached: using the eddy viscosity model; or Reynolds transport model. The eddy viscosity models employ the concept of turbulence viscosity to model T_t. The Boussinesq equation in Equation 4.6 is commonly used to model Reynolds stress tensor as a function of mean velocity gradient:

$$\boldsymbol{\tau}_{ij} = \mu_t \left(\frac{\partial V_i}{\partial x_j} + \frac{\partial V_j}{\partial x_i} \right) - \frac{2}{3} \rho k \delta_{ij}$$

Equation 4.6

$$T_t = 2\mu_t S_{ij} - \frac{2}{3} (\mu_t \nabla . \bar{V})$$

Equation 4.7

where μ_t is the eddy viscosity, and δ_{ij} is the Kronecker delta where ($\delta_{ij} = 1$ if $i = j$ and $\delta_{ij} = 0$ if $i \neq j$), k is the turbulent kinetic energy $k = \frac{1}{2}\left(\overline{u'^2} + \overline{v'^2} + \overline{w'^2}\right)$ and s_{ij} is the rate of deformation (strain) where it is the sum of the mean and fluctuating components $s_{ij} = S_{ij} + s'_{ij}$ and defined as $s_{ij} = \begin{bmatrix} s_{xx} & s_{xy} & s_{xz} \\ s_{yx} & s_{yy} & s_{yz} \\ s_{zx} & s_{zy} & s_{zz} \end{bmatrix}$

Various eddy viscosity models can be employed and they are generally classified based on the number of additional transport equations that needed to be solved along with the RANS equations. Some of the most common turbulence models used in tidal turbine analysis are the one transport equation Spalart-Allmaras, two transport equations *k*-*ε* model, and *k*-ω model (Consul *et al.*, 2009; Turnock *et al.*, 2011; Masters *et al.*, 2015).The *k*-*ε* model i.e. *k* representing

the mean kinetic energy and ε as the rate of dissipation of turbulent kinetic energy, express the eddy viscosity as a product of velocity scale and length scale (Jones and Launder, 1972). The model was found to be unable to represent the turbulence in the near wall regions. A two-layer model was proposed by placing a near-wall grid point in the viscous sublayer to improve the capture of turbulence flow near the wall at low Reynolds (low-Re) number (Versteeg and Malalasekera, 2007).

The Spalart-Allmaras model is another turbulence model with low-Re capabilities that is better at predicting turbulence at the near wall than the *k*-ε model with the latter over-predicting the wall shear stress by up to 50% (Menter, 1996). The equation for the model involves the kinematic eddy viscosity, ύ and the specification of a length defined by an algebraic formula. The *k*-ω model is an alternative to the *k*-ε model where the turbulent frequency ω, is used, which is defined as $\omega = \varepsilon/k$, instead of ε; this is a low-Re model that is superior at modelling the turbulence in the near-wall regions however the model is dependent on the ω values of the free stream conditions (Wilcox, 2008).

The Menter SST *k*-ω model is a hybrid model combining the capability of the *k*-ω at the near-wall regions with that of the *k*-ε in the fully turbulent region for the rest of the domain. Although no obvious advantage can be determined between the Spalart-Allmaras and the Menter SST *k*-ω model, the latter was found to be beneficial in reducing the dependency on the numerical grid for the flow transitional behaviour (Menter, 1994; Rumsey and Spalart, 2009).

In this study, the investigation adopted the RANS as the governing equation and the Menter SST *k*-ω turbulence model was used where the *k* and ω transport equations are presented in Equation 4.8 and Equation 4.9 respectively. In general, the transports equations were defined as the sum of the rate of change of k/ω and the transport of k/ω by convection is equal to the sum of the transport of k/ω by turbulent diffusion and the rate of production of k/ω minus the rate of dissipation of k/ω.

$$\frac{\partial}{\partial t}(\rho k) + \nabla.(\rho k \bar{V}) = \nabla.\left[\left(\mu + \frac{\mu_t}{\sigma_k}\right)\nabla k\right] + P_k + \beta^* \rho k \omega$$

Equation 4.8

$$P_k = \left(2\mu_t S_{ij}.S_{ij} - \frac{2}{3}\rho k\frac{\partial U_i}{\partial x_j}\delta_{ij}\right)$$

Equation 4.9

$$\frac{\partial}{\partial t}(\rho\omega) + \nabla.(\rho\omega\bar{V}) = \nabla.\left[\left(\mu + \frac{\mu_t}{\sigma_{\omega,1}}\right)\nabla\omega\right] + P_\omega - \beta_2\rho\omega^2 + 2\frac{\rho}{\sigma_{\omega,2}\omega}\frac{\partial k}{\partial x_k}\frac{\partial \omega}{\partial x_k}$$

Equation 4.10

$$P_\omega = \gamma_2\left(2\rho S_{ij}.S_{ij} - \frac{2}{3}\rho\omega\frac{\partial U_i}{\partial x_j}\delta_{ij}\right)$$

Equation 4.11

where $\sigma_k = 1.0,\ \sigma_{\omega,1} = 2.0,\ \sigma_{\omega,2} = 1.17,\ \beta^* = 0.09, \beta_2 = 0.083,\ \gamma_2 = 0.44$

4.2.2 Large Eddy Simulation

In the RANS equations, the turbulence is modelled as a whole by universal equations. The issue arising from the method is that there are different types of turbulent eddies present in the flow. Although the smaller eddies are isotropic and can be generalised, the larger eddies are anisotropic, interact with the flow, and are transporters of the conserved quantities. The characteristics of the larger eddies depend on the flow domain, boundary conditions and body forces (Versteeg and Malalasekera, 2007). The LES equation uses a spatial filtering operation to differentiate the small scale and the large scale eddies instead of the averaging techniques employed in RANS. The variable $\emptyset$ in Equation 4.3 is now redefined as the sum of the filtered component and the sub filtered or sub grid value as in Equation 4.12. The Reynolds stress tensor is also redefined in terms of the subgrid scale stresses as described in Equation 4.13.

$$\emptyset = \widetilde{\emptyset} + \emptyset'$$

Equation 4.12

$$T_t = 2\mu_{t,s}S_{ij} - \frac{2}{3}\left(\mu_t\vec{\nabla}.\tilde{V} + \rho k_s\right)$$

Equation 4.13

where $\tilde{V}$ is the filtered velocity component, $\mu_{t,s}$ is the subgrid scale viscosity and k_s is the subgrid scale turbulent kinetic energy.

By using spatial filtering such as the Gaussian filter in Equation 4.14, eddies below the length scale were modelled while eddies larger than the length scales were resolved. The LES numerical modelling in the Star-CCM+ software uses implicit filtering where the computational grid determines the size of the filtered eddies.

$$\widetilde{\emptyset}(x,t) = \int G(x,x',\Delta)\emptyset(x',t)\partial x'$$

Equation 4.14

where $G(x,\Delta)$ is the filter function characterised by the filter width $\Delta = \sqrt[3]{\Delta_x\Delta_y\Delta_z}$

Using the Boussinesq approximation, the subgrid scale viscosity can be formulated by different subgrid models such as the Smagorinsky Subgrid Scale (SGS), Dynamic Smagorinsky Subgrid Scale (DSGS) and Wall-Adapting Local-Eddy Viscosity (WALE) Subgrid Scale. In the numerical analysis involving the LES model adopted in this thesis, the WALE Subgrid Scale method was employed in the numerical model; the complete derivation was produced by Nicoud and Ducros (1999) where the subgrid eddy viscosity is defined in Equation 4.15.

$$\mu_t = \rho C_w \Delta^2 \left[\frac{\left(S_{ij}^d S_{ij}^d\right)^{3/2}}{\left(\bar{S}_{ij}\bar{S}_{ij}\right)^{5/2} + \left(S_{ij}^d S_{ij}^d\right)^{5/4}} \right]$$

Equation 4.15

where S_{ij}^d is a invariant strain operator and C_w is the non-universal model coefficient where the Star-CCM+ default value used in the model was 0.544.

4.2.3 Background Theory

Two factors are often considered when investigating the performance of a marine current turbine namely how much power is generated and how much axial loading is the turbine subjected to. These two factors are commonly defined in non-dimensional form, usually known as the power coefficient and the thrust coefficient, as defined in Equation 4.16 and Equation 4.17 respectively. Power coefficient is defined as the ratio of the power generated by the turbine to the power available in the flow. Similarly, thrust coefficient is defined as the thrust on the turbine over the axial load available in the flow.

$$C_P = \frac{Q\Omega}{0.5\,\rho A U^3}$$

Equation 4.16

$$C_T = \frac{T}{0.5\,\rho A U^2}$$

Equation 4.17

where Q is the torque, T is the thrust, Ω is the angular velocity of the turbine, ρ is the density of the fluid, A is the swept area of the turbine, A_S is the projected area of the system perpendicular to the flow direction and U is the flow velocity.

4.3 Domain Independency Analysis

In order to assess the reliability of the numerical model, domain independency analysis on the computational simulation was first carried out. It is common practice to conduct sensitivity analysis on computational simulations to reduce or eliminate the influence of the physical aspects of the numerical model and ensure the convergence of the solutions based solely on the hydrodynamics factors. The domain was made up of two sub-domains which were an outer stationary cylindrical domain defined for its' simplicity and convenience of geometry and a smaller inner dynamic (rotating) domain containing the turbine. The moving domain was used to model the rotation of the turbine using the Moving Reference Frame (MRF) method by imposing the forces in the cells' vertices induced by the motion. Rigid Body Motion (RBM) is another method of analysing a numerical model involving a rotating region, however the RBM method moves the mesh with the rotating region to a new position per time step which is more computationally intensive and time consuming.

Two aspects of the numerical model sensitivity analysis were conducted for the numerical domain presented in Figure 4.1. Firstly, domain size independence analysis of the numerical model was conducted where for the cylindrical domain, different domain sizes i.e. distance of the inlet, outlet and radius of the cylindrical domain were investigated. Four domain sizes were selected in the analysis where the distance of the inlet and outlet from the centre of the turbine and the radius of the domain are given in terms of the diameter of the HS500 which is 500 mm, as shown in Table 4.1.

Table 4.1 Dimension of the numerical domain where *D* is the diameter of the turbine

Domain Setting	Inlet	Outlet	Radius (R)
A	2 D	4 D	1 D
B	2 D	6 D	2 D
C	3 D	8 D	3 D
D	4 D	8 D	4 D

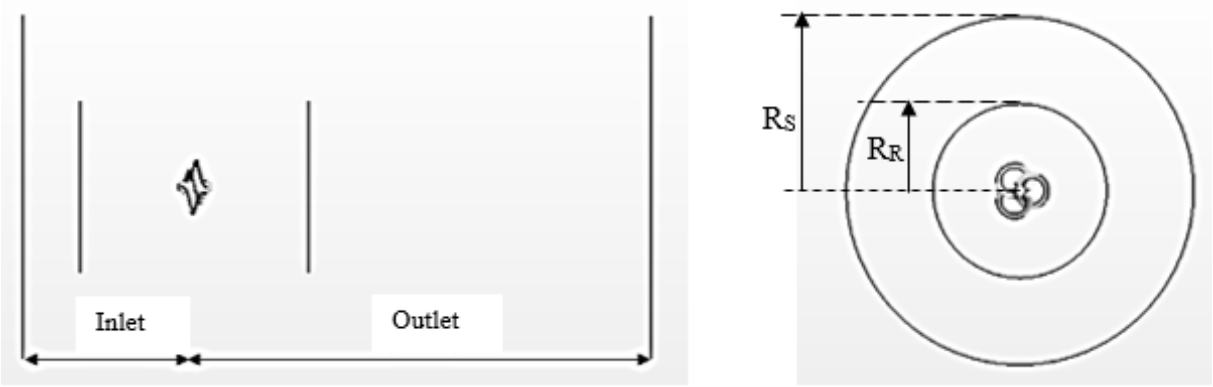

Figure 4.1 The numerical domain for the *P/D* investigations. The inner vertical lines represent the upstream and downstream boundary of the rotating domain. R_R and R_S is the radius of the rotating and stationary domain respectively.

It is known with the MRF method, that there is a pressure discontinuity at the boundary between the rotating and stationary regions. However, this method has been widely used to predict turbines performance by numerical method (O'Doherty *et al.*, 2010; Bai *et al.*, 2013a; Noruzi *et al.*, 2015). Mason-Jones *et al.* (2012) obtained a ±5% maximum error between their experimental and numerical data using the MRF method. The alternative RBM is computationally intensive and time consuming so the MRF was selected to be the suitable option. Furthermore, in the analysis later in this thesis, the numerical models were validated against the experimental results to ensure the consistency of the models used. To address and reduce the effect of the pressure discontinuity between the two regions, the rotating domain was set to be three times the radius of the turbine, with the upstream and downstream boundaries set at 2D distance.

The second independence analysis was to isolate the numerical model from the influence of its' mesh size. CFD software usually come with default mesh settings as is the case in Star-CCM+, however due to the complex design of the Hydro-Spinna turbine, it was decided to conduct an analysis on the mesh size and mesh number. Due to the complexity of the Hydro-Spinna turbine, an unstructured trimmed cell mesh was used in the computational domain. One of the advantages of using an unstructured mesh is the ability to easily alter the mesh input and operations. Refined prism layer mesh was used for the turbine surface to allow consideration of the boundary layer, flow separation and turbulence. The mesh for the downstream region of

the turbine was also refined to consider the turbulence in the flow. For the mesh sizes, three mesh settings were used in the independence tests, as listed in Table 4.2.

Table 4.2 Mesh setting with the corresponding mesh numbers

Setting	Base Value		Rotating (Rot)	Stationary (Stat)	Total
	Rot	Stat	Cell Number	Cell Number	
1	0.6	0.6	1,439,663	216,322	1,655,985
2	0.5	0.6	1,847,224	216,322	2,063,546
3	0.5	0.5	1,847,224	355,116	2,202,340

4.3.1 Boundary Conditions

For both analyses, the hydrodynamic parameters of the numerical model were kept constant as the baseline for solutions. The upstream water velocity was set at 0.5 m/s to obtain a range of operational *TSR* values corresponding to a Reynolds number of 2.5×10^5 with respect to the turbine diameter. A symmetry plane boundary was selected for the cylindrical domain wall which mirrors the mesh about the plane hence the shear stress at the boundary is zero, similar to a free-slip boundary.

4.3.2 Independency Test Results

The domain independency test considered four different domain sizes where the results converged as the domain size increased as shown in Figure 4.2. At domain sizes C and D, the results obtained from both the simulations are within 1% error from each other indicating that a converged solution had been achieved. The computational time involving Domain C simulations was only 20 minutes less than that of Domain D. However, since the results converged at the Domain C condition, there was no reason to apply the larger domain setting in further analysis.

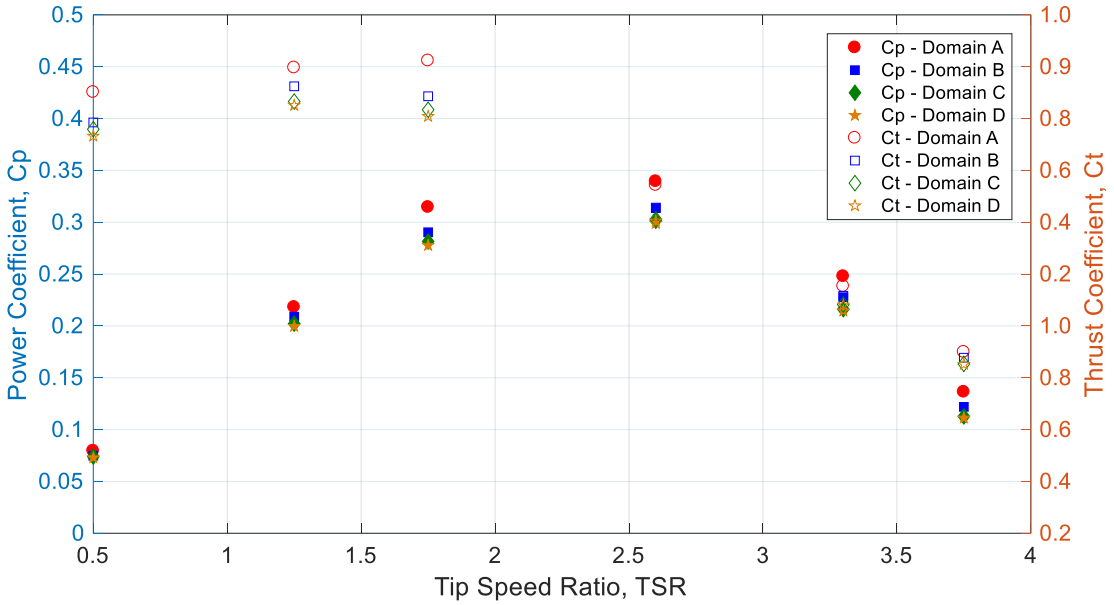

Figure 4.2 The domain size independency results for numerical domain

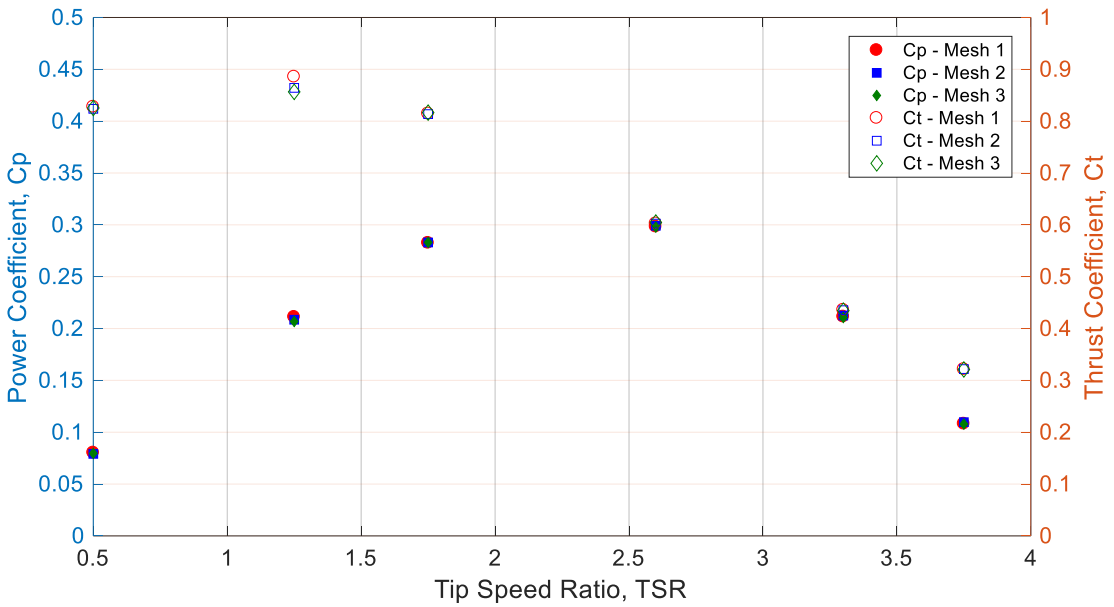

Figure 4.3 The mesh sensitivity results using Domain C

For the mesh size test shown in Figure 4.3, no significant differences were observed at the three different mesh settings. The consistency in the mesh results was probably due to the insignificant difference in the initial mesh settings with only a difference of approximately 200,000 cells between each setting. However, from the thrust coefficient results, a small difference was observed in the values and the results from Mesh 2 and 3 converged. These results gave confidence that a further increase in mesh would give the same converged results. Furthermore, numerical investigations for tidal turbine performance from other literature also yielded optimum mesh numbers of approximately 2 million cells. Bai *et al.* (2013a) employed a similar cylindrical domain with six times the radius of the turbine with a size of 1R and 8R distance from the inlet and outlet to the turbine, with MRF inner domain and a 2.4 million mesh number. A more detailed numerical model, engaging more than one sub domain sizing, conducted by Edmunds *et al.* (2017) using five mesh numbers from 1.2 to 5.1 million cells revealed no significant difference in the performance results generated. Based on the above outcomes, Domain C size with mesh setting 2 were used in the numerical investigation to assess the performance of the Hydro-Spinna turbine.

4.4 Calculation of Grid Convergence Index

Verification of the computational domain can also be analysed by using the grid convergence study to demonstrate its reliability and accuracy. The procedure for verification and validation of computational models can be found in many sources with the Richardson extrapolation (RE) being the recommended approach (Roache, 2003; NPARC Alliance, 2008; Ali *et al.,* 2009). In a CFD based study, the Grid Convergence Index (GCI) which is based on the RE is a widely established and accepted method of uncertainty estimation. Hence, the GCI is adopted in this thesis to verify and validate the numerical methods used to further reinforce the reliability of the models used in this research.

The step by step procedure for the GCI analysis was adopted from Celik *et al.* (2008) and is reproduced in Appendix H. Table 4.3 presents the results of the calculation for the GCI for the three selected mesh sizes defined previously in Table 4.2. The numerical uncertainty for the fine-grid solution for the power coefficient and thrust coefficient are 2.34% and 2.28% respectively.

Table 4.3 Calculation of the discretization error

	ϕ = power coefficient at TSR = 2.6	ϕ = thrust coefficient at TSR = 1.75
N_1, N_2, N_3	2202340, 2063546, 1655985	
r_{21}	1.021	1.021
r_{32}	1.076	1.076
ϕ_1	0.2982	0.8144
ϕ_2	0.2991	0.8165
ϕ_3	0.2978	0.8136
p	7.173	6.355
e_a^{21}	0.0030	0.0026
e_a^{32}	0.0043	0.0036
GCI_{coarse}^{32}	0.79%	0.75%
GCI_{fine}^{21}	2.34%	2.28%

4.5 Effect of Pitch to Diameter Ratio (*P/D*) on the Hydro-Spinna performance

One of the first questions that arises with the Hydro-Spinna turbine concept is the relation between the *P/D* and the turbine performance. Based on the BEMT calculation using the HS280 design, Wen (2011) concluded that a lower *P/D* ratio turbine gave a higher power performance. In order to verify this finding, an investigation using numerical methods was conducted with five *P/D* ratios ranging from 0.43 to 1.0 using the HS500 turbine design. While the blade profile and other parameters such as chord length were kept constant, the pitch angle of the turbine blades changed along with the change in the *P/D*'s. The key parameters of the turbine investigated are given in Table 4.4 for easy reference while the complete specification of the *P/D* of 0.7 and *P/D* of 1.0 turbines are provided in Appendix C and D respectively. The blade pitch angle versus *r/R* distribution of the blade at different P/D is presented in Figure 4.4.

As the *P/D* increased, the turbine structure was elongated further in the axial direction stretching the turbine blades and increasing the pitch angle of the turbine.

Table 4.4 A summary of the key parameters for the *P/D* ratio factor investigation

Pitch to Diameter Ratio, *P/D*	**Diameter, D (mm)**	**Pitch, *P* (mm)**	**Pitch Angle at Root Section, *β* (Deg)**	**Hub Diameter, D_H (mm)**
0.43	500	214	50.82	100
0.75		375	60.30	
1.00		500	68.11	

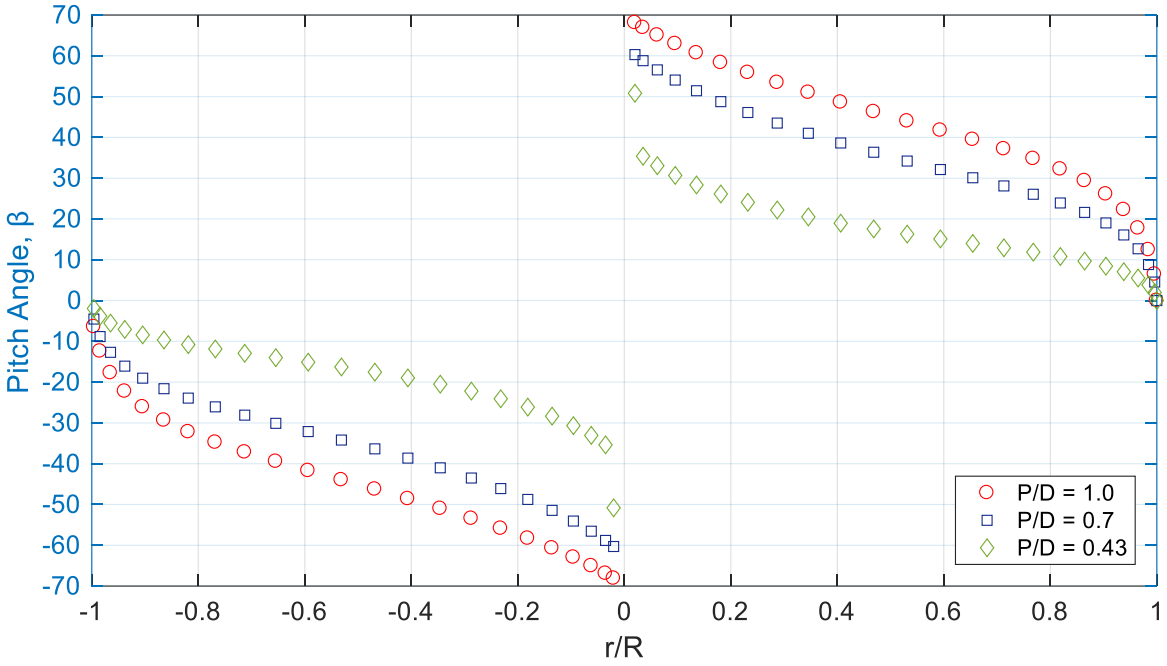

Figure 4.4 The distribution of the blade pitch angle along the radius

4.6 Results and Discussion

The numerical results demonstrated a general decrease in power coefficient as the pitch length of the turbine was increased. The turbine with *P/D* of 0.43 which is the standard *P/D* in the Hydro-Spinna turbine models, produced the highest power coefficient at a maximum of 0.32 at an optimal *TSR* of 2.25, as shown in Figure 4.5. It was also observed that as the *P/D* decreases, the operational range of the turbine also decreased with the lowest range of $0 < TSR < 1.9$ for the *P/D* of 1.0 turbine. The *P/D* of 0.7 turbine produced a maximum power coefficient of 0.25 at optimal *TSR* of 1.25 while the *P/D* of 1.0 turbine has a maximum value of 0.21 at *TSR* of 1. In the previous study conducted by Lin (2009) with the initial concept of the Hydro-Spinna turbine with a *P/D* of 1.0, it was found that the turbine has a *TSR* range of up to 2.5 with an optimal *TSR* of 1 with a C_P = 0.26. However, there were obvious differences between the two designs particularly with the chord length where the initial concept turbine had a fixed chord length of 0.04 m and a flat plate blade profile whereas the HS500 has a varying chord length due to the geometry of the leading and trailing edge and a NACA 0015 profile.

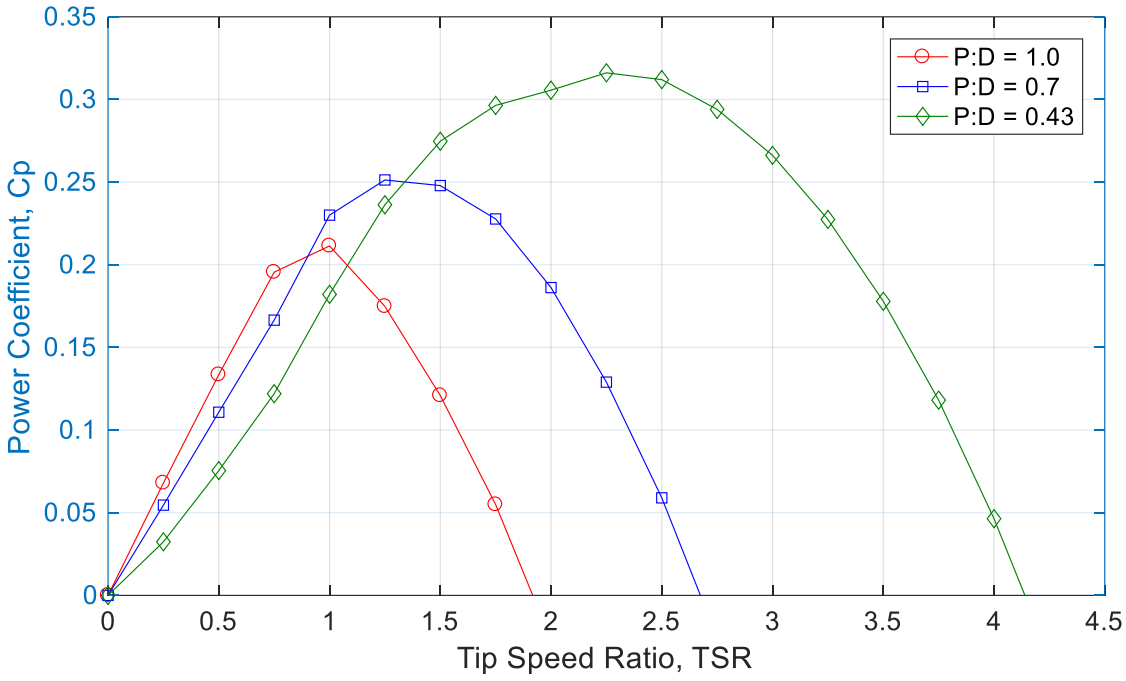

Figure 4.5 Numerical power coefficient of different *P/D* of Hydro-Spinna turbines

The thrust coefficient of the turbine also presented a similar trend to the power performance with decreasing thrust as the pitch length of the turbine increased, as shown in Figure 4.6. The *P/D* of 0.43 turbine yielded a maximum thrust coefficient of 0.95 at *TSR* of 1.25, whilst at its optimal *TSR* the thrust coefficient was only 0.66, 30% less than the maximum thrust. The behaviour of the thrust coefficient is further explained in Chapter 5. It was also noted that at *TSR* of 0, thrust values were recorded acting on the turbines even when they were stationary. This was believed to be caused by the high blockage area of the turbine surface obstructing the flow even when the turbine was not rotating.

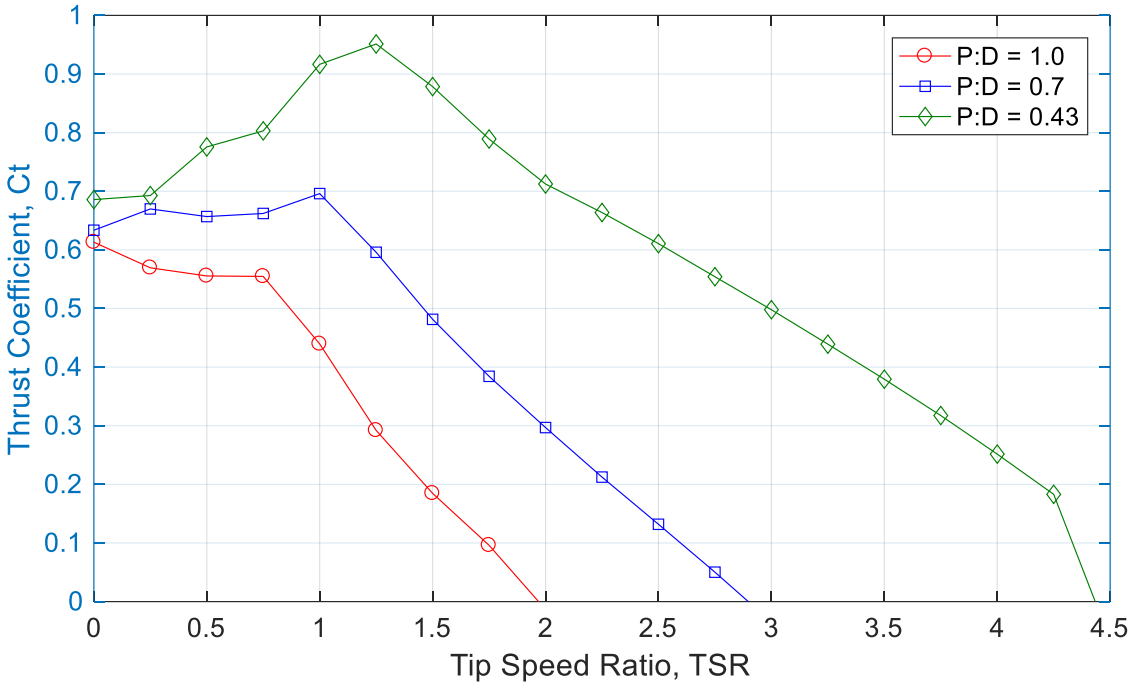

Figure 4.6 Numerical thrust coefficient of different *P/D* Hydro-Spinna turbines

The results obtained gave an overview of the performance of the Hydro-Spinna turbine with varying *P/D* values. The wake characteristic was observed by means of a velocity deficit which is defined in Equation 4.18.

$$U_{deficit} = 1 - \frac{U_W}{U_O}$$

Equation 4.18

where U_W is the wake velocity in the longitudinal direction while U_O is the incoming flow velocity.

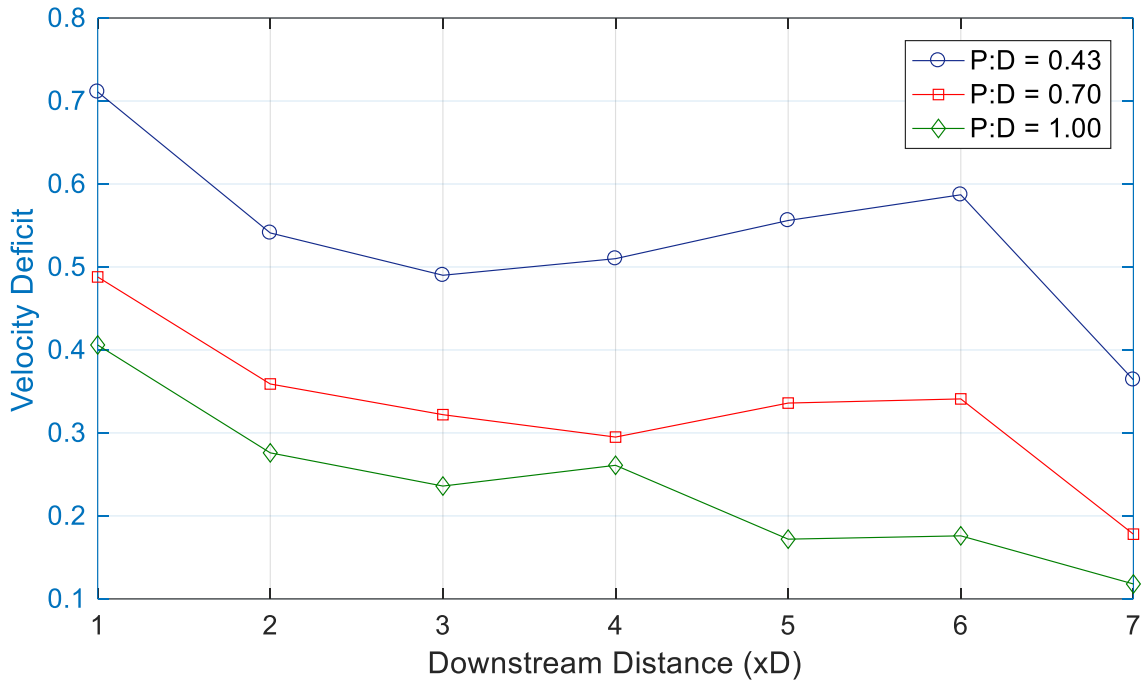

Figure 4.7 Velocity deficit at the measured downstream distance

Figure 4.7 represents the downstream wake velocity at the central line of the turbine i.e. (0, *y*, 0) with y the downstream distance from the turbine centre at which the velocity deficit is measured, where *y* is defined in terms of the turbine diameter i.e. multiples of D. The plot showed a higher velocity deficit indicating a lower wake velocity and high extraction of energy with the *P/D* of 0.43 turbine. In terms of the wake characteristic, Figure 4.8 shows the downstream velocity deficit behaviour where the wake was more structured and kept a streamtube form indicating a gradual mixing of the wake and freestream flow. The wake at *x* =

0 has the lowest wake velocity and gradually increases as the wake interacted with the freestream velocity. Regions of high velocity vortex corresponding to low pressure were observed at the outer tip of the turbine (at the highest radius) where cavitation inception is more likely to occur.

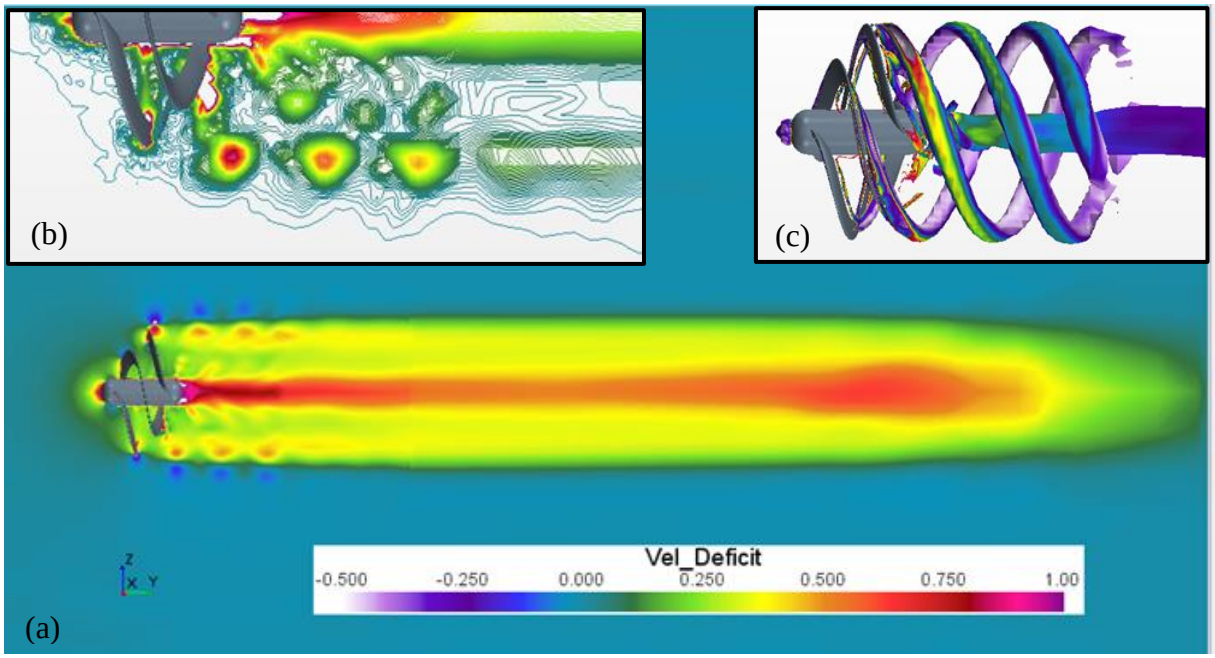

Figure 4.8 (a) The flow around and downstream of the *P/D* of 0.43 turbine, (b) close-up view of the wake at the turbine tip, (c) velocity extracted iso-surface around the blade tip region

The wake characteristic of the *P/D* of 0.43 turbine was further analysed in terms of the velocity deficit using a velocity probe at different depths, as presented in Figure 4.9. It was determined that at 0.3 m (in the radial direction) away from the centre of the turbine, the flow had resumed the free stream value. It was determined that at a distance of 1D immediately downstream of the turbine centre was a high velocity deficit region. In the subsequent

downstream distance, there was no clear trend whether the velocity had started to accelerate further downstream or otherwise, indicating turbulence in the flow.

.

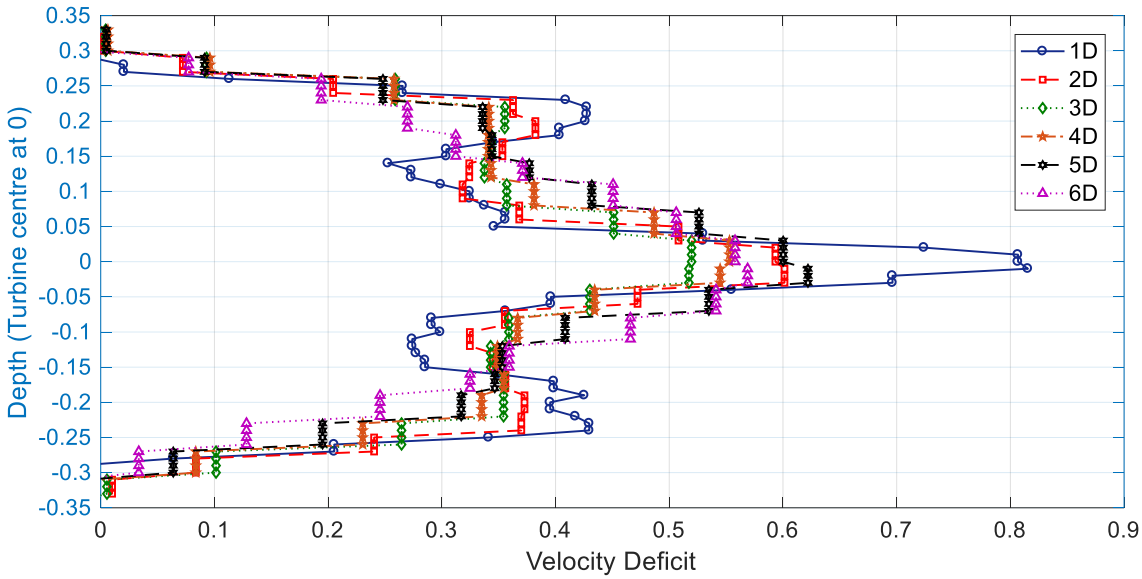

Figure 4.9 The velocity deficit distribution of the *P/D* of 0.43 Hydro-Spinna at different depths with respect to the turbine

The wake characteristic for the *P/D* of 0.7 turbine displayed a distorted streamtube form as shown in Figure 4.10. Regions of high velocity were also observed at the tip of the turbine in this condition as well as with the *P/D* of 1.0 turbine as shown in Figure 4.11. The wake characteristic of the *P/D* of 1.0 turbine was unstructured. It was believed that the Hydro-Spinna models with high *P/D* just obstruct the flow without developing an effective lift on their blades and hence not being able to extract energy efficiently while generating turbulence at the same time. The distribution of the blade pitch angle, as shown previously in Figure 4.4, which was at a higher value was believed to be a significant factor in the difference in the efficiency of power extraction. It was found that as the *P/D* of the turbine increased, not only was the energy extraction reduced but the wake generated by the turbine became more random. The wake from the *P/D* of 0.43 turbine progressed up to 4D downstream while with the low extracting *P/D* turbines, the wake progression was much less, up to about 3D.

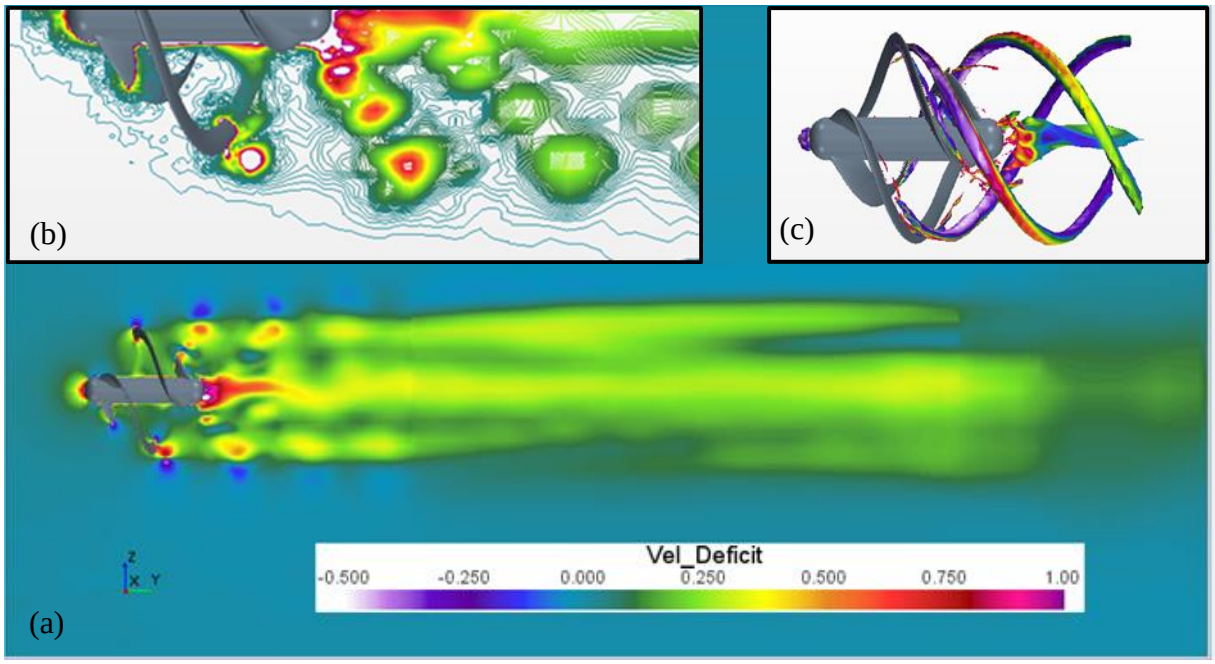

Figure 4.10 (a) The flow around and downstream of the *P/D* of 0.7 turbine, (b) close-up view of the wake at the turbine tip, (c) velocity extracted iso-surface around the blade tip region

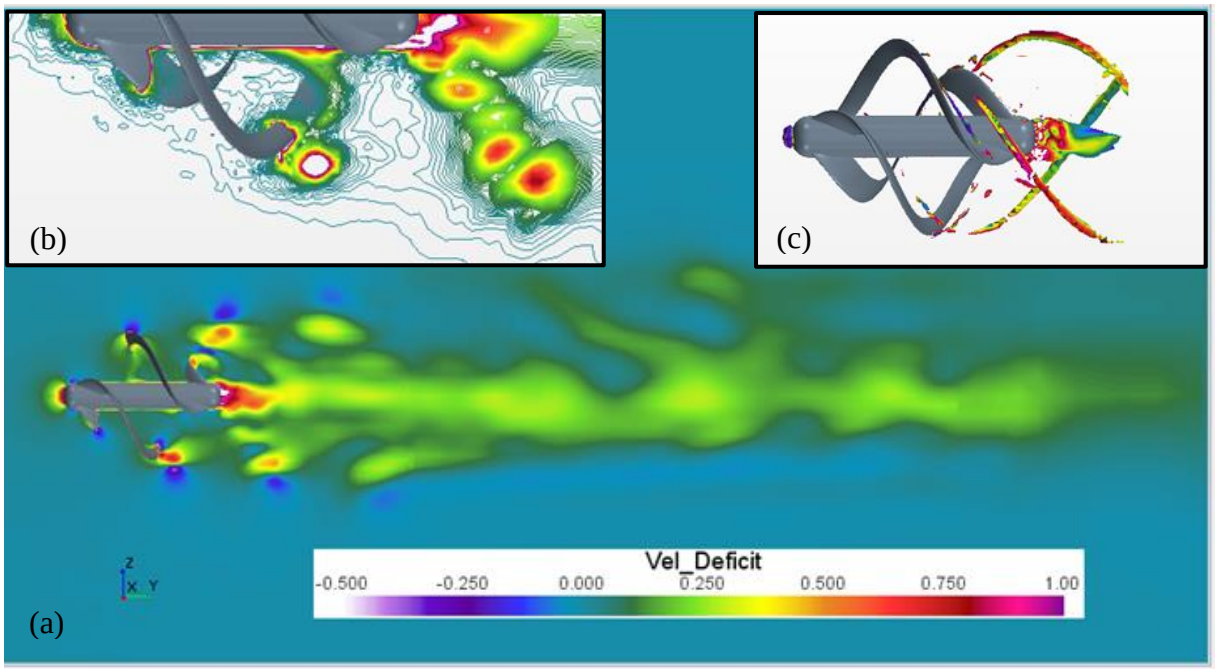

Figure 4.11 (a) The flow around and downstream of the *P/D* of 1.0 turbine, (b) close-up view of the wake at the turbine tip, (c) velocity extracted iso-surface around the blade tip region

4.7 Summary

This chapter presented a numerical investigation into the performance of the Hydro-Spinna turbine with different pitch to diameter ratios where the three *P/D* values were considered. Domain and mesh independency tests were conducted to adopt the best settings for the numerical model. The numerical investigations concluded that the efficiency performance of the turbine reduced as the *P/D* was increased. Another obvious difference was the reduction in the effective operational *TSR* range of the turbines where the range also decreased with higher ratio. The wake structure of the turbines was also evaluated where the wake downstream of the *P/D* of 0.43 turbine depicted a streamtube behaviour synonymous with tidal turbines while as the ratio increased, the wake became unstructured.

CHAPTER 5. FREE SURFACE INTERACTION WITH THE HYDRO-SPINNA PERFORMANCE

5.1 General Remarks

The objective of this chapter is to assess the experimental power performance of the 500 mm diameter Hydro-Spinna model, HS500 with *P/D* of 0.43. The performance of the turbine was evaluated at four different immersion depths to assess the effect of free surface and seabed proximity on its performance. The tests were carried out in the Towing Tank facility at Newcastle University. During initial exploratory tests conducted in the Wind Wave Current (WWC) tank of the same university, the Hydro-Spinna turbine was found to start rotating at a current flow of around 0.17 m/s. Based on this early result, the immersion depth tests were conducted at a flow velocity of 0.5 m/s to achieve a compromise between flow velocity and the time available for data acquisition. A 1 Nm electromagnetic brake was used to control the turbine rotational speed to cover the Tip Speed Ratio (*TSR*) range. The findings associated with the experimental portion of this chapter were reported in Rosli *et al.* (2016).

In this chapter, Section 5.3 outlines the test facility and equipment for the investigation as well as the details of the test procedure, test matrix and background theory. The experimental results and wake observation are discussed in Section 5.4 while Section 5.5 looks into analysis using numerical methods. Section 5.6 looks into the torque characteristic of the Hydro-Spinna turbine. Section 5.7 investigated the wake interaction with boundary proximities using numerical methods and the summary is presented in Section 5.8.

5.2 Hydro-Spinna Model (HS500) Key Parameters

The details of the Hydro-Spinna HS500 model was reported in Chapter 3 hence only the key parameters and specifications of this turbine are summarised in Table 5.1.

Table 5.1 The key details of the HS500 turbine model

	Values
Diameter	0.50 m
Pitch Length	0.21 m
Hub Diameter	0.10 m
Pitch to Diameter Ratio	0.43
Blade Cross-Section Profile	NACA 0015

5.3 Facility Set Up

5.3.1 Test Facility

The investigations into the performance of the Hydro-Spinna HS500 were conducted in the Towing Tank facility of Newcastle University with the main particulars listed in Table 5.2 below.

Table 5.2 Main particulars of the Towing Tank facility used for the investigations

Tank Length	37 m
Tank Width	3.7 m
Maximum Water Depth	1.25 m
Maximum Carriage Velocity	3 m/s

Before the investigations, the Hydro-Spinna HS500 system was placed in the WWC Tank of Newcastle University to test the integrity and strength of the system set up at different incoming flow velocities. The turbine system was found to be able to withstand the incoming flow velocity of up to 1 m/s which is the maximum velocity in that facility. It was observed that the turbine starts to rotate at a flow velocity of approximately 0.17 m/s. Based on these initial findings, it was concluded that the performance investigation of the Hydro-Spinna turbine at different immersion depths should be conducted at a flow velocity of 0.5 m/s in the Towing

Tank test. At this velocity, a range of *TSR*s with sufficient data acquisition period can be conducted.

5.3.2 Hydro-Spinna System for Towing Tank Test

The Hydro-Spinna turbine was mounted on a 6 mm steel shaft that was supported at both ends of the turbine by struts and bearings. For the experimental set up, two struts i.e. the front and main supports were employed to distribute the weight of the turbine and to reduce the stress on the shaft and the mechanical transmission components. In hindsight, the mechanical arrangement could have been better designed to support the turbine at only one end. However due to the small shaft diameter, it was decided to support the turbine at both end to avoid breaking the shaft. Furthermore, the system needs to be robust to withstand the unsteady forces on the turbine blades. The rotation of the turbine is transmitted to a shaft drive located on the towing carriage via a belt and pulley system. The drive shaft is connected to a torque transducer as well as the brake via couplings as shown in Figure 5.1. The pulley system was employed to protect the measuring equipment from water damage.

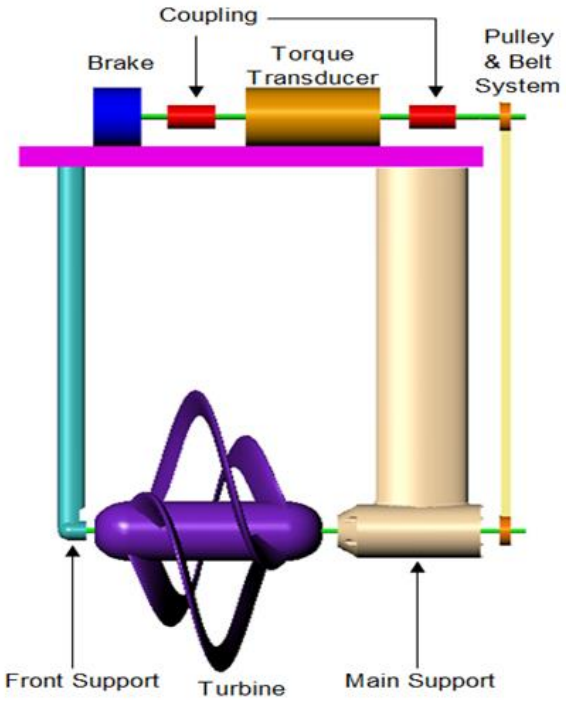

Figure 5.1 The Hydro-Spinna HS500 turbine set up for the Towing Tank test

The 1 Nm brake was used to control the rotational speed of the turbine via the drive shaft and pulley system whilst the torque transducer was used to measure the torque and rotational speed of the turbine. The carriage rig in the Towing Tank facility was equipped with load cells to measure drag so that the total drag of the whole turbine system could be determined. Figure 5.2 shows the close up photo of the turbine test set up for the performance assessment in the towing tank.

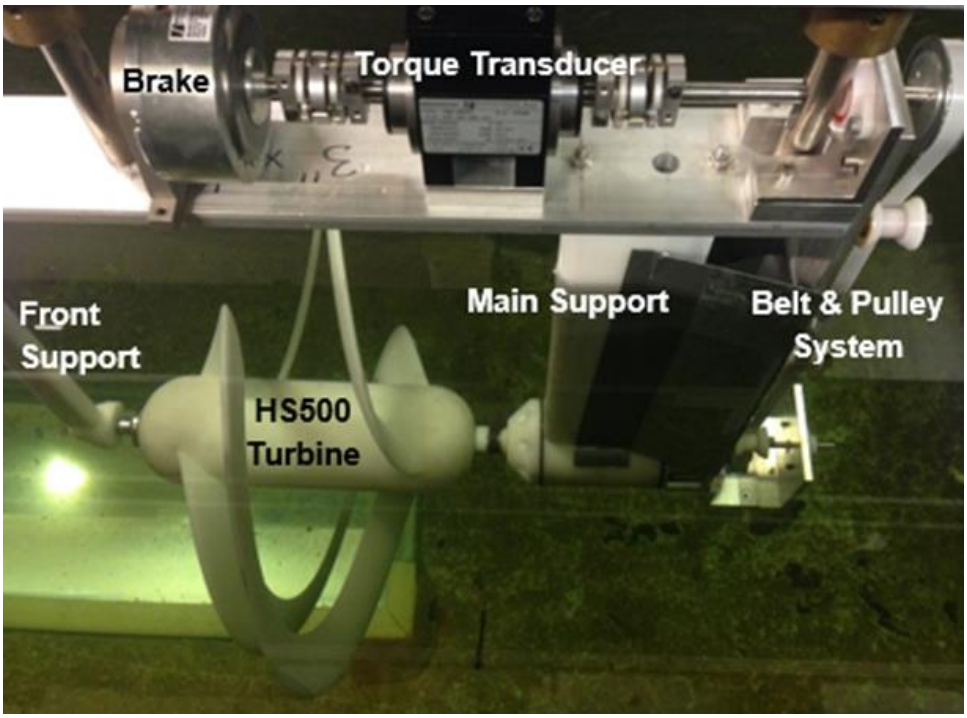

Figure 5.2 The Hydro-Spinna system arrangement for the performance test

For each experiment, data was recorded for a duration of 10 seconds, at 0.01 second sampling time, giving a total of 1001 data points. Each run was repeated three times to assess the repeatability of the experiments. The standard deviation and the standard error with 95% confidence level are listed in Table 5.3.

Table 5.3 Standard deviation and error for the experimental data

	Standard Deviation	Standard Error
Carriage Velocity (m/s)	0.13	± 0.008
Rotational Speed (rpm)	2.45	± 0.1
Torque (Nm)	0.02	± 0.001

5.3.3 Brake Calibration for Regulating Torque

In order to obtain the turbine performance for a range of operational *TSR*s, a 1 Nm Magtrol HB-140M-2 magnetic brake was used to regulate the rotational speed of the turbine. A voltage input to the brake was used to control the torque and hence rotational speed of the turbine. The amount of voltage corresponds to a torque applied to provide the braking action on the turbine rotation. The voltage versus torque calibration is shown in Figure 5.3 where the relationship was linear for voltage supplied from 2.5 V up to the maximum voltage of 5 V.

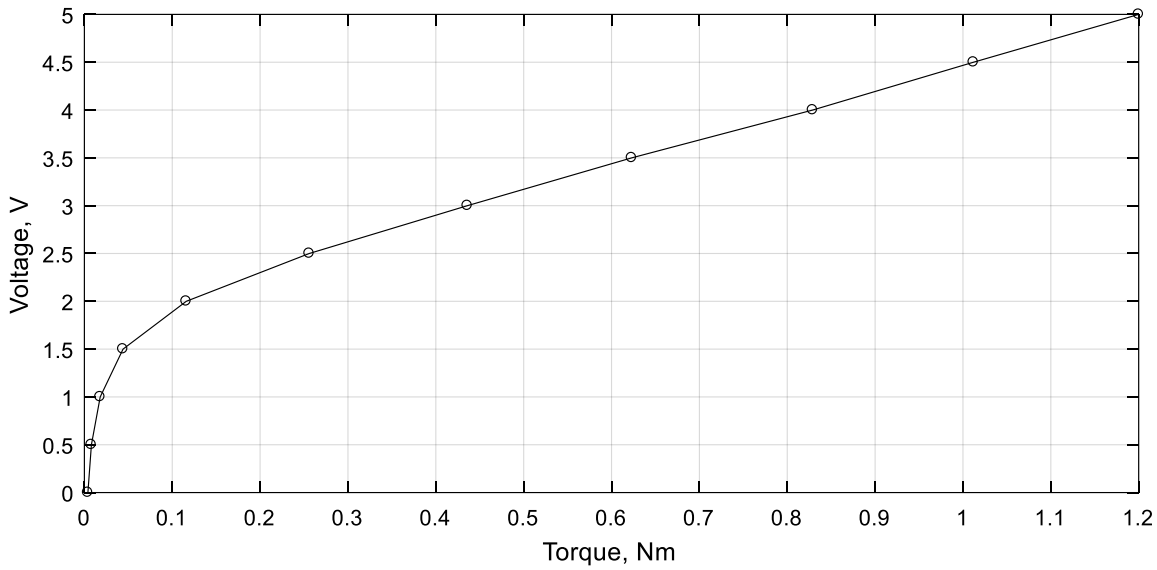

Figure 5.3 The voltage and torque relationship of the 1 Nm brake calibrated with increasing voltage

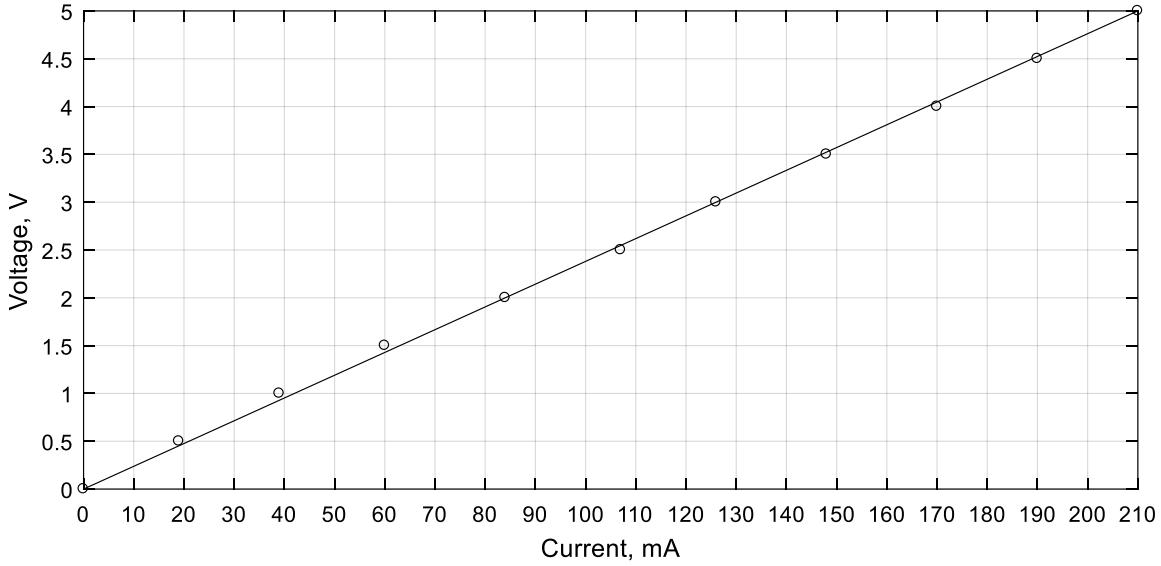

Figure 5.4 The linear relationship between the voltage and current of the electromagnetic brake

The trend for the current and torque calibration presented similar results and the relationship of the voltage and current was linear, as shown in Figure 5.4. Since the voltage and current relationships with the torque of the brake were identical, the torque applied by the brake to the Hydro-Spinna was regulated by controlling the voltage rather than the current. A voltage control box was used to regulate the voltage supplied with a trigger mechanism to maintain the same voltage level for each run. Since the voltage and torque had a linear relationship from 2.5 V onwards, the voltages were regulated between 2.5 V and 5 V only.

5.3.4 Test Procedure

The investigation into the performance of the Hydro-Spinna HS500 turbine was carried out in two parts. The first one was to measure the power coefficient of the HS500 at deep immersion, which was the deepest submersion configuration amongst the four different turbine submergences tested, at four varying incoming velocities. Secondly, the turbine was tested at a fixed incoming velocity of 0.5 m/s summarised in Table 5.4 where D is the diameter of the turbine as being 500 mm.

Table 5.4 Test matrix for the HS500 performance test

	Flow Velocity (m/s)	**Immersion Depth**	**Distance (mm) i.e. Turbine tip to water surface**
Test 1	0.5	0.36 D	180
	0.7		
	0.9		
	1		
Test 2	0.5	0.36 D (Deep)	180
		0.20 D (Shallow)	100
		0 D (Surface)	0
		Half Submerged	-250 (half of turbine is underwater)

The immersion depth was specified as the depth of water from the upper tip of the turbine to the water surface as illustrated in Figure 5.5. The distance from the turbine to the bottom of the tank remained unchanged where the distance between the shaft centre of the turbine and the bottom of the tank was 470 mm. The rationale for keeping the distance to the bottom of the tank constant was to eliminate the effect of the bottom boundary parameter in the results. Rather than lifting the turbine up to achieve different immersion depths, water was drained from the tank to keep the lower surface boundary constant while changing the upper boundary proximity. Therefore, the total water depth in the tank was 900 mm at deep immersion, 820 mm at shallow immersion, and 720 mm at surface immersion. The blockage ratio for this test was between 5.9% the deep immersion to 11.3% at the half submerged condition, therefore no blockage effect correction was done on the test results.

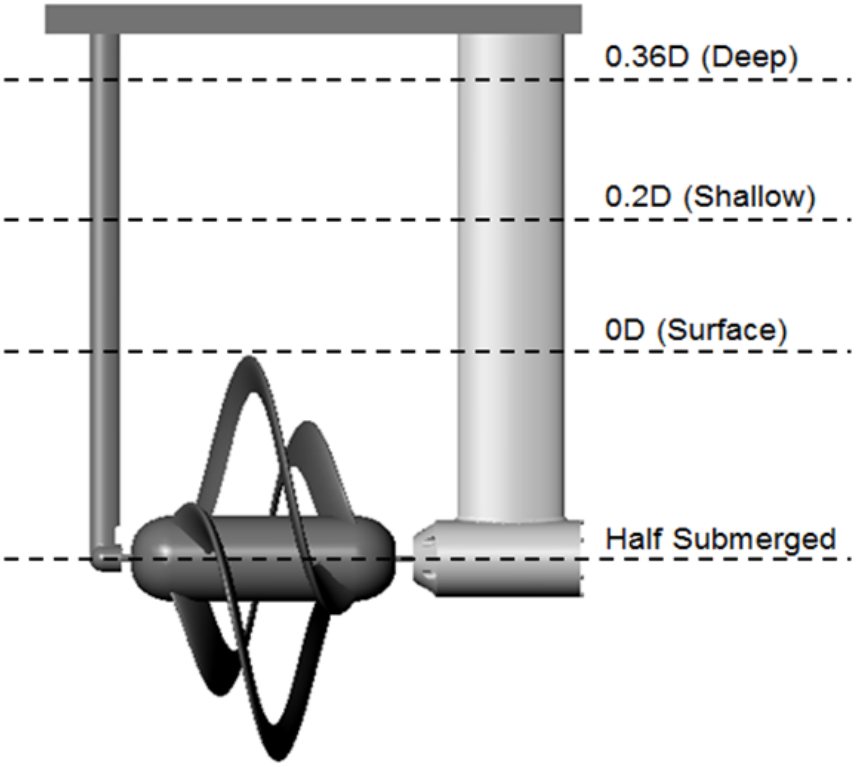

Figure 5.5 Illustration of different immersion depth

5.4 Results and Discussion

5.4.1 Performance Results at Different Flow Velocities

When conducting model scale testing, there is bound to be discrepancy in Reynold's Number between the model and full scale prototype. The difference in Reynold's Number can be disregarded as long as both the Reynold's Number in the model and that in the prototype lie in the same turbulence classification (Bahaj and Myers, 2013). However, the performance of a model scale turbine is said to be independent of Reynold's Number when the value exceeds 10^6 (Mason-Jones *et al.*, 2012) or even if it is more than 10^5, as reported by Bahaj and Myers (2013). Additionally, in open channel flows, the difference in Reynold's Number is usually compensated by keeping the Froude Number similar in both cases. However, the Froude Number has no influence on the hydrodynamic performance of a tidal current turbine (Doman *et al.*, 2015). In was also stated that the influence of a submerged obstruction on the water surface elevation is independent when Froude Number is kept below 0.25. The model tests in

the Towing Tank has a maximum Froude Number of 0.23 at the half-submerged condition where it is believed to have minimal impact on the Hydro-Spinna performance.

The first test was to determine the power performance of the HS500 turbine at the deep immersion for different flow velocities. Due to the limitation on the 1 Nm brake which was intended for a flow velocity of 0.5 m/s, a full *TSR* plot for velocities greater than 0.5 m/s could not be obtained. The HS500 reached a maximum power coefficient of 0.275 at the optimal *TSR* of 2.2 as shown in Figure 5.6.

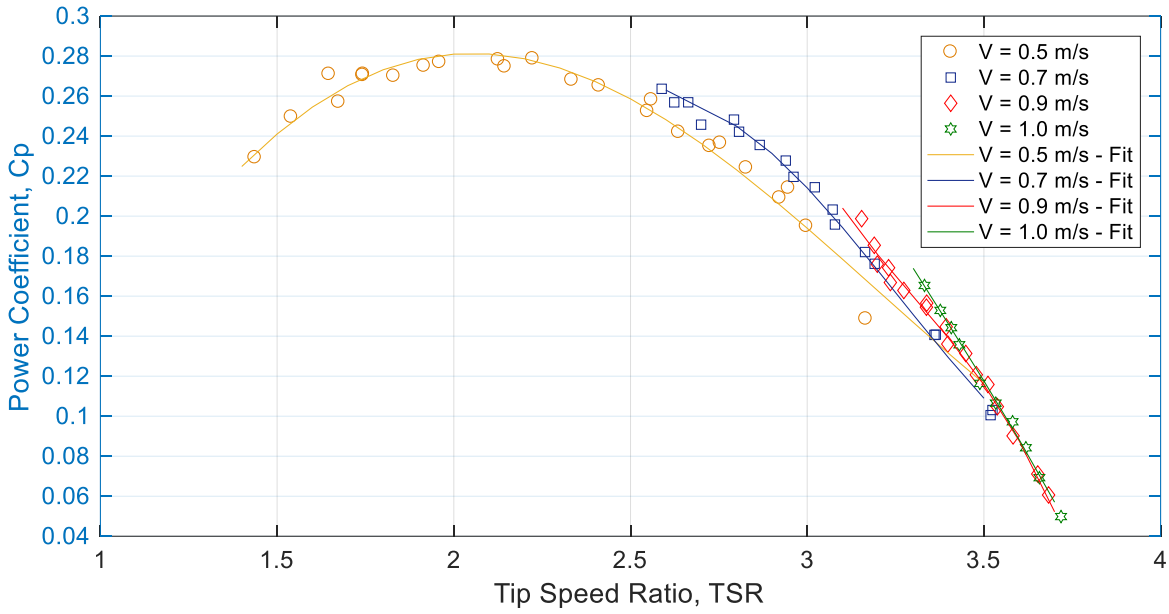

Figure 5.6 The power coefficient of the HS500 turbine with different incoming velocity

In comparison to other tidal turbines, obviously, the HS500 produces a lower power coefficient, as shown in Table 5.5 where a turbine investigated by Bahaj *et al.* (2007b) was found to operate at a peak power coefficient of 0.46, capturing almost half than the power available in the flow. In another study, a twin rotor, contra-rotating turbine design operated at a power coefficient of 0.45 with a $0 < TSR < 10$ range (Clarke *et al.*, 2007). Besides the difference in the power performance of the HS500, the range of operational *TSR* was also smaller than that of other conventional turbines where the maximum operational *TSR* of the HS500 was 4 while the conventional turbine operates up to a *TSR* of 12.

Table 5.5 A comparison of the HS500 and a conventional marine turbine design

	Hydro Spinna, HS500	**400 mm Turbine (Bahaj *et al.*, 2007b)**
Cp	0.275	0.46
Optimal *TSR*	2.2	6
***TSR* Range**	$0 < TSR < 4$	$0 < TSR < 12$

At a first glance, the low power coefficient of the HS500 may appear to be a shortcoming compared to other marine turbines. However, a high power coefficient is not the only important criterion for marine turbine designs especially when potential sites with adequate velocities are scarce. As the Hydro-Spinna turbine operates at much lower flow velocities, it is a more attractive option for sites than do not have remarkable tidal potential. The Hydro-Spinna has the potential to fill a niche application in tidal energy industry where conventional designs are unable to operate due to their requirement for sites with high velocities (EMEC, 2013).

In addition, as it operates at low velocities, its operational duration in a given tidal cycle is longer than a conventional turbine therefore the total energy captured may be comparable to other devices with lower operational and maintenance costs. The Hydro-Spinna turbine also operates at a much lower rotational speed at maximum efficiency. By operating at a low rotational speed, blade cavitation is less likely to occur. This is a major advantage as turbine blade erosion can be avoided and the underwater noise level is potentially greatly reduced.

The drag coefficient, defined in Equation 5.1, of the whole turbine system including the thrust, shown in Figure 5.7, shows a decreasing trend with increasing *TSR*. The drag coefficient of the HS500 turbine showed an opposite trend from that of conventional turbines (Bahaj *et al.*, 2007b; Batten *et al.*, 2007). Figure 5.8 is a thrust coefficient plot reproduced from the work by Luznik *et al.* (2012) to show the increasing nature of the thrust coefficient with increasing *TSR* for a conventional current turbine. The design of the Hydro-Spinna turbine where it is extended in the axial direction making it three-dimensional, rather than in the form of an actuator disc, is thought to be responsible for its distinctive trend in drag coefficient.

$$C_D = \frac{D}{0.5\rho A_S U^2}$$

Equation 5.1

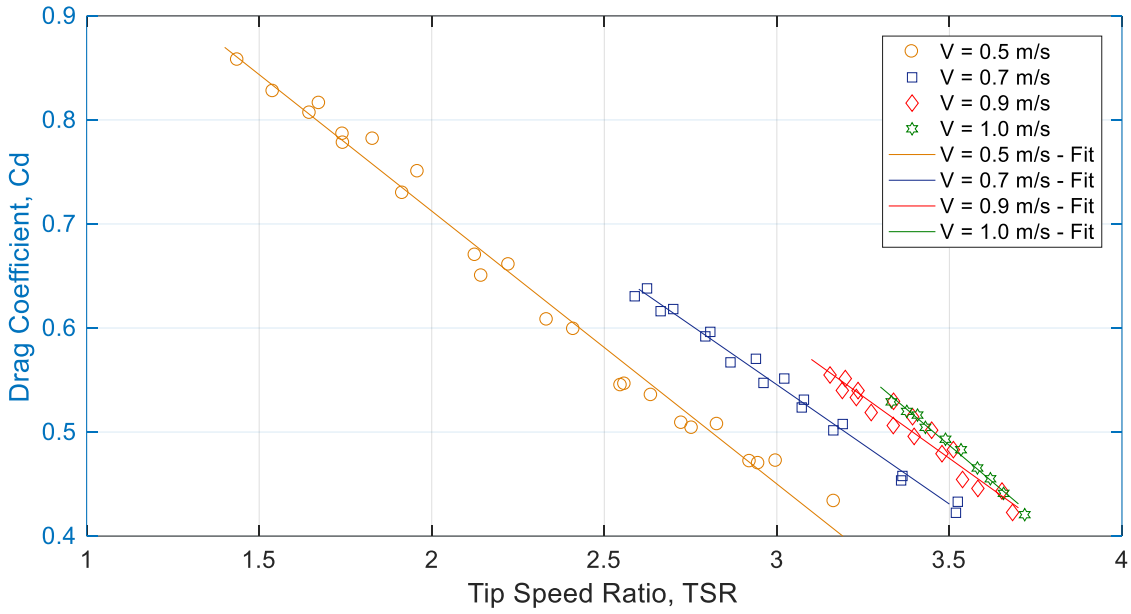

Figure 5.7 The drag coefficient of the HS500 turbine at different velocities

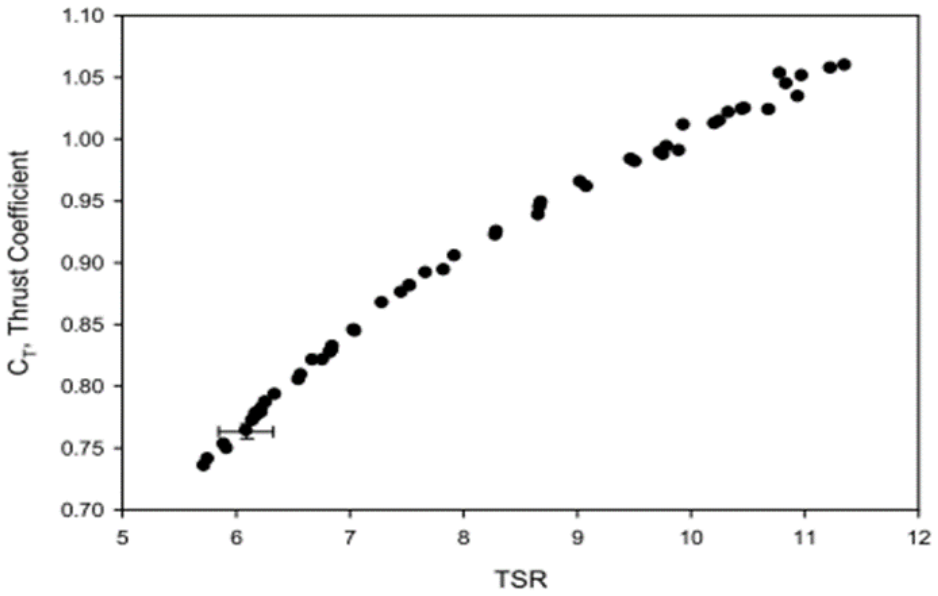

Figure 5.8 The increasing thrust coefficient profile of a three bladed conventional turbine with a NACA 63-618 blade profile (Luznik *et al.*, 2012)

In the axial direction, the turbine can be interpreted as having a front, upstream half and a downstream half. The pitch angles of the turbine blade on the upstream half is positive while they are negative on the downstream half. Therefore, the direction of the resultant velocity seen by one half of the turbine is different from the other. The total resultant force acting on the turbine is believed to be responsible for the trend in drag. However, further investigation should be carried out into the drag behaviour of the Hydro-Spinna turbine which was not explored in this study.

5.4.2 Performance Results at Different Immersion Depth

Interestingly, the HS500 showed an independence of performance with immersion depth where, in contrast to conventional turbines, the Hydro-Spinna turbine was found to generate higher or equivalent power as the immersion depth was reduced. The power and drag coefficients are plotted in Figure 5.9 and Figure 5.10 respectively where the Hydro-Spinna turbine displayed relatively less dependence on the immersion depths.

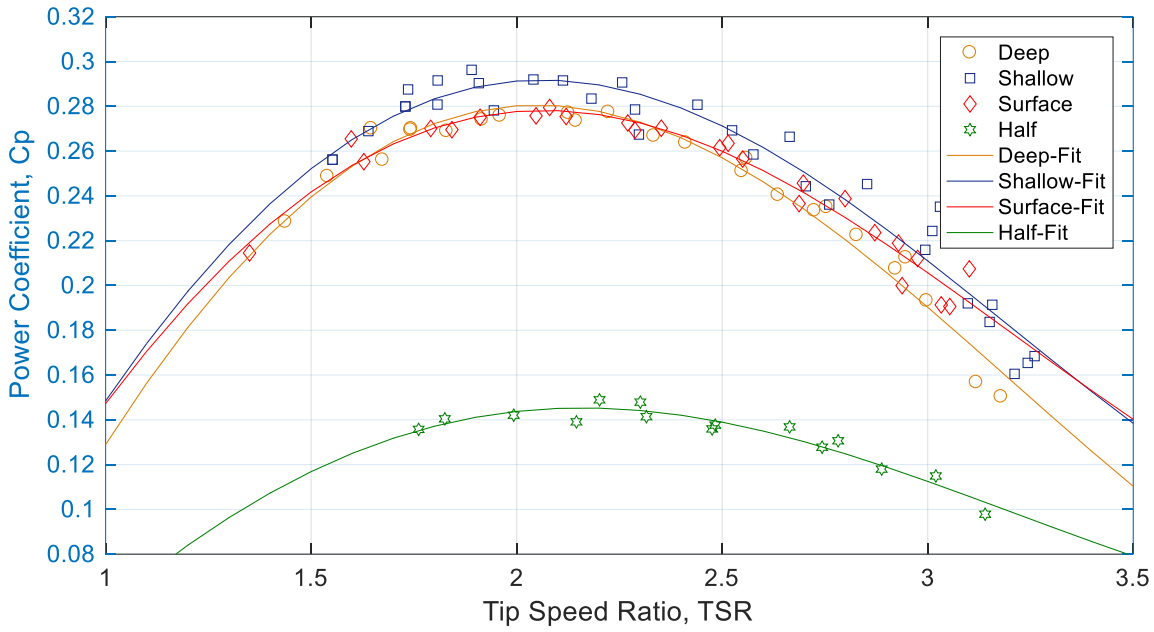

Figure 5.9 The power coefficient plots of the Hydro-Spinna at different immersion depths

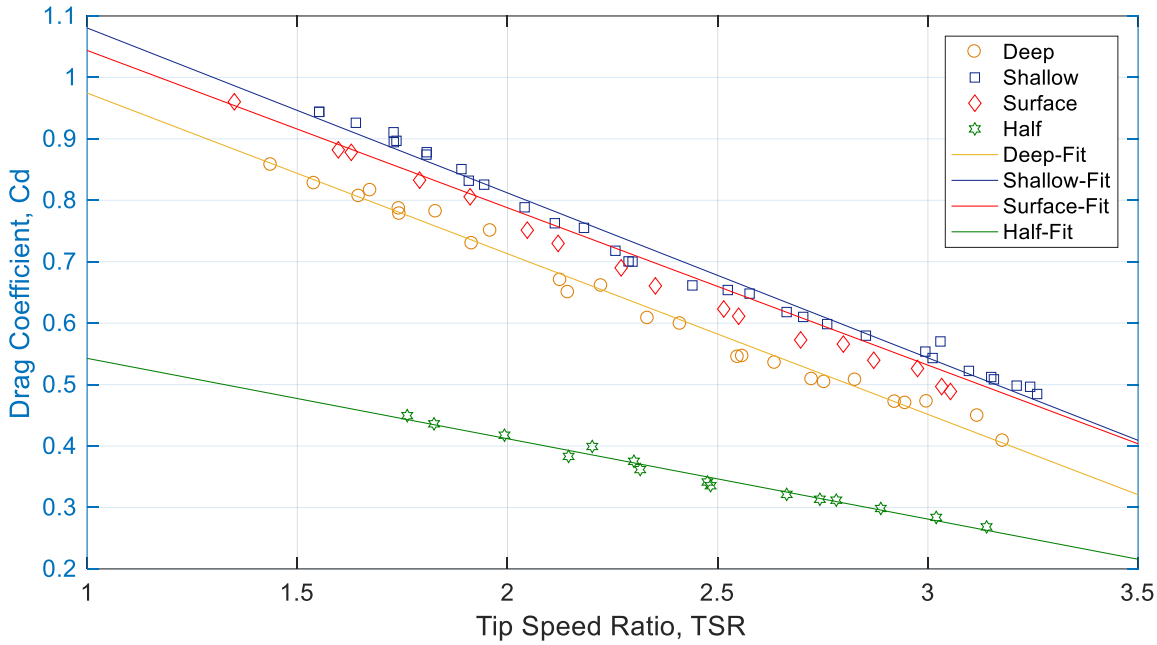

Figure 5.10 The drag coefficient plots of the Hydro-Spinna at different immersion depths

As discussed in the previous Section, the HS500 turbine reached a maximum power coefficient of 0.275 at a *TSR* of 2.2 when operating at the deep immersion depth. When the immersion level was reduced to the shallow immersion, the HS500 turbine was found to generate a slightly higher coefficient of 0.29, an increase of 5.5% at the same optimal *TSR*, as shown in Figure 5.11. Additionally, the performance at the surface condition was found to generate a similar peak power coefficient and trend to the deep immersion case, as shown in Figure 5.12.

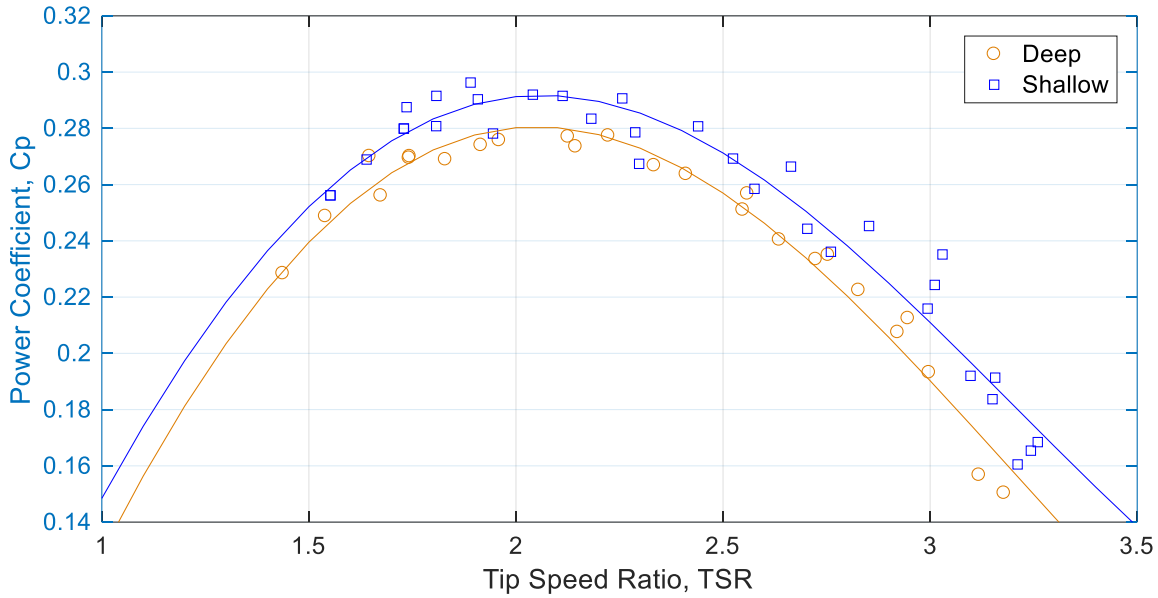

Figure 5.11 Power performance comparison between deep and shallow immersion

Generally, with conventional turbines, the performance of a turbine is diminished as the turbine gets closer to the surface. The proximity of the free surface is understood to constrain the full expansion of the wake, reducing the pressure difference across the turbine. In a study conducted by Bahaj *et al.* (2007b), a HATT performance were assessed at two different tip immersion depth of 0.55D and 0.19D where the performance decreased by up to 15% as the depth decreased. Based on the performance evaluated on the Hydro-Spinna turbine however, this does not appear to be the case.

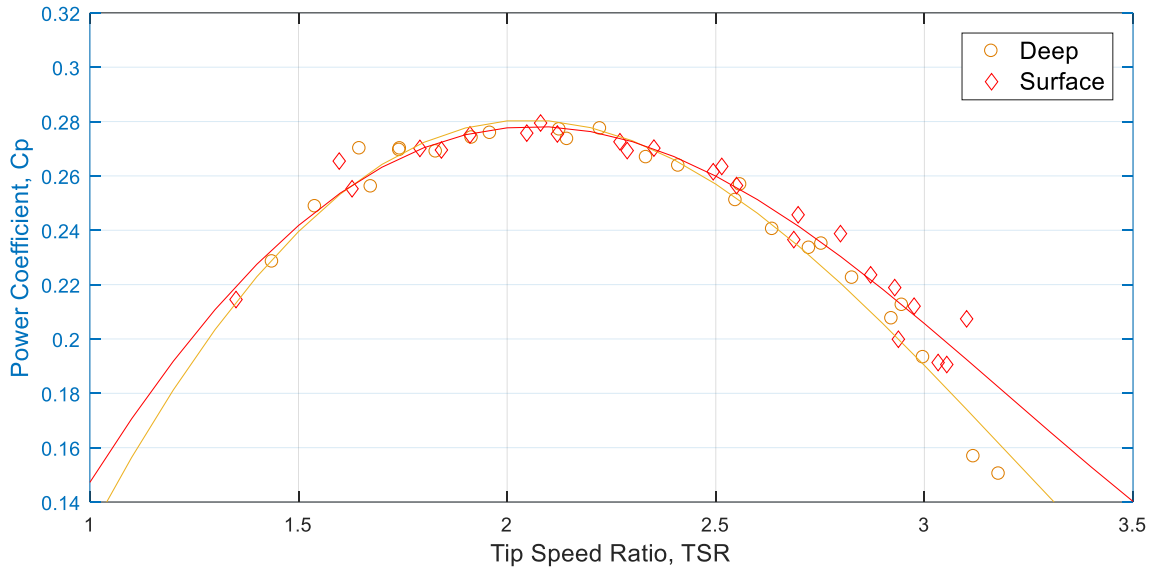

Figure 5.12 Power performance comparison between deep and surface immersion

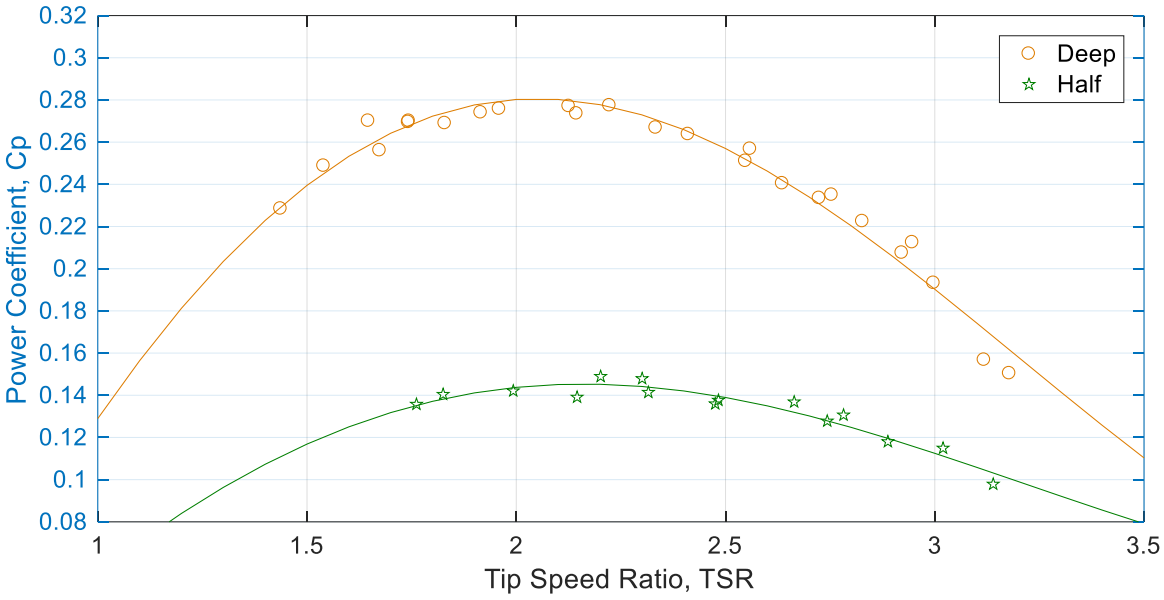

Figure 5.13 Power performance comparison between deep and half submerged

The Hydro-Spinna was observed to operate at the half submerged condition with a power coefficient of 0.15 at an optimal *TSR* of 2.25 compared to the deep immersion case, as shown in Figure 5.13. In the former case, the whole turbine area was used in the calculation of

the power coefficient even though only half the turbine was submerged. Any power generated by the turbine above the water surface, in the air, was assumed negligible and ignored in the calculation. Regardless of the reduction in the power coefficient, the adaptability and capability of the Hydro-Spinna turbine to operate in such a condition merits its consideration for locations that are outside the norm for other tidal turbines.

5.4.3 Downstream Wake Observation

Surface vortices were observed as the flow passed the front strut causing disturbance to the flow seen by the turbine. Moreover, the front strut appeared to cause more visible disturbance to the flow than the operation of the turbine itself as shown in Figure 5.14. Vortices were created as a result of the interaction of the strut wake and rotation of the turbine. This observation was much more distinct as the immersion depth of the turbine reduced as well as at low *TSR* as the slowly rotating turbines cuts more slowly across the disturbance.

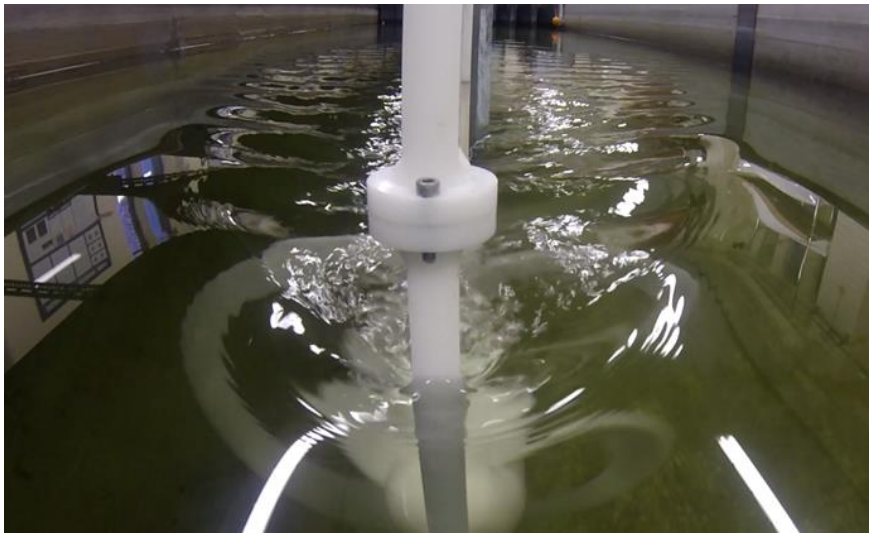

Figure 5.14 Wake generated mainly from the front support downstream of the system

At the surface, vortices are observed on both side of the downstream flow, as shown in Figure 5.15, where the turbine cuts across the downstream wake of the front strut at point X.

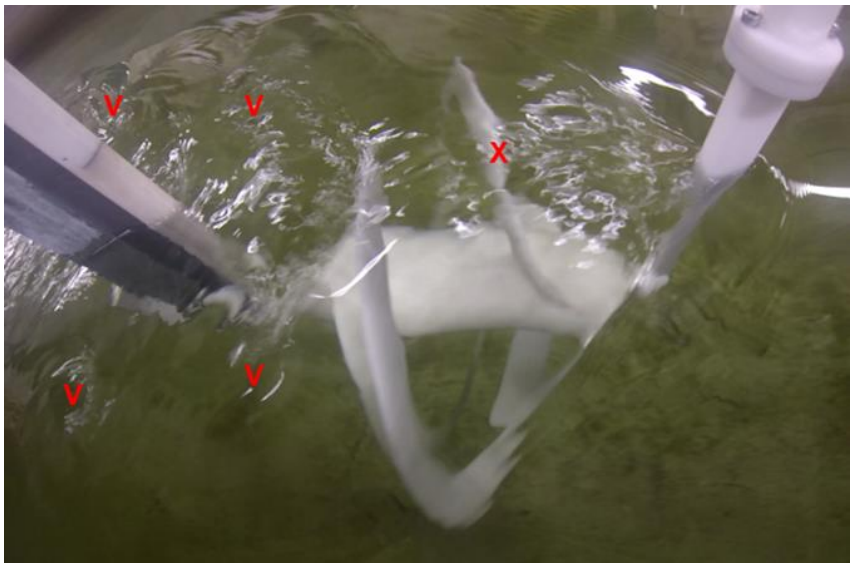

Figure 5.15 Point X where the turbine cuts across the wake of the front strut creating surface vortices downstream (Rosli *et al.*, 2016)

Similar surface wake expansion was observed in the half-submerged condition, shown in Figure 5.16, although the vortices were not as clearly defined as those in the surface immersion case. This was because there was less disturbance caused by the front support in the upstream flow seen by the turbine.

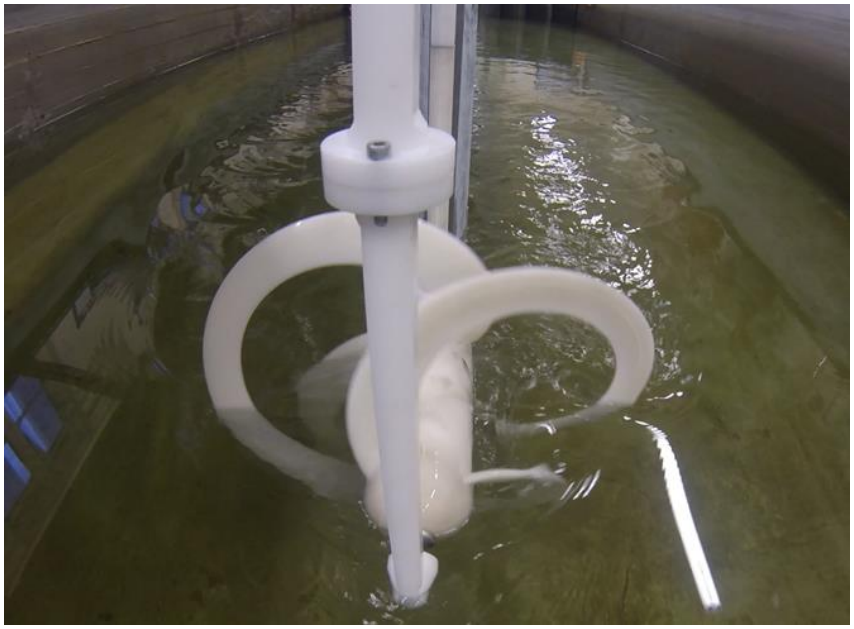

Figure 5.16 The surface wake expansion in the half-submerged condition

The fact that the Hydro-Spinna operation is relatively independent of the immersion depth offers a unique prospect for its effective deployment especially in sites with shallow water depth. Furthermore, the Hydro-Spinna turbine was found to operate in the half submerged condition which confirms the initial finding of the work done by Lin (2009) on the original concept design. Although, some might argue that the Hydro-Spinna turbine would not be competitive at high potential sites, the flexibility of its operation merits consideration of the Hydro-Spinna for deployment at other locations such as low velocity sites or even in remote sites where the water depths are not as great as offshore locations.

5.5 Numerical Modelling of the HS500 Power Performance

An investigation into the performance of the Hydro-Spinna turbine using numerical methods was also conducted in order to validate the numerical methods adopted in this thesis. The turbine system that interacted with the flow in the experimental investigation was considered in the numerical investigation including the front and main supports. It is important to replicate the experimental set up in the numerical analysis in order to eliminate inconsistency as much as possible. Provided that the experimental and numerical results agree with each other, it is convenient to use the computational simulations to analyse the flow behaviour around and downstream of the turbine.

The same governing physics and equations used in Chapter 4 were utilised as summarised in Table 5.6.

Table 5.6 Summary of the numerical details used in the investigation

Setting	**Remarks**
Governing Equation	RANS
Turbulence Model	k-ω model
Mesh Numbers	4,028,924

5.5.1 Computational Domain

For this investigation, the numerical domain was set to have the same dimensions as the HS500 as well as the width and depth of the Towing Tank while the upstream and downstream boundaries were 2 m and 5 m from the turbine centre respectively. Prism layers and refined mesh settings were set on the turbine and the front and main strut surfaces to enhance the flow around the structures, as shown in Figure 5.17. The mesh size downstream of the turbine was also refined to take into account the turbulence mixing in the wake.

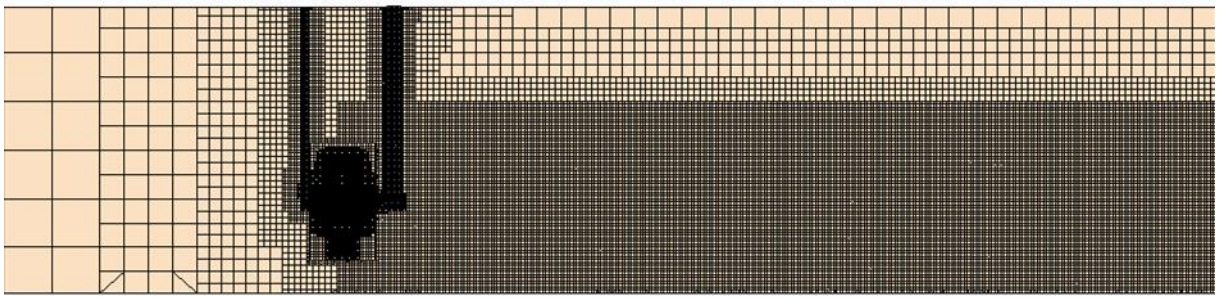

Figure 5.17 The mesh sizing of the turbine system and flow domain with heavy refined mesh around the turbine and support regions

The numerical investigation included the free surface setting to replicate the conditions of the experimental investigation. For each condition, the free surface level was set accordingly such as shown in Figure 5.18.

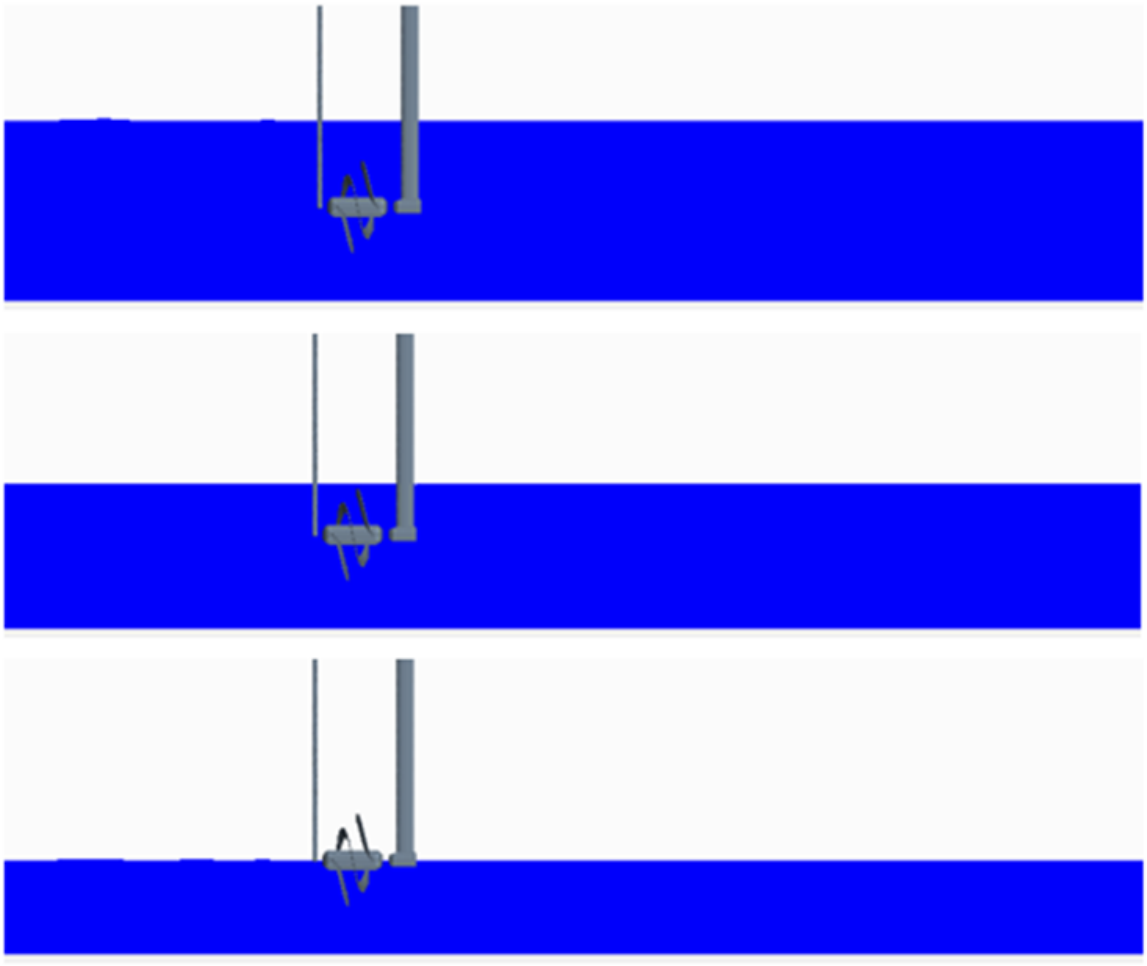

Figure 5.18 Different initial water level settings in the numerical domain (top: 0.36D immersion, middle: surface immersion and bottom: half-submerged)

5.5.2 Numerical Results

The trends of both the experimental and numerical data were found to largely agree, as shown in Figure 5.19, especially at the *TSR* region where the maximum power coefficient was generated. The numerical results appear to over predict the performance for *TSR* slightly above the optimal value. For the shallow immersion, in Figure 5.20, the experimental and numerical results followed the same trend. However, the numerical model under-predicted the power coefficient at $1.5 < TSR < 2.25$, slightly below the optimised speed.

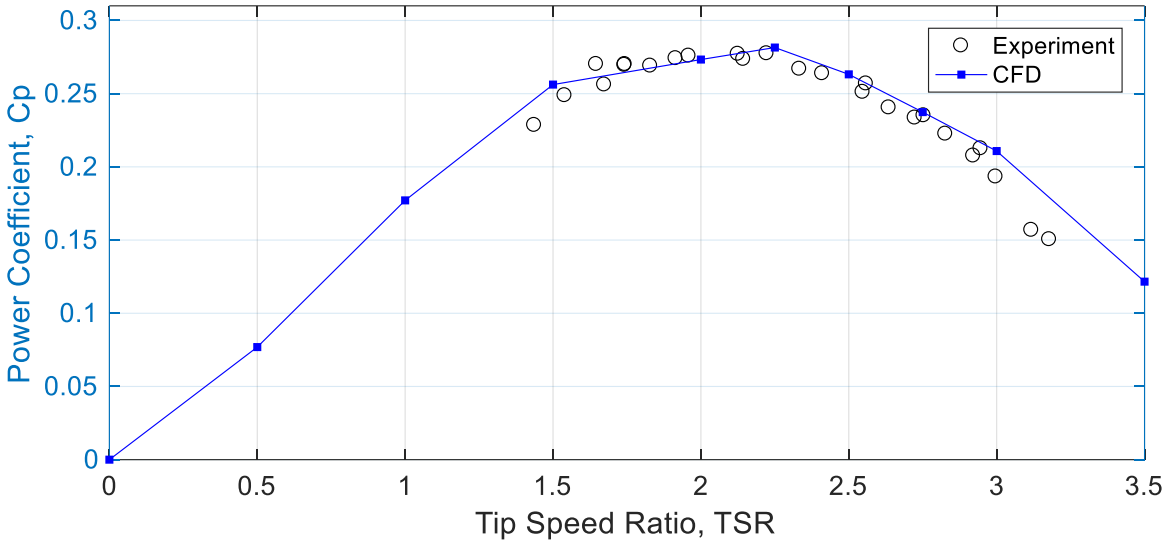

Figure 5.19 Comparison of experimental and numerical data at deep immersion

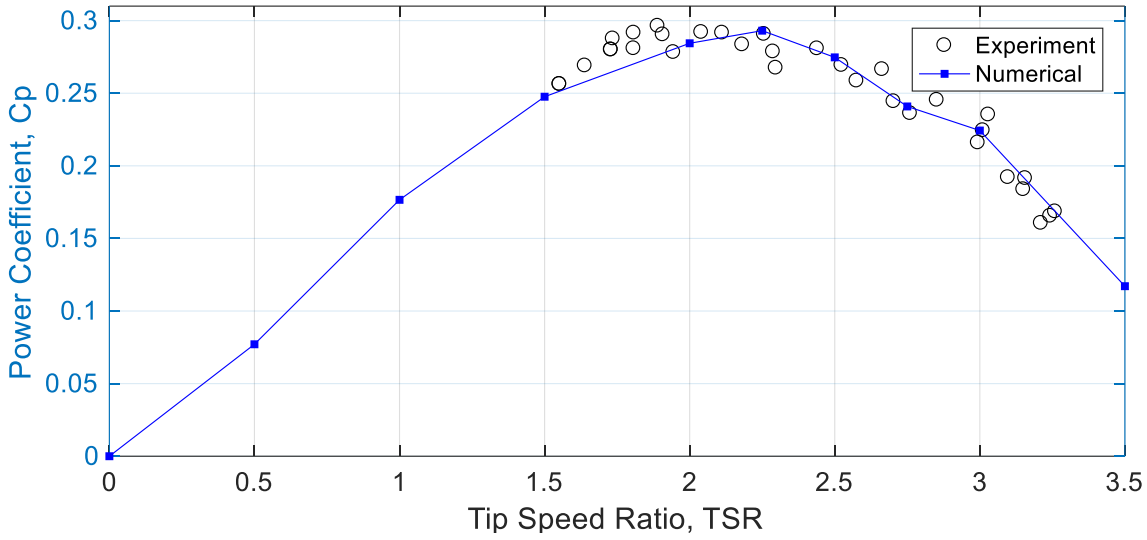

Figure 5.20 Comparison of experimental and numerical data at shallow immersion

At the surface immersion, the numerical results predicted a higher performance at $TSR \gg 2$; approximately 7% higher than the experimental result at the optimal *TSR* of 2.25 as shown in Figure 5.21. The numerical modelling may have underestimated the wake behaviour of the turbine and hence determined a higher power coefficient. For the half-submerged condition, shown in Figure 5.22, the numerical results largely followed the same trend as the

experimental data around the optimal *TSR* range as there were no regular trend in the difference between the two results.

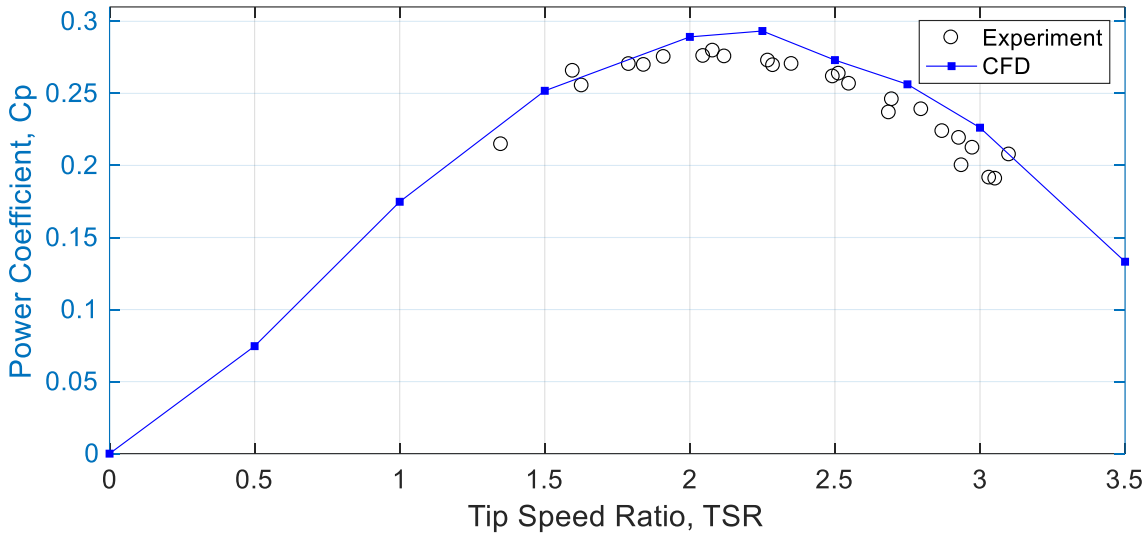

Figure 5.21 Comparison of experimental and numerical data at surface immersion

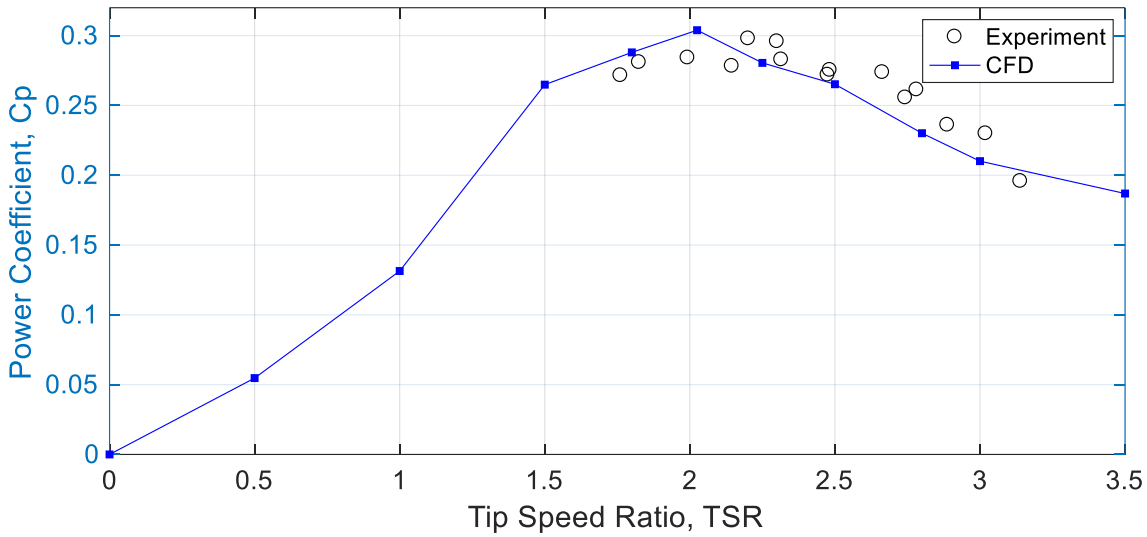

Figure 5.22 Comparison of experimental and numerical data at half-submerged

The thrust coefficient on the Hydro-Spinna was also evaluated in the numerical analysis. The thrust coefficient was found to follow a similar trend regardless of the immersion depth and reached its highest at *TSR* = 1 for the three fully submerged conditions shown in Figure 5.23. Whereas for the half submerged condition, the thrust coefficient was the highest at *TSR* = 1.5.

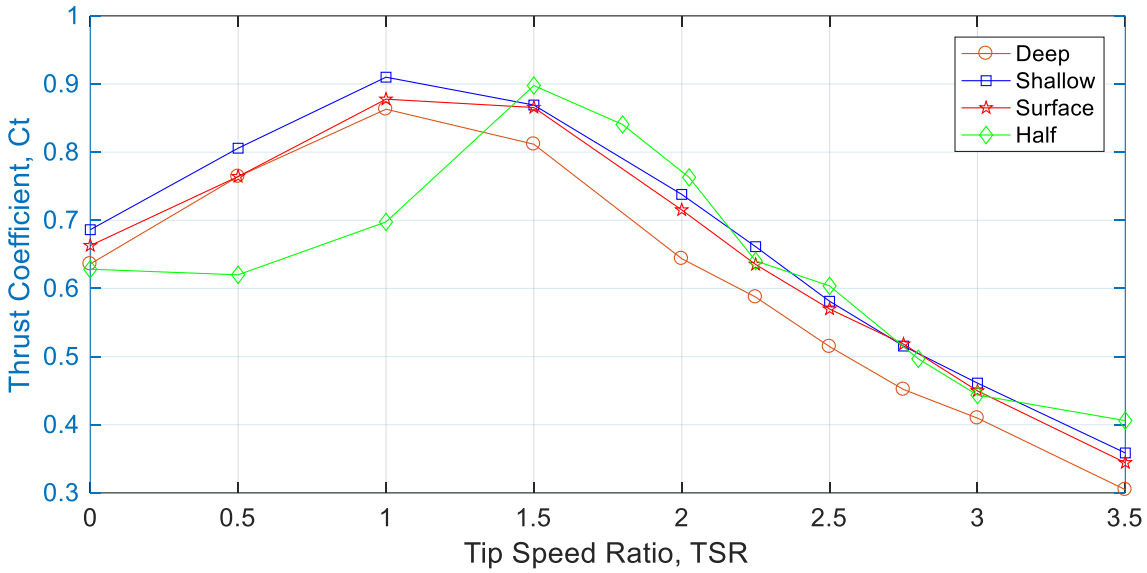

Figure 5.23 Thrust coefficients of the Hydro-Spinna HS500 at different immersion depths

5.6 Torque characteristics of the Hydro-Spinna

The torque coefficient, defined in Equation 5.2, of the Hydro-Spinna turbine were also evaluated both in the experimental and numerical investigations, as shown in Figure 5.24 below. Similar to the power and thrust coefficients, the torque coefficients displayed a reasonable correlation between the two cases. No experimental data was obtained for *TSR* < 1.25.

$$C_Q = \frac{Q}{0.5\,\rho A U^2 R}$$

Equation 5.2

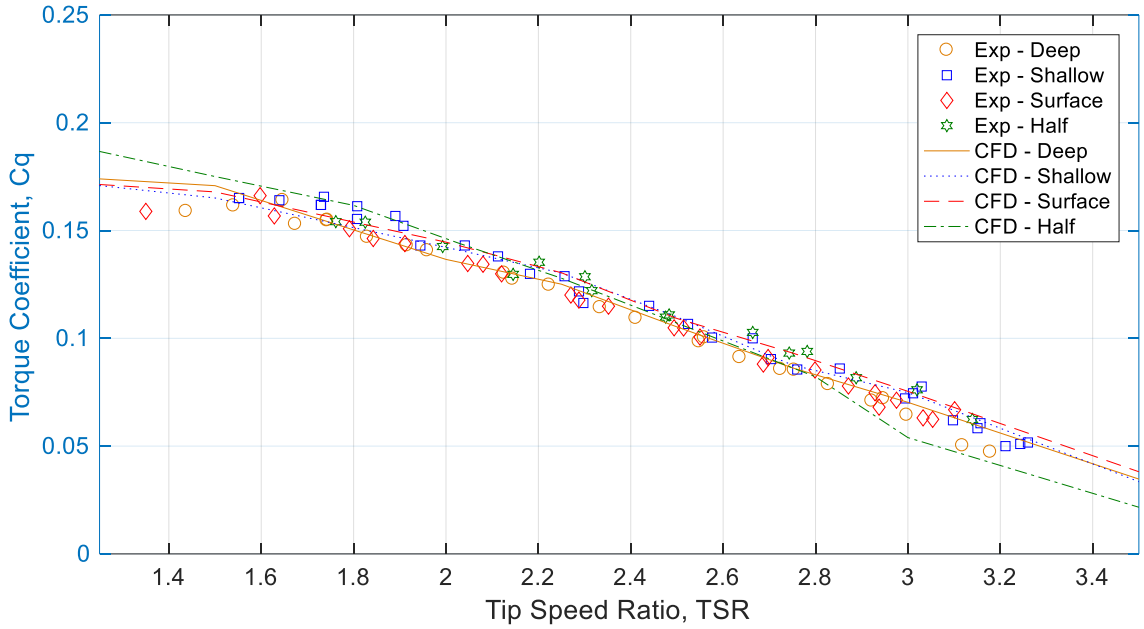

Figure 5.24 The torque coefficient at different immersion depth

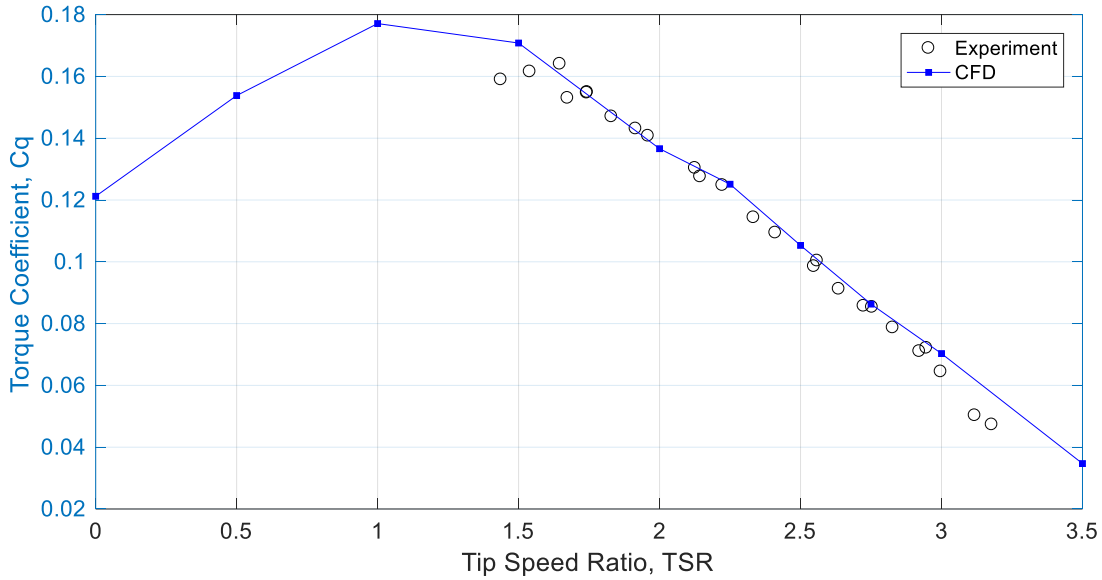

Figure 5.25 Torque coefficient at deep immersion condition

Figure 5.25 presents a closer look at the torque coefficient for the deep immersion condition from the experimental and numerical studies. From the numerical model, it was

determined that the torque coefficient reaches a maximum value of 0.177 at *TSR* of 1. At *TSR* of 0, the torque coefficient was found to be 0.12 and 0.125 at the optimal *TSR*.

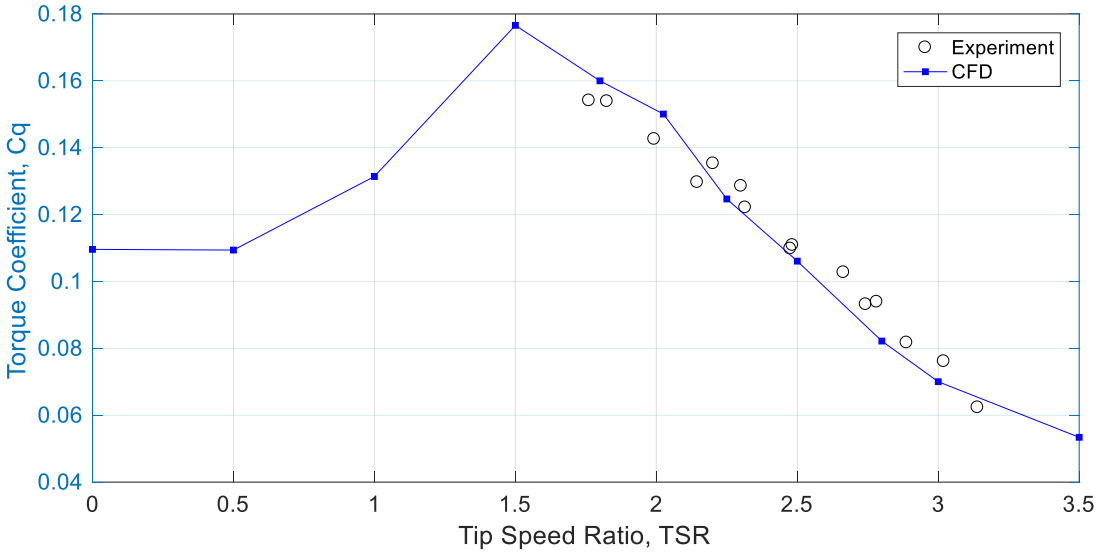

Figure 5.26 Torque coefficient at half submerged condition

Similarly, in the half submerged condition in Figure 5.26, the maximum torque coefficient was about 0.17 at *TSR* = 1.5 where at this speed, the thrust was also at its peak for the same condition, as shown previously in Figure 5.23. The torque coefficients associated with conventional HATT were much lower with an average value of about 0.075 at the optimal speed (Bahaj *et al.*, 2007b; Clarke *et al.*, 2007). This indicates that the Hydro-Spinna turbine operates at high torque and low speeds than conventional devices. At a relatively low rotational speed, the turbine generated higher torque which induced higher power than a conventional turbine at the same speed would generate.

5.7 Wake Interaction with Boundaries Proximities

Given the consistency of the trends between the experimental and numerical results, the numerical results were further analysed to investigate the flow behaviour around and downstream of the turbine. The wake behaviour downstream of the turbine and its interaction

with the boundary proximities of the free water surface and the bottom of the tank i.e. seabed was assessed. The distance of the seabed to the turbine was kept constant at a distance of 0.47 m which is almost one diameter of the turbine. With the knowledge that the Hydro-Spinna can be deployed in low velocities and shallow depth locations, the bottom distance was kept fixed and only the water level changed to represent the situation in practice. The wake characteristics of the turbine with the supporting structure are studied below.

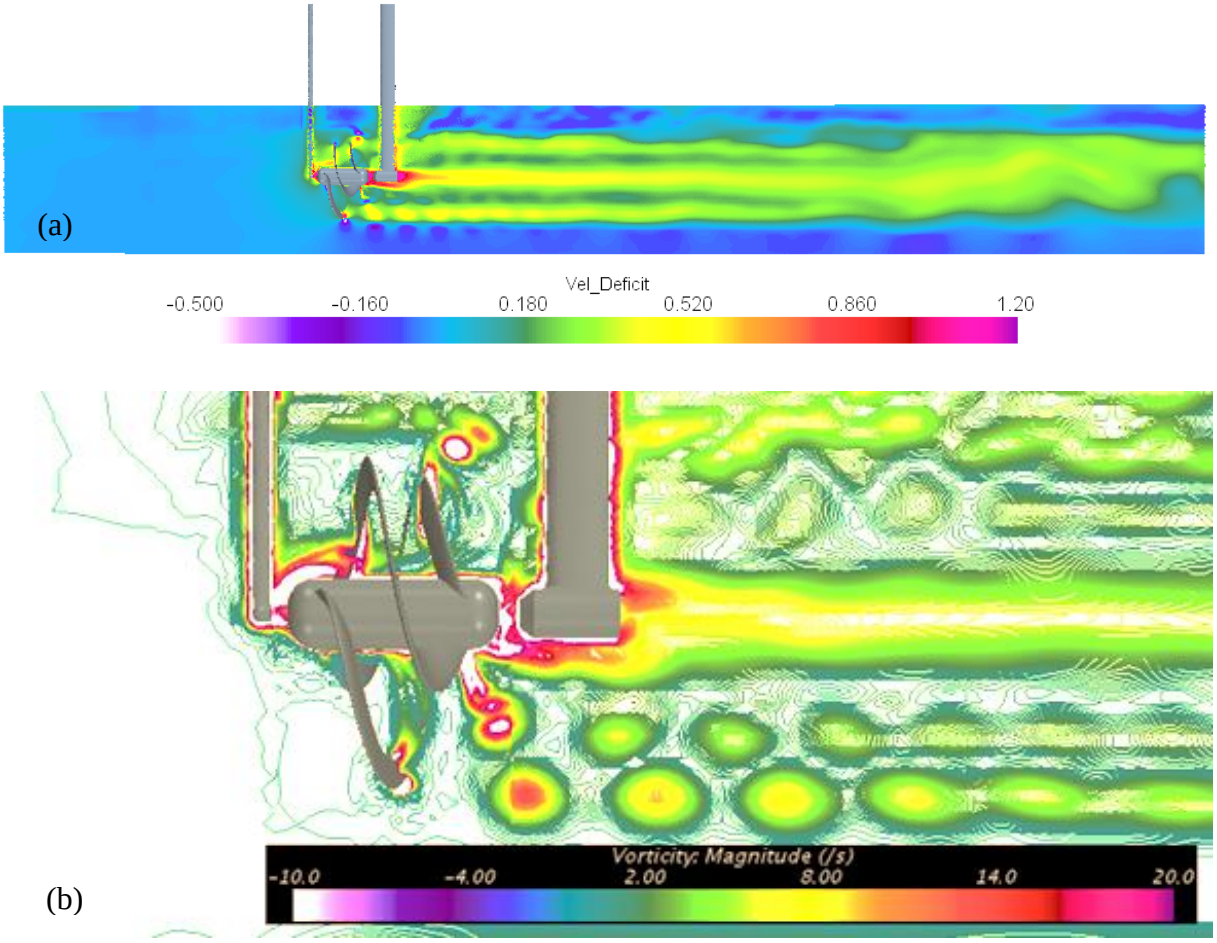

Figure 5.27 (a) The downstream wake characteristic at 0.36 D immersion depth (b) the vortices generated downstream of the turbine where similar vortices were also observed in the other immersion depth models.

It was observed that the front strut distorted the streamlined upstream flow seen by the turbine at all immersion depth conditions. Figure 5.27 shows low velocity regions as the flow passed the front support going on towards the top half of the turbine. The main support caused more disturbance to the flow slowing down the flow to as little as half of the upstream velocity.

The wake generated by the top half of the turbine was mixed with the wake generated by the supports. In comparison to the bottom half of the turbine where the upstream flow was undisturbed, the wake above was random and unstructured.

The wake of the bottom half of the turbine has the noticeable stream tube outline with defined reduction in flow velocity. Tip vortices were seen to be generated at the tip of the turbine blades and progressing along in the stream tube. Scattered high velocity regions were also observed near the top and bottom boundaries of the flow. The regions of high velocity flow were assumed to be caused by the freestream flow forcing through the limited channel of flow constrained by the free surface and seabed boundaries.

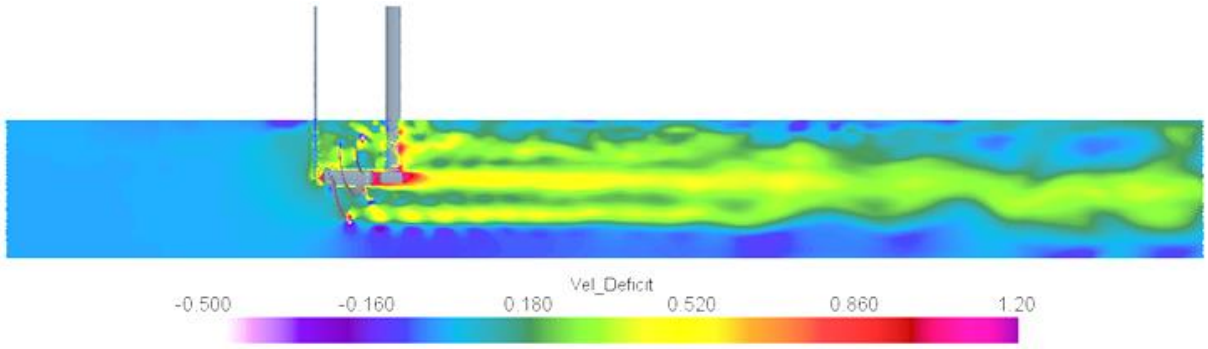

Figure 5.28 The downstream wake characteristic at 0.2 D immersion depth

At shallow immersion of 0.2 D, a similar wake characteristic was observed with bigger high velocity regions observed near the seabed, as shown in Figure 5.28. The combination of wakes generated by the turbine and the supports on the upper half of the turbine remained unstructured. At about a distance of 8 D, the wake downstream of the turbine was deflected downwards indicating the flow near the surface pushing the wake onwards towards the slower flow near the seabed. This behaviour was also observed in a study conducted by Bahaj *et al.* (2012) where the wake downstream of a HATT turbine was deflected downwards as the turbine was located closer to the seabed.

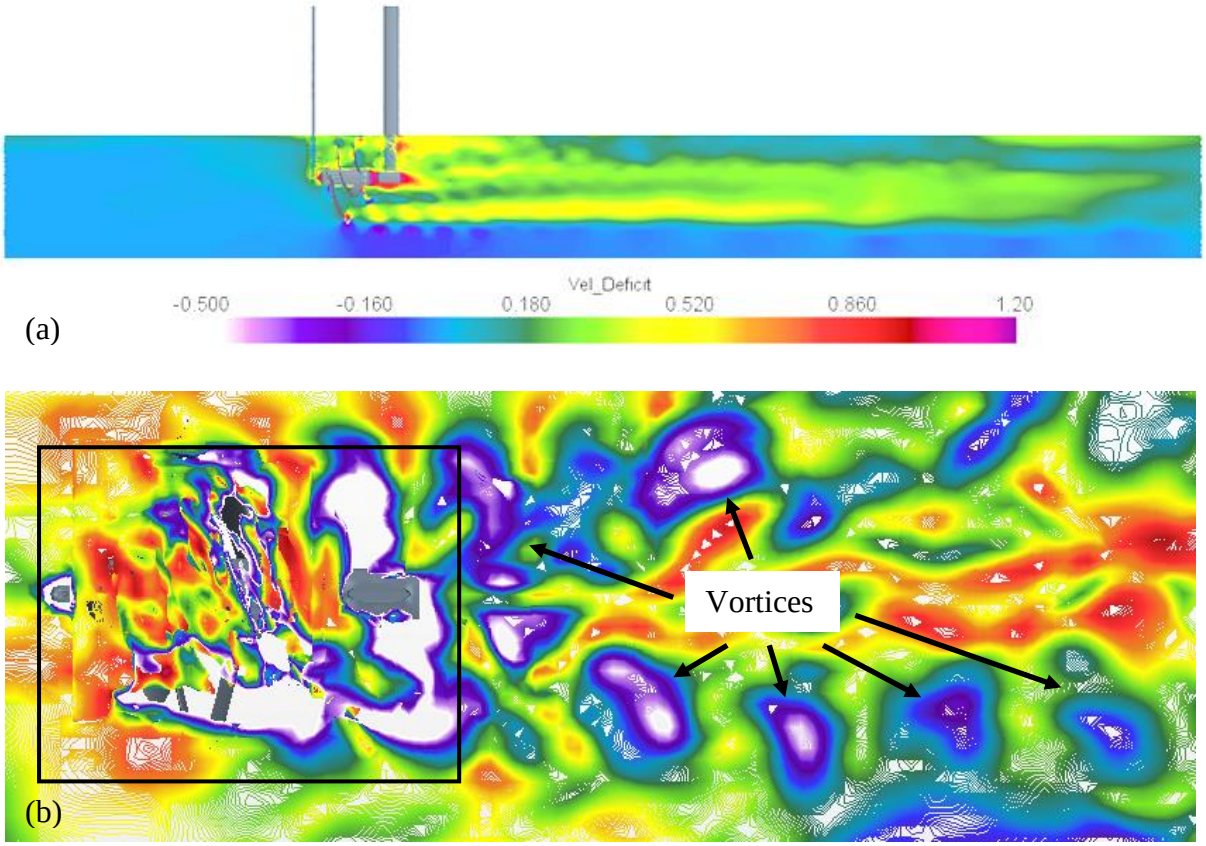

Figure 5.29 (a) The downstream wake characteristic at surface immersion (b) similar surface vortices initially observed in the experiment were also observed in the computational model (square box is where the turbine and supports are located)

At surface immersion, the wake expansion region on the top half of the turbine was not distinguished, as shown in Figure 5.29. The close proximity of the free surface not only limited the expansion of the wake but also eliminated the freestream flow around the wake for the top half of the turbine.

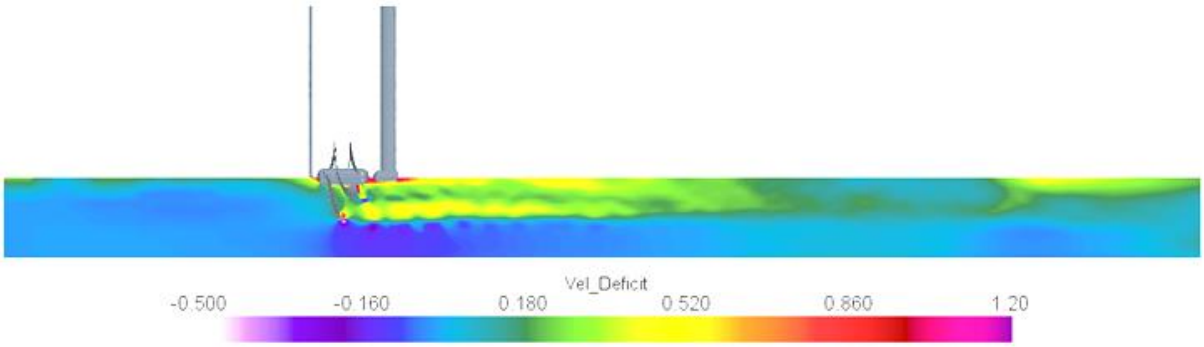

Figure 5.30 The downstream wake characteristic at half-submerged condition

For the half-submerged condition in Figure 5.30, the supporting structure did not cause major disturbance to the flow upstream of the turbine. A larger region of increased velocity was observed as the freestream flow was pushed through the confined channel between the turbine and the seabed. At 6 D downstream, there was a discontinuity in the wake as it mixed unevenly with the freestream velocities above and below.

5.8 Summary

Chapter 5 presented the performance of the Hydro-Spinna turbine, HS500, in the Towing Tank facility. The experiment was conducted at different shaft immersion depths to assess the power coefficient of the turbine with respect to the free surface proximity. Experimental results concluded that the free surface has an insignificant effect on the turbine performance. In fact, there was an increase of 5.5% in power coefficient as the immersion depth was reduced. Performance at surface immersion and half-submerged conditions also yielded power coefficients comparable to those obtained at the deep and shallow immersion conditions. Similar CFD investigations were conducted which yielded consistent results with the experimental data. The numerical model was also used to assess the wake characteristic of the Hydro-Spinna turbine system and its interaction with boundaries.

CHAPTER 6. PERFORMANCE OF THE HYDRO-SPINNA HS280 TURBINE

6.1 General Remarks

In the previous chapter, the operation of the HS500 Hydro-Spinna turbine was evaluated at different depths of immersion. The HS280 is the optimised turbine design that was evaluated by Wen (2011) using the Blade Element Momentum Theory (BEMT) method. This chapter presents an experimental investigation of the performance of the optimised turbine which was conducted in the Emerson Cavitation Tunnel. Its performance will be compared with the BEMT prediction of Wen (2011).

The optimisation study performed by Wen is summarised in Section 6.2 to provide the background information on the optimised design. Section 6.3 looks into the test facility and experimental set up and the results and analysis are covered in Section 6.4. Section 6.5 presents the performance analysis by numerical methods and the discussion in Section 6.6. Sectio 6.7 provides a summary of the investigations and results for this chapter

6.2 Optimisation of the HS280 Turbine

The study performed by Wen (2011) looked into the optimisation of the Hydro-Spinna blade based different pitch to diameter ratios (*P/D*). Three ratios were considered in the investigations for the 280 mm diameter turbine, namely *P/D* of 1, 0.75 and 0.5. Based on the BEMT calculations it was found that the turbine with the lowest *P/D* i.e. 0.5 produced the highest power coefficient. The results from the three turbines are presented in Table 6.1 for clarity.

Table 6.1 Summary of the *P/D* turbines performance

Turbine *P/D* Ratio	**Pitch, *P* (mm)**	**Power, C_P**	**Optimal *TSR***
1.0	280	0.232	1.3
0.75	210	0.338	1.8
0.5	140	0.529	2.4

There was an obvious trend of increasing power coefficient as the turbine *P/D* ratio decreased i.e. as the pitch of the turbine increased. This theory was supported through the investigation conducted by the present author using CFD methods with the HS500 turbine which was discussed in Chapter 4. The HS280 turbine was manufactured based on the numerical investigation above.

6.3 Experimental Facilities and Set Up

The HS280 performance test was conducted at two tunnel velocities of 2 and 3 m/s for the full range of operational *TSR* values at tunnel pressure of 850 mm Hg. For each test, the noise level produced by the turbine was acquired. Visual monitoring of cavitation was also carried out.

6.3.1 Test Facility

The radiated noise measurements and cavitation observations investigation of the 280 mm Hydro-Spinna turbine were conducted in the Emerson Cavitation Tunnel, Newcastle University. The cavitation tunnel has a test section as described in Table 6.2 and shown in Figure 6.1.

Table 6.2 Emerson Cavitation Tunnel specification

Test Section	**Dimension**
Dimension	3.1 m x 1.21 m x 0.8 m (L x B x H)
Area	1.008 m^2
Contraction Ratio	4.271
Maximum Velocity	8 m/s

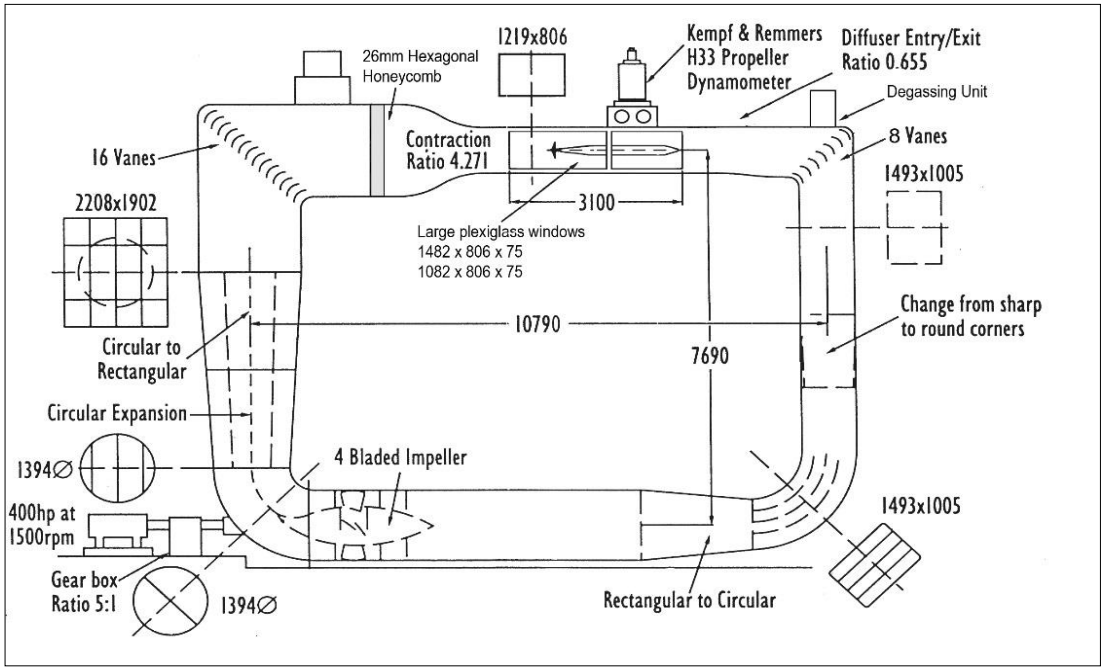

Figure 6.1 The structure of the Emerson Cavitation Tunnel

6.3.2 Test Equipment

The Hydro-Spinna turbine was driven by an H33 Kempf & Remmers dynamometer and secured in place with a boss cap. The dynamometer was used to control the rotational speed of the turbine as well as to measure the torque and the thrust of the turbine for efficiency evaluation. A Bruel and Kjaer Type 8103 miniature hydrophone and a Bruel and Kjaer Type 8105 spherical hydrophone were positioned inside the tunnel to measure the underwater noise levels. A dedicated data acquisition system, (B&K) PULSE Type 3023 system was used to process the noise results both in 1 Hz and 1/3 Octave Band. Visual cavitation observations of the turbine were recorded by two High-Speed Video (HSV) cameras triggered by the tunnel rpm counter, and synchronized with a continuous Plasma Lite 400 light to illuminate the tunnel during recording. Further specifications of the equipment used are presented in Table 6.3. An overview of the position of the turbine and hydrophone in the cavitation tunnel is given in Figure 6.2

Table 6.3 Specifications of the equipment used for the investigation

Measurement	**Equipment**	**Specifications**
Power / Thrust	H33 Kempf & Remmers dynamometer	Maximum Thrust: 2943 N Maximum Torque: 147 Nm Maximum Rotational Speed: 4000
Radiated Noise	Bruel and Kjaer type 8103 Miniature Hydrophone	
	Bruel and Kjaer type 8105 Miniature Hydrophone	
Graphic	Nano Sense MK II	10000 Hz 8Gb ram 512 x 512 Pixels 5000 pfs
	Nano Sense MK III	2000 Hz 8Gb ram 1024 x 1024 Pixels 1000 pfs

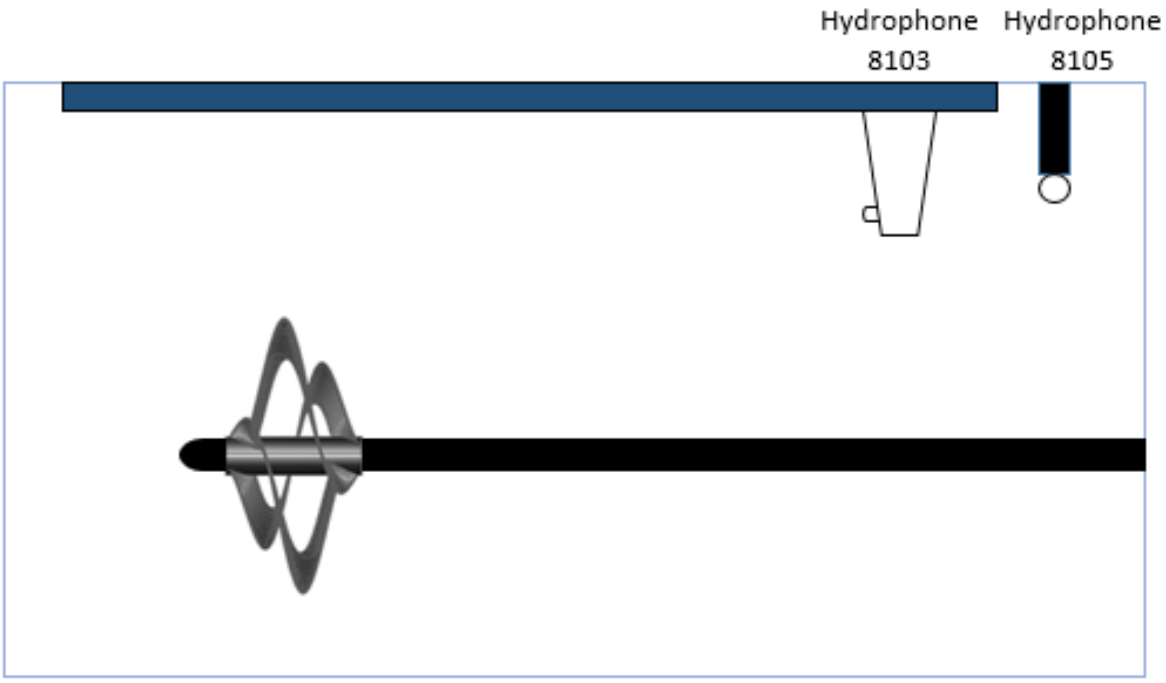

Figure 6.2 An overview of the turbine in the Emerson Cavitation Tunnel and the location of the miniature hydrophones

6.4 Results and Discussion

6.4.1 Power Performance

The power and thrust on the Hydro-Spinna turbine were assessed at two incoming velocities of 2 and 3 m/s. In both tests, the power coefficient peaked at optimal *TSR* = 3. However, at 2 m/s the power coefficient was 0.38, 3.9% higher than the coefficient recorded at 3 m/s which was 0.365, as shown in Figure 6.3 below. The blockage ratio for the cavitation tunnel test was at 6.4% hence it was assumed that it has no effect on the turbine performance.

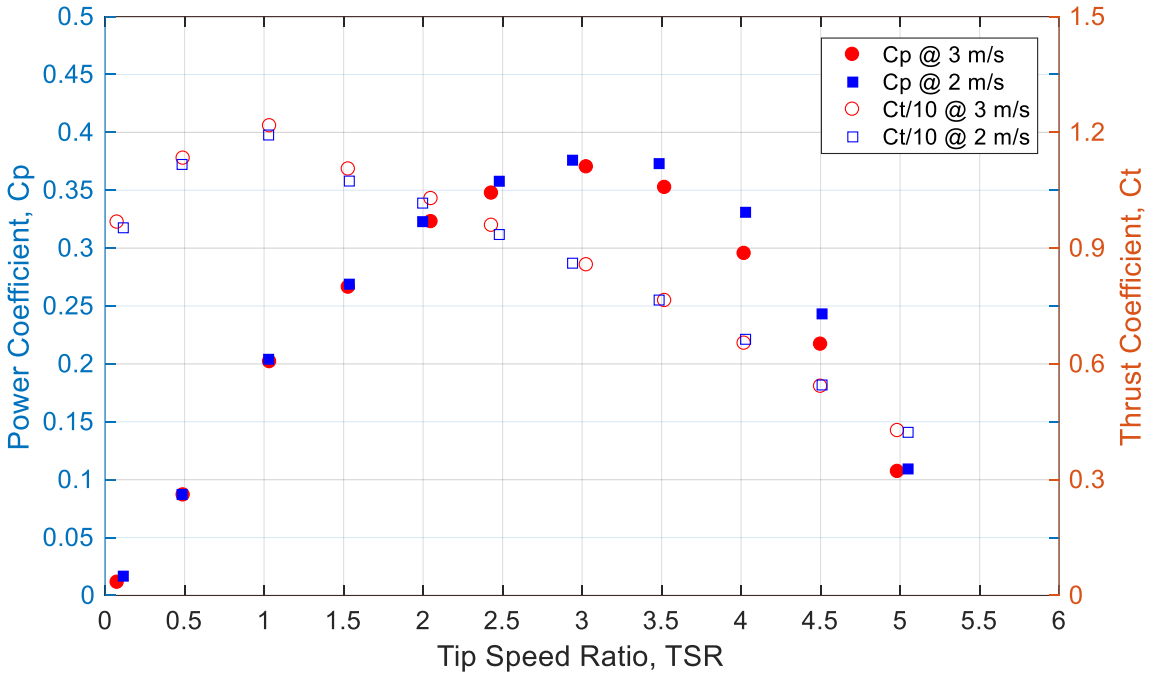

Figure 6.3 The power and thrust coefficients of the Hydro-Spinna, HS280

The performance of the HS280 in terms of power coefficient was higher than that of the HS500 and would be more competitive with other, more conventional, turbine designs. A comparison of the two Hydro-Spinna turbines' performances along with other turbine designs are listed in Table 6.4 to highlight the difference of their optimum operating conditions. Additionally, the contrast between the performance of the Hydro-Spinna and more conventional

turbines is emphasised in terms of the potential deployment in areas that would be considered unsuitable for the other designs, as discussed in the previous chapter.

Table 6.4 Comparison of the Hydro-Spinna performance against other turbines

Turbine	**Maximum Power Coefficient, C_P**	**Maximum Thrust Coefficient, C_t**	**Optimal *TSR***
HS500	0.28	0.90	$1.5 < TSR < 2.5$
HS280	0.37	1.20	$2.0 < TSR < 4.0$
Bahaj *et al.* (2007b)	0.46	0.93	$5.0 < TSR < 7.0$
Luznik *et al.* (2012)	0.43	1.05	$5.5 < TSR < 7.0$
Clarke *et al.* (2007)	0.43	0.80	$4.0 < TSR < 8.0$

The thrust coefficient of the HS280 peaked at *TSR* = 1 before dropping off with increasing *TSR* which was consistent with the previous findings for the HS500 turbine. There was no obvious difference in the thrust coefficient between the two flow velocities that could explain the slight decrease in the power coefficient as the velocity increased.

6.4.2 Noise Measurement Data

The results from the noise level data offered an explanation for the decrease in the turbine performance. Figure 6.4 shows the noise data level recorded by the two hydrophones at flow velocity of 2 m/s. The data values obtained at all *TSR*s were consistent with each other unlike the data obtained at flow velocity of 3 m/s, shown in Figure 6.5. There was a clear surge in noise produced at the starting condition and *TSR* of 1 at the flow velocity of 3 m/s. At these two conditions, the thrust coefficients of the turbine were the highest.

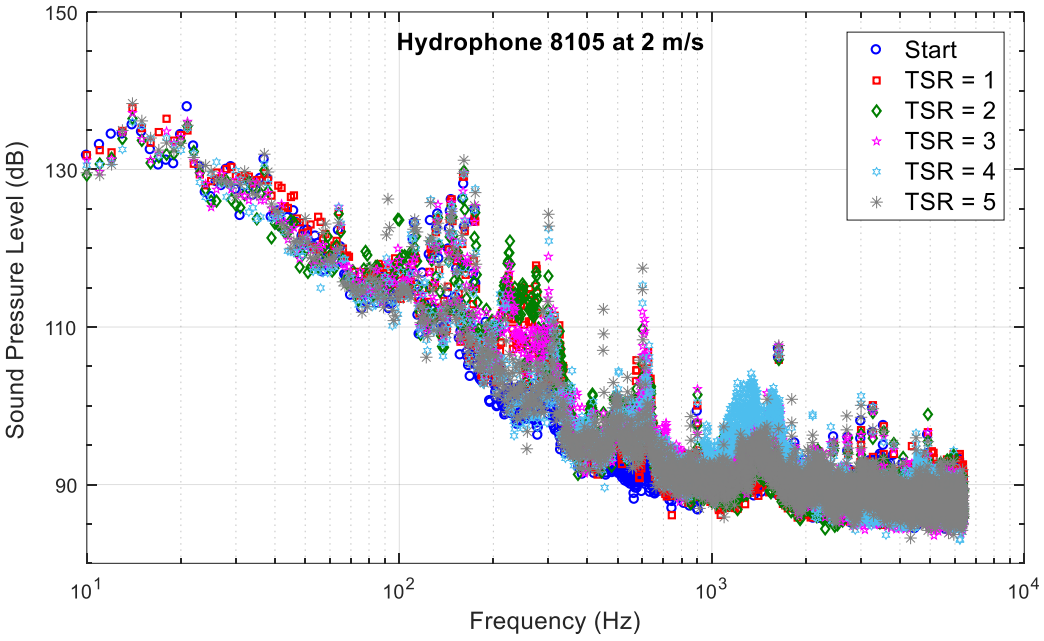

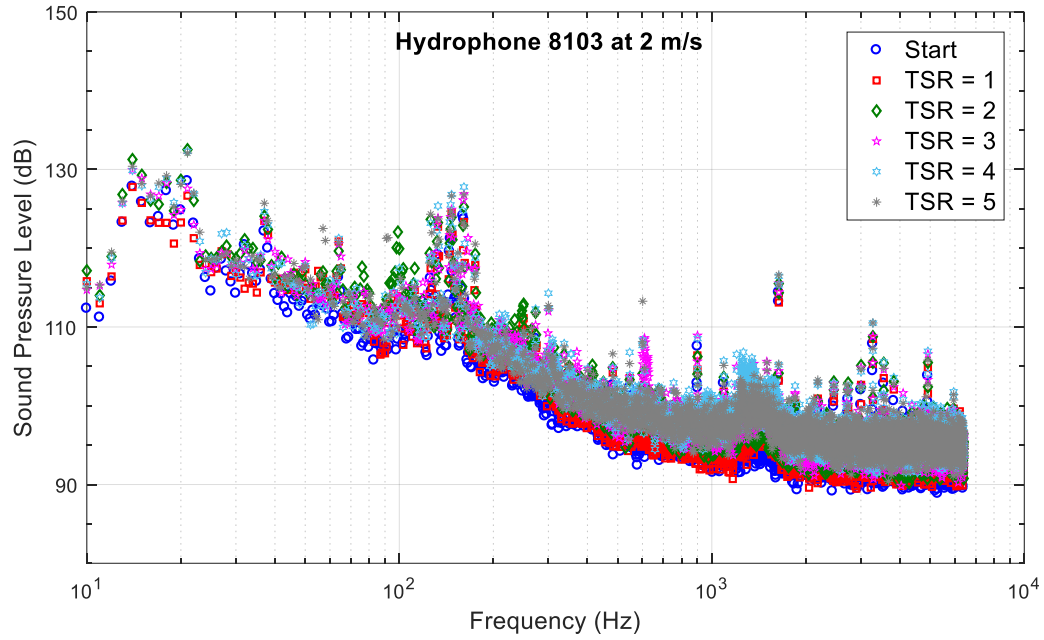

Figure 6.4 Noise level data from at flow velocity of 2 m/s

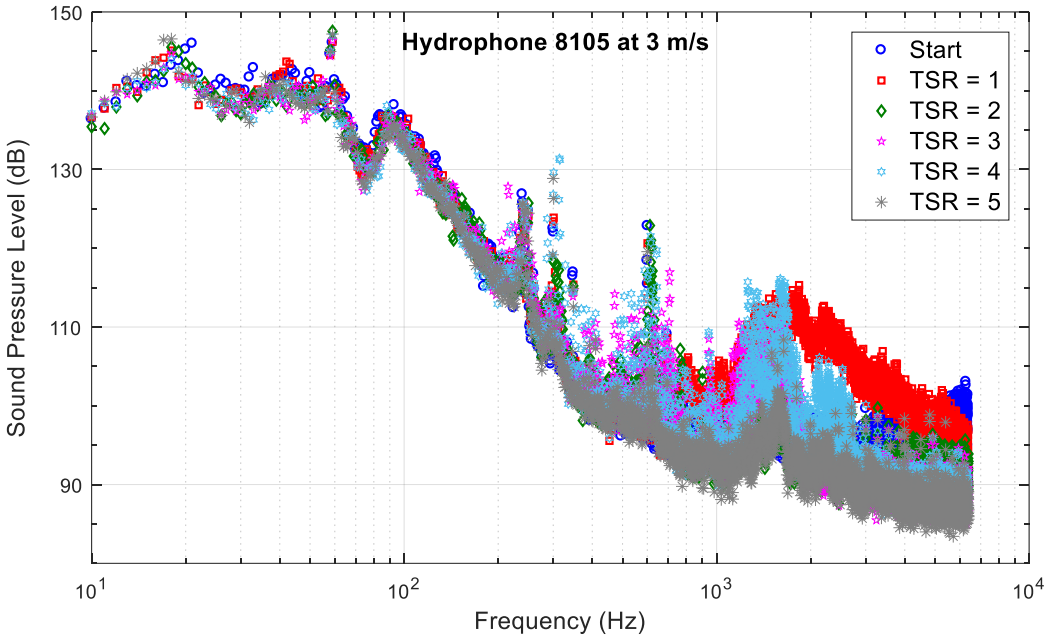

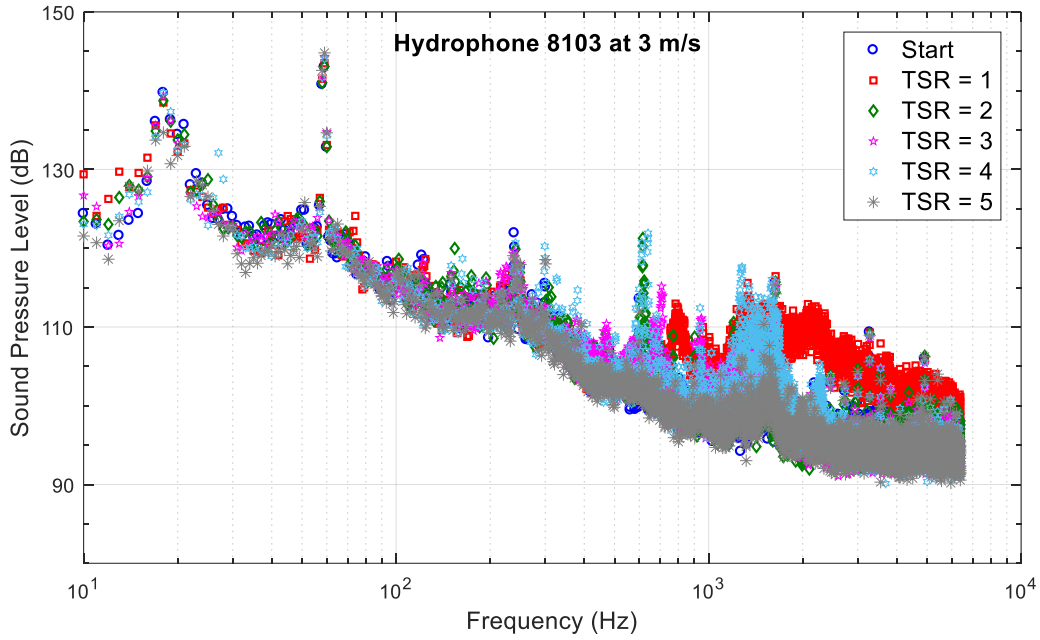

Figure 6.5 Noise level data from at flow velocity of 3 m/s

The surge in the noise data could indicate the inception of cavitation due to increased tip vortex activity although the inception may not be visible and hence cannot be recorded visually, as demonstrated by Figure 6.6. Regardless of this, the increase in noise levels at the

high frequency (broadband) ranges had to originate from a source and that can be attributed to the inception of cavitation even though it was not visually observed.

Based on the performance results of the two Hydro-Spinna turbines tested, it was established that the turbine operates at low rotational speed and *TSR* range. From the Cavitation Tunnel test, it was found that the Hydro-Spinna operates cavitation free at Atmospheric Condition.

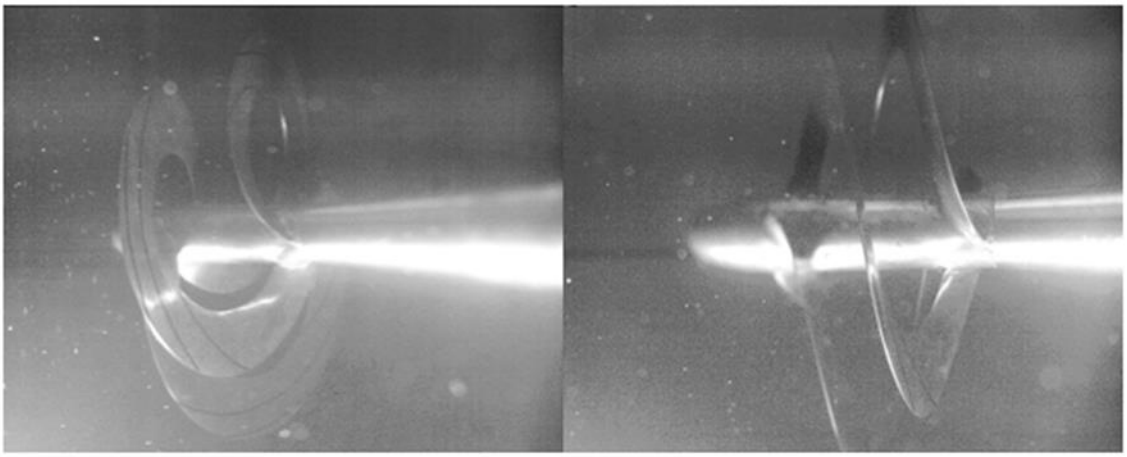

Figure 6.6 Images for the cavitation observation showing no cavitation at *TSR* = 1; U = 3 m/s

6.5 The HS280 Performance Analysis by Numerical Methods

With the availability of the experimental results obtained for the HS280 turbine from the ECT investigations, a numerical validation using the previous settings in Chapter 4 was produced. The numerical theory and the mesh settings were exactly the same as in the previous model however, the domain size in this model was set to the dimensions of the ECT. The rotating domain had three times the radius of the turbine, with the upstream and downstream boundaries set at 2D distance, similar to the previous investigation in Chapter 4. Figure 6.7 illustrates the numerical domain with the cavitation tunnel dimension for the HS280 investigation.

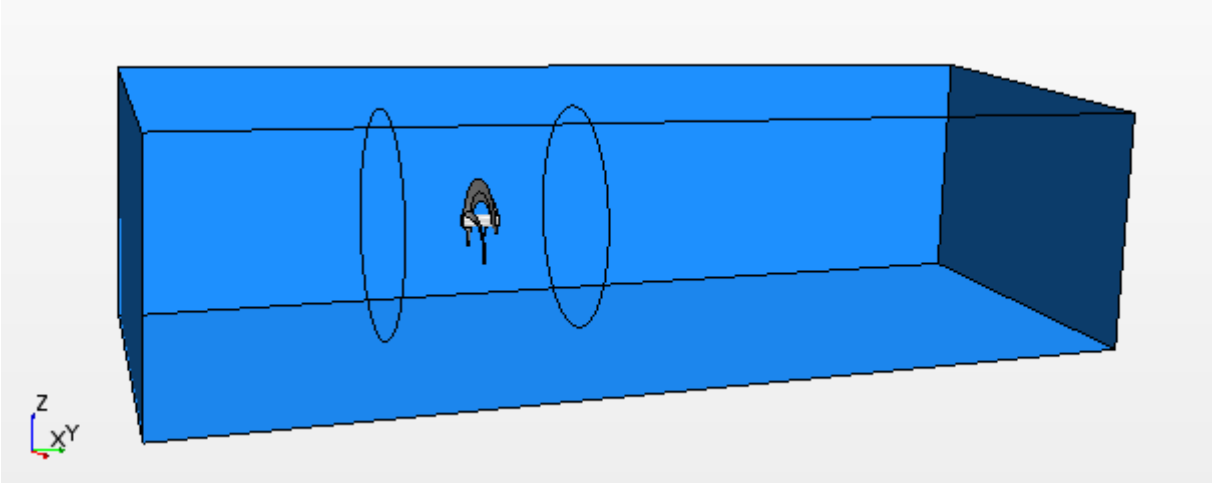

Figure 6.7 The numerical domain for the HS 280 with the cavitation tunnel dimensions

6.5.1 Blade Profile of the Hydro-Spinna

As the numerical model for the HS280 performance had been validated against the experimental results, the numerical model was further used to assess the performance of the optimized Hydro-Spinna turbine with different blade profiles. The existing turbine has a blade profile of the NACA 0006, and two other profiles were considered in the study which are NACA 0015 and a bidirectional BDA 65-21 profile. The NACA 0015 was selected as the HS500 has the same blade profile. It is also thicker and has a wider range of operational angle of attack before stall and higher lift to drag coefficient compared to the NACA 0006. The BDA65-21 is a bidirectional aerofoil profile modified from NACA 65-021 profile developed by researchers at the Harbin Institute of Technology (Shi *et al.*, 2013; Guo *et al.*, 2015a). The lift to drag ratio of the blade profiles are presented in Figure 6.8. The NACA profiles values were obtained from XFoil and the BDA65-21 values were reproduced from (Guo *et al.*, 2015b). The three blade profiles are presented in Figure 6.9 where the BDA65-21 has the thickest profile.

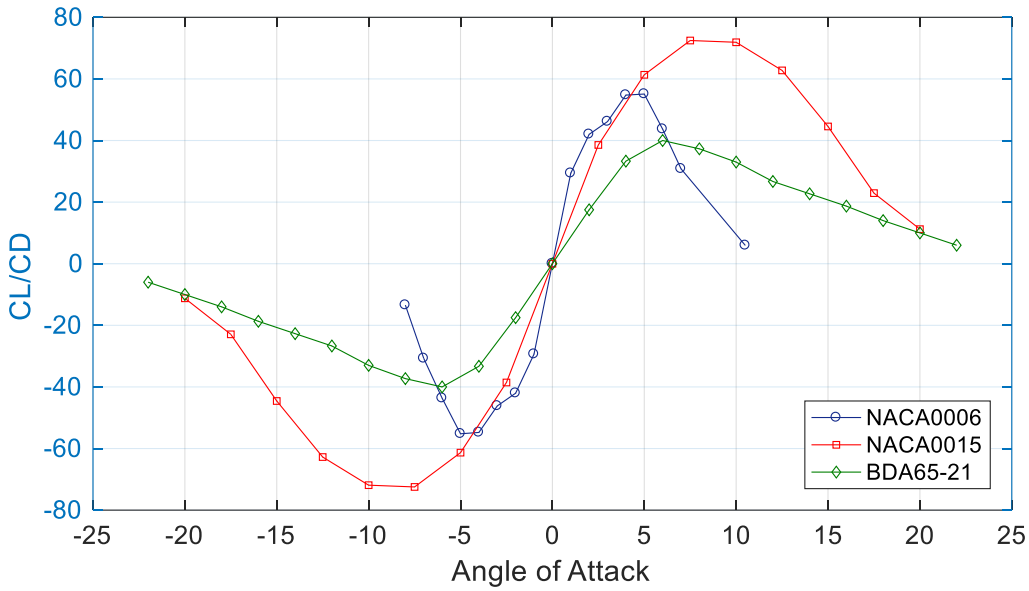

Figure 6.8 Lift to drag ratio of the blades profile investigated

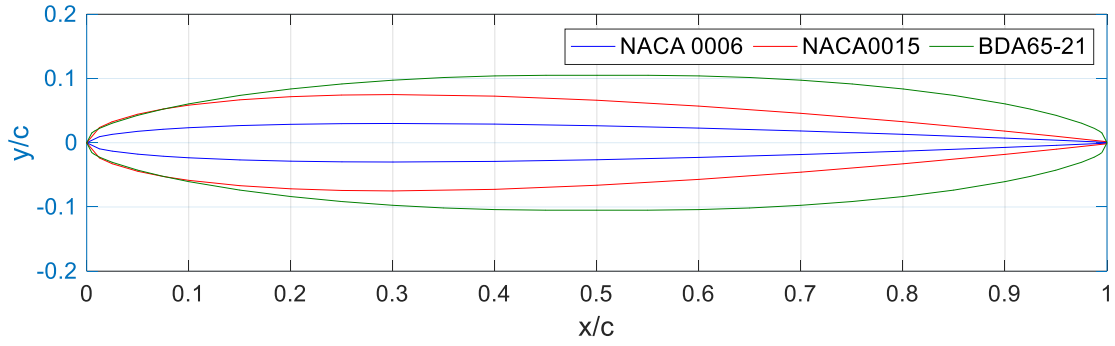

Figure 6.9 The profiles of the cross section of the blade in this investigation

6.6 Results and Discussion

6.6.1 HS280 Numerical Model

The numerical model was first validated against the experimental data obtained earlier, where the both power coefficient results were analogous to each other, as shown in Figure 6.10. The numerical model however under predicted the thrust coefficient by 8% at the peak value. The result has shown the reliability of the numerical model to predict the power performance

of the Hydro-Spinna turbine. Therefore, there are assurances in the numerical model to be further adapted to predict the variation of the performance with different turbine profiles.

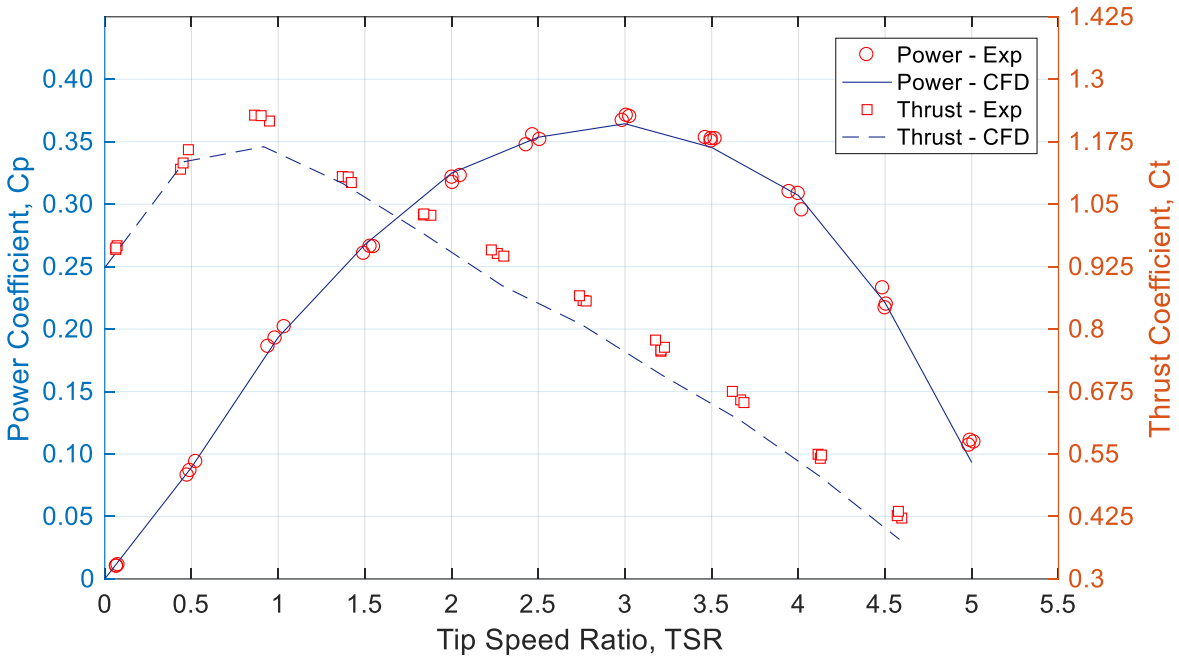

Figure 6.10 Performance from numerical model against the experimental results for the HS280 turbine with the NACA 0006 profile

The velocity deficit flow profile of the HS280 model is shown in Figure 6.11 where a velocity deficit of 0.5 was observed in the downstream wake indicating at least half of the kinetic energy was extracted and lost. Regions of vorticity were also observed downstream of the turbine originating from the tip of the blade. Downstream of the turbine, the wake mixed with the free velocity flow at about 1.25R distance from the centre of the turbine as shown in Figure 6.12 below.

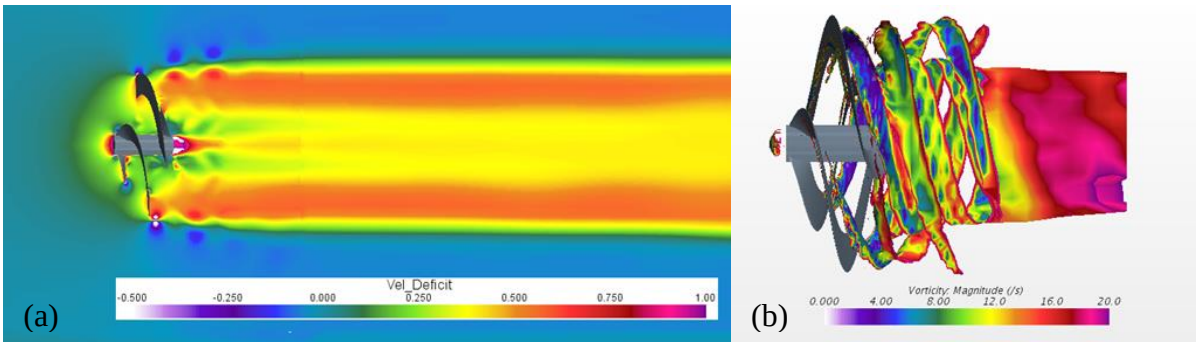

Figure 6.11 (a) The wake structure around the HS280 turbine and downstream of the turbine, (b) Velocity extracted ISO-surface variation of the vorticity around the turbine

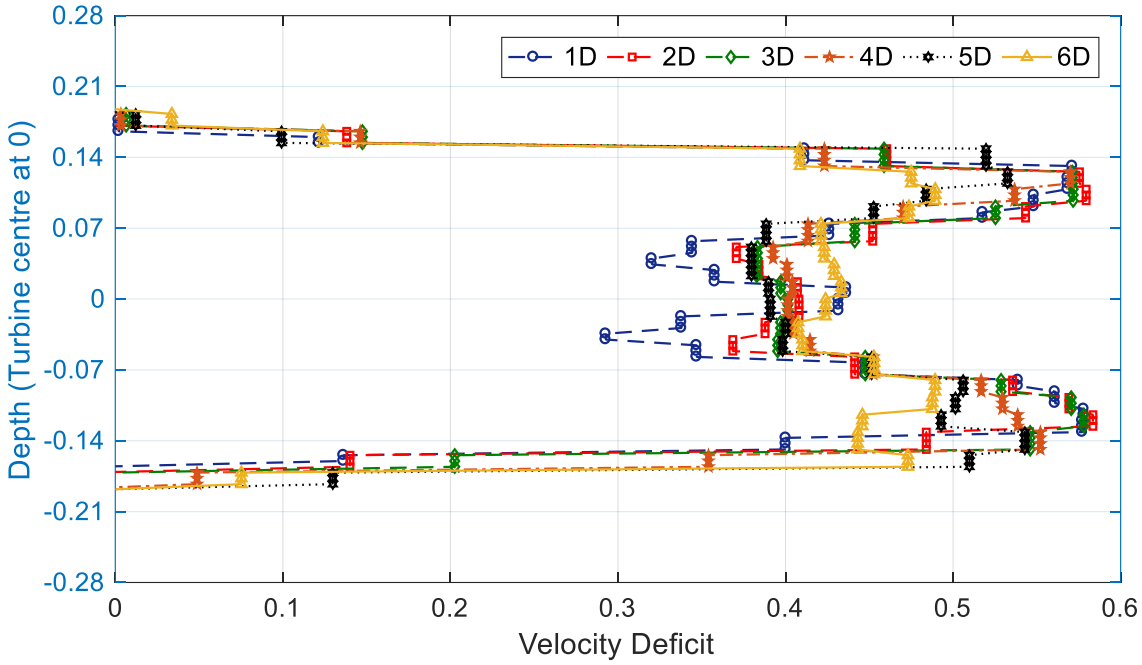

Figure 6.12 The wake velocity deficit characteristic of the HS280 turbine

6.6.2 Performance Characteristic with Turbine Blade Profile

Three different blade profiles were investigated namely the NACA 0006 which is the blade profile of the existing HS280 model, the NACA 0015 and a bi directional profile BDA65-21. It was evaluated from the numerical investigation that performance of the turbine relied on the blade profile as observed in Figure 6.13 although the difference might seem insignificant.

Importantly, the three profiles exhibited similar performance characteristics with the power peaking at an optimal *TSR* of 3.

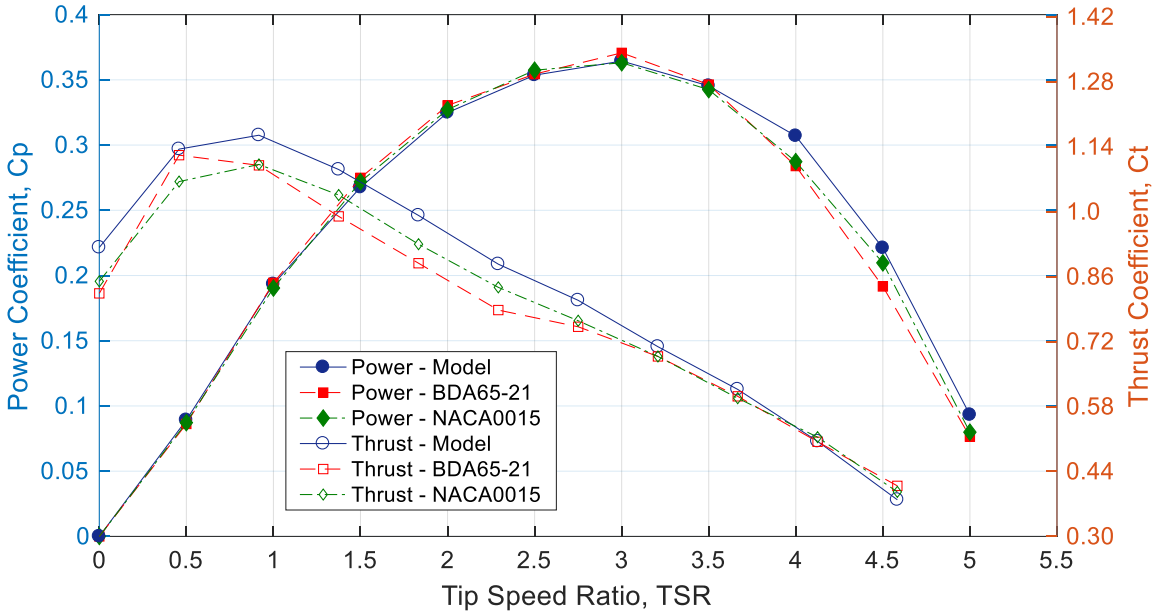

Figure 6.13 Performance variation with different turbine blade profiles

Figure 6.14 shows the percentage difference in the performance coefficient between the NACA 0006 and NACA 0015 profiles with respect to the former profile. It was determined that at optimal *TSR*, the NACA 0006 profile exhibited a slightly lower power performance with a decrease of 0.36%. The value was insignificant in comparison to the thrust difference where the NACA 0006 profile exhibited a thrust 5.4% higher than the NACA 0015 profile. At the *TSR* region between $1 < TSR < 2.5$, the NACA 0006 revealed a higher thrust coefficient with a maximum difference of 7.8% at the starting condition. For a 10 m Hydro-Spinna at flow velocity of 2 m/s the difference in thrust could be up to 13 kN which is a significant amount of force on the turbine.

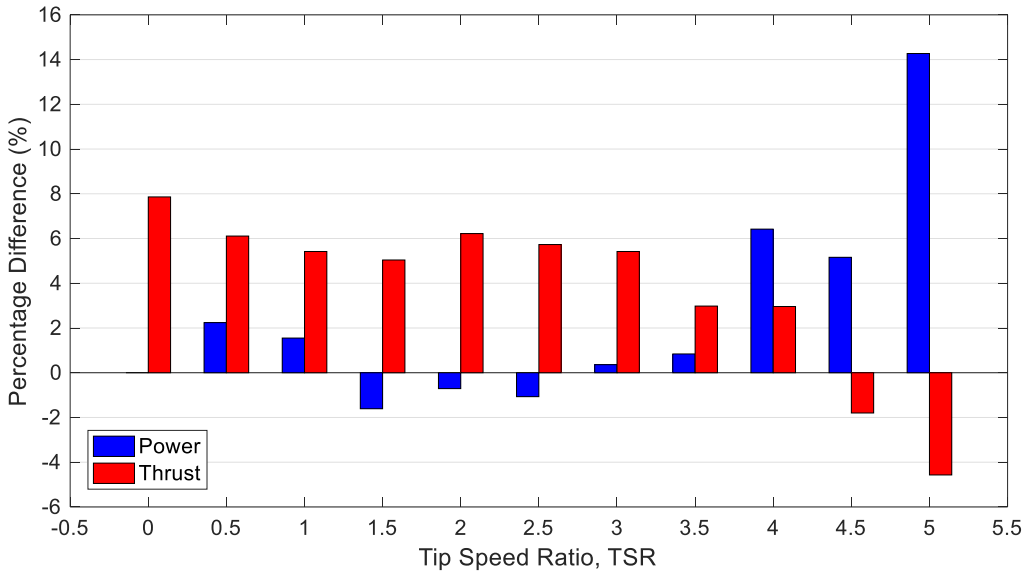

Figure 6.14 Performance difference between the NACA 0006 and NACA 0015 profiles where the difference is calculated by using Equation 6.1.

$$\text{Percentage difference}(\%) = \frac{C_{P(NACA0006)} - C_{P(BLADE)}}{C_{P(NACA0006)}} \times 100$$

Equation 6.1

where $C_{P(BLADE)}$ is the power coefficient of the blade profile investigated.

Similarly, the performance results from the NACA 0006 and the bidirectional BDA65-21 profile were also analysed in Figure 6.15. When the bidirectional profile was adopted in a conventional HATT model of 0.3 m diameter, it generated a power coefficient of 0.405 (Guo *et al.*, 2015a). The BDA65-21 profile was determined to generate a higher power coefficient by 1.73% at the optimal speed. Additionally, the difference in thrust coefficient was larger, where the bidirectional profile experienced lower thrust by up to 11.3% and 7% at *TSR* = 2.5 and 3 respectively, about 19 kN and 11 kN, in the previous full-scale estimation. Considering the small difference in power generation but the greater difference in thrust coefficient, the bidirectional profile may be a more appealing option than the NACA profiles. The bidirectional

profile turbine would be subjected to lower thrust which could prove a crucial factor when considering the turbine for full-scale deployment.

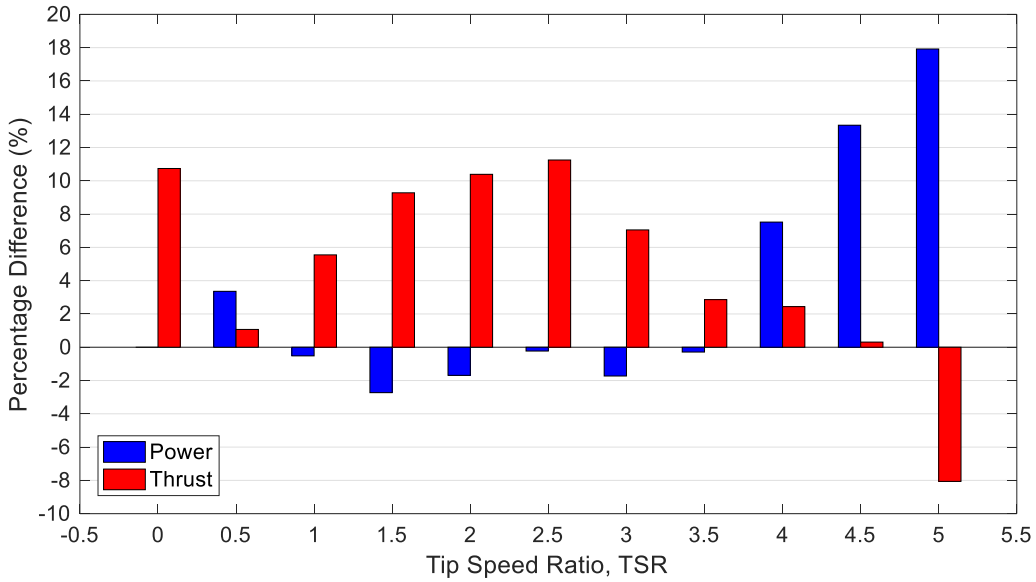

Figure 6.15 Performance difference between the NACA 0006 and BDA65-21 profiles where the difference is calculated by using Equation 6.1.

6.7 Summary

The performance of the Hydro-Spinna turbine, HS280, was presented demonstrating that it has a power coefficient that could be competitive with other turbine designs. The performance was found to drop at higher velocity conditions which was attributed to the inception of cavitation. Although there was no cavitation observed during the tests, the noise level data recorded indicated the inception of cavitation. There was an increase in noise level in the high frequency region that supported the theory of the manifestation of cavitation at higher velocities. This chapter also acts an introduction to the noise level measurement and cavitation performance investigation which will be explored further in the next chapter.

In the second part of this chapter, the experimental data was used to validate the numerical model which showed close agreement between the model tests and CFD results. The numerical model was further used to predict the performance with different blade profiles. The outcomes had showed that although the NACA 0006 profile generated the lowest power at the optimal *TSR*, the difference was minute. In addition, the thrust experienced by the turbine was

higher, up to 11.3% higher compared to the other two profiles where the bidirectional blade profile may be a more appealing choice instead.

CHAPTER 7. CAVITATION AND RADIATED NOISE LEVEL OF HYRO-SPINNA TURBINE

7.1 General Remarks

Full-scale operation of marine turbines disturbs the acoustic level of the marine environment and interferes with the acoustic-dependent communication of marine life. This chapter looks into the measurement of the URN from the model of the Hydro-Spinna turbine during the Emerson Cavitation Tunnel tests. The measured noise level, commonly known as Sound Pressure Level (SPL), obtained from the investigation was corrected to 1 Hz band level and 1 m source level, a common procedure with propeller noise measurements that is recommended by the appropriate technical committees of the International Towing Tank Conference (ITTC). The cavitation and noise investigation was conducted systematically at different tunnel pressures starting from 850 mm Hg and down to a vacuum pressure of 250 mm Hg, for the full range of operational *TSR*.

Section 7.2 briefly looks into the test facility and test procedure while Section 7.3 describes the analysis of the noise data obtained using the ITTC recommended noise format. Section 7.4 presents the cavitation observed during the investigation and the full-scale cavitation number analysis. The noise band level results are discussed in Section 7.5 together with the full-scale URN prediction. The findings of this chapter are summarised in Section 7.6.

7.2 Experimental Facilities and Set Up

The facilities and set up in this investigation were the same as those in the previous chapter. The position of the visual capture for cavitation observation was altered in this investigation to ensure that a larger section of the turbine and downstream flow were included.

7.2.1 Test Procedure and Conditions

The investigations were conducted for 7 different tunnel pressures ranging from 850 mm Hg to a vacuum pressure of 250 mm Hg to be able to observe potential cavitation. Initial investigations suggested that the Hydro-Spinna appeared to be operating cavitation-free. The

pressure in the tunnel was reduced to vacuum pressures to induce cavitation in order to understand the nature of the Hydro-Spinna operation at extreme conditions. For each pressure, the noise data was recorded for a full range of *TSR*. A total of 42 tests were conducted with the matrix for the investigation described in Table 7.1.

Table 7.1 Test matrix for the noise and cavitation investigation

Test	**Pressure (mm Hg)**	**Tunnel Velocity (m/s)**	***TSR* Range**
1	850	3	0
2	750		1
3	650		2
4	550		3
5	450		4
6	350		5
7	250		

7.3 Presentation of Noise Data

7.3.1 Correction of Noise Data

The noise data was processed using the PULSE lab-shop of Bruel and Kjear noise and vibration data acquisition system of ECT using Constant Percentage Bandwidth (CPB) and Fast Fourier Transform (FFT) analysers. Two types of noise level output were processed by the dedicated software which were in 1/3 Octave band levels for 20 Hz to 20 kHz and 1 Hz band levels at a reference pressure of 1 µPa. For both measurements, data was acquired for an average duration of 50 seconds. The raw noise output from the operations was measured with the hydrophone 0.38 m away from the turbine. As is common practice with propeller noise data, and recommended by the ITTC (1987), the Sound Pressure Level (SPL) in each 1/3 Octave band was corrected to an equivalent 1 Hz bandwidth and standard distance of measurements of 1 m, as given in Equation 7.1 and Equation 7.2 respectively.

$$SPL_1 = SPL_M - 10\log\Delta f$$

Equation 7.1

$$SPL = SPL_1 + 20log(r)$$

Equation 7.2

where *SPL* is the Sound Pressure Level in 1 Hz band in dB relative to 1 µPa at 1m, *r* is the distance of the location of the hydrophone from the turbine centreline, SPL_1 is the Sound Pressure Level in 1 Hz band in dB relative to 1 µPa. SPL_M is the Sound Pressure Level in 1/3 Octave band in dB relative to 1 µPa, and Δf is the frequency bandwidth for the 1/3 Octave band for each centre frequency.

The background noise in the test environment was also measured and processed accordingly and it was then eliminated from the total *SPL* measured to give a nett *SPL* value as described in Equation 7.3, taking into consideration the expected uncertainty of measurements of 3dB and less (Bertschneider *et al.*, 2012).

$$SPL_N = 10log\left[10^{(SPL_T/10)} - 10^{(SPL_B/10)}\right]$$

Equation 7.3

where SPL_N is the nett Sound Pressure Level, SPL_T is the total Sound Pressure Level and SPL_B is the background noise Sound Pressure Level.

7.3.2 Analysis of Full-Scale URN Level Prediction

Various methods for full-scale noise predictions are available whether by means of numerical analysis or by extrapolation methods from model scale data (Lloyd *et al.*, 2013; Yamada *et al.*, 2015; Aktas *et al.*, 2016b). Moreover, different noise prediction analysis can be conducted depending on the origin of the noise. Other studies looked into different numerical

prediction formulations from cavitating propellers URN using various models such as propeller flow panel method, tip vortex noise model and sheet cavitation noise model (Lafeber *et al.*, 2015). Firenze and Valdenazzi (2015) developed URN prediction method that considered the tonal pressure fluctuations which was calculated based on the noise sources corresponding to the hull pressures and broadband noise which was contributed from two cavitation sources i.e. tip vortex and sheet cavitation. The numerical method used was concluded to be able to predict the important aspect of the propeller hydrodynamic and acoustic behaviour. However, there were still limitations on the model that was attributed to the potential flow model. In non-cavitating conditions, various numerical methods can also be employed to predict noise levels in propellers. Noise levels can be predicted by using the time dependent pressure data obtained from flow field analysis using the potential based panel method in acoustic formulations such as the Ffowcs William Hawkings equation (Seol *et al.*, 2002; Seol *et al.*, 2004; Seol *et al.*, 2005; Seol *et al.*, 2012).

There are various scaling methods that can be used to predict full-scale noise level from model measurements which are mainly used in the propellers industry (Bark, 1985; Leggat and Sponagle, 1985).Similarly, full-scale noise prediction can also be evaluated using the ITTC recommended scaling laws for propellers noise (ITTC, 1987) that have been applied in propellers and also turbine noise prediction (Atlar *et al.*, 2001; Wang *et al.*, 2004; Wang *et al.*, 2007; Aktas *et al.*, 2016b). The ITTC scaling laws were applied in this study, mainly because the model noise measurement and full-scale prediction studies were conducted in the same facility employed in the verification of this law.

Propeller full-scale noise prediction from cavitation tunnel model measurements has been validated against full-scale measurement in studies such as those conducted by Aktas *et al.* (2016b) with the Emerson Cavitation tunnel where the predictions underestimated the noise level for non-cavitating propellers. For the cavitating case, the model also underestimated the noise level at the high frequency level. This was attributed to the various noise emitting mechanisms and cavitation dynamics created by the tip vortex cavitation. Perhaps, these influence could have been reduced or eliminated if the cavitation number and Reynolds number were included in their full-scale extrapolation. On the contrary, Tani *et al.* (2017) also conducted a full-scale noise prediction investigation based on model data obtained from another cavitation tunnel facility. One of the issues raised was that full-scale prediction normally overestimates the full-scale noise level due to the model measurement being carried out in a

controlled and confined environment. The acoustic profile of facilities such as that of a cavitation tunnel was found to differ from the actual environment due to issues such as motor noise and proximity of the tunnel boundary (ITTC, 1987).

Two ITTC recommended scaling laws were utilised in the full-scale noise prediction. Equation 7.4 presents the extrapolation of SPL level from model scale to full-scale taking into consideration the turbine's diameter and the operating point at which the noise level was measured in terms of the rotational speed, as well as the cavitation numbers to take into account the operational difference between the model and full scale condition. The density of the fluid in which the turbines operate was also considered and finally the reference distance at which the noise level was measured which was set at a standard of 1 m for both conditions. The model to full-scale noise level extrapolation also includes a frequency shift to account for the difference in operating conditions in terms of the rotational speed and cavitation number, as described in Equation 7.5

$$\Delta L_{(F)} = 20 \log \left[\left(\frac{D_F}{D_M} \right)^z \left(\frac{r_M}{r_F} \right)^x \left(\frac{\sigma_F}{\sigma_M} \right)^{y/2} \left(\frac{n_F D_F}{n_M D_M} \right)^y \left(\frac{\rho_F}{\rho_M} \right)^{y/2} \right] dB$$

Equation 7.4

$$\frac{f_F}{f_M} = \frac{n_F}{n_M} \left(\sqrt{\frac{\sigma_F}{\sigma_M}} \right)$$

Equation 7.5

where subscripts *F* and *M* refer to full-scale and model scale respectively, *D* is the turbine diameter, *r* is the reference distance at which the noise level is measured or predicted which was 1 *m* in both cases, σ is the cavitation number, *n* is the turbine rotational speed and ρ is the density of water which is 1002 kg/m^3 for the model test and the standard sea water value of 1025.9 kg/m^3 for the full-scale turbine, while $x = 1$, $y = 2$ and $z = 1$.

In order to relate the model size noise measurements to the full-scale for practical purposes, three different sizes of full-scale turbine with the following design conditions were considered.

Turbine Diameter	5 *m*, 10 *m*, 15 *m*
Immersion depth (surface to shaft)	1 x Turbine Diameter
Tidal Stream Velocity	2 *m/s*

As with model testing, there is a discrepancy in Reynolds number between the model and full scale conditions. Therefore, in order to reduce the scale effect, the Reynolds number in the model test was set as high as possible. It was understood that the Reynolds Number scale effect can be considered negligible if the value is above 10^6 (Wang *et al.*, 2007). In this test, taking into consideration the blockage effect and other limitation, the Reynolds number was set about 0.1-0.5 x 10^5.

The predictions of the Hydro-Spinna full-scale URN levels were intended to offer an indication of the turbine operation under real conditions. As the URN generated from the operation of the turbine, either in designed or extreme conditions, disturbs the ambient marine acoustic level in the local environment, the analysed full-scale URN levels can be represented in comparison with a reference noise threshold level established by the International Council for the Exploration of the Sea (ICES). This threshold level was originally developed to restrict the URN generated by vessels involved in fisheries research. However, in recent years, it has been used for a representative reference for other URN investigations. The ICES threshold levels are defined by Equation 7.6 (Bertschneider *et al.*, 2012):

$$SL = 135 - 1.66 \log_{10}\left({f_{\text{Hz}}}/{1\ \text{Hz}}\right)$$

for 1 Hz $\leq f \leq$ 1 kHz, and

$$SL = 130 - 22\log_{10}\left({f_{\mathrm{kHz}}}/{1\ \mathrm{Hz}}\right)$$

for 1 kHz ≤ f ≤ 100 kHz

Equation 7.6

where SL is the underwater noise source level given in dB re: 1 µPa/Hz at 1 m.

7.4 Cavitation Observations and Discussion

As stated earlier, the images presented in Chapter 6 did not reveal any visually observable cavitation during the tests at a flow velocity of 3 m/s while the detected increase in *SPL* suggested for an inception of tip vortex cavitation. In order to prove this inception and further development of cavitation, while the static pressure level of the tunnel systematically reduced, the image and video capture areas were repositioned and an additional camera was used to include the flow downstream of the turbine. Figure 7.1 shows the camera set-up to observe any cavitation. A complete set of the cavitation observation images at all *TSR* are available in Appendix E.

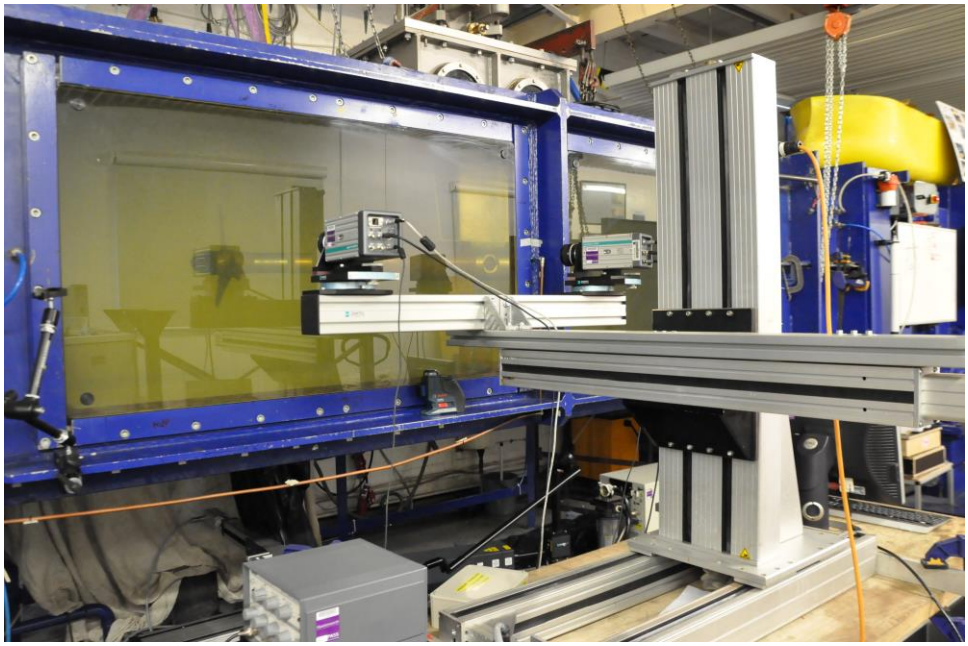

Figure 7.1 High speed cameras set-up for cavitation observation

Under the above set up and at the target areas specified one could record the inception for the tip vortex cavitation and with the systematic reduction of the tunnel pressure the developed vortex became stronger propagating downstream of the turbine, as shown in Figure 7.2, which was not seen in the previous set up. The vortex cavitation was similar to tip vortex cavitation that would usually be found in a conventional turbine design with a defined tip. The nature of the incepted cavitation observed at the initial pressure condition was faint and intermittent. This discovery correlated with the increase in noise identified in the previous investigation. Moreover, the noise data recorded in this investigation also showed a surge in *SPL* at the same *TSR* condition. The noise data will be discussed in detail in Section 7.5. No cavitation was observed at other *TSR*s at a tunnel pressure of 850 mm Hg. At a tunnel pressure of 750 mm Hg, immediately below Atmospheric Pressure, weak and intermittent vortex cavitation was observed at *TSR* = 1. At *TSR* = 2, a weaker intermittent vortex cavitation was also observed as shown in Figure 7.3.

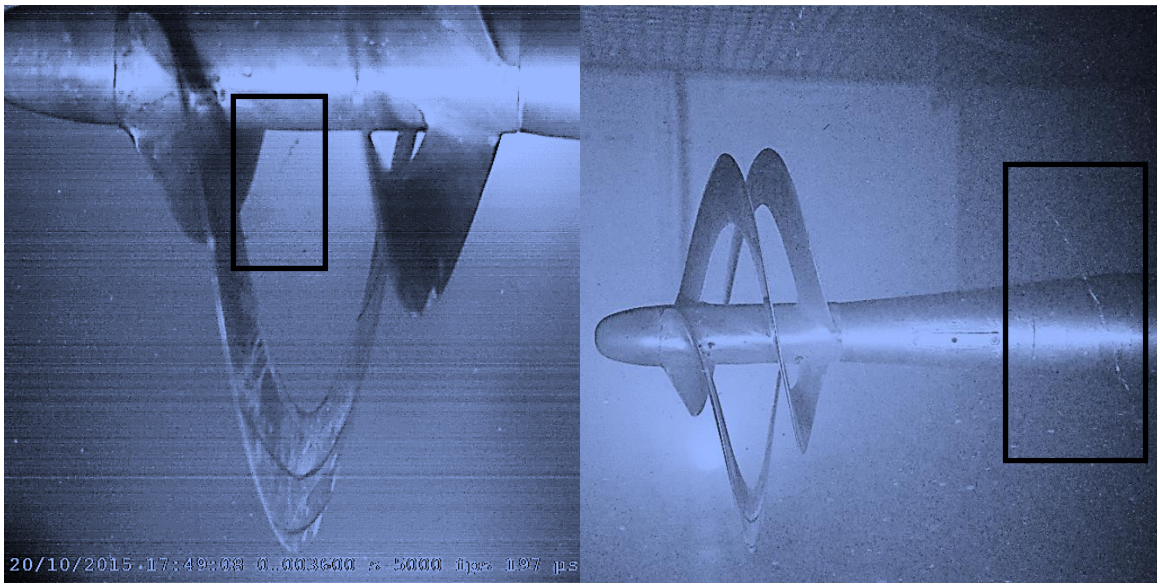

Figure 7.2 Vortex cavitation detected at 850 mm Hg, *TSR* = 1 condition

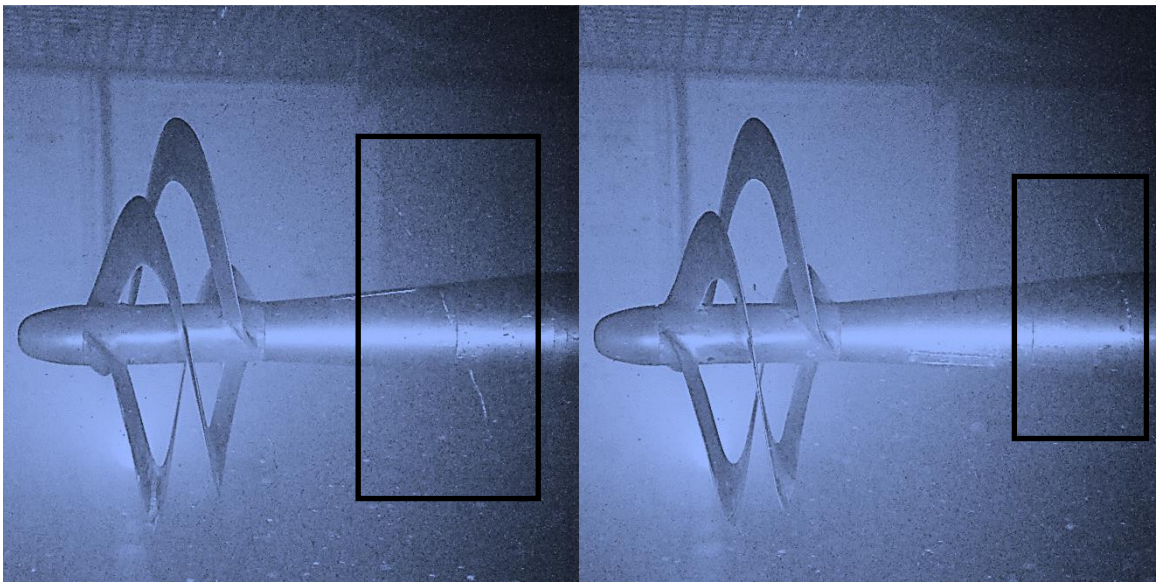

Figure 7.3 The vortex cavitation at 750 mm Hg observed at *TSR* = 1 (left) and *TSR* = 2 (right)

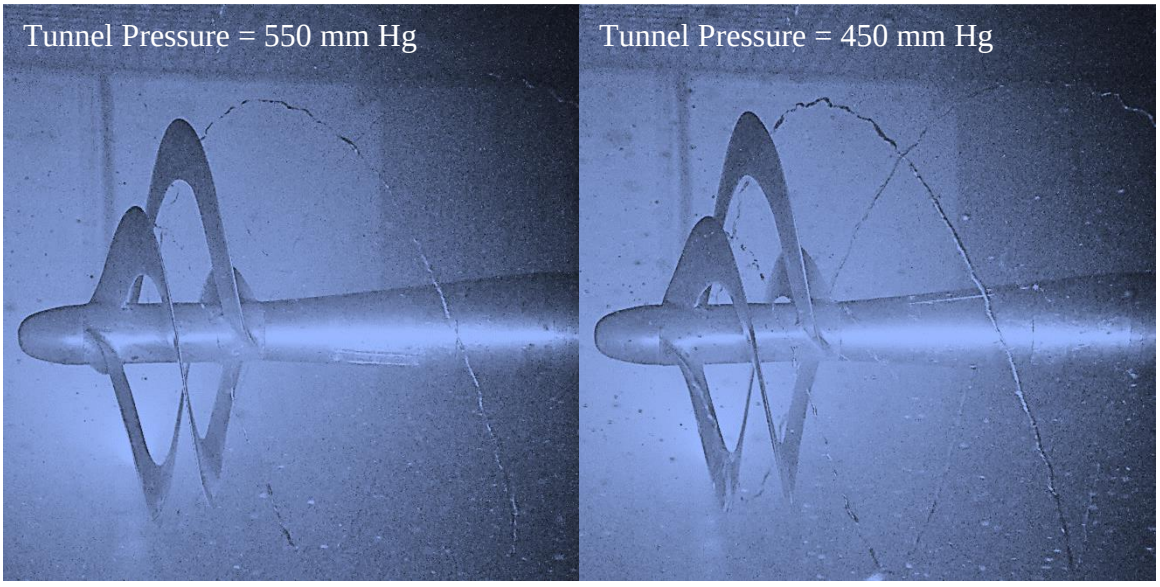

Figure 7.4 Cavitation observation at *TSR* = 1 at the different tunnel pressures indicated

As the tunnel pressure was further reduced, the vortex cavitation grew stronger and became more developed. For each pressure condition, the vortex cavitation was the strongest at *TSR* = 1, as observed in Figure 7.4, where the thrust coefficient was the highest, and it then reduced in strength as *TSR* was increased. At low pressures, it was found that the vortex

cavitation originated at the leading edge of the blade roots near the hub suggesting high resultant velocities at this region.

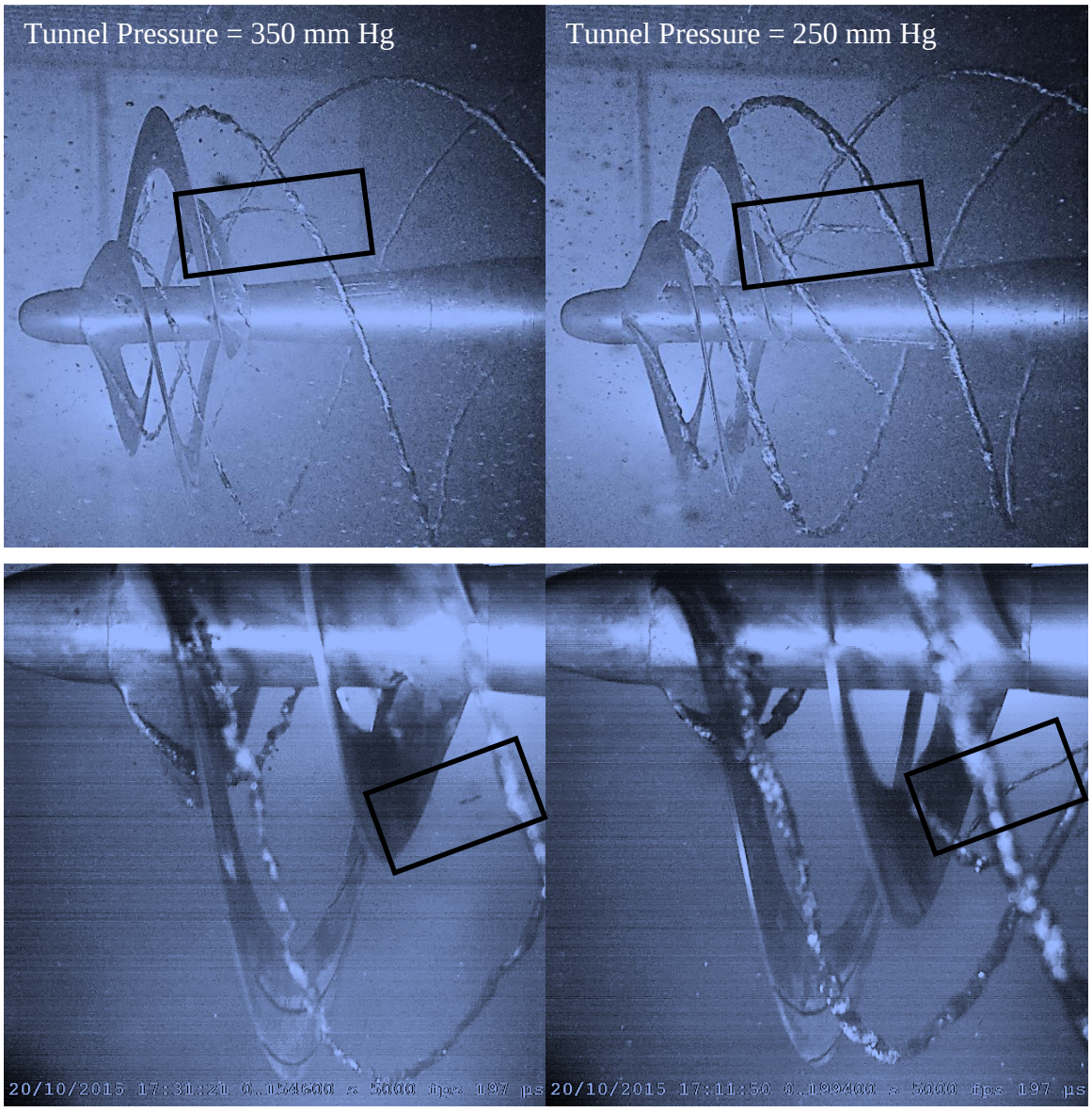

Figure 7.5 The outer and inner (rectangle) tip vortex cavitation at vacuum pressures

At a tunnel pressure of 350 mm Hg, in addition to a well-developed outer vortex cavitation, it was observed that another vortex cavitation occurred originating from the inner trailing edge of the downstream portion of the turbine blade, as shown in Figure 7.5. The inner vortex was observed to originate from the trailing edge of the turbine blade when the blade was

at its maximum radius. When the pressure was reduced to 250 mm Hg, the outer tip vortex intensified such that the diameter of the vortex was visibly larger and the inner vortex was more visible and attached to the trailing edge of the blade section. It was also observed that while the outer vortex expanded as it progressed downstream, the inner vortex converged, as shown in Figure 7.6.

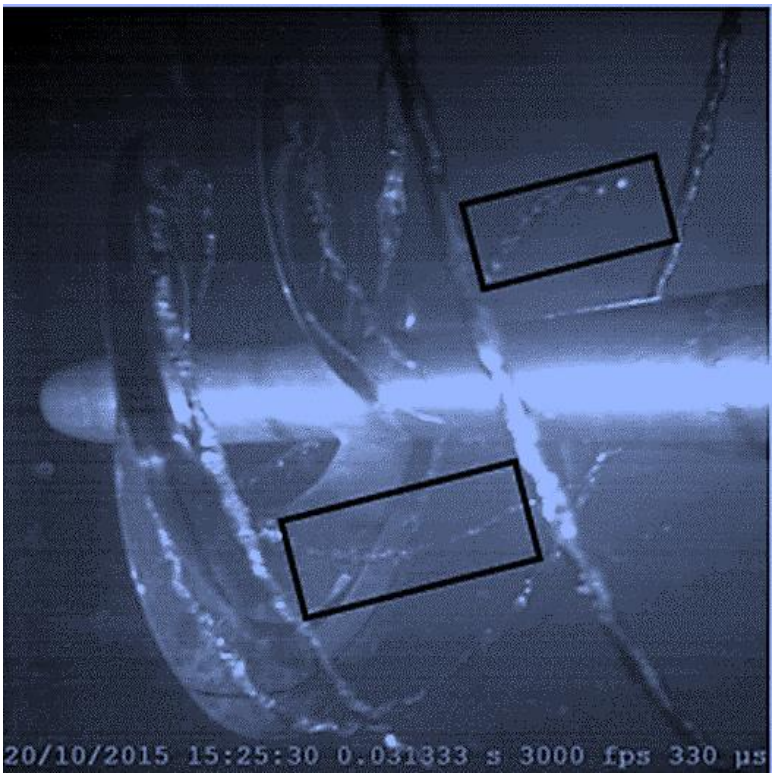

Figure 7.6 The outer and inner vortex (in black rectangles) cavitation observed at tunnel pressure of 250 mm Hg

In marine propellers, tip vortex cavitation is tolerated as it has minimal impact on the propeller blades whereas sheet or cloud cavitation can cause structural blade damage (Sharma *et al.*, 1990). These types of cavitation are also observed in tidal current turbines where it affected their operation although minimal (Bahaj *et al.*, 2007b; Wang *et al.*, 2007; Shi *et al.*, 2016b). Moreover, tip vortex cavitation is generally understood to generate the least amount of noise compared to other types of cavitation.

It was also found that in the case of the Hydro-Spinna, the Cavitation Number is not a reliable parameter to predict cavitation. In general, turbines are prone to cavitation at low

Cavitation Number due to the high rotational speed which induces low pressure regions (Bahaj and Myers, 2003; Buckland *et al.*, 2013). This is true for conventional turbines where, as the *TSR* increases, the thrust coefficient on the turbine also increases. However, in the case of the Hydro-Spinna turbine, the thrust coefficient peaks at *TSR* = 1 and decreases with increasing *TSR*. For each pressure condition, strongest cavitation was observed at *TSR* = 1 where the thrust is the highest. Since the strongest cavitation was observed at maximum thrust coefficient, it is concluded that the thrust coefficient contributes to the Hydro-Spinna cavitation rather more than the rotational speed of the turbine. As *TSR* increased, the thrust coefficient decreased and the cavitation dissipated. This trend can be observed in Figure 7.7 where a summary of the cavitation observed in the investigation at various tunnel pressures is presented.

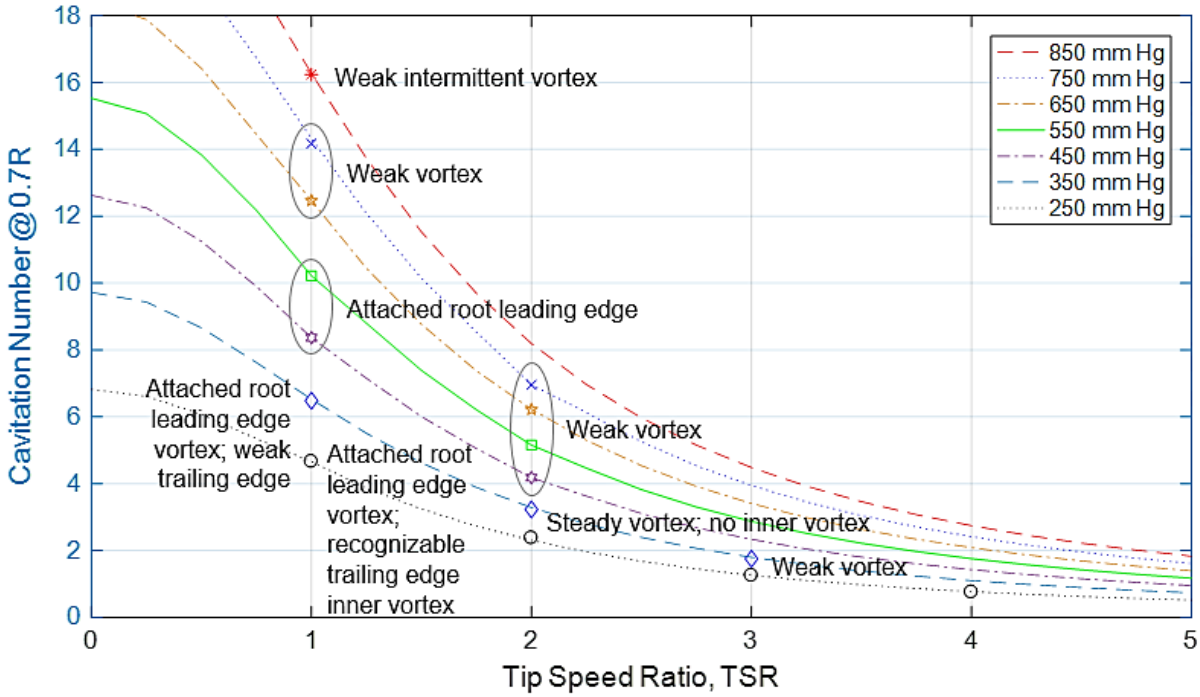

Figure 7.7 Cavitation Number against *TSR* plot with a summary of where cavitation was observed during the investigation

7.4.1 Full-Scale Cavitation Number

In order to evaluate whether cavitation would occur in the full-scale turbine, the full-scale cavitation number, σ_{FS}, was calculated using Equation 7.7. The corresponding tunnel pressure for the full-scale conditions was calculated using Equation 7.8 and is presented under

the design condition at *TSR* of 3, a flow velocity of 2 m/s and designed immersion of 1D depth as given in Table 7.2. The full-scale cavitation number at immersion depth of 0D i.e. the turbine just below the water surface was also calculated to consider the shallow immersion condition.

$$\sigma_{FS} = \frac{P_O + \rho_{sea} g(H_I - 0.7R) - P_V}{0.5\rho V_r^2}$$

Equation 7.7

$$H_M = \frac{0.5\rho U_r^2 \sigma_{FS} + P_V}{\rho_{Hg} g}$$

Equation 7.8

where H_I is the immersion depth of the turbine from the water surface to the shaft, P_V is the vapour pressure, U_r is the resultant velocity of the turbine at 0.7*R*, ρ is the density of the fluid and H_M is the height of mercury level in the static head gauge in the Emerson Cavitation Tunnel.

Table 7.2 The full-scale cavitation number and its corresponding tunnel pressure

	Full-Scale						**Model**
D (m)	5		10		15		0.28
U (m/s)	2		2		2		3
TSR	3		3		3		3
N (rpm)	22.9		11.5		7.6		613.9
H (m)	5	2.5	10	5	15	7.5	
σ_{FS}	11.91	9.65	14.86	10.33	17.81	11.01	
P_{tunnel} (Pa)	292408	237116	364287	253704	436166	270291	
H_M (m)	2.19	1.78	2.73	1.90	3.27	2.03	

From the above calculation, it was found that to obtain the operational cavitation number of the full-scale models, the corresponding tunnel condition had to be under pressured. It was therefore concluded that in these conditions, cavitation will not be incepted and that the full-scale turbine will operate cavitation free. The full-scale cavitation numbers at all *TSR*s were calculated and plotted against the pressure condition at which the experimental investigation took place, as presented in Figure 7.8.

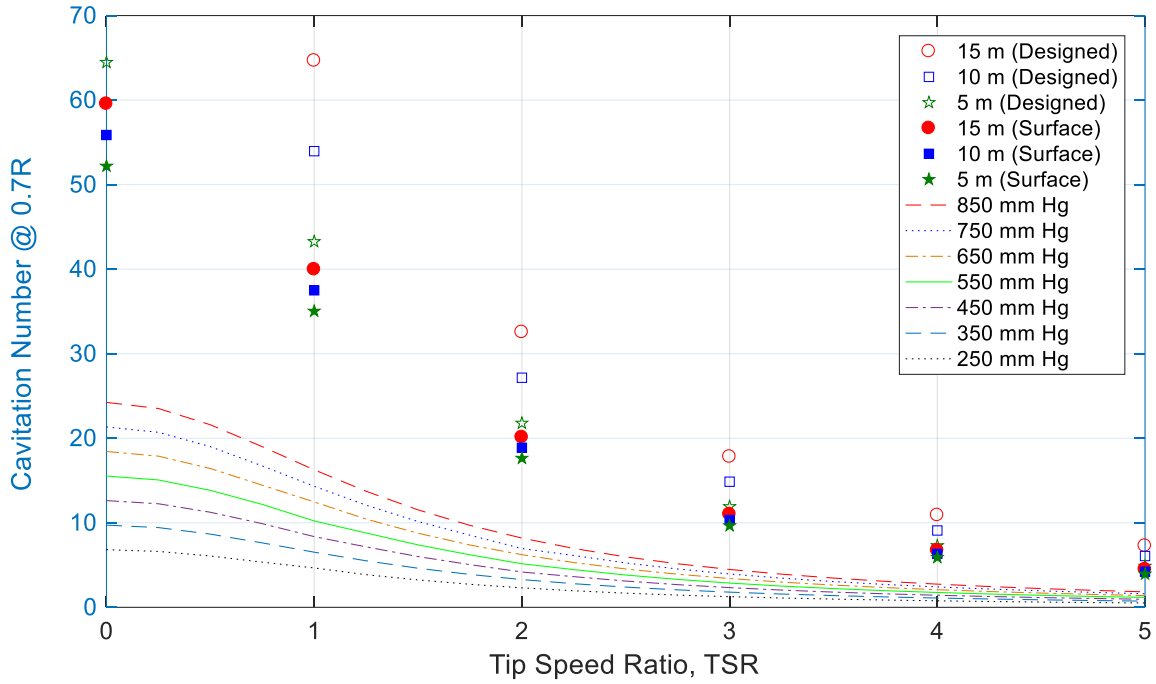

Figure 7.8 Cavitation numbers at full-scale design condition for the three full-scale diameters

7.5 Noise Results and Discussion

7.5.1 URN Band Level

The noise measurement data corresponded analogously with the cavitation observations. The corrected 1 Hz band level at the tunnel pressure of 850 mm Hg, shown in Figure 7.9, was found to exhibit an increase in SPL at *TSR* = 1 where the inception for a weak and intermittent tip vortex cavitation was observed. The observations in the 1 Hz band level were analogous with those in the 1/3 Octave band level. The 1/3 Octave band level also presented a similar

observation, as shown in Figure 7.10 although the analysis only yielded radiated noise at *TSR* = 1 and 2. Both the 1 Hz and 1/3 Octave band level exhibited an increase in SPL level in a region between 800 Hz and 6000 Hz. At *TSR* = 2, the turbine produced a maximum of 120 dB in the low frequency region. A complete SPL graphs for both the 1 Hz and 1/3 Octave band levels at all pressures are presented in Appendix F and G.

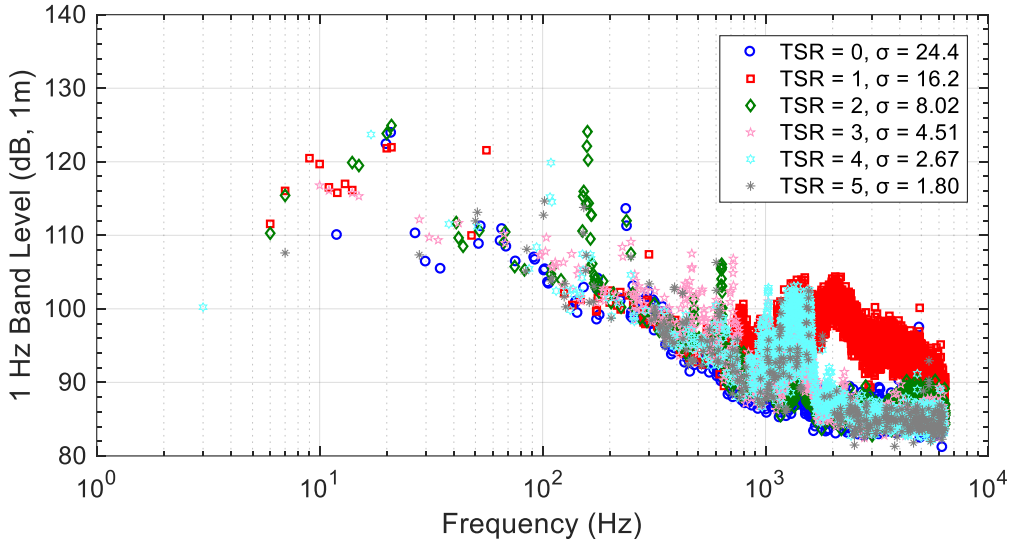

Figure 7.9 The corrected 1 Hz band level at all *TSR* at 850 mm Hg tunnel pressure

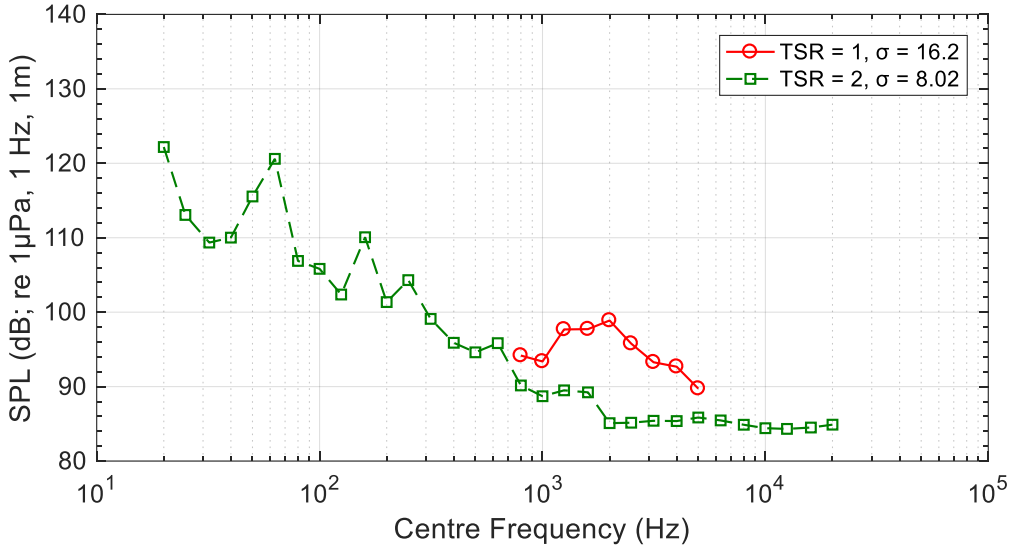

Figure 7.10 The corrected 1/3 Octave band level at 850mm Hg tunnel pressure

At a tunnel pressure of 550 mm Hg the corresponding noise levels were measured as shown in Figure 7.11, where attached leading edge vortex cavitation was observed at *TSR* = 1. At this condition, the band level ranged between a maximum value of 107 dB at 400 Hz and a minimum value of 87 dB at 5000 Hz.

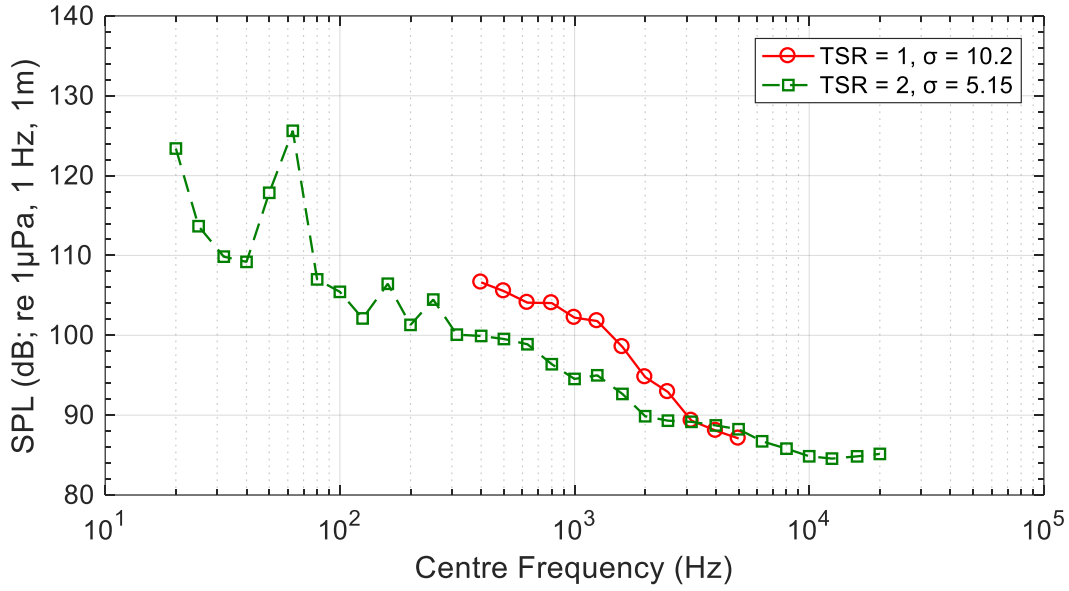

Figure 7.11 1/3 Octave Band Level at tunnel pressure 550 mm Hg

Similarly, at high vacuum pressure of 250 mm Hg, where strong developed outer vortex and considerable inner vortex cavitation were observed, the noise level significantly increased as shown in Figure 7.12. At *TSR* = 1, the band level ranged from 50 to 1000 Hz between 119 dB and 95 dB. Obviously, the band level trend evaluated at this condition was contributed to by the presence of the outer and inner cavitation. However, in the mid frequency range i.e. 300 Hz to 1000 Hz, the noise from *TSR* = 2 is higher even though the turbine is cavitating less. This increase in SPL is believed to have been caused by the collapse of the cavitation bubbles as they travel in the slipstream and this was detected by the hydrophone. As observed, the turbine was cavitating more at *TSR* = 1, in this condition, the tip vortex was strong due to the high axial load, hence the cavitation bubbles were able to travel along the slipstream and passed the hydrophone without collapsing.

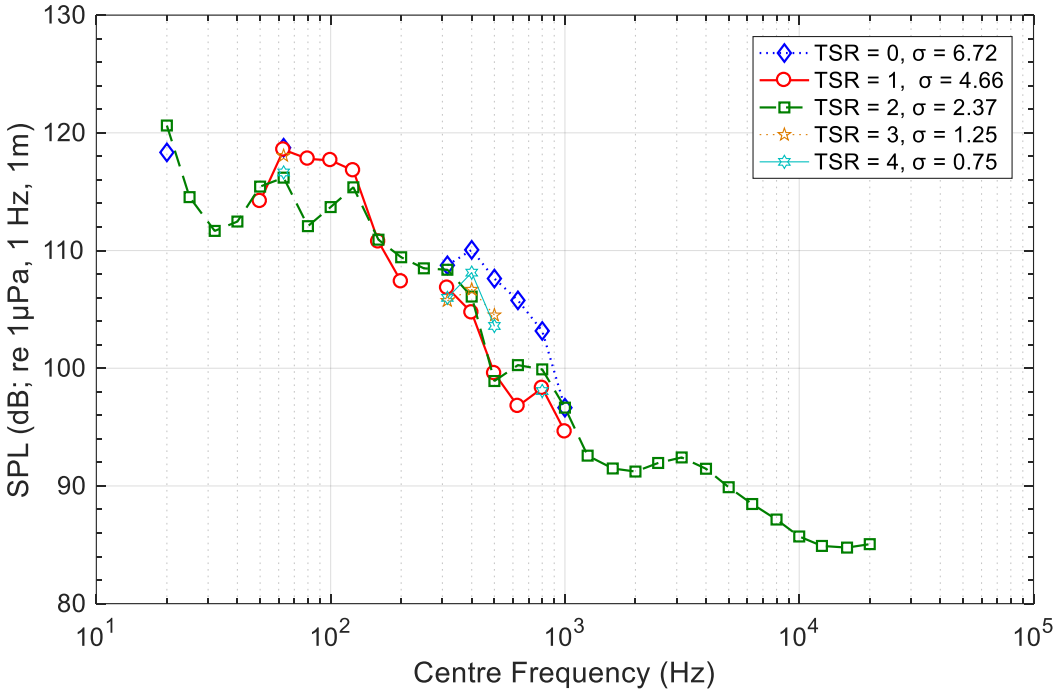

Figure 7.12 1/3 Octave Band Level at tunnel pressure 250 mm Hg

As previously mentioned, vortex cavitation is tolerable since it has minimal impact on the blade structure and generation of noise. As the tunnel pressure was reduced, more cavitation was observed and the SPL level at *TSR* = 1 increased and shifted towards the lower frequency region, as observed in Figure 7.13. Pennings *et al.* (2015) performed a study on the sound signature of propeller tip vortex cavitation where vortex cavity has a direct correlation with the noise generated. It was found that as the vortex cavitation, i.e. vortex cavities, gets bigger the frequency of the noise reduces. This finding supports the SPL data obtained in this investigation where, as the vortex cavitation grew in strength, the SPL level shifted from the high frequency to the low frequency region.

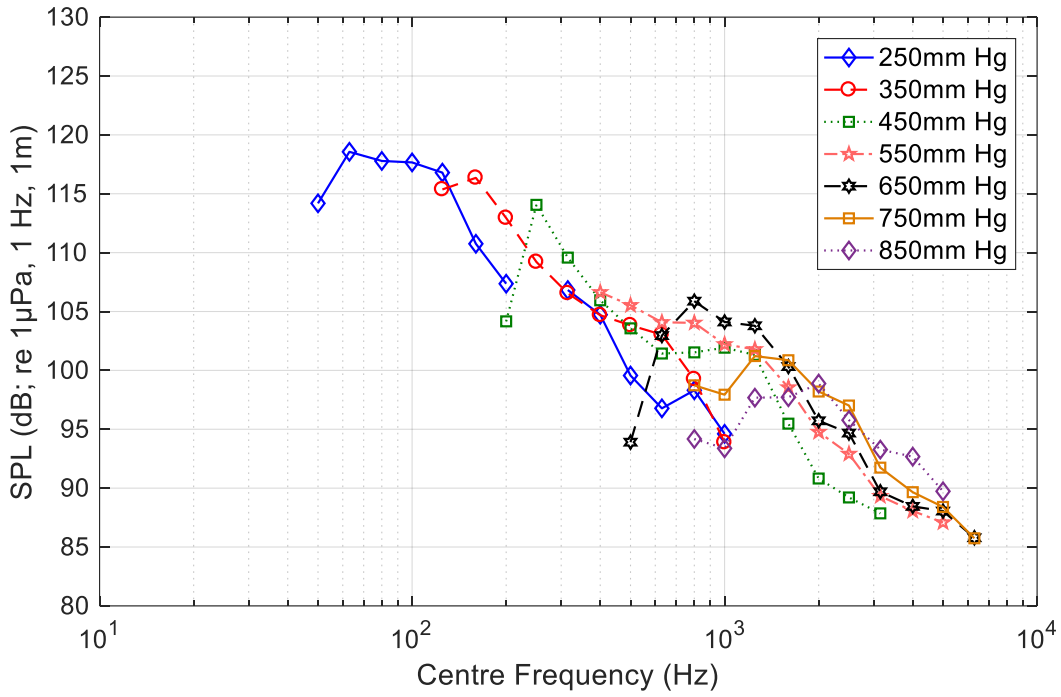

Figure 7.13 The trend in SPL level as tunnel pressure reduces at *TSR* = 1

With the corrected noise level, only the noise data obtained at *TSR* = 2 produced a complete data set. Figure 7.14 shows the 1/3 Octave band level at all pressure conditions where the blade rate frequency which is a product of the blade number and the rotational speed of the turbine in revolution per second (rps) was calculated to be 20.5 Hz. At this frequency and its harmonics, noise peaks were observed especially at normal tunnel pressure. In the case of high vacuum pressure however, the noise generated by the cavitation was more prominent and masked the noise peaks caused by the blade rate frequency.

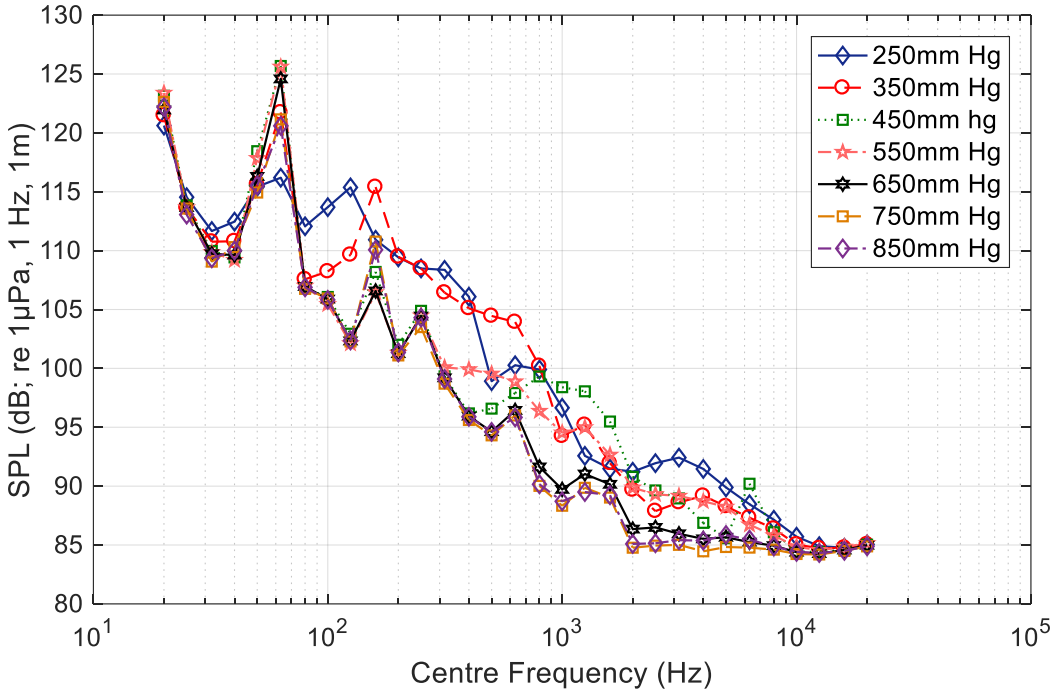

Figure 7.14 1/3 Octave band level at *TSR* = 2 at all pressure conditions

7.5.2 Full-Scale Noise Level

The full-scale noise level prediction discussed in this section involved the extrapolation of results from three tunnel pressures, firstly at 850 mm Hg (normal tunnel pressure) to predict the URN generated under the pressure condition at the inception of intermittent detached cavitation. Secondly, the noise band level from the 550 mm Hg (medium vacuum pressure) was extrapolated to predict the URN where attached vortex cavitation was observed on the turbine. Finally, to predict the full-scale URN level at extreme conditions of 250 mm Hg (high vacuum pressure) where a strong attached leading edge vortex was observed. The three band levels were considered to provide an overview of the full-scale URN under different observations of cavitation behaviour.

The URN prediction based on the normal tunnel pressure produced band level above the reference ICES threshold for *TSR* of 2 at all full-scale diameters, as shown in Figure 7.15. At *TSR* of 1, only the 10 m and 15 m turbine produced results that were above the reference threshold, as shown in Figure 7.16 and Figure 7.17 respectively. For the optimal turbine operating condition at *TSR* of 3, the predicted noise level was below the ICES threshold level.

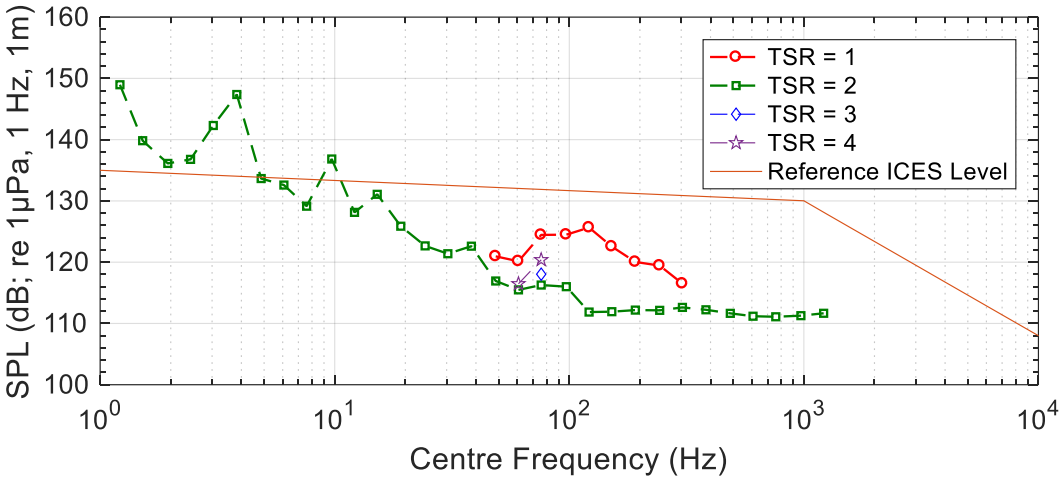

Figure 7.15 1/3 Octave band level of 5 m turbine at vortex cavitation inception

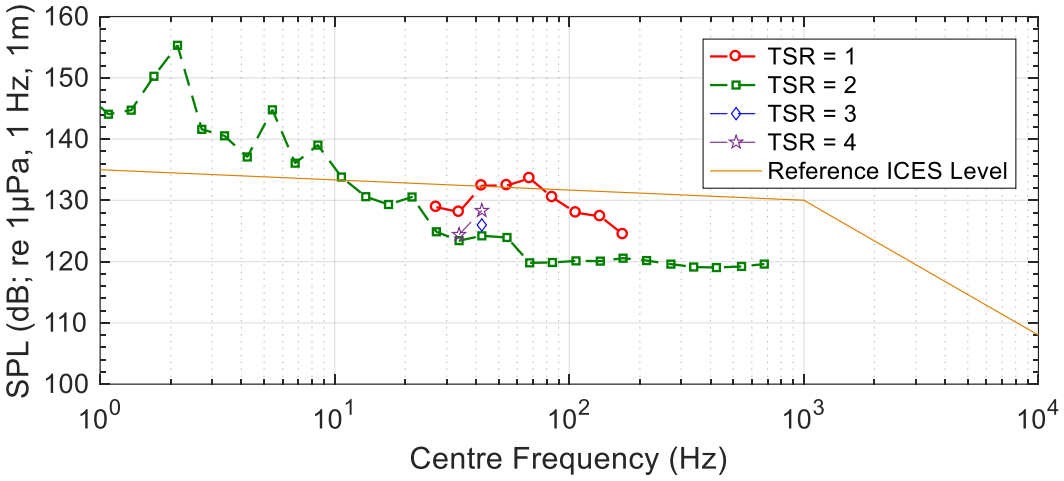

Figure 7.16 1/3 Octave band level of 10 m turbine at vortex cavitation inception

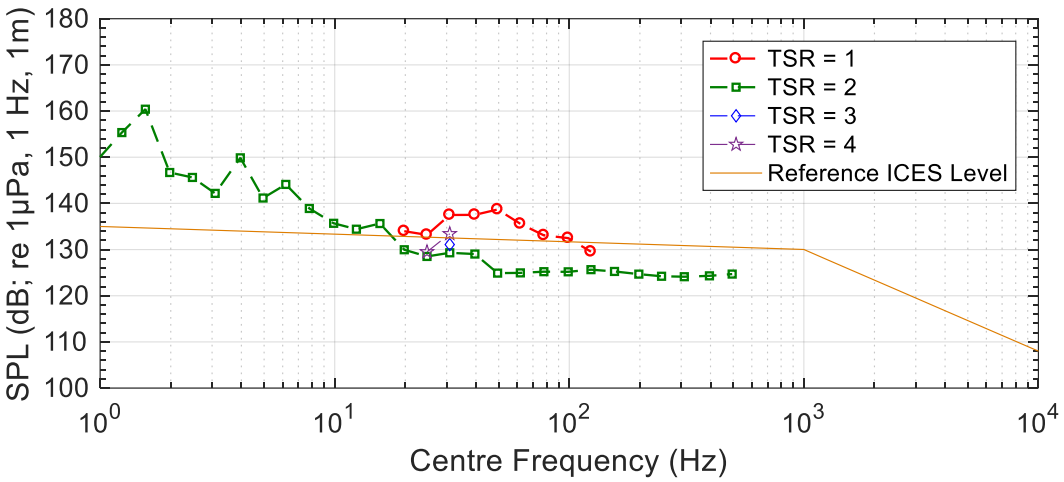

Figure 7.17 1/3 Octave band level of 15 m turbine at vortex cavitation inception

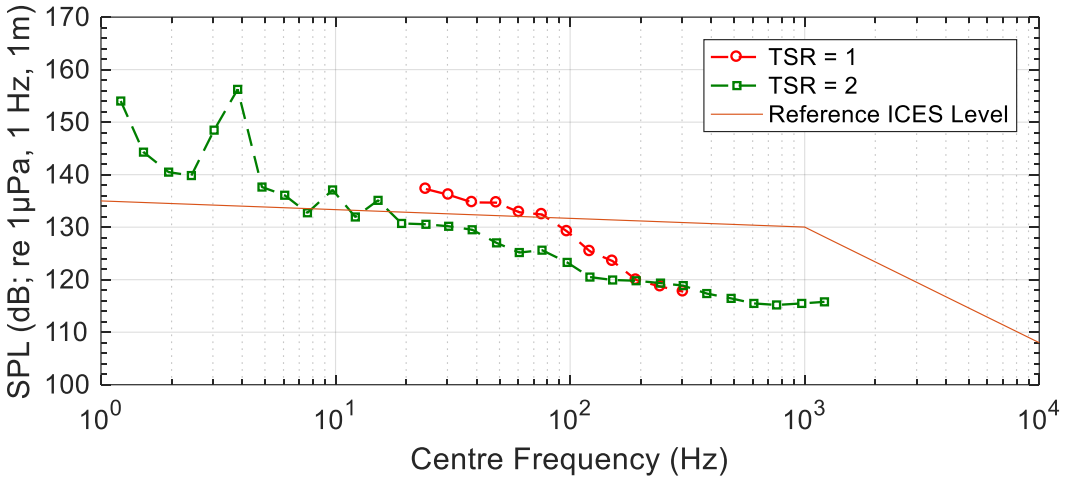

Figure 7.18 1/3 Octave band level of 5 m turbine at attached vortex condition

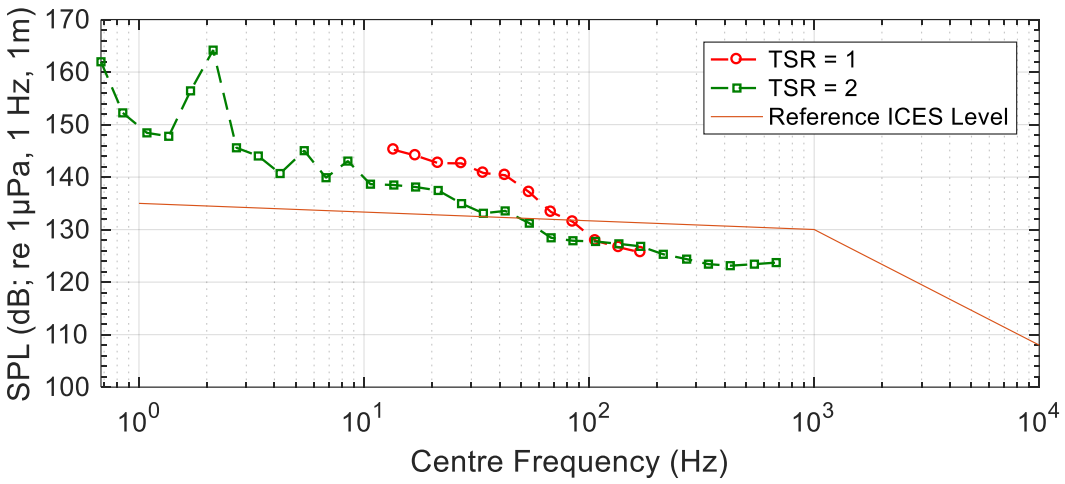

Figure 7.19 1/3 Octave band level of 10 m turbine at attached vortex condition

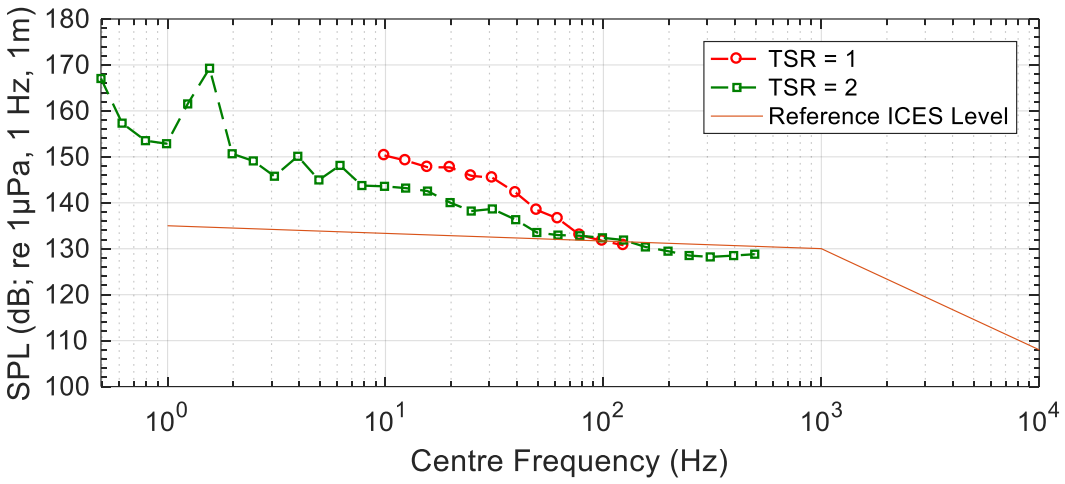

Figure 7.20 1/3 Octave band level of 15 m turbine at attached vortex condition

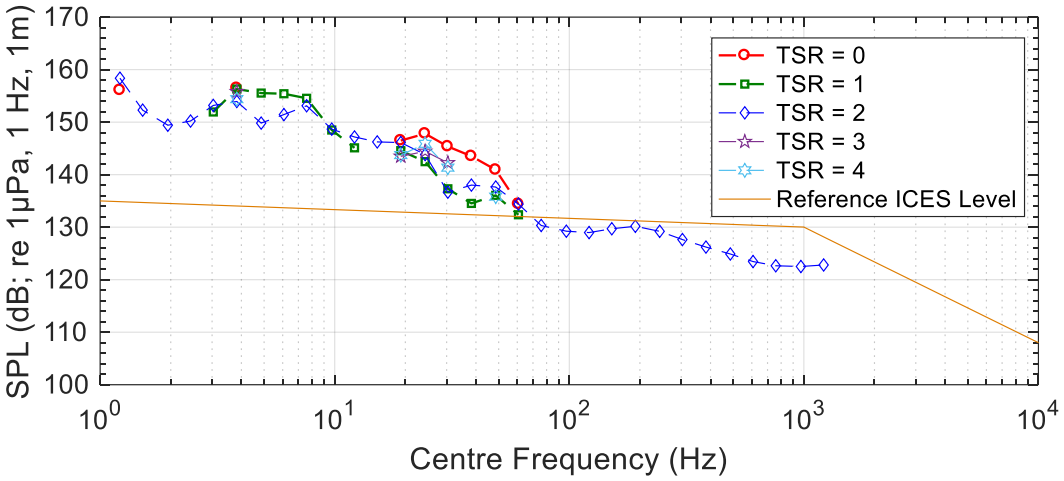

Figure 7.21 1/3 Octave band level of 5 m turbine at extreme cavitation

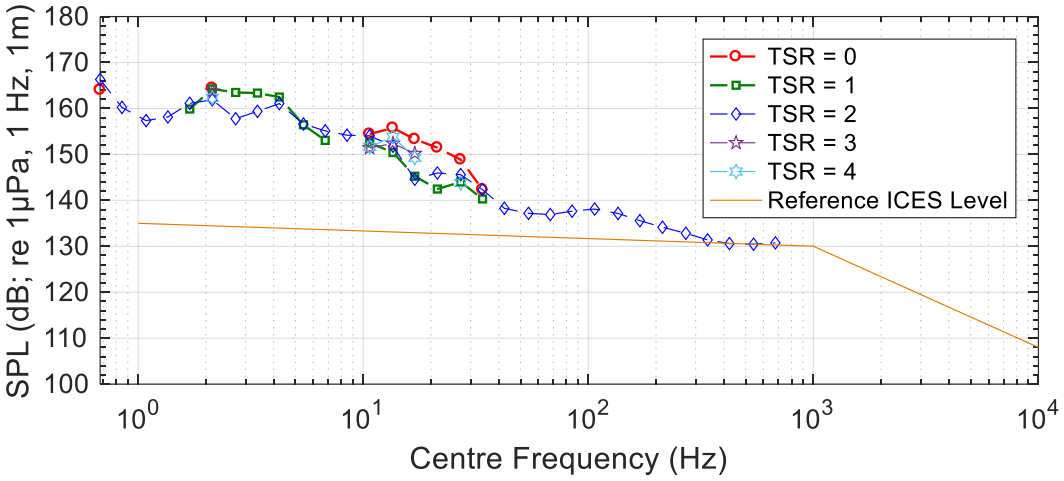

Figure 7.22 1/3 Octave band level of 10 m turbine at extreme cavitation

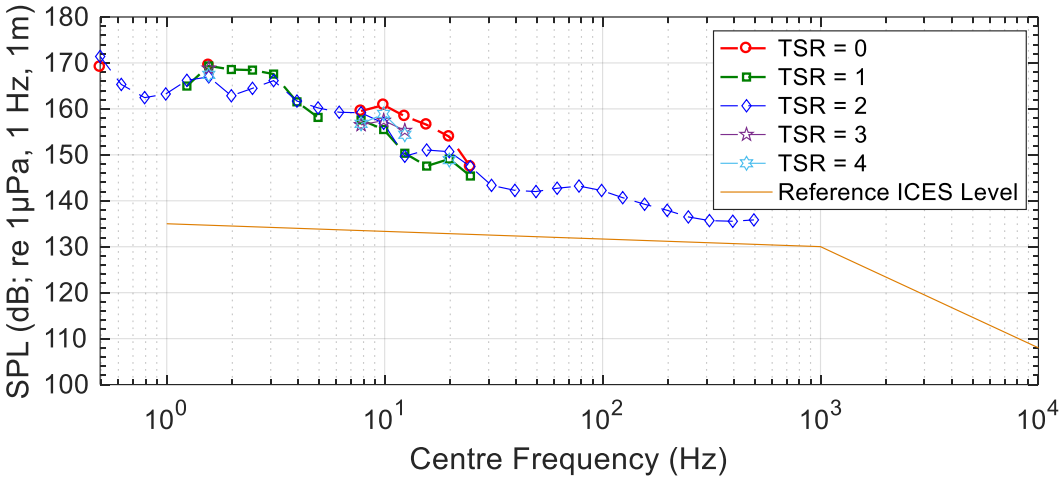

Figure 7.23 1/3 Octave band level of 15 m turbine at extreme cavitation

At the condition where attached leading edge vortex cavitation was observed, the full-scale URN data predicted band levels above the reference ICES level for all three full-scale diameters, as shown in Figure 7.18, Figure 7.19 and Figure 7.20. The results indicated an acoustic disturbance to the ambient noise level in the environment in which the turbine is deployed. At the extreme vortex cavitation condition, a much higher band level was observed as shown in Figure 7.21, Figure 7.22 and Figure 7.23, presenting a detrimental noise level in comparison to the threshold reference values. It was evaluated that the URN level increased with increasing turbine diameter, and with the severity of the cavitation observed.

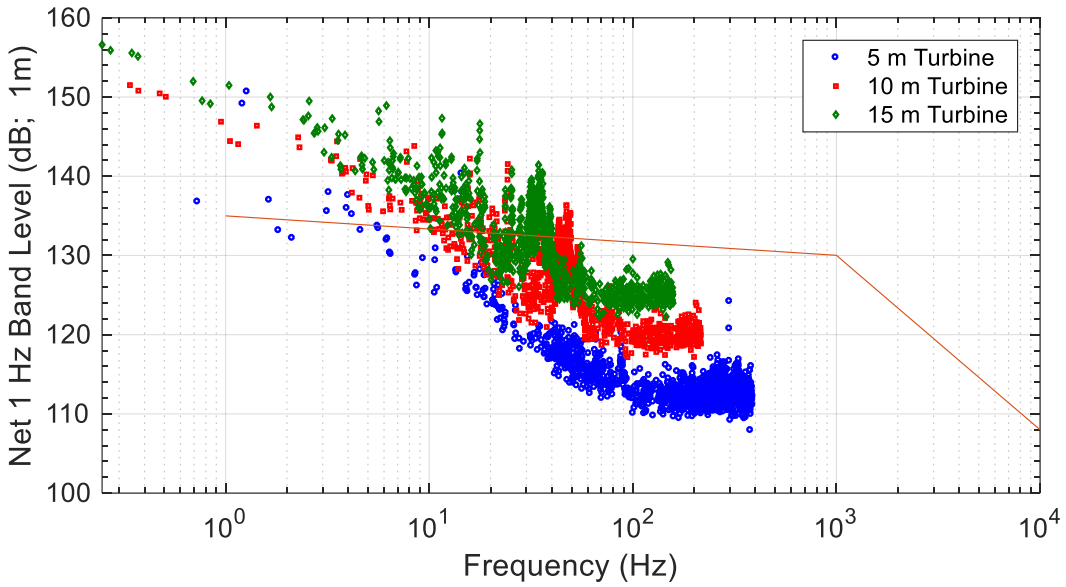

Figure 7.24 The 1 Hz band level at the designed *TSR* = 3 for the full-scale turbines

The analysis of the 1/3 Octave band level did not yield noise data for the designed condition at *TSR* = 3 but Figure 7.24 presents the 1 Hz band level for the designed condition for the three full-scale turbines. The designed operation for the 5 m turbine was mostly below the reference threshold level indicating that the URN is below the threshold level. For the 10 and 15 m turbine however, the URN levels were higher than the reference level signifying that their operations would contribute to an increase in the marine acoustic level.

A similar full-scale URN prediction work was conducted by Wang *et al.* (2007), for the designed, pre and post stall conditions at deep and shallow immersion. The URN prediction for deep immersion was well below the ICES reference level for all conditions. Whereas the URN level for the designed and post stall condition were found to exceed the threshold level at the low frequency region. A direct comparison from this study and the results from the Hydro-Spinna prediction cannot be done due to the different conditions and purpose for conducting the investigations.

7.6 Summary

This chapter presented the cavitation observations and noise band level measurements of the Hydro-Spinna turbine model. The inception for the tip vortex cavitation was observed at a tunnel pressure condition of 850 mm Hg at the operating point where the thrust coefficient was the highest. As vacuum pressures were induced cavitation developed further to the point where at a tunnel pressure 550 mm Hg, the vortex was observed to be attached to the root of the leading edge of the turbine. At high vacuum pressures of 250 mm Hg, a strong outer vortex was observed as well as a weak inner vortex originating from the trailing edge of the turbine. The full-scale turbines were however analysed to be operating cavitation free.

Noise band level measurements from the model tests were found to agree with the cavitation observations where peaks in noise level were observed together with the cavitation occurrence. As only vortex cavitation was observed in the Hydro-Spinna turbine, the noise band level increased and propagated towards the lower pressure region with increasing strength of cavitation. The full-scale URN prediction projected the operation of the 5 m turbine to be below the reference noise level. The 10 m and 15 m turbines generated URN levels higher than the ICES reference level at *TSR* of 1 and 2, whereas the level at the designed *TSR* is expected to be below indicating that the Hydro-Spinna operations would be less invasive against this threshold level.

CHAPTER 8. CONCLUSION AND RECOMMENDATIONS FOR FUTURE WORK

8.1 General Remarks

This chapter summarises the findings of the research and its contribution to the progress in marine turbine technology. Section 8.2 reviews the motivation for the research and summarise on the general findings while Section 8.3 concludes the main findings. Recommendations for future work are addressed in Section 8.4 while Section 8.5 wraps up the whole thesis.

8.2 Research Review

This thesis introduced the Hydro-Spinna turbine which offers a distinct design in the abundance of marine energy converters. In an industry where HATT is swamped with a conventional horizontal axis design, initiated from the wind industry, the Hydro-Spinna turbine is unique in its own right. It can be said that common HATTs are more 'two-dimensional' and are often approximated as a thin disc in their analysis. The Hydro-Spinna turbine is a 'three-dimensional' design where the turbine is extended in the axial direction.

The main objective of this research was to present the capability of the Hydro-Spinna turbine to generate power not only as an efficient device but also as a competitive one. The main aim of the thesis was not only to prove the Hydro-Spinna as an efficient marine turbine but to also demonstrate its effectiveness at different conditions and develop it further.

The design concept of the Hydro-Spinna was introduced with the geometry and parameters of the blade defined. A key parameter highlighting the uniqueness of the design, the pitch to diameter ratio (*P/D)* was described. As it is a significant and obvious parameter, one of the first questions raised from introducing the ratio was how it would affect the performance of the turbine. Hence, this was the first investigation that was conducted using numerical modelling to assess the performance of the Hydro-Spinna. At the initial stage of the research, numerical modelling was agreed to be the best approach in terms of the resources available and three *P/D* values were selected. The investigation concluded that the *P/D* is a significant factor

influencing the turbine performance. Not only is the efficiency of the Hydro-Spinna turbine increased with decreasing ratio, the operational Tip Speed Ratio (*TSR*) of the turbine also increased. It was decided that the Hydro-Spinna with a P/D ratio of 0.43 would be selected for further investigations.

Another turbine operation characteristic that researchers and developers are interested in is the variation of turbine performance at different immersion depths (Wang *et al.*, 2004; Bahaj *et al.*, 2007b; Bahaj *et al.*, 2012). The next investigation to explore the performance characteristics of the Hydro-Spinna turbine was conducted at different immersion depths. Interestingly, the Hydro-Spinna performance has little to no dependency on the immersion depth. The investigations were both conducted experimentally and numerically where both showed parallel trends and similar results. It is the first time, this significant finding, which is distinctive to the Hydro-Spinna, has been demonstrated as the performance of conventional HATTs is susceptible to decreasing immersion depth. This finding was published in the journal Renewable Energy (Rosli *et al.*, 2016). In terms of the power coefficient, the optimal *TSR* for the Hydro-Spinna turbine is around *TSR* of 2.25 with an operational range of $0 < TSR < 4$. The optimal speed is lower than those of conventional HATT indicating that the turbine operates effectively at low speed. Therefore, the Hydro-Spinna is an attractive prospect for power generation in areas where water depth and tidal velocity are low. One clear possibility is operation in rural areas that are not grid connected which could greatly improve the standard of living of the residents.

The thrust characteristic of the Hydro-Spinna turbine also presented a unique trend. Due to the design of the turbine, even when the turbine is not operating, it is subjected to axial loading which increases with *TSR* of up to *TSR* of 1 where the maximum thrust is reached before the thrust steadily declines with increasing speed. Hence, this reveals that the Hydro-Spinna operates at a much lower thrust coefficient at its designed condition which is in contrast to the normal characteristic of the HATTs. The decrease in thrust with increasing TSR indicates that the turbine operates at a much lower thrust compared to conventional HATT. The Hydro-Spinna turbine was also evaluated to yield higher torque than conventional HATT would produce with a torque coefficient of 0.125 at optimal condition. This indicates that the Hydro-Spinna produces higher torque at low speed and is therefore suitable for low speed applications. Consequently, the correlation between the experimental and numerical data validates the

reliability and accuracy of the numerical model which was based on the CFD model developed in this thesis.

Marine turbines are susceptible to cavitation and it was only reasonable for the cavitation behaviour of the Hydro-Spinna turbine to be explored. Further exploration of the turbine cavitation characteristics was conducted where the noise level measurements were assessed. At higher than Atmospheric condition, the Hydro-Spinna turbine operates free of cavitation at its optimal speed. Systematically reduced static pressures were induced in the cavitation tunnel to encourage cavitation to occur to give an understanding of the types of cavitation the turbine generates. It was found that only tip vortex type cavitation was observed at these conditions while other types of cavitation were not present at all. As tip vortex cavitation has minimal impact on the blade structure and integrity, this highlights that the turbine is free from other cavitation types that would be detrimental to the turbine blades, another interesting feature of the Hydro-Spinna turbine. At its operational condition, the turbine is able to operate cavitation free which is a major advantage, adding another desirable characteristic to the Hydro-Spinna portfolio.

The noise measurements from the model testing were analysed and extrapolated to predict the full-scale URN levels of three full-scale Hydro-Spinna with different diameter. The extrapolation of the model noise data was done by using the ITTC recommended scaling law that were recognised in marine propeller analysis. The predicted URN levels were plotted alongside a reference value to appreciate the level of URN generated against actual threshold level. As URN level from turbine operations are somewhat of an unknown subject, and study on URN could only possibly be assessed when a full-scale turbine is deployed. The URN prediction could be adopted in the tidal industries to give an overview of the noise level that can be generated from marine turbines whilst at its development stage. The prediction could provide an indication of the URN level that full-scale turbines might produce. Furthermore, it could be used for environmental assessment when identifying a potential site.

8.3 Conclusions

The thesis has shown that the Hydro-Spinna offers a novel and exciting prospect to the thriving marine energy industries. The major findings from this research includes the following.

1. The Hydro-Spinna was evaluated to optimally operate at a lower range of *TSR* with a distinctive thrust characteristic. The performance characteristic is different from that of common HATT hence introducing an alternative performance that are suitable for applications incompatible to other turbines.
2. The torque coefficient of the turbine was found to be higher than that of conventional HATT indicating that the turbine generates high torque at low speed which is suitable for low speed application. This feature is appealing to sites where the tidal resources are not abundant and may be applicable to river applications.
3. The Hydro-Spinna turbine was determined to operate relatively independent of turbine immersion depth and providing more flexible operations for this restriction compare to conventional HATTs again emphasising its suitability for low resources sites especially those with limited water depth.
4. Impressively, Hydro-Spinna is able to operate even at half submerged condition while maintaining its performance, another exceptional feature. This feature further supports the suitability of the turbine to adapt to different conditions and may be a significant characteristic when considering it for the real sea deployment.
5. Remarkably, the Hydro-Spinna was found to operate free from cavitation at its optimal condition, another attractive characteristic. This feature makes the turbine less prone to blade surface damage and structural integrity of the turbine is maintained.
6. The adopted method of predicting full-scale turbine URN from model measurements provides full-scale noise level that could be used to assess the environmental impacts of the Hydro-Spinna for full-scale deployment.

8.4 Recommendations for future work

This thesis focused on the hydrodynamic characteristics of the Hydro-Spinna turbine at different hydrodynamic conditions. Undoubtedly, this leaves various aspects of the turbine for further development. In order to develop the Hydro-Spinna turbine as a complete system, the following subjects could be considered.

1. Due to its design, the Hydro-Spinna is constantly subjected to a thrust force even when it is not operating; this would require a robust supporting structure. Selection of blade and turbine system material is important to ensure that the turbine is able to withstand the thrust force acting on it. A system mechanism could be considered to address this issue for example implementing a yawing support mechanism to regulate the orientation of the turbine in different conditions.
2. As the Hydro-Spinna operates cavitation free, Hydro-Spinna will be more resistance to erosion caused from cavitation and may require less maintenance and blade replacement. However, as with the current model design, the blades are fixed to the hub, so damage to parts of the turbine blade may cause extended downtime as the whole turbine will need to be replaced. The turbine could be redesigned such that individual blades can be replaced when damaged.
3. As briefly discussed in the previous chapter, further development of the Hydro-Spinna turbine can be carried out with regard to the electrical power take off. Studies could be made of the selection of suitable generators and power electronics while also investigating the impact of the mechanical loading on the electrical generation.
4. Identification of potential sites for deployment can also be performed with the relevant resource assessment analysis although this would be at a later stage once a complete Hydro-Spinna system had been produced.

8.5 Concluding remarks

The Hydro-Spinna offers a fascinating concept with multi-functionality that it can operate effectively with bi-directional flow, both in deep and shallow water. The Hydro-Spinna also has a good free-surface adaptability giving a wide range of operational depths. Moreover, the design concept of the turbine makes it to be suitable for both wind and tidal applications, although it has never been properly tested in a wind tunnel environment.

This thesis has successfully explored the potential of the Hydro-Spinna turbine as an efficient marine current energy converter. This thesis offers the Hydro-Spinna turbine as an alternative for other applications that may not be practicable for common marine turbines. The

hydrodynamic performance under different conditions presents exciting prospects for further development. Nonetheless, there is room for improvements and further research to develop the turbine into a complete energy converter system.

References

Ahmed, M.R. (2012) 'Blade sections for wind turbine and tidal current turbine applications-current status and future challenges', *International Journal of Energy Research*, 36(7), pp. 829-844.

Aktas, B., Atlar, M., Turkmen, S., Korkut, E. and Fitzsimmons, P. (2016a) 'Systematic cavitation tunnel tests of a Propeller in uniform and inclined flow conditions as part of a round robin test campaign', *Ocean Engineering*, 120, pp. 136-151.

Aktas, B., Atlar, M., Turkmen, S., Shi, W., Sampson, R., Korkut, E. and Fitzsimmons, P. (2016b) 'Propeller cavitation noise investigations of a research vessel using medium size cavitation tunnel tests and full-scale trials', *Ocean Engineering*, 120, pp. 122-135.

Ali, M.S.M., Doolan, C.J. and Wheatley, V. (2009) 'Grid convergence study for a two-dimensional simulation of flow around a square cylinder at a low Reynolds Number', *7th International Conference on CFD in the Minerals and Process Industries*. Melbourne, Australia, 9th - 11th December 2009.

Aly, H.H.H. and El-Hawary, M.E. (2011) 'State of the art for tidal currents electric energy resources', *Canadian Conference on Electrical and Computer Engineering*. pp. 1119-1124.

Antheaume, S., Maître, T. and Achard, J.-L. (2008) 'Hydraulic Darrieus turbines efficiency for free fluid flow conditions versus power farms conditions', *Renewable Energy*, 33(10), pp. 2186-2198.

Ashuri, T., van Bussel, G. and Mieras, S. (2013) 'Development and validation of a computational model for design analysis of a novel marine turbine', *Wind Energy*, 16(1), pp. 77-90.

Asim, T., Mishra, R., Ubbi, K. and Zala, K. (2013) 'Computational Fluid Dynamics Based Optimal Design of Vertical Axis Marine Current Turbines', *Procedia CIRP*, 11, pp. 323-327.

Atlantis Resources Corporation (2017) *Atlantis Resources Corporation*. Available at: http://www.atlantisresourcescorporation.com/ (Accessed: 5th August 2016).

Atlar, M., Takinaci, A.C., Korkut, E., Sasaki, N. and Takeshi, A. (2001) 'Cavitation tunnel tests for propeller noise of a FRV and comparisons with full-scale measurements', *Fourth International Symposium on Cavitation*. Pasadena, California.

Bae, Y.H., Kim, K.O. and Choi, B.H. (2010) 'Lake Sihwa tidal power plant project', *Ocean Engineering*, 37(5), pp. 454-463.

Bahaj, A.S. (2011) 'Generating electricity from the oceans', *Renewable and Sustainable Energy Reviews*, 15(7), pp. 3399-3416.

Bahaj, A.S., Batten, W.M.J. and McCann, G. (2007a) 'Experimental verifications of numerical predictions for the hydrodynamic performance of horizontal axis marine current turbines', *Renewable Energy*, 32(15), pp. 2479-2490.

Bahaj, A.S., Molland, A.F., Chaplin, J.R. and Batten, W.M.J. (2007b) 'Power and thrust measurements of marine current turbines under various hydrodynamic flow conditions in a cavitation tunnel and a towing tank', *Renewable Energy*, 32(3), pp. 407-426.

Bahaj, A.S. and Myers, L.E. (2003) 'Fundamentals applicable to the utilisation of marine current turbines for energy production', *Renewable Energy*, 28(14), pp. 2205-2211.

Bahaj, A.S. and Myers, L.E. (2013) 'Shaping array design of marine current energy converters through scaled experimental analysis', *Energy*, 59, pp. 83-94.

Bahaj, A.S., Myers, L.E., Rawlinson-Smith, R.I. and Thomson, M. (2012) 'The Effect of Boundary Proximity Upon the Wake Structure of Horizontal Axis Marine Current Turbines', *Journal of Offshore Mechanics and Arctic Engineering*, 134(2), pp. 021104-1 - 021104-08.

Bai, C.J., Hsiao, F.B., Li, M.H., Huang, G.Y. and Chen, Y.J. (2013a) 'Design of 10 kW Horizontal-Axis Wind Turbine (HAWT) Blade and Aerodynamic Investigation Using Numerical Simulation', *Procedia Engineering*, 67, pp. 279-287.

Bai, G., Li, J., Fan, P. and Li, G. (2013b) 'Numerical investigations of the effects of different arrays on power extractions of horizontal axis tidal current turbines', *Renewable Energy*, 53, pp. 180-186.

Bai, X., Avital, E.J., Munjiza, A. and Williams, J.J.R. (2014) 'Numerical simulation of a marine current turbine in free surface flow', *Renewable Energy*, 63, pp. 715-723.

Bailey, H., Senior, B., Simmons, D., Rusin, J., Picken, G. and Thompson, P.M. (2010) 'Assessing underwater noise levels during pile-driving at an offshore windfarm and its potential effects on marine mammals', *Marine Pollution Bulletin*, 60(6), pp. 888-897.

Baker, C. (1991) 'Tidal power', *Energy Policy*, 19(8), pp. 792-797.

Bark, G. (1985) 'Prediction of propeller cavitation noise from model tests and its comparison with full scale data', *Journal of Fluids Engineering, Transactions of the ASME*, 107(1), pp. 112-120.

Barltrop, N., Varyani, K.S., Grant, A., Clelland, D. and Pham, X.P. (2007) 'Investigation into wave—current interactions in marine current turbines', *Proceedings of the Institution of Mechanical Engineers, Part A: Journal of Power and Energy*, 221(2), pp. 233-242.

Batten, W.M.J., Bahaj, A.S., Molland, A.F. and Chaplin, J.R. (2006) 'Hydrodynamics of marine current turbines', *Renewable Energy*, 31(2), pp. 249-256.

Batten, W.M.J., Bahaj, A.S., Molland, A.F. and Chaplin, J.R. (2007) 'Experimentally validated numerical method for the hydrodynamic design of horizontal axis tidal turbines', *Ocean Engineering*, 34(7), pp. 1013-1020.

Batten, W.M.J., Bahaj, A.S., Molland, A.F. and Chaplin, J.R. (2008) 'The prediction of the hydrodynamic performance of marine current turbines', *Renewable Energy*, 33(5), pp. 1085-1096.

Bertschneider, H., Bosschers, J., Choi, G.H., Ciappi, E., Farabee, T., Kawakita, C. and Tang, D. (2012) '27th ITTC Report of Specialist Committee on Hydrodynamic Noise, ' *International Towing Tank Conference*. Copenhagen, Denmark, 31st August - 5th September 2014.

Bevelhimer, M.S., Deng, Z.D. and Scherelis, C. (2016) 'Characterizing large river sounds: Providing context for understanding the environmental effects of noise produced by hydrokinetic turbines', *Journal of the Acoustical Society of America*, 139(1), pp. 85-92.

Billet, M.L. and Holl, J.W. (1981) 'Scale effects on various types of limited cavitation', *Journal of Fluids Engineering, Transactions of the ASME*, 103(3), pp. 405-414.

Binnie, C. (2016) 'Tidal energy from the severn estuary, UK', *Proceedings of the Institution of Civil Engineers: Transport*, 169, pp. 3-17.

Birjandi, A.H., Bibeau, E.L., Chatoorgoon, V. and Kumar, A. (2013) 'Power measurement of hydrokinetic turbines with free-surface and blockage effect', *Ocean Engineering*, 69, pp. 9-17.

Blunden, L.S. and Bahaj, A.S. (2007) 'Tidal energy resource assessment for tidal stream generators', *Proceedings of the Institution of Mechanical Engineers, Part A: Journal of Power and Energy*, 221(2), pp. 137-146.

Breuer, M., Jovičić, N. and Mazaev, K. (2003) 'Comparison of DES, RANS and LES for the separated flow around a flat plate at high incidence', *International Journal for Numerical Methods in Fluids*, 41(4), pp. 357-388.

Brownell, B., Cato, D., Clark, C.W., Costa, D., Evans, P., Gedamke, J., Gentry, R., Giniser, B., Giordon, J., Jepson, P., Miller, P., Rendell, L., Tasker, M., Tyack, P., Vos, E., Whitehead, H., Wartzok, D. and Zimmer, W. (2008) *The effects of anthropogenic sound on marine mammals A draft research strategy*. Available at: http://archives.esf.org/fileadmin/Public_documents/Publications/MBpp13.pdf (Accessed: 16th October 2016).

Bryden, I.G., Couch, S.J., Owen, A. and Melville, G. (2007) 'Tidal current resource assessment', *Proceedings of the Institution of Mechanical Engineers, Part A: Journal of Power and Energy*, 221(2), pp. 125-135.

Buckland, B.C., Masters, I., Chapman, J.C. and Orme, J.A.C. (2010) 'Blade element momentum theory in modelling tidal stream turbines', *UK Conference on Computational Mechanics*. Southampton.

Buckland, H.C., Masters, I., Orme, J.A. and Baker, T. (2013) 'Cavitation inception and simulation in blade element momentum theory for modelling tidal stream turbines', *Proceedings of the Institution of Mechanical Engineers, Part A: Journal of Power and Energy*, 227(4), pp. 479-485.

Burton, T., Jenkins, N., Sharpe, D. and Bossanyi, E. (2011) *Wind Energy Handbook*. India: Wiley.

Carlton, J. (2012) *Marine Propellers and Propulsion*. 3rd edn. Elsevier Ltd.

CD-Adapco (2013) *Reynolds-Averaged Navier-Stokes (RANS) Turbulence Models*. Available at: https://stevedocs.cd-adapco.com/starccmplus_latest_en/index.html?param=jzRq1&authLoc=https://steve.cd-adapco.com/AuthoriseRedirect#page/STARCCMP%2FGUID-235E939A-BC77-4988-AE0A-D79B17FD6072%3Den%3D.html%23 (Accessed: 6th March 2013).

Celik, I.B., Ghia, U., Roache, P.J., Freitas, C.J., Coleman, H. and Raad, P.E. (2008) 'Procedure for estimation and reporting of uncertainty due to discretization in CFD applications', *Journal of Fluids Engineering, Transactions of the ASME*, 130(7), pp. 0780011-0780014.

Chamorro, L.P., Troolin, D.R., Lee, S.-J., Arndt, R.E.A. and Sotiropoulos, F. (2013) 'Three-dimensional flow visualization in the wake of a miniature axial-flow hydrokinetic turbine', *Experiments in Fluids*, 54(2), p. (Research Article).

Chen, L. and Lam, W.-H. (2014) 'Slipstream between marine current turbine and seabed', *Energy*, 68, pp. 801-810.

Cho, Y.S., Lee, J.W. and Jeong, W. (2012) 'The construction of a tidal power plant at Sihwa Lake, Korea', *Energy Sources, Part A: Recovery, Utilization and Environmental Effects*, 34(14), pp. 1280-1287.

Clarke, J.A., Connor, G., Grant, A.D. and Johnstone, C.M. (2007) 'Design and testing of a contra-rotating tidal current turbine', *Proceedings of the Institution of Mechanical Engineers, Part A: Journal of Power and Energy*, 221(2), pp. 171-179.

Climate Vulnerable Forum (2015) *Major Economies Declare Support for 1.5°C*. Available at: http://www.thecvf.org/major-economies-declare-support-for-1-5c/ (Accessed: 18th June 2017).

Consul, C.A., Willden, R.H.J., McIntosh, S.C. and McCulloch, M.D. (2009) 'Influence of Solidity on the Performance of a Cross-Flow Turbine', *The 8th European Wave and Tidal Energy Conference*. Uppsala, Sweden, 7th - 10th September 2009.

Cuerva, A. and Sanz-Andrés, A. (2005) 'The extended Betz–Lanchester limit', *Renewable Energy*, 30(5), pp. 783-794.

DBEIS UK (2013) *Wave and tidal energy: part of the UK's energy mix*. Available at: https://www.gov.uk/guidance/wave-and-tidal-energy-part-of-the-uks-energy-mix (Accessed: 4th April 2017).

de Jesus Henriques, T.A., Hedges, T.S., Owen, I. and Poole, R.J. (2016) 'The influence of blade pitch angle on the performance of a model horizontal axis tidal stream turbine operating under wave–current interaction', *Energy*, 102, pp. 166-175.

de Jesus Henriques, T.A., Tedds, S.C., Botsari, A., Najafian, G., Hedges, T.S., Sutcliffe, C.J., Owen, I. and Poole, R.J. (2014) 'The effects of wave–current interaction on the performance of a model horizontal axis tidal turbine', *International Journal of Marine Energy*, 8, pp. 17-35.

DECC UK (2004) *Energy Act 2004*. Available at: https://www.gov.uk/government/uploads/system/uploads/attachment_data/file/490993/Energy_Act_2004__Energy_Bill_2015-16_Keeling_Schedule_.pdf (Accessed: 4th April 2017).

DECC UK (2013) *UK renewable energy roadmap: 2011*. Available at: https://www.gov.uk/government/publications/renewable-energy-roadmap (Accessed: 4th April 2017).

DIT UK (2014) *Marine energy in the UK: investments and opportunities*. Available at: https://www.gov.uk/government/publications/marine-energy-in-the-uk-investment-opportunities/marine-energy-in-the-uk-investment-opportunities (Accessed: 4th April 2017).

Doman, D.A., Murray, R.E., Pegg, M.J., Gracie, K., Johnstone, C.M. and Nevalainen, T. (2015) 'Tow-tank testing of a 1/20th scale horizontal axis tidal turbine with uncertainty analysis', *International Journal of Marine Energy*, 11, pp. 105-119.

DUKES (2015) *Chapter 6: Renewable sources of energy*. Available at: https://www.gov.uk/government/uploads/system/uploads/attachment_data/file/633782/Chapter_6.pdf (Accessed: 4th April 2017).

Edmunds, M., Williams, A.J., Masters, I. and Croft, T.N. (2017) 'An enhanced disk averaged CFD model for the simulation of horizontal axis tidal turbines', *Renewable Energy*, 101, pp. 67-81.

EIA (2017a) *International Energy Outlook 2016* (DOE/EIA-0484(2016)). U.S Energy Information Administration.

EIA (2017b) *Monthly renewable electricity generation surpasses nuclear for the first time since 1984*. Available at: https://www.eia.gov/todayinenergy/detail.php?id=31932 (Accessed: 18th August 2017).

El-Geziry, T.M. and Couch, S.J. (2009) 'Environmental impact assessment for tidal energy schemes: An exemplar case study of the Strait of Messina', *Proceedings of the Institute of Marine Engineering, Science and Technology Part A: Journal of Marine Engineering and Technology*, (13), pp. 39-48.

El Tawil, T., Charpentier, J.F. and Benbouzid, M. (2017) 'Tidal energy site characterization for marine turbine optimal installation: Case of the Ouessant Island in France', *International Journal of Marine Energy*, 18, pp. 57-64.

EMEC (2013) *European Marine Energy Centre*. Available at: http://www.emec.org.uk/marine-energy/tidal-devices/ (Accessed: 13th June 2016).

EMEC (2016) *Scotrenewables Tidal Power*. Available at: http://www.emec.org.uk/about-us/our-tidal-clients/scotrenewables/ (Accessed: 6th June 2017).

Environmental Agency (2011) *Tidal power developments: environmental impact assessment (EIA)*. Available at: https://www.gov.uk/government/publications/tidal-power-developments-environmental-impact-assessment-eia (Accessed: 1st August 2017).

Esteban, M. and Leary, D. (2012) 'Current developments and future prospects of offshore wind and ocean energy', *Applied Energy*, 90(1), pp. 128-136.

European Commision (1996) *The exploitation of tidal marine currents* (EUR16683EN). European Commission.

Fairley, I., Masters, I. and Karunarathna, H. (2015) 'The cumulative impact of tidal stream turbine arrays on sediment transport in the Pentland Firth', *Renewable Energy*, 80, pp. 755-769.

Fernandez-Rodriguez, E., Stallard, T.J. and Stansby, P.K. (2014) 'Experimental study of extreme thrust on a tidal stream rotor due to turbulent flow and with opposing waves', *Journal of Fluids and Structures*, 51, pp. 354-361.

Ferro, B.D. (2006) 'Wave and tidal energy', *Refocus*, 7(3), pp. 46-48.

Firenze, E. and Valdenazzi, F. (2015) 'A method to predict underwater noise from cavitating propellers', *MTS/IEEE OCEANS 2015 - Genova: Discovering Sustainable Ocean Energy for a New World*.

Frisk, G.V. (2012) 'Noiseonomics: The relationship between ambient noise levels in the sea and global economic trends', *Scientific Reports*, 2.

Galloway, P.W., Myers, L.E. and Bahaj, A.S. (2011) 'Experimental and numerical results of rotor power and thrust', *World Renewable Energy Congress 2011*. Linkoping, Sweden, 8th - 13th May 2011.

Garrett, C. and Cummins, P. (2007) 'The efficiency of a turbine in a tidal channel', *Journal of Fluid Mechanics*, 588, pp. 243-251.

Garrett, C. and Cummins, P. (2008) 'Limits to tidal current power', *Renewable Energy*, 33(11), pp. 2485-2490.

Gaurier, B., Davies, P., Deuff, A. and Germain, G. (2013) 'Flume tank characterization of marine current turbine blade behaviour under current and wave loading', *Renewable Energy*, 59, pp. 1-12.

Gebreslassie, M.G., Tabor, G.R. and Belmont, M.R. (2013) 'Numerical simulation of a new type of cross flow tidal turbine using OpenFOAM – Part I: Calibration of energy extraction', *Renewable Energy*, 50, pp. 994-1004.

Gross, R., Leach, M. and Bauen, A. (2003) 'Progress in renewable energy', *Environment International*, 29(1), pp. 105-122.

Guo, B., Wang, D. and Shi, W. (2015a) 'Power output performance characteristics of bidirectional tidal current turbine in a circulating water channel', *The 4th International*

Conference on Advance Model Measurement Technologies for the Maritme Industry. Istanbul, Turkey, 28-30 September 2015.

Guo, Q., Zhou, L. and Wang, Z. (2015b) 'Comparison of BEM-CFD and full rotor geometry simulations for the performance and flow field of a marine current turbine', *Renewable Energy*, 75, pp. 640-648.

Halvorsen, M.B., Carlson, T.J. and Copping, A.E. (2011) *Effects of Tidal Turbine Noise on Fish*. Pacific Northwest National Laboratory for U.S. Department of Energy.

Hammar, L., Gullström, M., Dahlgren, T.G., Asplund, M.E., Goncalves, I.B. and Molander, S. (2017) 'Introducing ocean energy industries to a busy marine environment', *Renewable and Sustainable Energy Reviews*, 74, pp. 178-185.

Hammerfest Strom (2013) *ANDRITZ HYDRO Hammerfest*. Available at: www.hammerfeststrom.com (Accessed: 6th November 2014).

Harvey, F. (2013) *Severn tidal power barrage plans slammed by MPs*. Available at: https://www.theguardian.com/business/2013/jun/10/severn-tidal-power-barrage-plans-mps (Accessed: 18th June 2017).

Hawkins, A., Hughes, D. and Cheesman, S. (2008) *Criteria and Metrics for Assessing the Effects of Underwater Sound on Fish and Invertebrates*. The SoundWaves Consortium.

Hildebrand, J.A. (2009) 'Anthropogenic and natural sources of ambient noise in the ocean', *Marine Ecology Progress Series*, 395, pp. 5-20.

Hooper, T. and Austen, M. (2013) 'Tidal barrages in the UK: Ecological and social impacts, potential mitigation, and tools to support barrage planning', *Renewable and Sustainable Energy Reviews*, 23, pp. 289-298.

IAEA (2015) *IAEA Annual Report 2015*. International Atomic Energy Agency Agency, I.A.E.

ITTC (1987) *18th Report of Cavitation Committee, Kobe, Japan*. International Towing Tank Conference.

Jing, F.-m., Ma, W.-j., Zhang, L., Wang, S.-q. and Wang, X.-h. (2017) 'Experimental study of hydrodynamic performance of full-scale horizontal axis tidal current turbine', *Journal of Hydrodynamics, Ser. B*, 29(1), pp. 109-117.

Jones, W.P. and Launder, B.E. (1972) 'The prediction of laminarization with a two-equation model of turbulence', *International Journal of Heat and Mass Transfer*, 15(2), pp. 301-314.

Kerr, D. (2005) 'Marine energy: Getting power from tides and waves', *Proceedings of the Institution of Civil Engineers: Civil Engineering*, 158(6), pp. 32-39.

Khan, M.J., Bhuyan, G., Iqbal, M.T. and Quaicoe, J.E. (2009) 'Hydrokinetic energy conversion systems and assessment of horizontal and vertical axis turbines for river and tidal applications: A technology status review', *Applied Energy*, 86(10), pp. 1823-1835.

Klann, S. (2017) *Analysts: Global cost of oil lowest since 2005*. Available at: https://www.epmag.com/analysts-global-cost-oil-lowest-2005-1596136 (Accessed: 5th June 2017).

Kolekar, N. and Banerjee, A. (2015) 'Performance characterization and placement of a marine hydrokinetic turbine in a tidal channel under boundary proximity and blockage effects', *Applied Energy*, 148, pp. 121-133.

Kuiper, G. (2012) *Cavitation in ship propulsion*. Available at: https://ocw.tudelft.nl/wp-content/uploads/Chapter_6.pdf (Accessed: 15th April 2017).

Lafeber, F.H., Bosschers, J. and Van Wijngaarden, E. (2015) 'Computational and experimental prediction of propeller cavitation noise', *MTS/IEEE OCEANS 2015 - Genova: Discovering Sustainable Ocean Energy for a New World*.

Lago, L.I., Ponta, F.L. and Chen, L. (2010) 'Advances and trends in hydrokinetic turbine systems', *Energy for Sustainable Development*, 14(4), pp. 287-296.

Lee, K., Lee, J., Kim, D., Kim, K. and Seong, W. (2014) 'Propeller sheet cavitation noise source modeling and inversion', *Journal of Sound and Vibration*, 333(5), pp. 1356-1368.

Leggat, L.J. and Sponagle, N.C. (1985) 'The Study of Propeller Cavitation Noise Using Cross-Correlation Methods', *Journal of Fluids Engineering*, 107(1), pp. 127-133.

Lewis, M., Neill, S.P., Robins, P.E. and Hashemi, M.R. (2015) 'Resource assessment for future generations of tidal-stream energy arrays', *Energy*, 82, pp. 403-415.

Lin, H. (2009) *Evaluating the Performance of an Innovative Marine Current Turbine based on "Wind Spinner" Concept*. MSc Dissertation thesis. Newcastle University.

Lloyd, T.P., Turnock, S.R. and Humphrey, V.F. (2011) 'Modelling techniques for underwater noise generated by tidal turbines in shallow waters', *Proceedings of the International Conference on Offshore Mechanics and Arctic Engineering - OMAE*. pp. 777-785.

Lloyd, T.P., Turnock, S.R. and Humphrey, V.F. (2013) 'Computation of inflow turbulence noise of a tidal turbine', *10th European Wave and Tidal Energy Conference*. Aalborg, Denmark.

Lloyd, T.P., Turnock, S.R. and Humphrey, V.F. (2014) 'Assessing the influence of inflow turbulence on noise and performance of a tidal turbine using large eddy simulations', *Renewable Energy*, 71, pp. 742-754.

Luznik, L., Flack, K.A., Lust, E.E. and Baxter, D.P. (2012) 'Hydrodynamic performance of a horizontal axis tidal turbine under steady flow conditions', *OCEANS 2012 MTS/IEEE Hampton Roads Conference: Harnessing the Power of the Ocean*. Virginia Beach, USA, 14th - 19th October 2012.

Luznik, L., Flack, K.A., Lust, E.E. and Taylor, K. (2013) 'The effect of surface waves on the performance characteristics of a model tidal turbine', *Renewable Energy*, 58, pp. 108-114.

Madsen, H.A., Mikkelsen, R., Øye, S., Bak, C. and Johansen, J. (2007) 'A Detailed investigation of the Blade Element Momentum (BEM) model based on analytical and numerical results and proposal for modifications of the BEM model', *Journal of Physics: Conference Series*, 75, p. 012016.

Madsen, P.T., Wahlberg, M., Tougaard, J., Lucke, K. and Tyack, P. (2006) 'Wind turbine underwater noise and marine mammals: Implications of current knowledge and data needs', *Marine Ecology Progress Series*, 309, pp. 279-295.

Maganga, F., Germain, G., King, J., Pinon, G. and Rivoalen, E. (2010) 'Experimental characterisation of flow effects on marine current turbine behaviour and on its wake properties', *IET Renewable Power Generation*, 4(6), pp. 498-509.

Malki, R., Williams, A.J., Croft, T.N., Togneri, M. and Masters, I. (2013) 'A coupled blade element momentum – Computational fluid dynamics model for evaluating tidal stream turbine performance', *Applied Mathematical Modelling*, 37(5), pp. 3006-3020.

Marine Current Turbines (2013) *SeaGen Tidal Technology*. Available at: http://www.marineturbines.com/Seagen-Technology (Accessed: 5th February 2017).

Mason-Jones, A., O'Doherty, D.M., Morris, C.E., O'Doherty, T., Byrne, C.B., Prickett, P.W., Grosvenor, R.I., Owen, I., Tedds, S. and Poole, R.J. (2012) 'Non-dimensional scaling of tidal stream turbines', *Energy*, 44(1), pp. 820-829.

Masters, I., Chapman, J.C., Willis, M.R. and Orme, J.A.C. (2011) 'A robust Blade Element Momentum Theory model for tidal stream turbines including tip and hub loss corrections', *Proceedings of the Institute of Marine Engineering, Science and Technology Part A: Journal of Marine Engineering and Technology*, 10(1), pp. 25-35.

Masters, I., Williams, A., Croft, T.N., Togneri, M., Edmunds, M., Zangiabadi, E., Fairley, I. and Karunarathna, H. (2015) 'A comparison of numerical modelling techniques for tidal stream turbine analysis', *Energies*, 8(8), pp. 7833-7853.

Menter, F.R. (1994) 'Two-equation eddy-viscosity turbulence models for engineering applications', *AIAA Journal*, 32(8), pp. 1598-1605.

Menter, F.R. (1996) 'A comparison of some recent eddy-viscosity turbulence models', *Journal of Fluids Engineering, Transactions of the ASME*, 118(3), pp. 514-519.

Mitson, R.B. and Knudsen, H.P. (2003) 'Causes and effects of underwater noise on fish abundance estimation', *Aquatic Living Resources*, 16(3), pp. 255-263.

Molland, A.F., Bahaj, A.S., Chaplin, J.R. and Batten, W.M.J. (2004) 'Measurements and predictions of forces, pressures and cavitation on 2-D sections suitable for marine current turbines', *Proceedings of the Institution of Mechanical Engineers, Part M: Journal of Engineering for the Maritime Environment*, 218(2), pp. 127-138.

Moriarty, P. and Honnery, D. (2011) 'Is there an optimum level for renewable energy?', *Energy Policy*, 39(5), pp. 2748-2753.

Moriarty, P. and Honnery, D. (2012) 'What is the global potential for renewable energy?', *Renewable and Sustainable Energy Reviews*, 16(1), pp. 244-252.

Myers, L. and Bahaj, A.S. (2005) 'Simulated electrical power potential harnessed by marine current turbine arrays in the Alderney Race', *Renewable Energy*, 30(11), pp. 1713-1731.

Myers, L. and Bahaj, A.S. (2006) 'Power output performance characteristics of a horizontal axis marine current turbine', *Renewable Energy*, 31(2), pp. 197-208.

Myers, L. and Bahaj, A.S. (2007) 'Wake studies of a 1/30th scale horizontal axis marine current turbine', *Ocean Engineering*, 34(5-6), pp. 758-762.

Myers, L.E. and Bahaj, A.S. (2012) 'An experimental investigation simulating flow effects in first generation marine current energy converter arrays', *Renewable Energy*, 37(1), pp. 28-36.

Ng, K.-W., Lam, W.-H. and Ng, K.-C. (2013) '2002–2012: 10 Years of Research Progress in Horizontal-Axis Marine Current Turbines', *Energies*, 6(3), pp. 1497-1526.

Nicoud, F. and Ducros, F. (1999) 'Subgrid-scale stress modelling based on the square of the velocity gradient tensor', *Flow, Turbulence and Combustion*, 62(3), pp. 183-200.

Noruzi, R., Vahidzadeh, M. and Riasi, A. (2015) 'Design, analysis and predicting hydrokinetic performance of a horizontal marine current axial turbine by consideration of turbine installation depth', *Ocean Engineering*, 108, pp. 789-798.

NPARC Alliance (2008) *NPARC Alliance CFD Verifications and Validation Website*. Available at: https://www.grc.nasa.gov/WWW/wind/valid/tutorial/overview.html (Accessed: 28th November 2017).

O'Doherty, T., Mason-Jones, A., O'Doherty, D.M., Evans, P.S., Wooldridge, C.F. and Fryett, I. (2010) 'Considerations of a horizontal axis tidal turbine', *Proceedings of Institution of Civil Engineers: Energy*, 163(3), pp. 119-130.

O Rourke, F., Boyle, F. and Reynolds, A. (2010) 'Tidal energy update 2009', *Applied Energy*, 87(2), pp. 398-409.

O'Sullivan, D., Bard, J., Kracht, P., Ceballos, S. and Robles, E. (2013) 'Electrical generators in ocean energy converters', in *Electrical Design for Ocean Wave and Tidal Energy Systems*. London, United Kingdom: The Institution of Engineering and Technology, pp. 3-41.

Ocean Flow Energy (2013) *Evopod*. Available at: www.oceanflowenergy.com (Accessed: 8th July 2015).

Olczak, A., Stallard, T., Feng, T. and Stansby, P.K. (2016) 'Comparison of a RANS blade element model for tidal turbine arrays with laboratory scale measurements of wake velocity and rotor thrust', *Journal of Fluids and Structures*, 64, pp. 87-106.

OpenHydro (2016) *OpenHydro*. Available at: http://www.openhydro.com/ (Accessed: 6th June 2017).

Ossai, C.I., Boswell, B. and Davies, I.J. (2014) 'Sustainable asset integrity management: Strategic imperatives for economic renewable energy generation', *Renewable Energy*, 67, pp. 143-152.

Pelc, R. and Fujita, R.M. (2002) 'Renewable energy from the ocean', *Marine Policy*, 26(6), pp. 471-479.

Pennings, P., Westerweel, J. and van Terwisga, T. (2015) 'Sound signature of propeller tip vortex cavitation', *Journal of Physics: Conference Series*, 656, p. 012186.

Pinon, G., Mycek, P., Germain, G. and Rivoalen, E. (2012) 'Numerical simulation of the wake of marine current turbines with a particle method', *Renewable Energy*, 46, pp. 111-126.

REN21 (2017a) *Advancing the global renewable energy transition*. Renewable Energy Policy Network for the 21st Century Century, R.E.P.N.f.t.s.

REN21 (2017b) *Renewables 2017 Global Status Report*. Renewable Energy Policy Network for the 21st Century Century, R.E.P.N.f.t.s.

Reuters (2016) *US oil falls on unexpectedly large inventory build*. Available at: http://www.cnbc.com/2016/01/19/oil-prices-fall-further-on-glut-worries-us-crude-slumps-below-28.html (Accessed: 17th January 2017).

Richardson, W.J., Greene, C.R., Jr., Malme, C.I. and Thomson, D.H. (2013) *Marine Mammals and Noise*. USA: Academic Press Ltd.

Roache, P.J. (2003) 'Conservatism of the grid convergence index in finite volume computations on steady-state fluid flow and heat transfer', *Journal of Fluids Engineering, Transactions of the ASME*, 125(4), pp. 731-732.

Rogner, H.-H. (2013) 'World outlook for nuclear power', *Energy Strategy Reviews*, 1(4), pp. 291-295.

Rosli, R., Norman, R. and Atlar, M. (2016) 'Experimental investigations of the Hydro-Spinna turbine performance', *Renewable Energy*, 99, pp. 1227-1234.

Rosli, R., Shi, W., Norman, R. and Atlar, M. (2015) 'Cavitation tunnel investigation on the performance, cavitation and noise generation of marine current turbine: Hydro-Spinna', *The 4th International Conference on Advance Model Measurement Technologies for the Maritme Industry*. Istanbul, Turkey, 28-30 September 2015.

Ross, D. (1976) *Mechanics of Underwater Noise*. California,USA: Peninsula Publishing.

Rumsey, C.L. and Spalart, P.R. (2009) 'Turbulence model behavior in low reynolds number regions of aerodynamic flowfields', *AIAA Journal*, 47(4), pp. 982-993.

Sangiuliano, S.J. (2017) 'Turning of the tides: Assessing the international implementation of tidal current turbines', *Renewable and Sustainable Energy Reviews*, 80, pp. 971-989.

Saruwatari, A., Ingram, D.M. and Cradden, L. (2013) 'Wave–current interaction effects on marine energy converters', *Ocean Engineering*, 73, pp. 106-118.

Schluntz, J. and Willden, R.H.J. (2015) 'The effect of blockage on tidal turbine rotor design and performance', *Renewable Energy*, 81, pp. 432-441.

ScotRenewables (2017) *SR 2000*. Available at: http://www.scotrenewables.com/ (Accessed: 6th June 2017).

Scottish Marine Renewables SEA (2007a) *Strategic Environmental Assessment, Chapter 1 - Bathymetry*. Available at: http://www.gov.scot/Resource/Doc/1086/0048535.pdf (Accessed: 13th June 2017).

Scottish Marine Renewables SEA (2007b) *Strategic Environmental Assessment, Chapter 6 - Benthic Ecology*. Available at: http://www.gov.scot/Resource/Doc/1086/0048548.pdf (Accessed: 13th June 2017).

Seol, H., Jung, B., Suh, J.C. and Lee, S. (2002) 'Prediction of non-cavitating underwater propeller noise', *Journal of Sound and Vibration*, 257(1), pp. 131-156.

Seol, H., Park, C., Kim, G.D. and Ha Park, Y. (2012) 'A numerical study and model scale measurement of large commercial vessel's propeller noise', *41st International Congress and Exposition on Noise Control Engineering 2012*. pp. 3318-3326.

Seol, H., Pyo, S., Suh, J.C. and Lee, S. (2004) 'Numerical study of non-cavitating underwater propeller noise', *Noise and Vibration Worldwide*, 35(6), pp. 11-26.

Seol, H., Suh, J.C. and Lee, S. (2005) 'Development of hybrid method for the prediction of underwater propeller noise', *Journal of Sound and Vibration*, 288(1-2), pp. 345-360.

Sharma, S.D., Mani, K. and Arakeri, V.H. (1990) 'Cavitation noise studies on marine propellers', *Journal of Sound and Vibration*, 138(2), pp. 255-283.

Shi, W., Atlar, M., Norman, R., Aktas, B. and Turkmen, S. (2016a) 'Numerical optimization and experimental validation for a tidal turbine blade with leading-edge tubercles', *Renewable Energy*, 96, pp. 42-55.

Shi, W., Atlar, M., Rosli, R., Aktas, B. and Norman, R. (2016b) 'Cavitation observations and noise measurements of horizontal axis tidal turbines with biomimetic blade leading-edge designs', *Ocean Engineering*, 121, pp. 143-155.

Shi, W., Rosli, R., Atlar, M., Norman, R., Wang, D. and Yang, W. (2016c) 'Hydrodynamic performance evaluation of a tidal turbine with leading-edge tubercles', *Ocean Engineering*, 117, pp. 246-253.

Shi, W., Wang, D., Atlar, M. and Seo, K.C. (2013) 'Flow separation impacts on the hydrodynamic performance analysis of a marine current turbine using CFD', *Proceedings of the Institution of Mechanical Engineers, Part A: Journal of Power and Energy*, 227(8), pp. 833-846.

Silva, P.A.S.F., Shinomiya, L.D., de Oliveira, T.F., Vaz, J.R.P., Amarante Mesquita, A.L. and Brasil Junior, A.C.P. (2016) 'Analysis of cavitation for the optimized design of hydrokinetic turbines using BEM', *Applied Energy*, 185, pp. 1281-1291.

SONIC (2012) 'Suppression Of underwater Noise Induced by Cavitation. In European Union Framework programme 7. FP7-SST-2012-RTD-1- SST.2012.1.1-1. - Assessment and mitigation of noise impacts of the maritime transport on the marine environment (coordinated topic within the framework of the "Ocean of Tomorrow")'.

Spiga, I. (2016) 'Acoustic response to playback of pile-driving sounds by snapping shrimp', in *Advances in Experimental Medicine and Biology*. Springer International Publishing, pp. 1081-1088.

Spiga, I., Cheesman, S., Hawkins, A., Perez-Dominguez, R., Roberts, L., Hughes, D., Elliott, M., Nedwell, J. and Bentley, M. (2012) *Understanding the Scale and Impacts of Anthropogenic Noise upon Fish and Invertebrates in the Marine Environment.* SoundWaves Consortium Technical Review (ME5205).

Spratt, D. (2010) *The case for sustainability emergency*. Available at: http://www.climatecodered.org/2010/09/what-would-3-degrees-mean.html (Accessed: 25th June 2017).

Stallard, T., Collings, R., Feng, T. and Whelan, J. (2013) 'Interactions between tidal turbine wakes: experimental study of a group of three-bladed rotors', *Philos Trans A Math Phys Eng Sci*, 371(1985), p. 20120159.

Sun, H. and Kyozuka, Y. (2012) 'Analysis of performances of a shrouded horizontal axis tidal turbine', *Program Book - OCEANS 2012 MTS/IEEE Yeosu: The Living Ocean and Coast - Diversity of Resources and Sustainable Activities*.

Tani, G., Aktas, B., Viviani, M. and Atlar, M. (2017) 'Two medium size cavitation tunnel hydro-acoustic benchmark experiment comparisons as part of a round robin test campaign', *Ocean Engineering*, 138, pp. 179-207.

Teske, S., Pregger, T., Simon, S., Naegler, T., Graus, W. and Lins, C. (2010) 'Energy [R]evolution 2010—a sustainable world energy outlook', *Energy Efficiency*, 4(3), pp. 409-433.

Thiébot, J., Guillou, S. and Nguyen, V.T. (2016) 'Modelling the effect of large arrays of tidal turbines with depth-averaged Actuator Disks', *Ocean Engineering*, 126, pp. 265-275.

Thomsen, F., Mueller-Blenkle, C., Gill, A., Metcalfe, J., McGregor, P.K., Bendall, V., Andersson, M.H., Sigray, P. and Wood, D. (2012) 'Effects of pile driving on the behavior of cod and sole', *Advances in experimental medicine and biology*, 730, pp. 387-388.

Tidal Energy Ltd (2013) *Delta Stream Turbine*. Available at: www.tidalenergyltd.com (Accessed: 15 May 2017).

Tidal Energy Today (2015) *Estimate of global potential tidal resources*. Available at: http://tidalenergytoday.com/2015/02/17/estimate-of-global-potential-tidal-resources/ (Accessed: 17th August 12016).

Tidal Lagoon Power (2017) *Swansea bay tidal project*. Available at: http://www.tidallagoonpower.com/projects/swansea-bay/key-statistics/ (Accessed: 1st June 2017).

Turnock, S.R., Phillips, A.B., Banks, J. and Nicholls-Lee, R. (2011) 'Modelling tidal current turbine wakes using a coupled RANS-BEMT approach as a tool for analysing power capture of arrays of turbines', *Ocean Engineering*, 38(11-12), pp. 1300-1307.

United Nations (2016) *Framework Convention on Climate Change*. Available at: http://unfccc.int/files/essential_background/convention/application/pdf/english_paris_agreement.pdf (Accessed: 15th July 2017).

United Nations (2017) *Climate Change*. Available at: http://www.un.org/en/sections/issues-depth/climate-change/index.html (Accessed: 19th January 2017).

Vennell, R. (2012a) 'The energetics of large tidal turbine arrays', *Renewable Energy*, 48, pp. 210-219.

Vennell, R. (2012b) 'Realizing the potential of tidal currents and the efficiency of turbine farms in a channel', *Renewable Energy*, 47, pp. 95-102.

Vennell, R. (2013) 'Exceeding the Betz limit with tidal turbines', *Renewable Energy*, 55, pp. 277-285.

Versteeg, H.K. and Malalasekera, W. (2007) *An introduction to Computational Fluid Dynamics*. 2 edn. England: Pearson Education Limited.

Walker, J.M., Flack, K.A., Lust, E.E., Schultz, M.P. and Luznik, L. (2014) 'Experimental and numerical studies of blade roughness and fouling on marine current turbine performance', *Renewable Energy*, 66, pp. 257-267.

Walsh, J., Bashir, I., Thies, P.R., Johanning, L. and Blondel, P. (2015) 'Acoustic emission health monitoring of marine renewables: Illustration with a wave energy converter in Falmouth Bay (UK)', *MTS/IEEE OCEANS 2015 - Genova: Discovering Sustainable Ocean Energy for a New World*.

Wang, D., Atlar, M. and Paterson, I. (2004) *Performance Tests of the Second Tidal Stream Rotor* (MT-2004-027). Newcastle University.

Wang, D., Atlar, M. and Sampson, R. (2007) 'An experimental investigation on cavitation, noise, and slipstream characteristics of ocean stream turbines', *Proceedings of the Institution of Mechanical Engineers, Part A: Journal of Power and Energy*, 221(2), pp. 219-231.

Waters, S. and Aggidis, G. (2016) 'A world first: Swansea Bay tidal lagoon in review', *Renewable and Sustainable Energy Reviews*, 56, pp. 916-921.

Wen, Y. (2011) *Optimisation and Experimental Validation of a Novel Marine Turbine Device*. MSc Dissertation thesis. Newcastle University.

Wenz, G.M. (1972) 'Review of Underwater Acoustics Research: Noise', *Journal of the Acoustical Society of America*, 51(3B), pp. 1010-1024.

Westwood, A. (2007) 'Wave and tidal – project review', *Renewable Energy Focus*, 8(4), pp. 30-33.

Whelan, J.I., Graham, J.M.R. and PeirÓ, J. (2009) 'A free-surface and blockage correction for tidal turbines', *Journal of Fluid Mechanics*, 624, pp. 281-291.

Wilcox, D.C. (2008) 'Formulation of the k-ω turbulence model revisited', *AIAA Journal*, 46(11), pp. 2823-2838.

Williams, R., Wright, A.J., Ashe, E., Blight, L.K., Bruintjes, R., Canessa, R., Clark, C.W., Cullis-Suzuki, S., Dakin, D.T., Erbe, C., Hammond, P.S., Merchant, N.D., O'Hara, P.D., Purser, J., Radford, A.N., Simpson, S.D., Thomas, L. and Wale, M.A. (2015) 'Impacts of anthropogenic noise on marine life: Publication patterns, new discoveries, and future directions in research and management', *Ocean & Coastal Management*, 115, pp. 17-24.

Yamada, T., Sato, K., Kawakita, C. and Oshima, A. (2015) 'Study on Prediction of Underwater Radiated Noise from Propeller Tip Vortex Cavitation', *Journal of Physics: Conference Series* 656(1).

Young, J., Lai, J.C.S. and Platzer, M.F. (2014) 'A review of progress and challenges in flapping foil power generation', *Progress in Aerospace Sciences*, 67, pp. 2-28.

Zhang, F., Dai, C.N., Xu, X.F., Wang, C.K. and Ye, Q. (2017) 'Resource Assessment of Tidal Current Energy in Hangzhou Bay Based on Long Term Measurement', *IOP Conference Series: Earth and Environmental Science.*

Zhou, M. (2013) *World energy consumption to increase 56% by 2040 led by Asia*. Available at: http://www.bloomberg.com/news/articles/2013-07-25/world-to-use-56-more-energy-by-2040-led-by-asia-eia-predicts (Accessed: 13th June 2016).

Zhou, Z., Benbouzid, M., Charpentier, J.-F., Scuiller, F. and Tang, T. (2017) 'Developments in large marine current turbine technologies – A review', *Renewable and Sustainable Energy Reviews*, 71, pp. 852-858.

Appendix A: HS280 Blade Specifications

r/R	C/R	Beta	Leading edge			Trailing edge		
			x/R	y/R	z/R	x/R	y/R	z/R
0.1000	0.2007	57.86	0.1024	0.0800	0.0600	0.2724	-0.0140	0.0990
0.1155	0.2045	54.04	0.1104	0.0888	0.0738	0.2758	-0.0187	0.1140
0.1319	0.2095	50.35	0.1183	0.0971	0.0893	0.2796	-0.0244	0.1297
0.1493	0.2156	46.84	0.1263	0.1047	0.1064	0.2835	-0.0312	0.1460
0.1675	0.2228	43.54	0.1342	0.1114	0.1251	0.2877	-0.0393	0.1628
0.1866	0.2310	40.47	0.1422	0.1170	0.1454	0.2921	-0.0487	0.1801
0.2064	0.2400	37.63	0.1501	0.1212	0.1671	0.2967	-0.0597	0.1976
0.2270	0.2498	35.04	0.1581	0.1239	0.1902	0.3015	-0.0721	0.2152
0.2483	0.2603	32.66	0.1660	0.1250	0.2145	0.3065	-0.0863	0.2328
0.2702	0.2714	30.51	0.1740	0.1242	0.2399	0.3117	-0.1022	0.2501
0.2926	0.2831	28.54	0.1819	0.1212	0.2663	0.3172	-0.1199	0.2669
0.3156	0.2953	26.76	0.1899	0.1164	0.2934	0.3228	-0.1394	0.2831
0.3390	0.3080	25.15	0.1978	0.1091	0.3210	0.3287	-0.1609	0.2984
0.3629	0.3212	23.68	0.2058	0.0995	0.3490	0.3348	-0.1844	0.3126
0.3871	0.3350	22.35	0.2137	0.0874	0.3771	0.3411	-0.2098	0.3253
0.4115	0.3494	21.14	0.2217	0.0728	0.4050	0.3477	-0.2371	0.3364
0.4362	0.3645	20.05	0.2296	0.0556	0.0556	0.3546	-0.2664	0.3454
0.4611	0.3803	19.05	0.2376	0.0359	0.4597	0.3617	-0.2976	0.3521
0.4860	0.3970	18.13	0.2455	0.0136	0.4858	0.3691	-0.3307	0.3562
0.5110	0.4149	17.30	0.2535	-0.0112	0.5109	0.3769	-0.3656	0.3570
0.5359	0.4342	16.54	0.2614	-0.0385	0.5346	0.3850	-0.4021	0.3543
0.5608	0.4553	15.85	0.2694	-0.0682	0.5566	0.3937	-0.4403	0.3473
0.5855	0.4788	15.21	0.2774	-0.1001	0.5769	0.4029	-0.4800	0.3354
0.6100	0.5055	14.62	0.2853	-0.1342	0.5951	0.4129	-0.5210	0.3174
0.6342	0.5369	14.09	0.2933	-0.1703	0.6109	0.4239	-0.5631	0.2917
0.6581	0.5754	13.60	0.3012	-0.2081	0.6243	0.4365	-0.6064	0.2558
0.6816	0.6267	13.14	0.3092	-0.2476	0.6351	0.4517	-0.6504	0.2038
0.7046	0.7113	12.73	0.3171	-0.2884	0.6429	0.4738	-0.6951	0.1154
0.7143	0.8254	12.56	0.3205	-0.3061	0.6454	0.5000	-0.7143	0.0000
0.7424	0.8084	12.10	0.3305	-0.3599	0.6493	0.5000		
0.7705	0.7861	11.67	0.3410	-0.4168	0.6480	0.5000		
0.7911	0.7661	11.38	0.3489	-0.4607	0.6432	0.5000		
0.8111	0.7433	11.10	0.3569	-0.5046	0.6350	0.5000		
0.8302	0.7180	10.85	0.3648	-0.5483	0.6234	0.5000		
0.8486	0.6902	10.62	0.3728	-0.5916	0.6084	0.5000		
0.8660	0.6599	10.41	0.3807	-0.6340	0.5900	0.5000		

0.8826	0.6273	10.22	0.3887	-0.6753	0.5682	0.5000
0.8982	0.5925	10.05	0.3966	-0.7153	0.5432	0.5000
0.9128	0.5555	9.89	0.4046	-0.7536	0.5151	0.5000
0.9264	0.5166	9.75	0.4125	-0.7900	0.4839	0.5000
0.9389	0.4758	9.62	0.4205	-0.8241	0.4498	0.5000
0.9503	0.4333	9.51	0.4284	-0.8558	0.4131	0.5000
0.9606	0.3892	9.41	0.4364	-0.8849	0.3738	0.5000
0.9697	0.3437	9.32	0.4443	-0.9110	0.3323	0.5000
0.9777	0.2969	9.25	0.4523	-0.9341	0.2887	0.5000
0.9845	0.2491	9.18	0.4602	-0.9539	0.2434	0.5000
0.9900	0.2004	9.13	0.4682	-0.9703	0.1965	0.5000
0.9944	0.1509	9.09	0.4761	-0.9832	0.1485	0.5000
0.9975	0.1009	9.07	0.4841	-0.9925	0.0995	0.5000
0.9994	0.0506	9.05	0.4920	-0.9981	0.0499	0.5000
1.0000	0.0000	9.05	0.5000	-1.0000	0.0000	0.5000

Appendix B: HS500 (P/D = 0.43) Blade Specifications

r/R	C/R	Beta	Leading edge			Trailing edge		
			x/R	y/R	z/R	x/R	y/R	z/R
0.0200	0.2740	50.82	0.0192	0.0056	0.0628	-0.1540	0.0037	0.2752
0.0352	0.2180	35.38	0.0328	0.0128	0.0516	-0.1448	0.0088	0.1776
0.0620	0.2208	33.06	0.0540	0.0296	0.0688	-0.1304	0.0200	0.1892
0.0956	0.2248	30.67	0.0772	0.0560	0.0860	-0.1152	0.0376	0.2008
0.1356	0.2296	28.34	0.0988	0.0928	0.1032	-0.1008	0.0620	0.2120
0.1812	0.2344	26.13	0.1156	0.1396	0.1204	-0.0896	0.0932	0.2236
0.2320	0.2388	24.08	0.1244	0.1960	0.1376	-0.0836	0.1308	0.2352
0.2872	0.2428	22.20	0.1224	0.2596	0.1548	-0.0852	0.1732	0.2464
0.3456	0.2456	20.50	0.1068	0.3284	0.1720	-0.0956	0.2192	0.2580
0.4064	0.2472	18.96	0.0760	0.3992	0.1892	-0.1160	0.2660	0.2696
0.4684	0.2468	17.56	0.0296	0.4676	0.2064	-0.1472	0.3116	0.2808
0.5312	0.2452	16.29	-0.0332	0.5304	0.2236	-0.1888	0.3536	0.2924
0.5936	0.2420	15.11	-0.1112	0.5832	0.2408	-0.2408	0.3888	0.3040
0.6544	0.2372	14.00	-0.2024	0.6224	0.2580	-0.3016	0.4148	0.3152
0.7128	0.2308	12.93	-0.3036	0.6452	0.2752	-0.3692	0.4300	0.3268
0.7680	0.2228	11.87	-0.4116	0.6484	0.2924	-0.4408	0.4324	0.3384
0.8188	0.2140	10.80	-0.5220	0.6308	0.3096	-0.5144	0.4204	0.3496
0.8644	0.2048	9.67	-0.6300	0.5916	0.3268	-0.5868	0.3944	0.3612
0.9044	0.1956	8.43	-0.7316	0.5316	0.3440	-0.6544	0.3544	0.3728
0.9380	0.1864	7.07	-0.8220	0.4520	0.3612	-0.7148	0.3012	0.3840
0.9648	0.1784	5.53	-0.8972	0.3552	0.3784	-0.7648	0.2368	0.3956
0.9844	0.1720	3.82	-0.9532	0.2448	0.3956	-0.8024	0.1632	0.4072
0.9960	0.1680	1.95	-0.9880	0.1248	0.4128	-0.8256	0.0832	0.4184
1.0000	0.1668	0.00	-1.0000	0.0000	0.4300	-0.8332	0.0000	0.4300
-0.9960	0.1680	-1.95	-0.9880	-0.1248	0.4472	-0.8256	-0.0832	0.4416
-0.9844	0.1720	-3.82	-0.9532	-0.2448	0.4644	-0.8024	-0.1632	0.4528
-0.9648	0.1784	-5.53	-0.8972	-0.3552	0.4816	-0.7648	-0.2368	0.4644
-0.9380	0.1864	-7.07	-0.8220	-0.4520	0.4988	-0.7148	-0.3012	0.4760
-0.9044	0.1956	-8.43	-0.7316	-0.5316	0.5160	-0.6544	-0.3544	0.4872
-0.8644	0.2048	-9.67	-0.6300	-0.5916	0.5332	-0.5868	-0.3944	0.4988
-0.8188	0.2140	-10.80	-0.5220	-0.6308	0.5504	-0.5144	-0.4204	0.5104
-0.7680	0.2228	-11.87	-0.4116	-0.6484	0.5676	-0.4408	-0.4324	0.5216
-0.7128	0.2308	-12.93	-0.3036	-0.6452	0.5848	-0.3692	-0.4300	0.5332
-0.6544	0.2372	-14.00	-0.2024	-0.6224	0.6020	-0.3016	-0.4148	0.5448
-0.5936	0.2420	-15.11	-0.1112	-0.5832	0.6192	-0.2408	-0.3888	0.5560
-0.5312	0.2452	-16.29	-0.0332	-0.5304	0.6364	-0.1888	-0.3536	0.5676

-0.4684	0.2468	-17.56	0.0296	-0.4676	0.6536	-0.1472	-0.3116	0.5792
-0.4064	0.2472	-18.96	0.0760	-0.3992	0.6708	-0.1160	-0.2660	0.5904
-0.3456	0.2456	-20.50	0.1068	-0.3284	0.6880	-0.0956	-0.2192	0.6020
-0.2872	0.2428	-22.20	0.1224	-0.2596	0.7052	-0.0852	-0.1732	0.6136
-0.2320	0.2388	-24.08	0.1244	-0.1960	0.7224	-0.0836	-0.1308	0.6248
-0.1812	0.2344	-26.13	0.1156	-0.1396	0.7396	-0.0896	-0.0932	0.6364
-0.1356	0.2296	-28.34	0.0988	-0.0928	0.7568	-0.1008	-0.0620	0.6480
-0.0956	0.2248	-30.67	0.0772	-0.0560	0.7740	-0.1152	-0.0376	0.6592
-0.0620	0.2208	-33.06	0.0540	-0.0296	0.7912	-0.1304	-0.0200	0.6708
-0.0352	0.2180	-35.38	0.0328	-0.0128	0.8084	-0.1448	-0.0088	0.6824
-0.0200	0.2740	-50.82	0.0192	-0.0056	1.3368	-0.1540	-0.0037	1.1248

Appendix C: HS500 (*P/D* = 0.7) Blade Specifications

r/R	C/R	Beta	Leading edge			Trailing edge		
			x/R	y/R	z/R	x/R	y/R	z/R
0.0200	0.3492	60.30	0.0192	0.0056	0.0900	-0.1540	0.0037	0.3932
0.0352	0.3428	58.81	0.0328	0.0128	0.1200	-0.1448	0.0088	0.4132
0.0620	0.3356	56.55	0.0540	0.0296	0.1600	-0.1304	0.0200	0.4400
0.0956	0.3292	54.06	0.0772	0.0560	0.2000	-0.1152	0.0376	0.4668
0.1356	0.3240	51.44	0.0988	0.0928	0.2400	-0.1008	0.0620	0.4932
0.1812	0.3192	48.76	0.1156	0.1396	0.2800	-0.0896	0.0932	0.5200
0.2320	0.3144	46.10	0.1244	0.1960	0.3200	-0.0836	0.1308	0.5468
0.2872	0.3100	43.51	0.1224	0.2596	0.3600	-0.0852	0.1732	0.5732
0.3456	0.3048	41.01	0.1068	0.3284	0.4000	-0.0956	0.2192	0.6000
0.4064	0.2992	38.63	0.0760	0.3992	0.4400	-0.1160	0.2660	0.6268
0.4684	0.2924	36.36	0.0296	0.4676	0.4800	-0.1472	0.3116	0.6532
0.5312	0.2848	34.20	-0.0332	0.5304	0.5200	-0.1888	0.3536	0.6800
0.5936	0.2760	32.12	-0.1112	0.5832	0.5600	-0.2408	0.3888	0.7068
0.6544	0.2660	30.10	-0.2024	0.6224	0.6000	-0.3016	0.4148	0.7332
0.7128	0.2548	28.10	-0.3036	0.6452	0.6400	-0.3692	0.4300	0.7600
0.7680	0.2428	26.06	-0.4116	0.6484	0.6800	-0.4408	0.4324	0.7868
0.8188	0.2300	23.92	-0.5220	0.6308	0.7200	-0.5144	0.4204	0.8132
0.8644	0.2172	21.61	-0.6300	0.5916	0.7600	-0.5868	0.3944	0.8400
0.9044	0.2044	19.03	-0.7316	0.5316	0.8000	-0.6544	0.3544	0.8668
0.9380	0.1924	16.08	-0.8220	0.4520	0.8400	-0.7148	0.3012	0.8932
0.9648	0.1820	12.69	-0.8972	0.3552	0.8800	-0.7648	0.2368	0.9200
0.9844	0.1736	8.83	-0.9532	0.2448	0.9200	-0.8024	0.1632	0.9468
0.9960	0.1684	4.54	-0.9880	0.1248	0.9600	-0.8256	0.0832	0.9732
1.0000	0.1668	0.00	-1.0000	0.0000	1.0000	-0.8332	0.0000	1.0000
-0.9960	0.1684	-4.54	-0.9880	-0.1248	1.0400	-0.8256	-0.0832	1.0268
-0.9844	0.1736	-8.83	-0.9532	-0.2448	1.0800	-0.8024	-0.1632	1.0532
-0.9648	0.1820	-12.69	-0.8972	-0.3552	1.1200	-0.7648	-0.2368	1.0800
-0.9380	0.1924	-16.08	-0.8220	-0.4520	1.1600	-0.7148	-0.3012	1.1068
-0.9044	0.2044	-19.03	-0.7316	-0.5316	1.2000	-0.6544	-0.3544	1.1332
-0.8644	0.2172	-21.61	-0.6300	-0.5916	1.2400	-0.5868	-0.3944	1.1600
-0.8188	0.2300	-23.92	-0.5220	-0.6308	1.2800	-0.5144	-0.4204	1.1868
-0.7680	0.2428	-26.06	-0.4116	-0.6484	1.3200	-0.4408	-0.4324	1.2132
-0.7128	0.2548	-28.10	-0.3036	-0.6452	1.3600	-0.3692	-0.4300	1.2400
-0.6544	0.2660	-30.10	-0.2024	-0.6224	1.4000	-0.3016	-0.4148	1.2668

-0.5936	0.2760	-32.12	-0.1112	-0.5832	1.4400	-0.2408	-0.3888	1.2932
-0.5312	0.2848	-34.20	-0.0332	-0.5304	1.4800	-0.1888	-0.3536	1.3200
-0.4684	0.2924	-36.36	0.0296	-0.4676	1.5200	-0.1472	-0.3116	1.3468
-0.4064	0.2992	-38.63	0.0760	-0.3992	1.5600	-0.1160	-0.2660	1.3732
-0.3456	0.3048	-41.01	0.1068	-0.3284	1.6000	-0.0956	-0.2192	1.4000
-0.2872	0.3100	-43.51	0.1224	-0.2596	1.6400	-0.0852	-0.1732	1.4268
-0.2320	0.3144	-46.10	0.1244	-0.1960	1.6800	-0.0836	-0.1308	1.4532
-0.1812	0.3192	-48.76	0.1156	-0.1396	1.7200	-0.0896	-0.0932	1.4800
-0.1356	0.3240	-51.44	0.0988	-0.0928	1.7600	-0.1008	-0.0620	1.5068
-0.0956	0.3292	-54.06	0.0772	-0.0560	1.8000	-0.1152	-0.0376	1.5332
-0.0620	0.3356	-56.55	0.0540	-0.0296	1.8400	-0.1304	-0.0200	1.5600
-0.0352	0.3428	-58.81	0.0328	-0.0128	1.8800	-0.1448	-0.0088	1.5868
-0.0200	0.3492	-60.30	0.0192	-0.0056	1.9100	-0.1540	-0.0037	1.6068

Appendix D: HS500 (*P/D* = 1.0) Blade Specifications

r/R	C/R	Beta	Leading edge			Trailing edge		
			x/R	y/R	z/R	x/R	y/R	z/R
0.0200	0.4640	68.11	0.0192	0.0056	0.1276	-0.1540	0.0037	0.5584
0.0352	0.4528	66.91	0.0328	0.0128	0.1704	-0.1448	0.0088	0.5868
0.0620	0.4384	65.05	0.0540	0.0296	0.2272	-0.1304	0.0200	0.6248
0.0956	0.4252	62.95	0.0772	0.0560	0.2840	-0.1152	0.0376	0.6628
0.1356	0.4124	60.69	0.0988	0.0928	0.3408	-0.1008	0.0620	0.7004
0.1812	0.4004	58.31	0.1156	0.1396	0.3976	-0.0896	0.0932	0.7384
0.2320	0.3888	55.87	0.1244	0.1960	0.4544	-0.0836	0.1308	0.7764
0.2872	0.3772	53.43	0.1224	0.2596	0.5112	-0.0852	0.1732	0.8140
0.3456	0.3656	51.00	0.1068	0.3284	0.5680	-0.0956	0.2192	0.8520
0.4064	0.3532	48.61	0.0760	0.3992	0.6248	-0.1160	0.2660	0.8900
0.4684	0.3408	46.27	0.0296	0.4676	0.6816	-0.1472	0.3116	0.9276
0.5312	0.3272	43.98	-0.0332	0.5304	0.7384	-0.1888	0.3536	0.9656
0.5936	0.3128	41.72	-0.1112	0.5832	0.7952	-0.2408	0.3888	1.0036
0.6544	0.2980	39.46	-0.2024	0.6224	0.8520	-0.3016	0.4148	1.0412
0.7128	0.2820	37.17	-0.3036	0.6452	0.9088	-0.3692	0.4300	1.0792
0.7680	0.2656	34.78	-0.4116	0.6484	0.9656	-0.4408	0.4324	1.1172
0.8188	0.2488	32.21	-0.5220	0.6308	1.0224	-0.5144	0.4204	1.1548
0.8644	0.2316	29.36	-0.6300	0.5916	1.0792	-0.5868	0.3944	1.1928
0.9044	0.2152	26.09	-0.7316	0.5316	1.1360	-0.6544	0.3544	1.2308
0.9380	0.2000	22.26	-0.8220	0.4520	1.1928	-0.7148	0.3012	1.2684
0.9648	0.1864	17.74	-0.8972	0.3552	1.2496	-0.7648	0.2368	1.3064
0.9844	0.1760	12.43	-0.9532	0.2448	1.3064	-0.8024	0.1632	1.3444
0.9960	0.1692	6.43	-0.9880	0.1248	1.3632	-0.8256	0.0832	1.3820
1.0000	0.1668	0.00	-1.0000	0.0000	1.4200	-0.8332	0.0000	1.4200
-0.9960	0.1692	-6.43	-0.9880	-0.1248	1.4768	-0.8256	-0.0832	1.4580
-0.9844	0.1760	-12.43	-0.9532	-0.2448	1.5336	-0.8024	-0.1632	1.4956
-0.9648	0.1864	-17.74	-0.8972	-0.3552	1.5904	-0.7648	-0.2368	1.5336
-0.9380	0.2000	-22.26	-0.8220	-0.4520	1.6472	-0.7148	-0.3012	1.5716
-0.9044	0.2152	-26.09	-0.7316	-0.5316	1.7040	-0.6544	-0.3544	1.6092
-0.8644	0.2316	-29.36	-0.6300	-0.5916	1.7608	-0.5868	-0.3944	1.6472
-0.8188	0.2488	-32.21	-0.5220	-0.6308	1.8176	-0.5144	-0.4204	1.6848
-0.7680	0.2656	-34.78	-0.4116	-0.6484	1.8744	-0.4408	-0.4324	1.7228
-0.7128	0.2820	-37.17	-0.3036	-0.6452	1.9312	-0.3692	-0.4300	1.7608
-0.6544	0.2980	-39.46	-0.2024	-0.6224	1.9880	-0.3016	-0.4148	1.7984

-0.5936	0.3128	-41.72	-0.1112	-0.5832	2.0448	-0.2408	-0.3888	1.8364
-0.5312	0.3272	-43.98	-0.0332	-0.5304	2.1016	-0.1888	-0.3536	1.8744
-0.4684	0.3408	-46.27	0.0296	-0.4676	2.1584	-0.1472	-0.3116	1.9120
-0.4064	0.3532	-48.61	0.0760	-0.3992	2.2152	-0.1160	-0.2660	1.9500
-0.3456	0.3656	-51.00	0.1068	-0.3284	2.2720	-0.0956	-0.2192	1.9880
-0.2872	0.3772	-53.43	0.1224	-0.2596	2.3288	-0.0852	-0.1732	2.0256
-0.2320	0.3888	-55.87	0.1244	-0.1960	2.3856	-0.0836	-0.1308	2.0636
-0.1812	0.4004	-58.31	0.1156	-0.1396	2.4424	-0.0896	-0.0932	2.1016
-0.1356	0.4124	-60.69	0.0988	-0.0928	2.4992	-0.1008	-0.0620	2.1392
-0.0956	0.4252	-62.95	0.0772	-0.0560	2.5560	-0.1152	-0.0376	2.1772
-0.0620	0.4384	-65.05	0.0540	-0.0296	2.6128	-0.1304	-0.0200	2.2152
-0.0352	0.4528	-66.91	0.0328	-0.0128	2.6696	-0.1448	-0.0088	2.2528
-0.0200	0.4640	-68.11	0.0192	-0.0056	2.7120	-0.1540	-0.0037	2.2812

Appendix E: Cavitation Images

Cavitation images at all tunnel pressure between 850 mm to 250 mm Hg, for all range of Tip Speed Ratio (*TSR*). Condition where cavitation was observed are in bold.

Tunnel Pressure: 850 mm Hg, *TSR* = 0

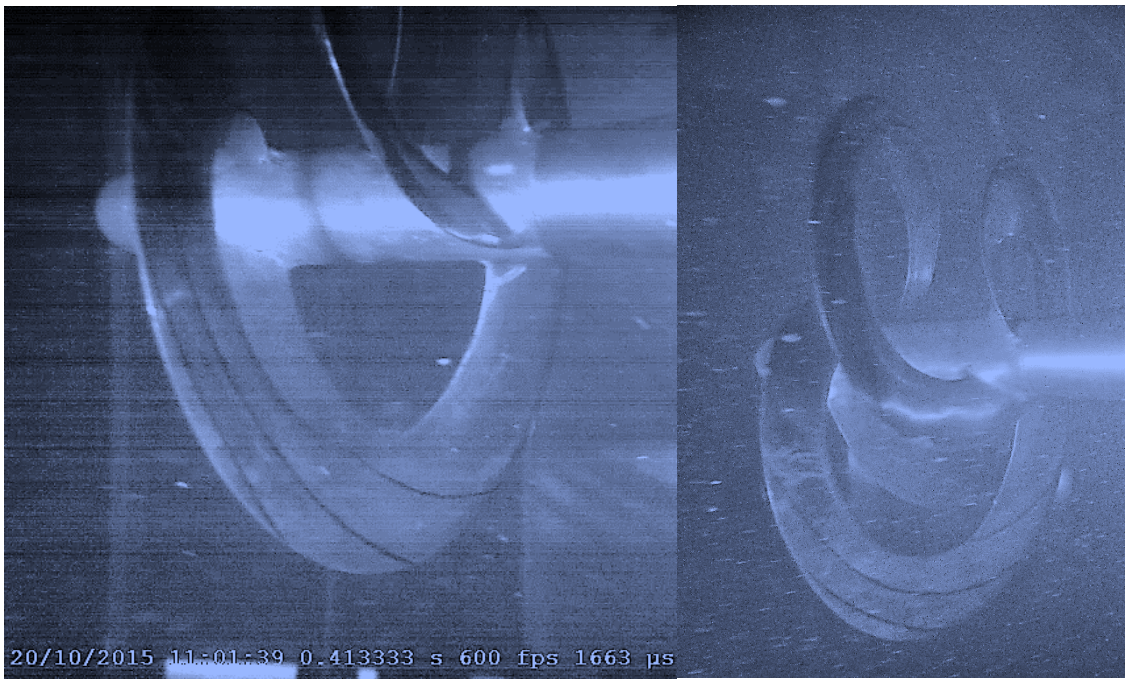

Tunnel Pressure: 850 mm Hg, *TSR* = 1

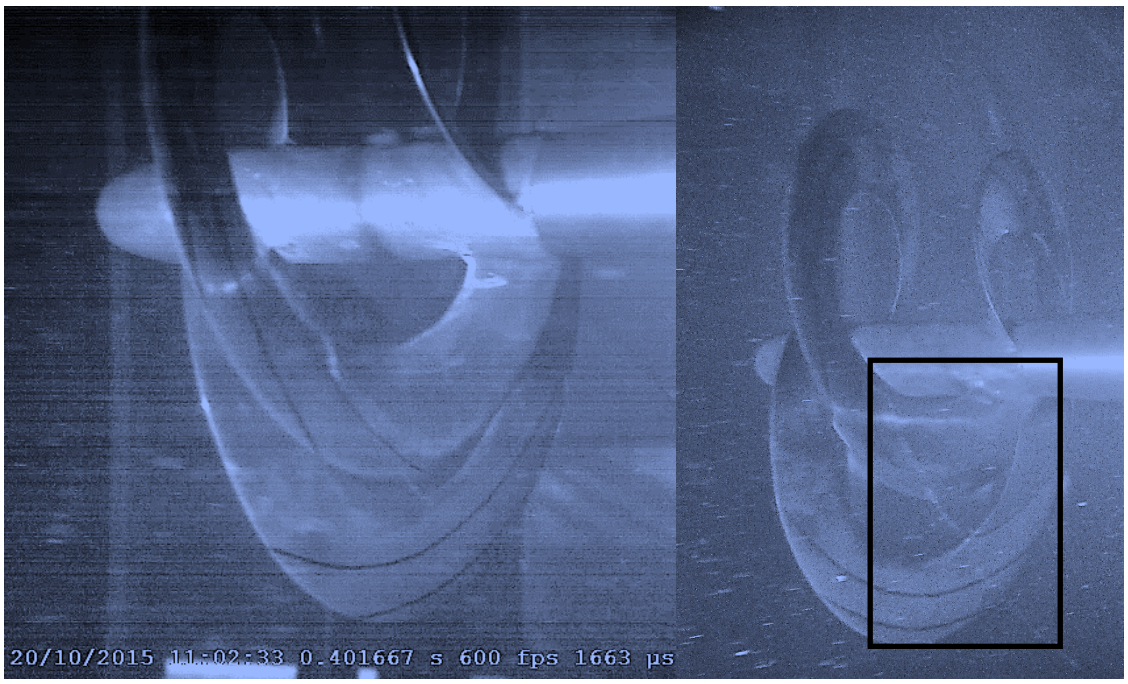

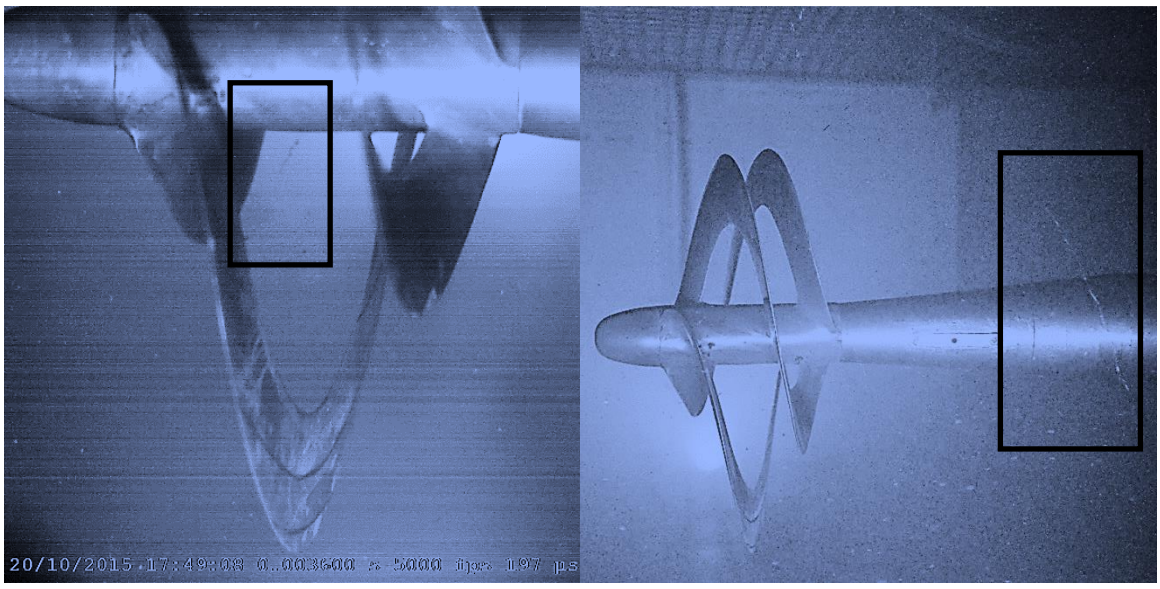

Tunnel Pressure: 850 mm Hg, *TSR* = 2

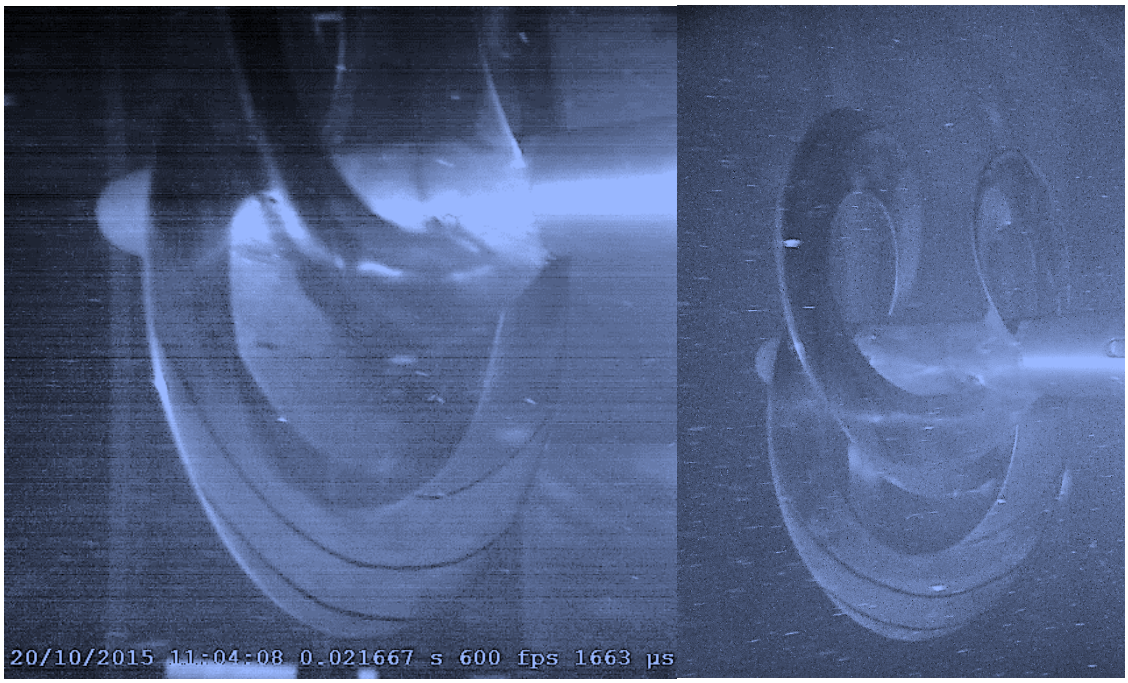

Tunnel Pressure: 850 mm Hg, *TSR* = 3

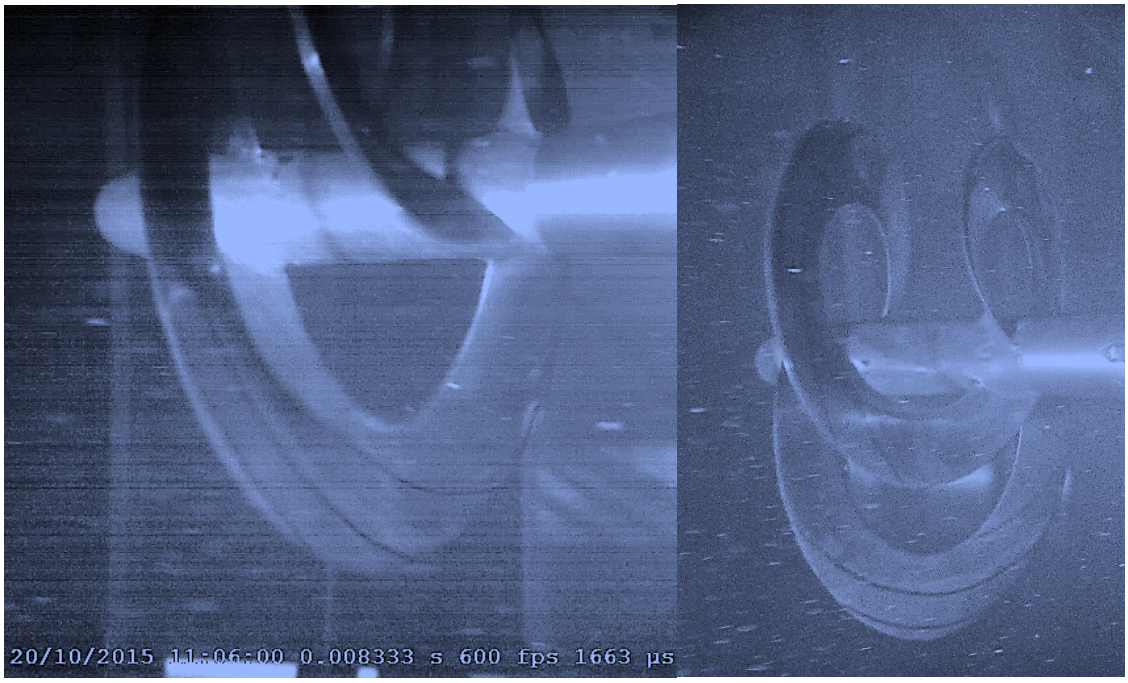

Tunnel Pressure: 850 mm Hg, *TSR* = 4

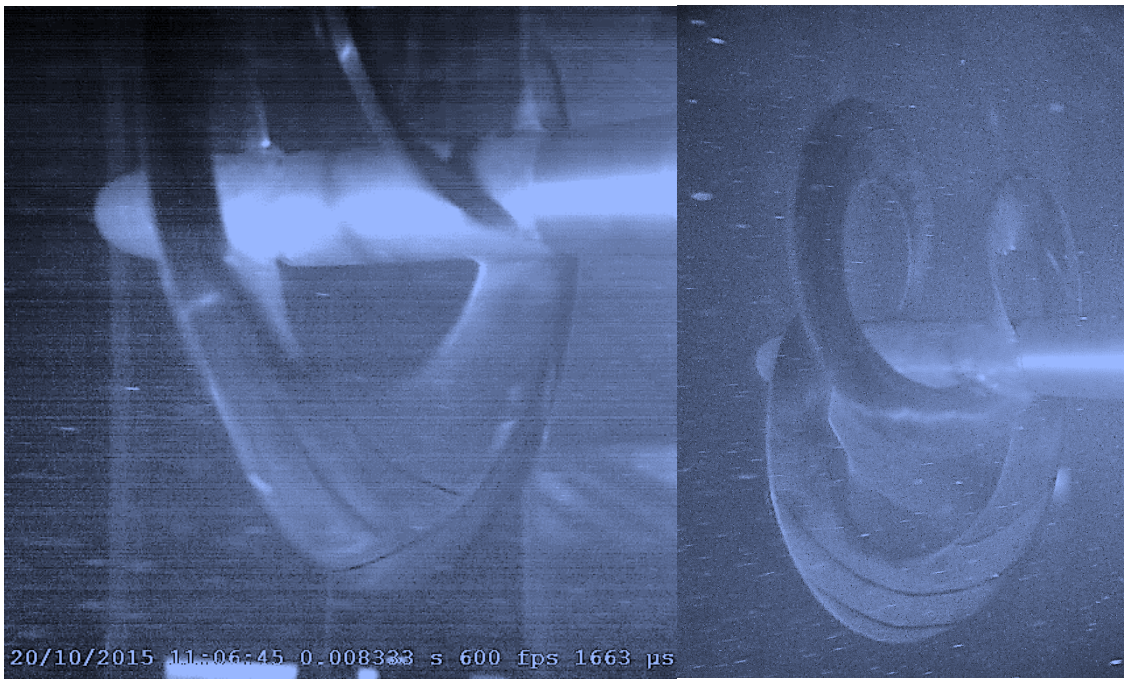

Tunnel Pressure: 850 mm Hg, *TSR* = 5

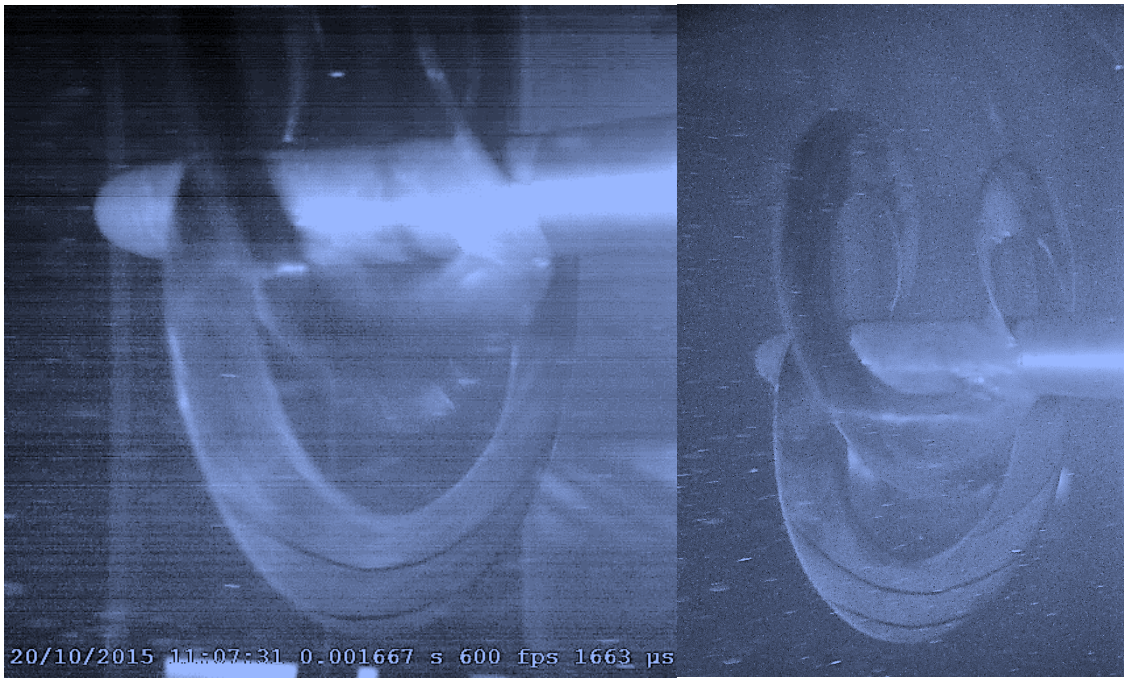

Tunnel Pressure: 750 mm Hg, *TSR* = 0

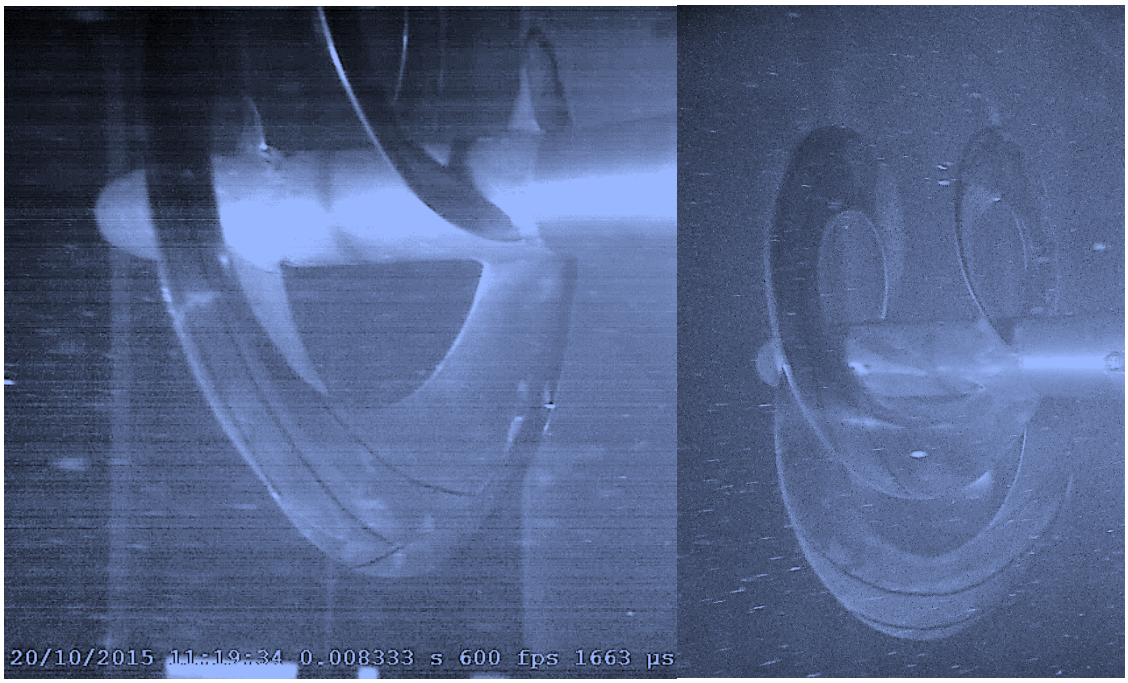

Tunnel Pressure: 750 mm Hg, *TSR* = 1

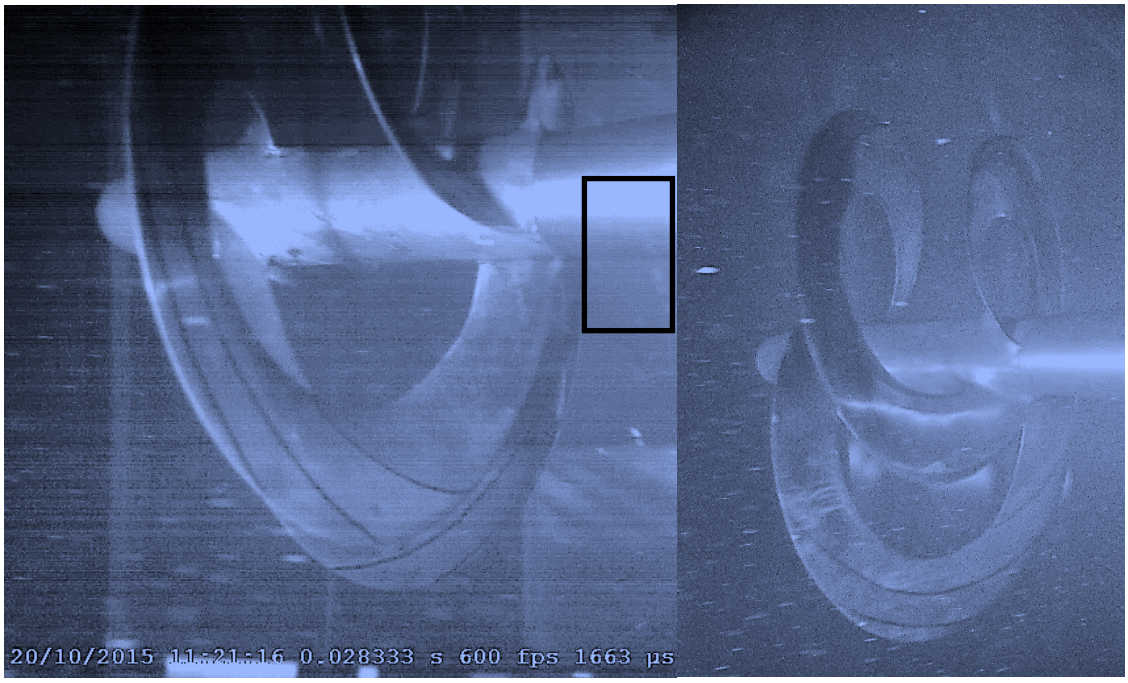

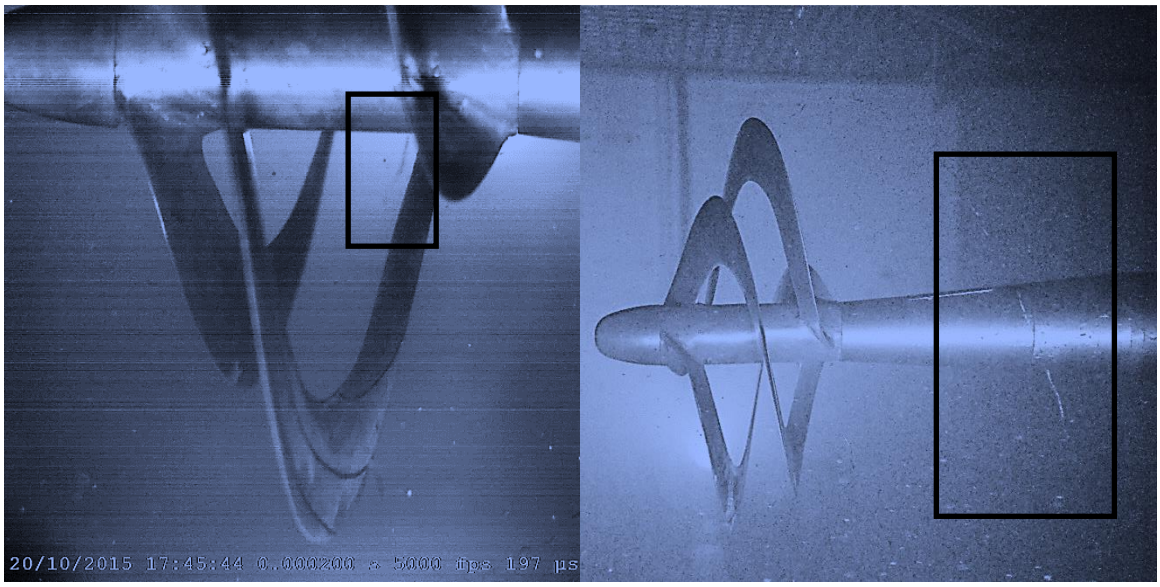

Tunnel Pressure: 750 mm Hg, *TSR* = 2

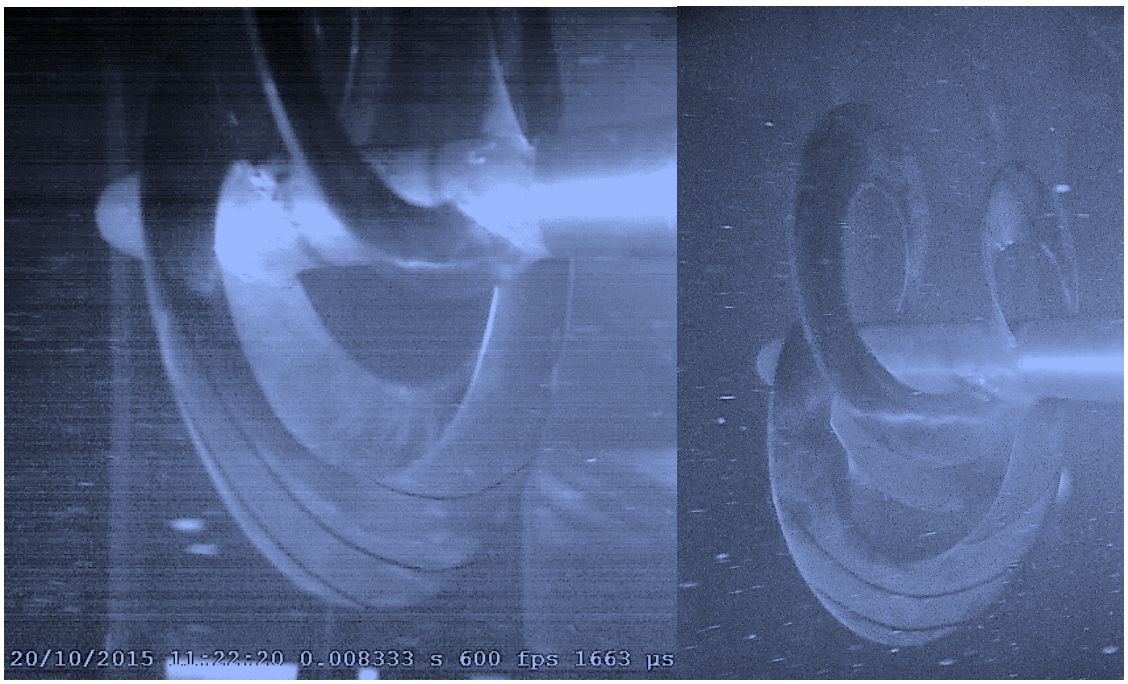

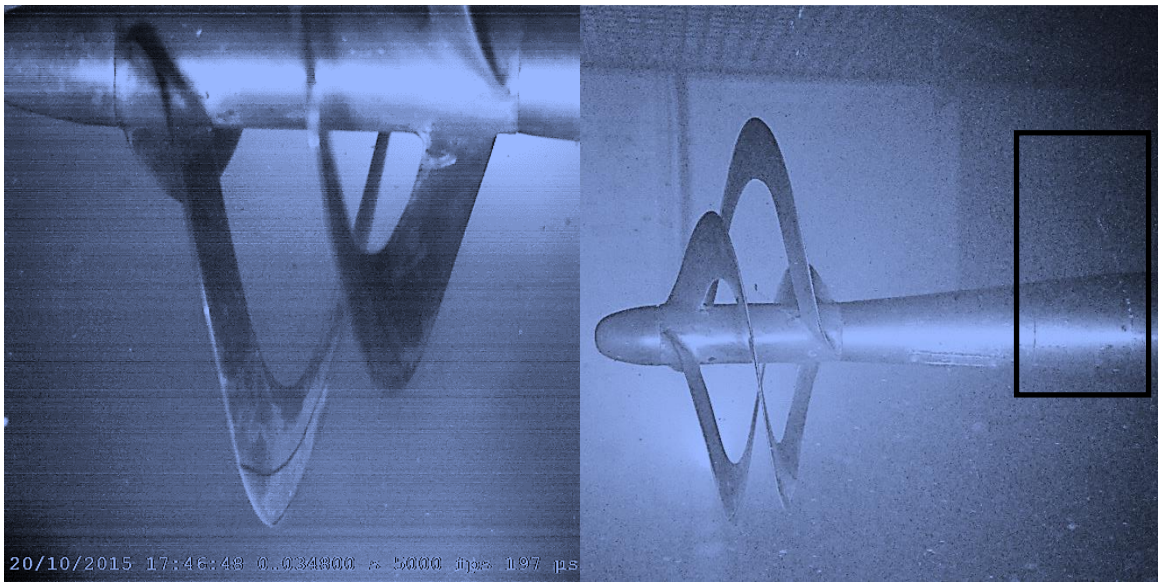

Tunnel Pressure: 750 mm Hg, *TSR* = 3

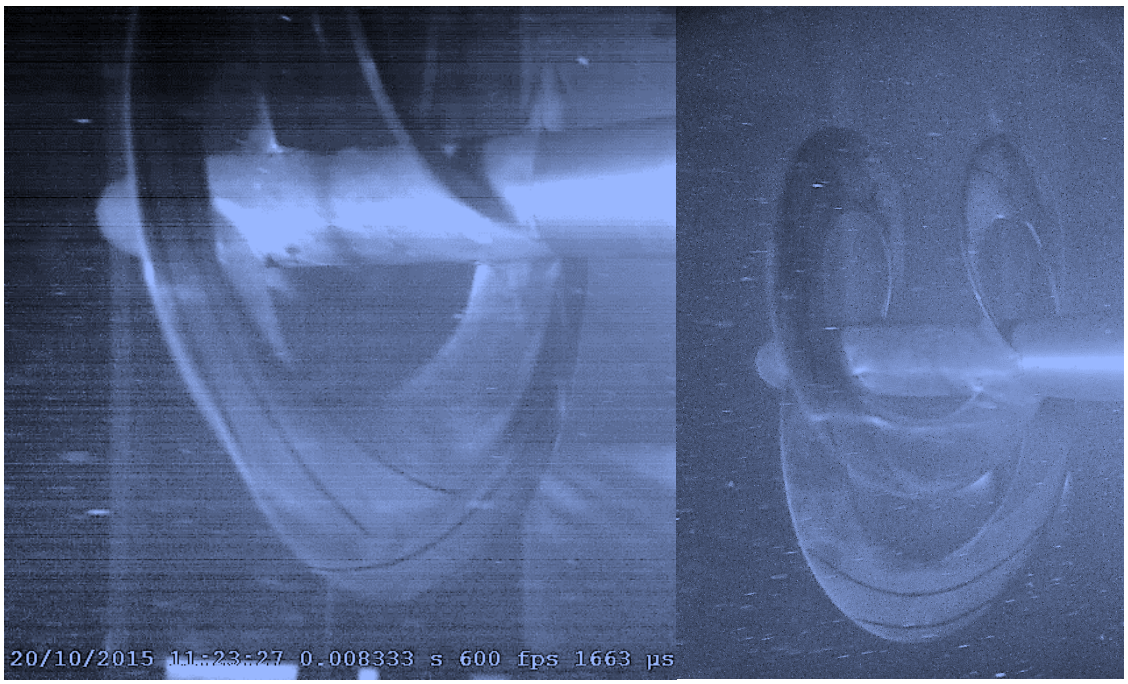

Tunnel Pressure: 750 mm Hg, *TSR* = 4

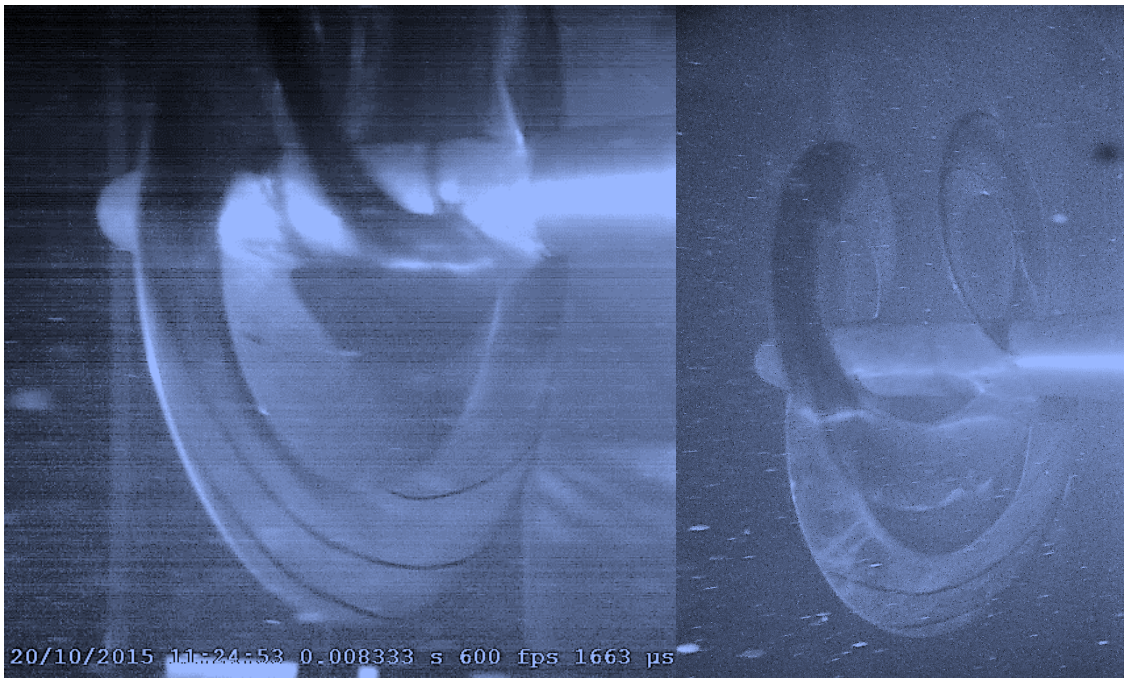

Tunnel Pressure: 750 mm Hg, *TSR* = 5

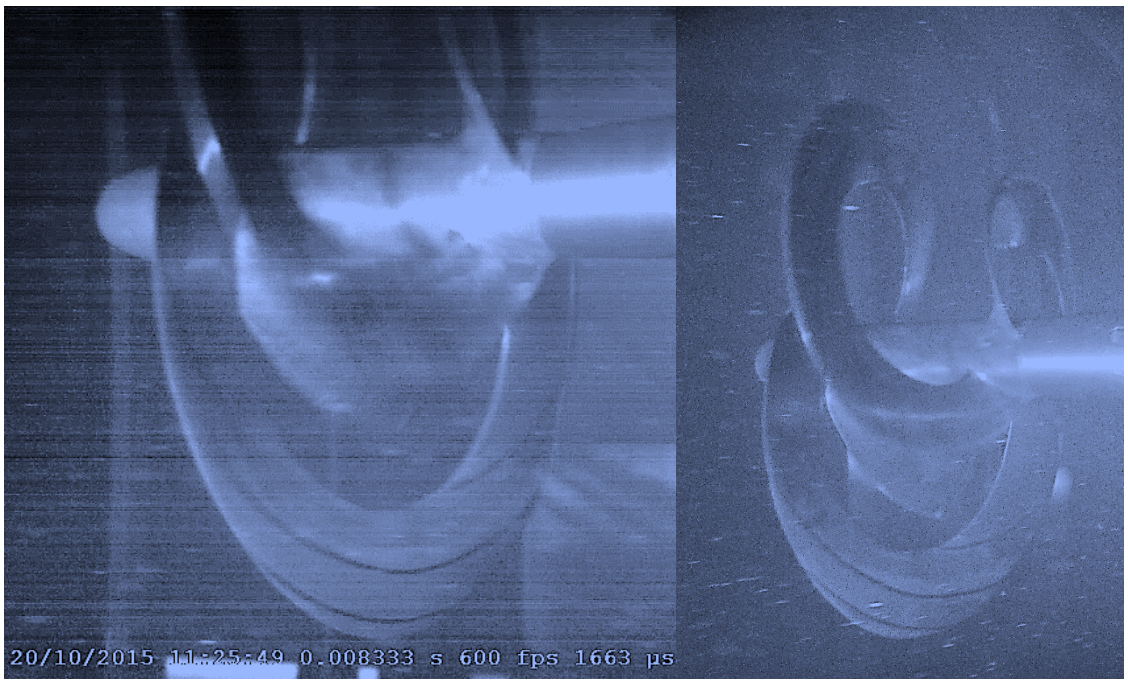

Tunnel Pressure: 650 mm Hg, *TSR* = 0

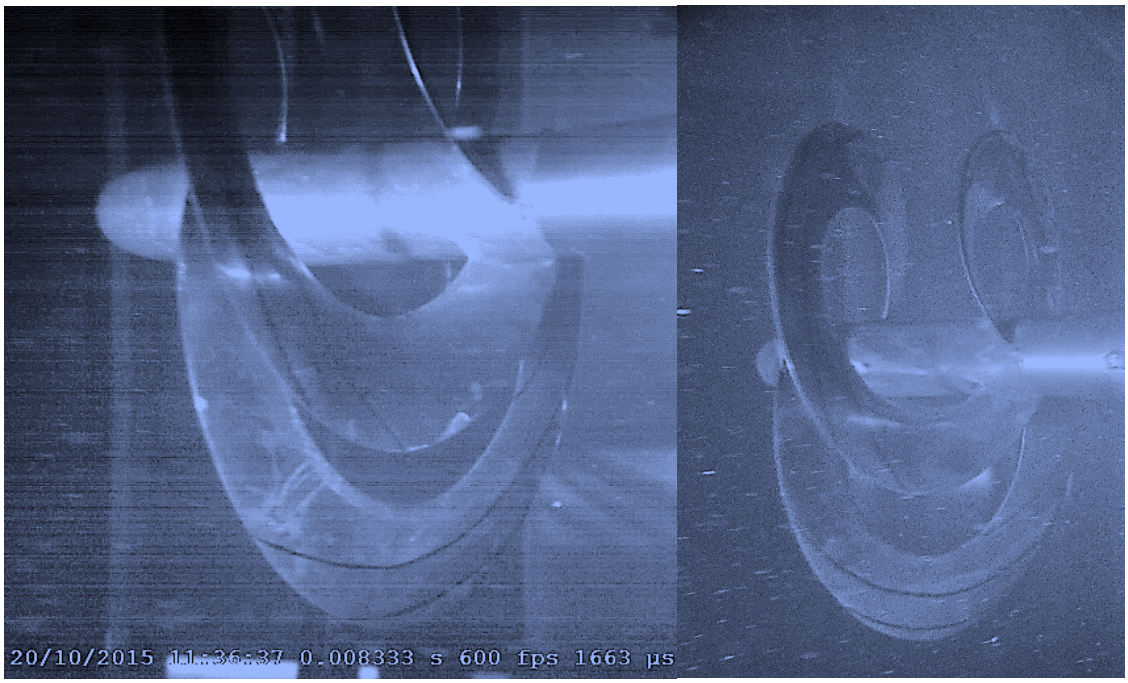

Tunnel Pressure: 650 mm Hg, *TSR* = 1

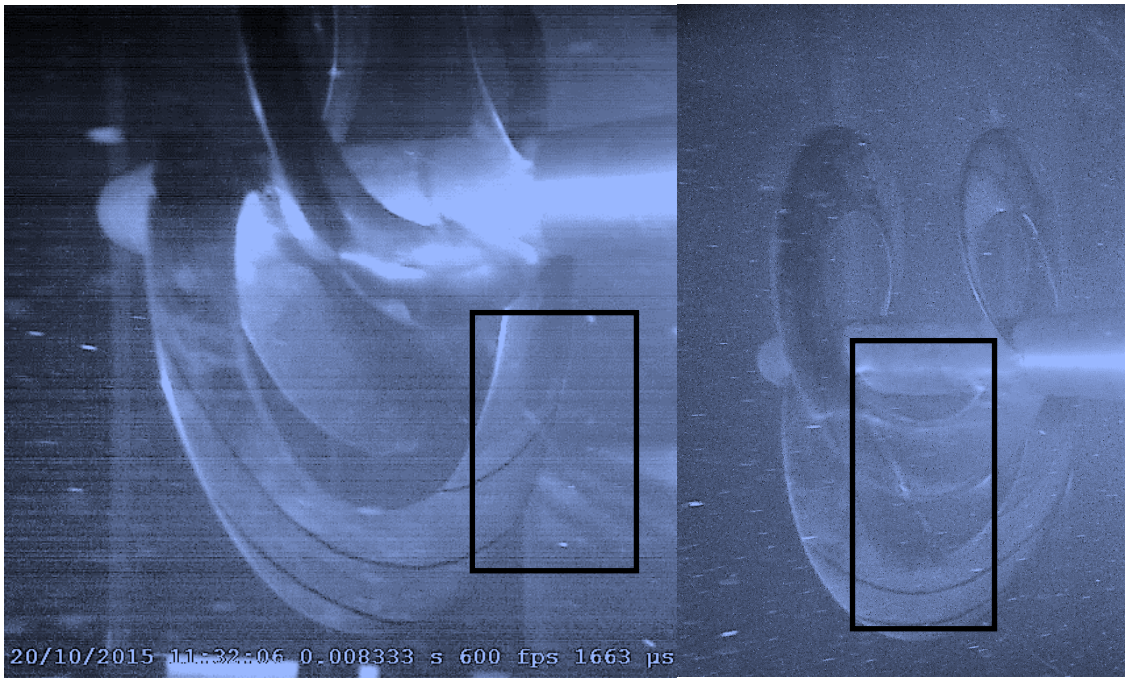

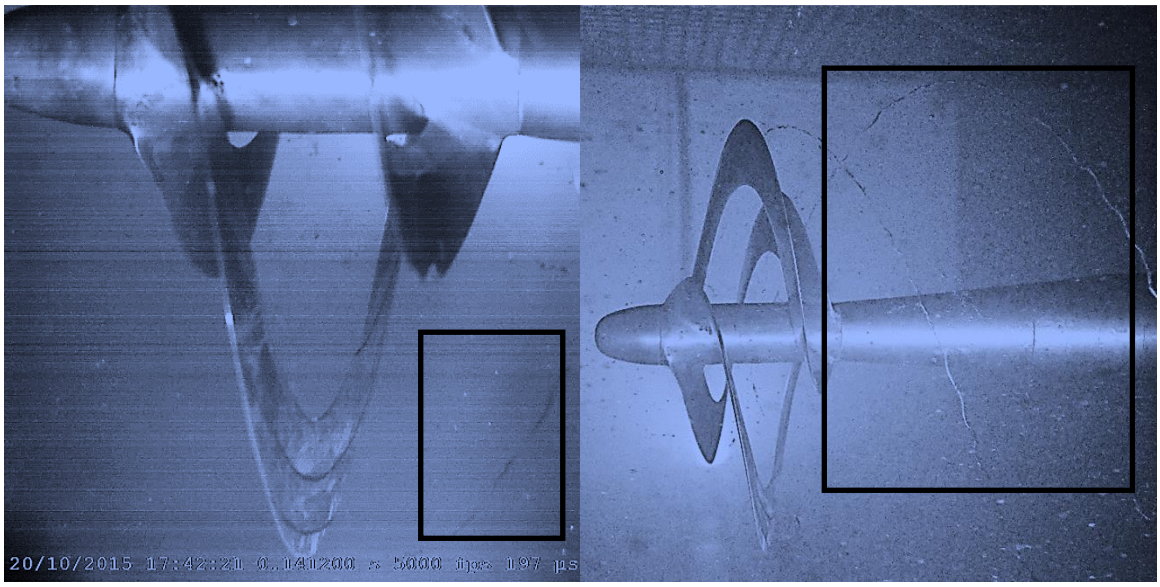

Tunnel Pressure: 650 mm Hg, *TSR* = 2

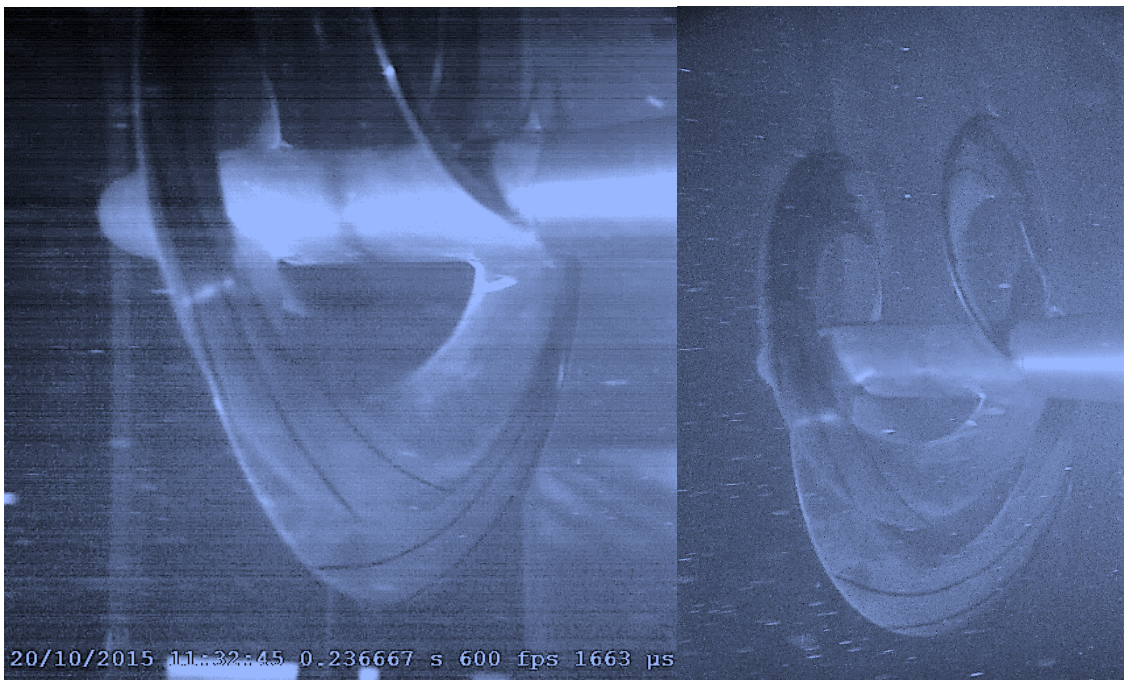

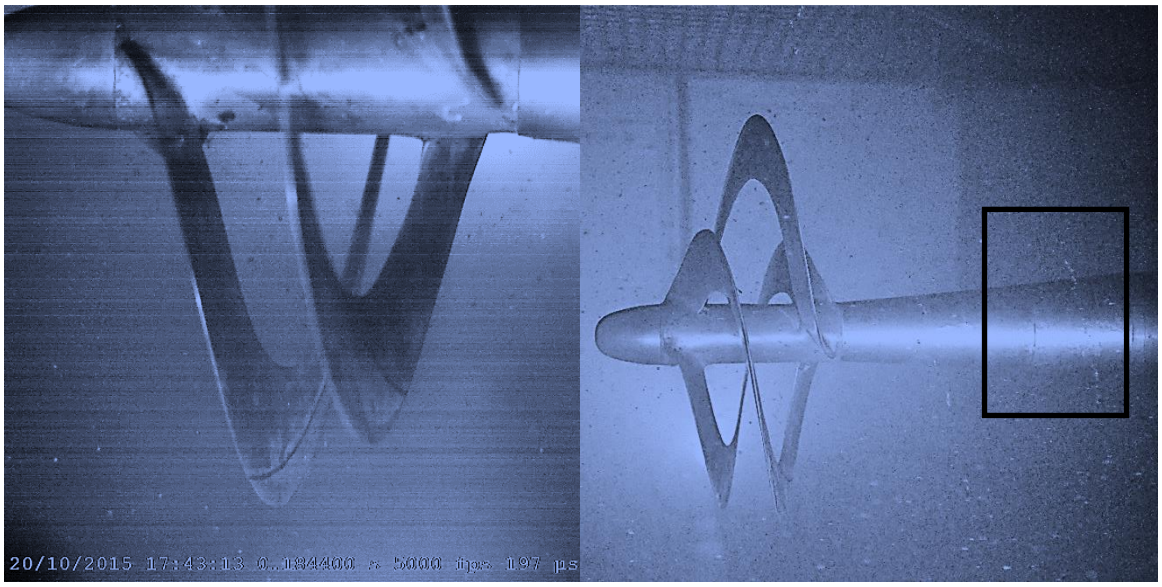

Tunnel Pressure: 650 mm Hg, *TSR* = 3

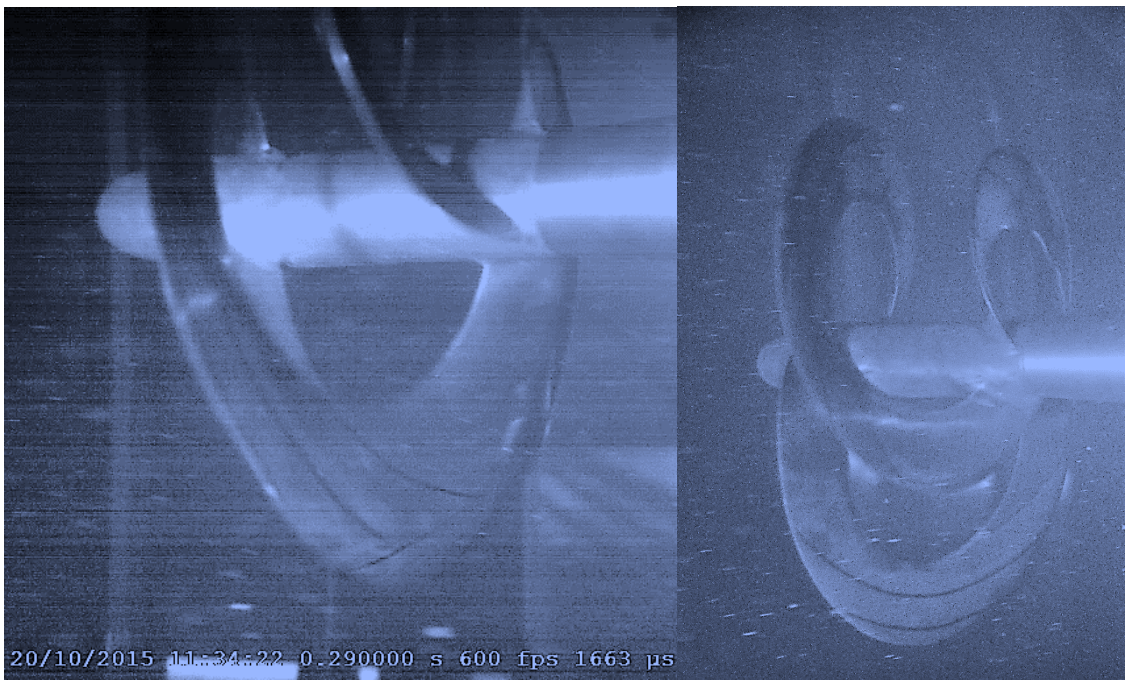

Tunnel Pressure: 650 mm Hg, *TSR* = 4

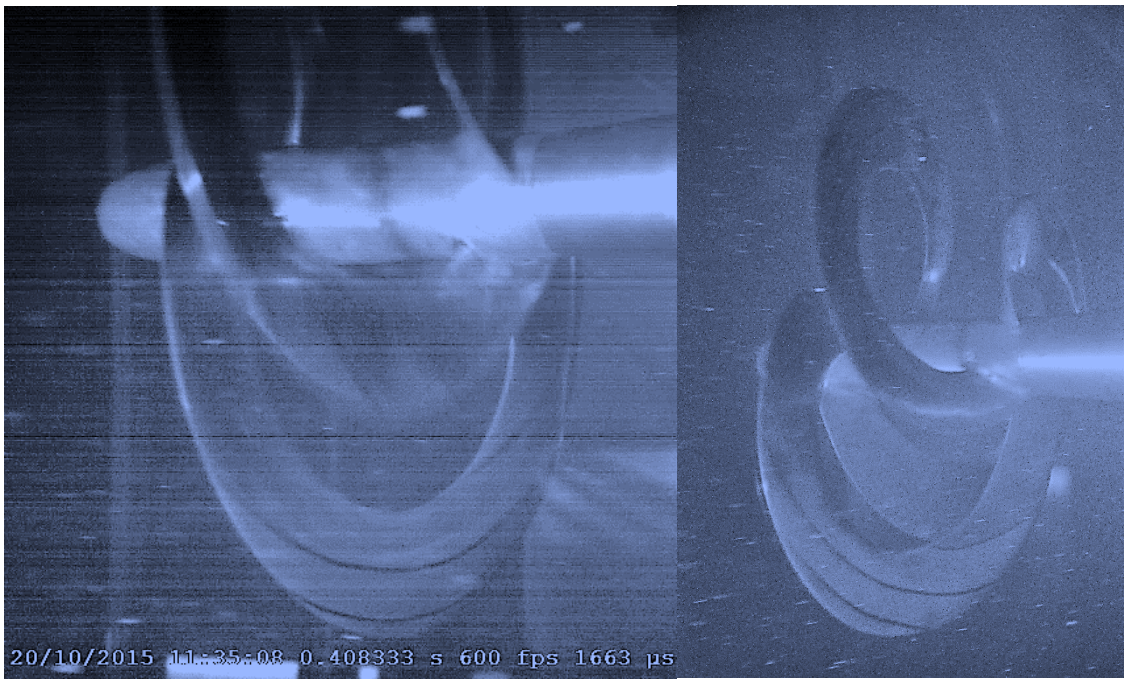

Tunnel Pressure: 650 mm Hg, *TSR* = 5

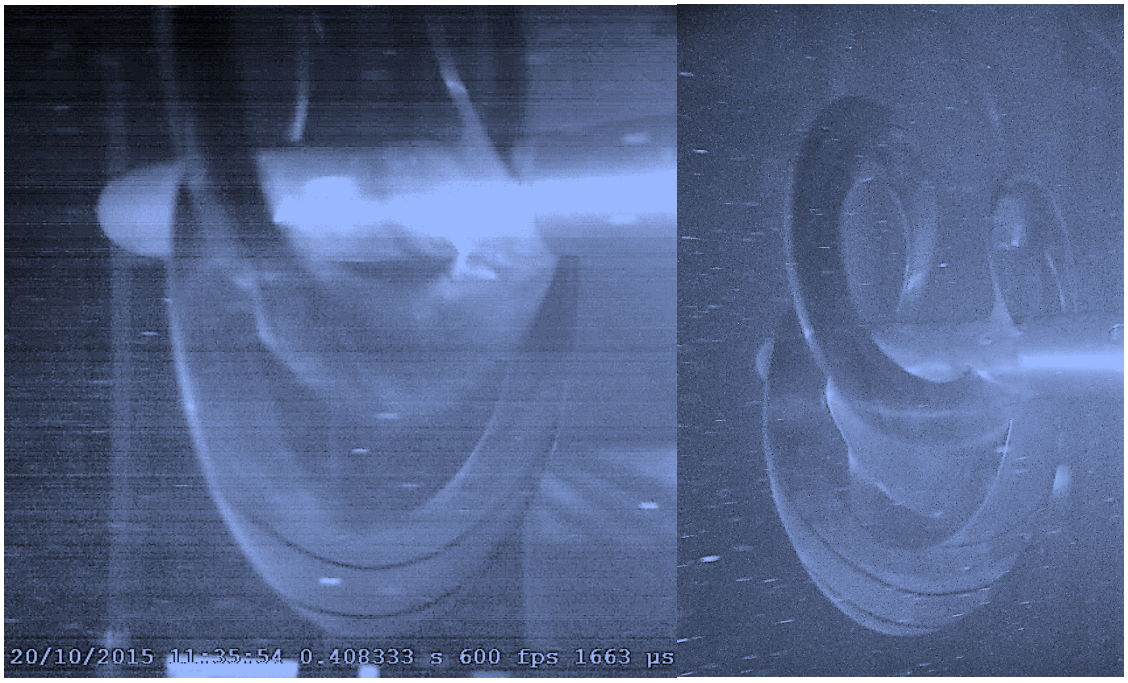

Tunnel Pressure: 550 mm Hg, *TSR* = 0

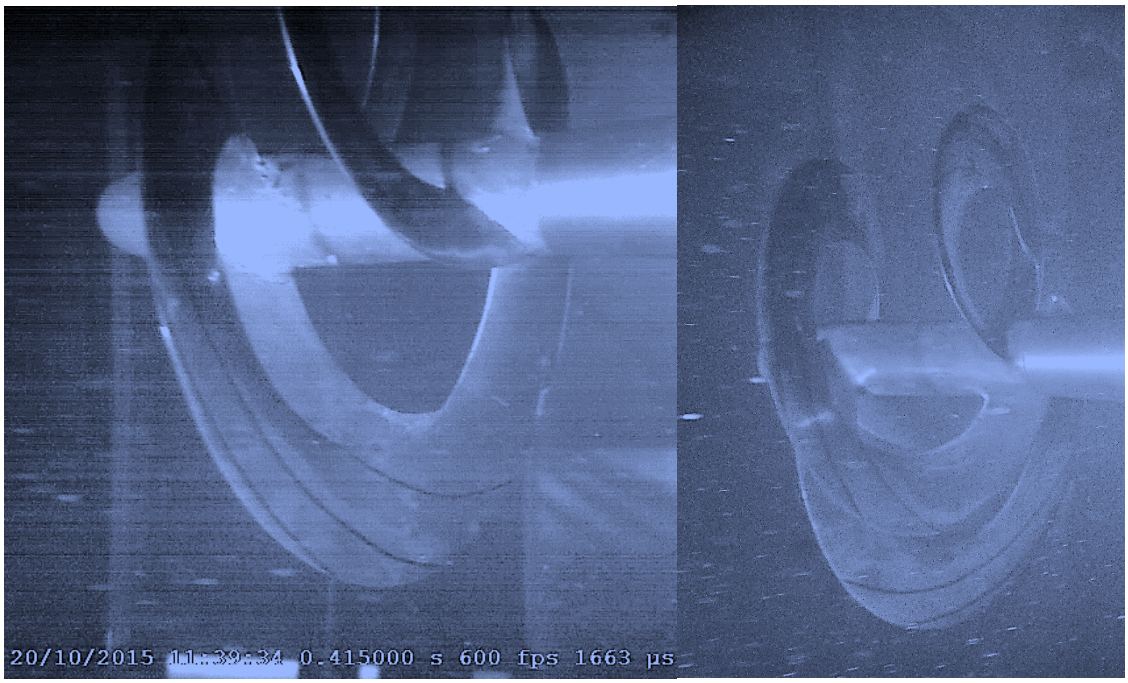

Tunnel Pressure: 550 mm Hg, *TSR* = 1

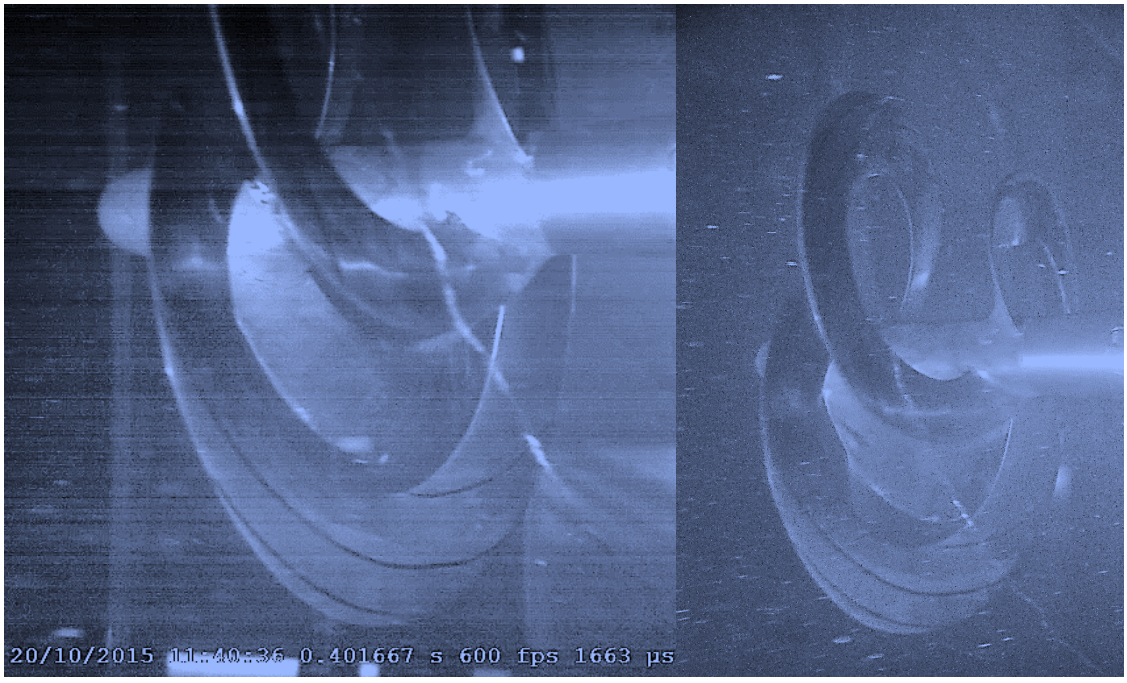

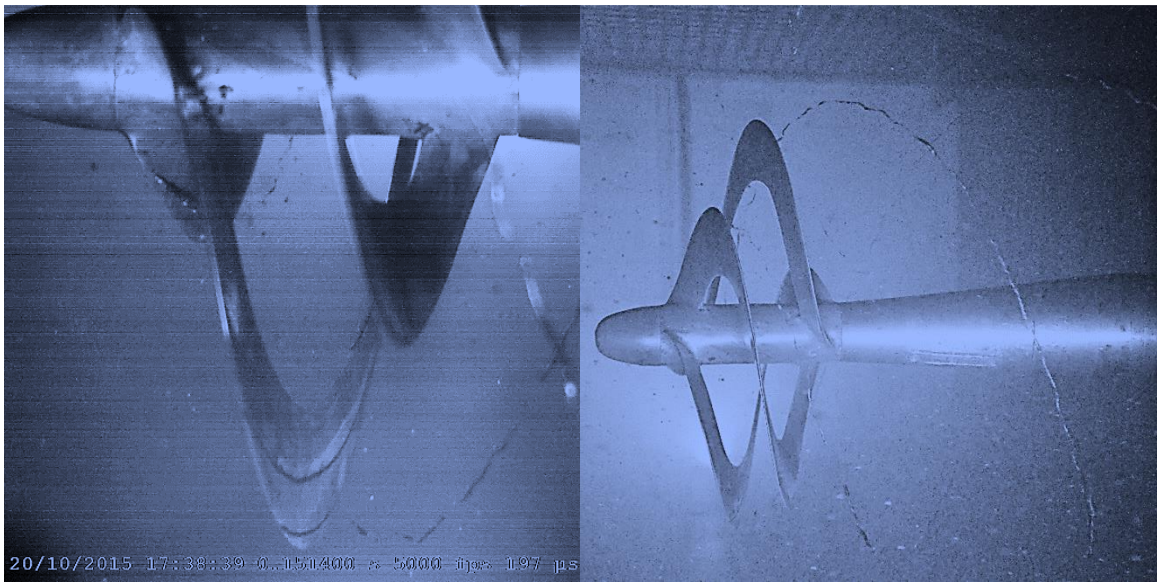

Tunnel Pressure: 550 mm Hg, *TSR* = 2

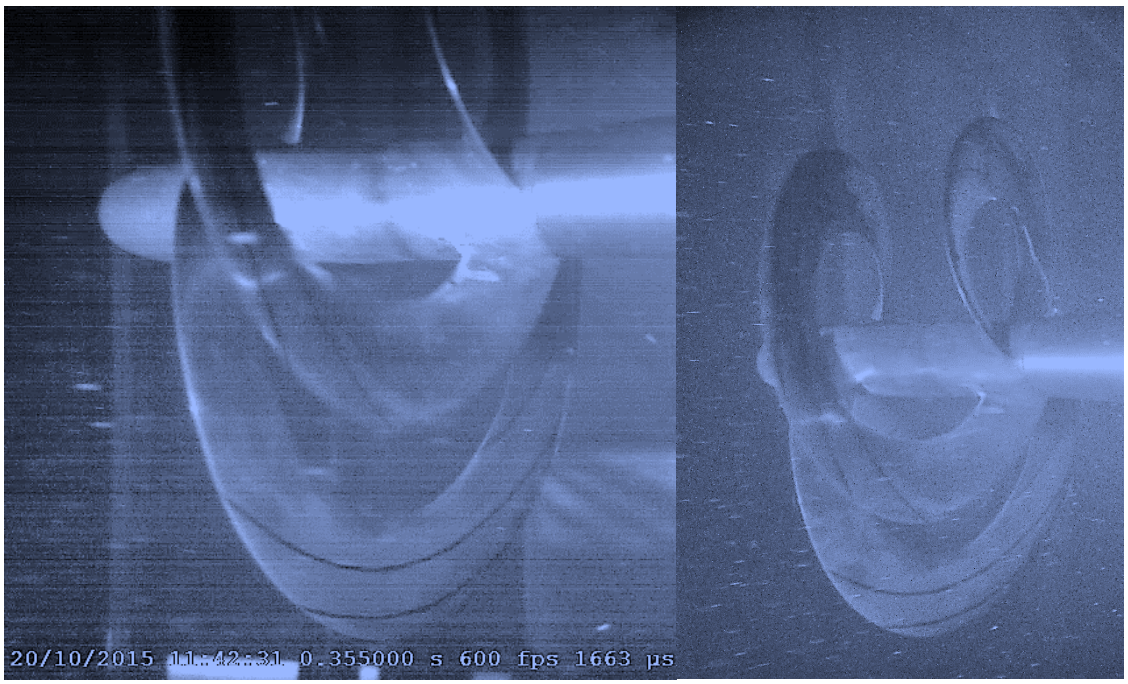

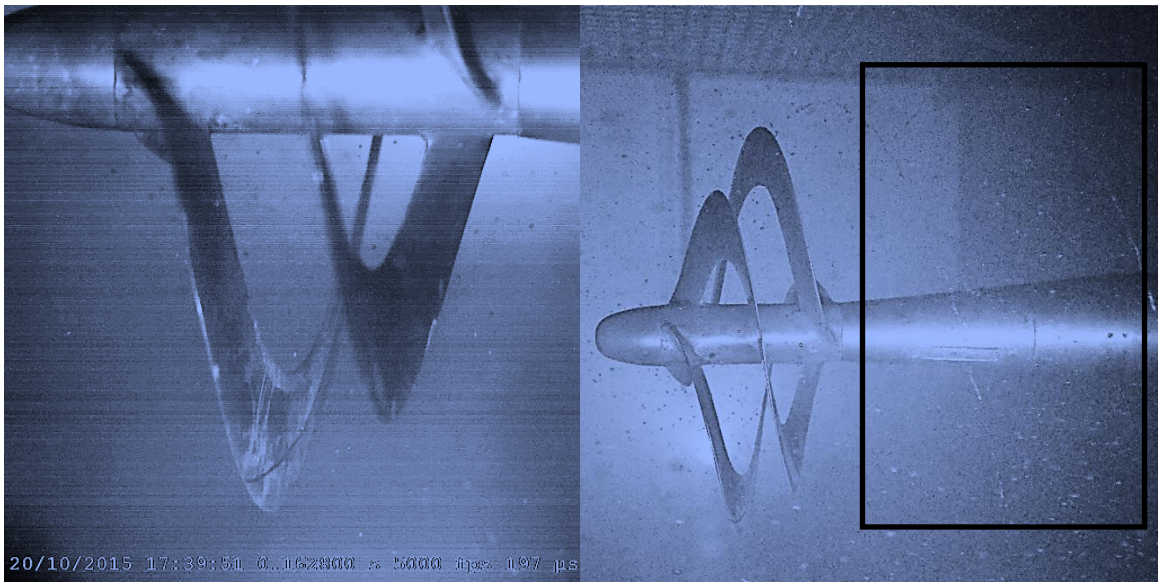

Tunnel Pressure: 550 mm Hg, *TSR* = 3

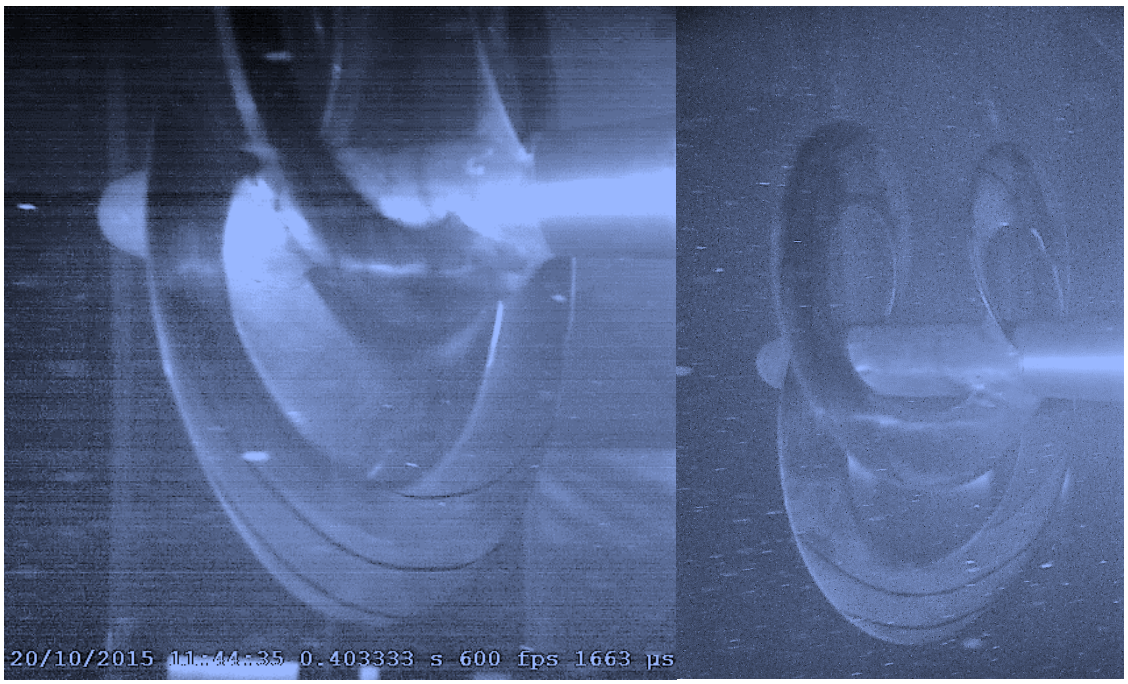

Tunnel Pressure: 550 mm Hg, *TSR* = 4

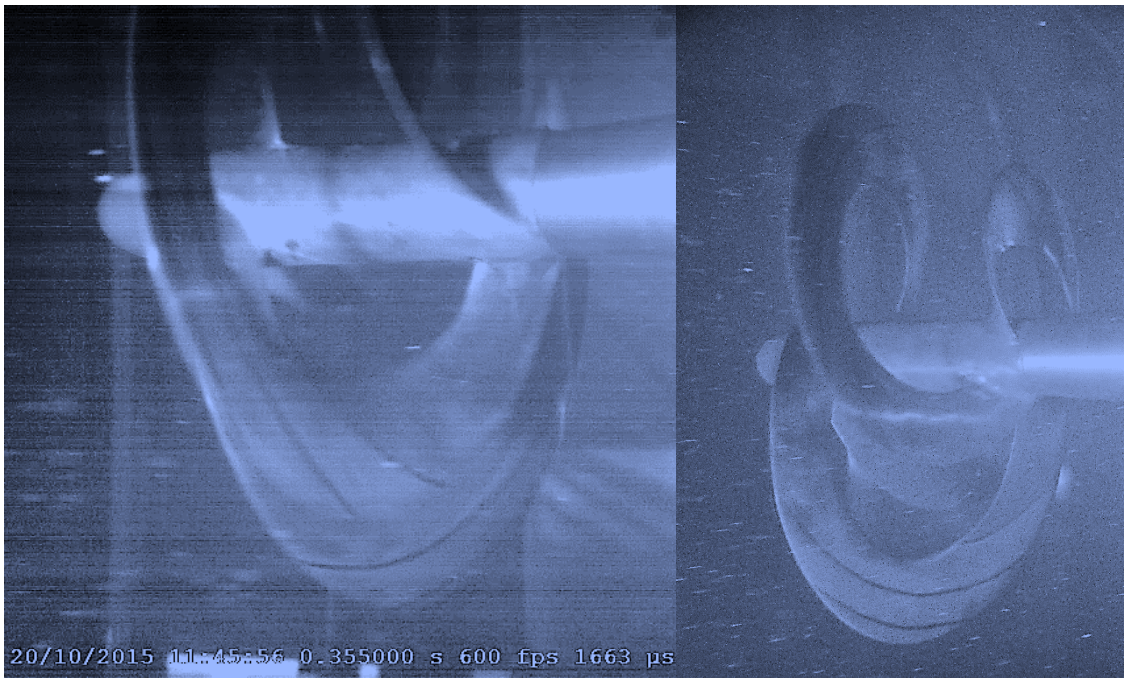

Tunnel Pressure: 550 mm Hg, *TSR* = 5

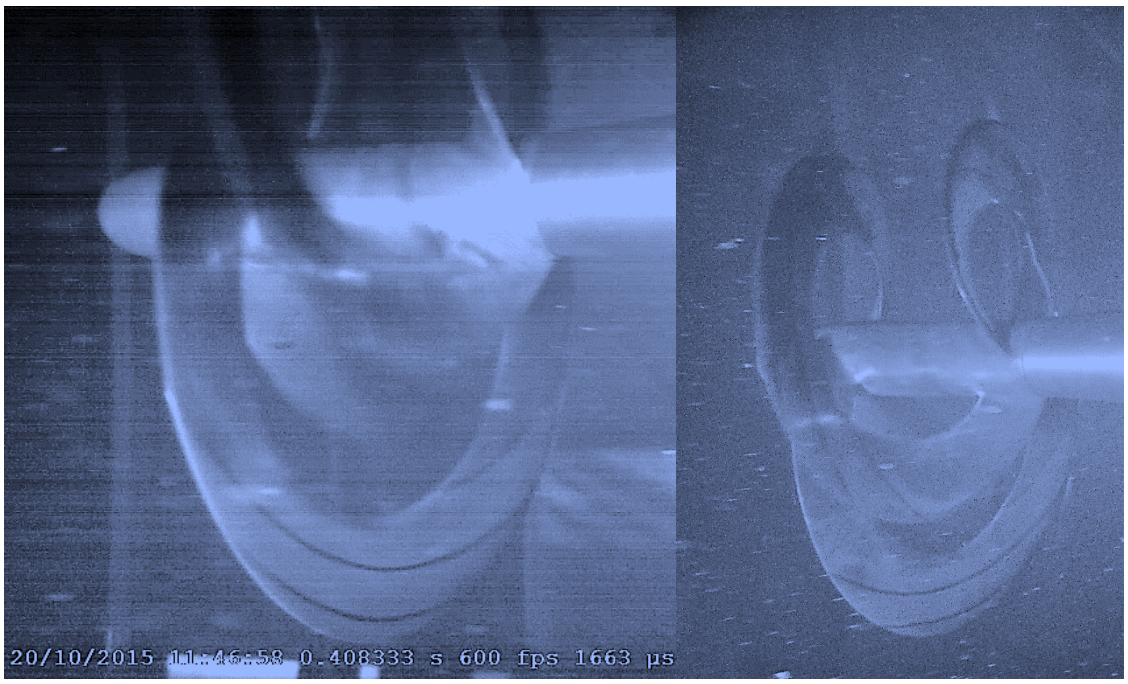

Tunnel Pressure: 450 mm Hg, *TSR* = 0

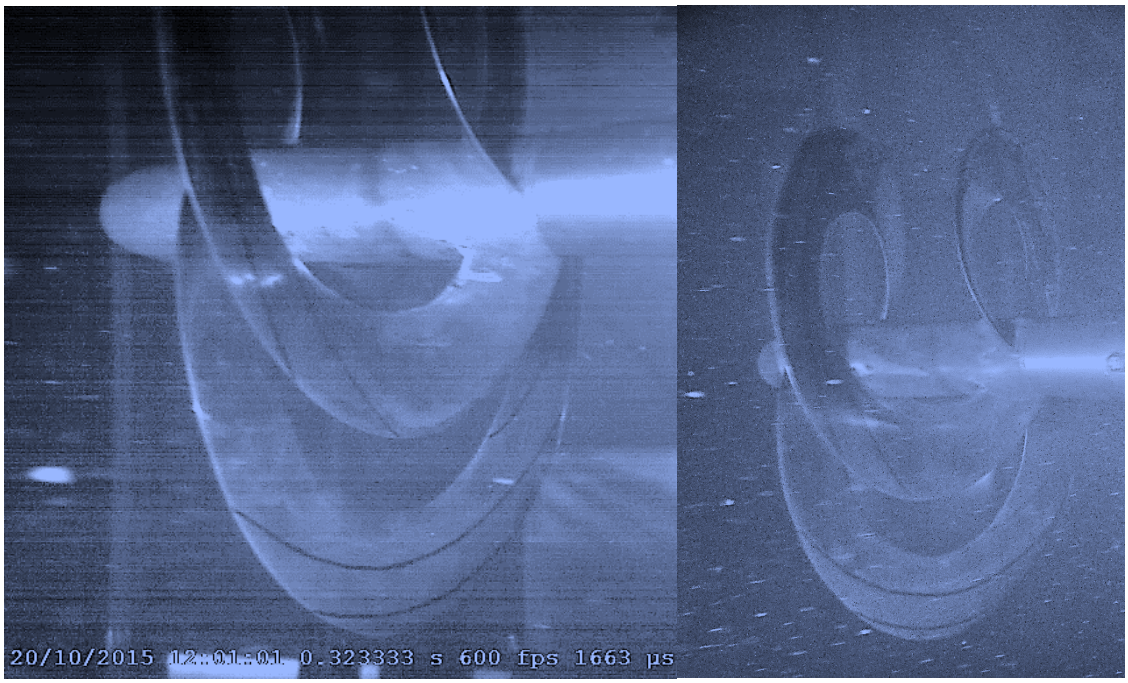

Tunnel Pressure: 450 mm Hg, *TSR* = 1

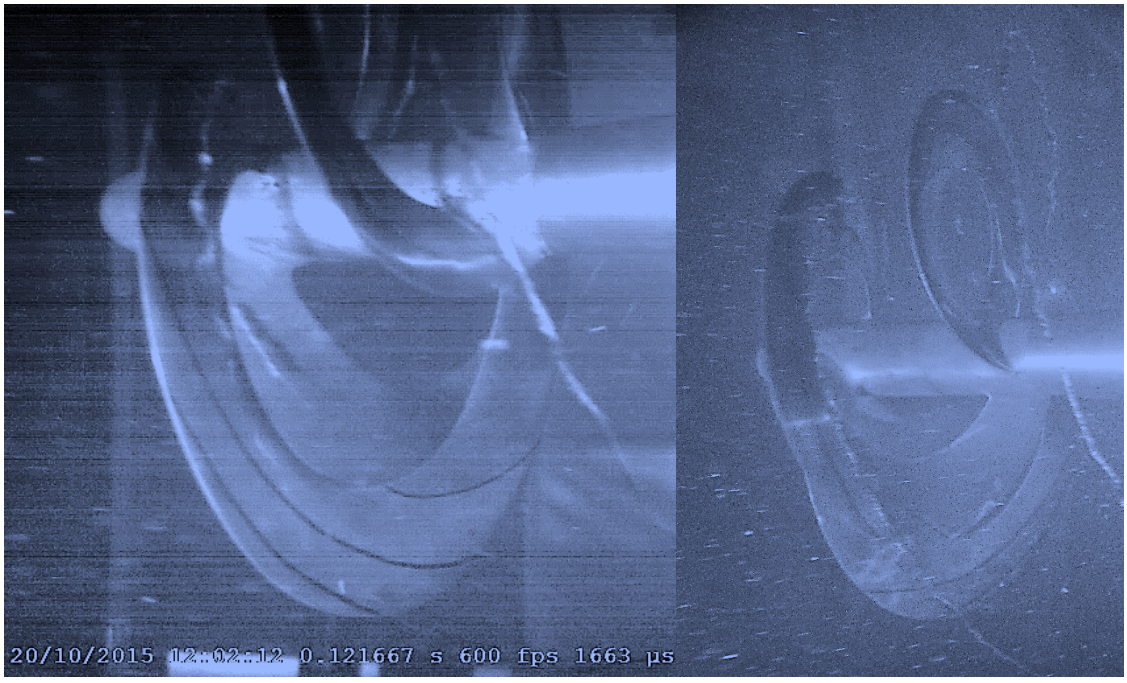

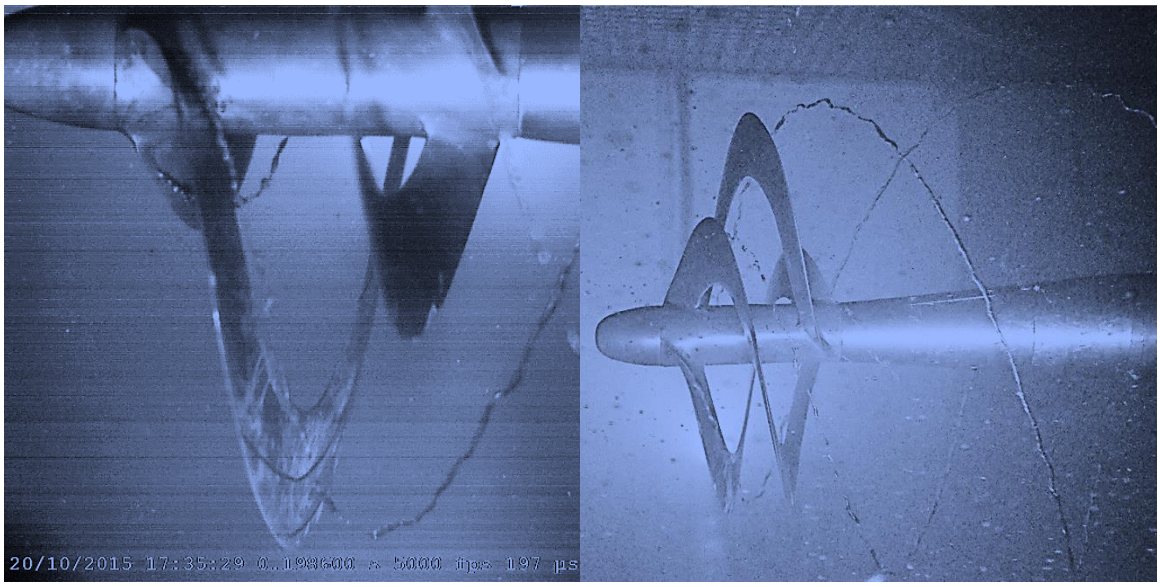

Tunnel Pressure: 450 mm Hg, *TSR* = 2

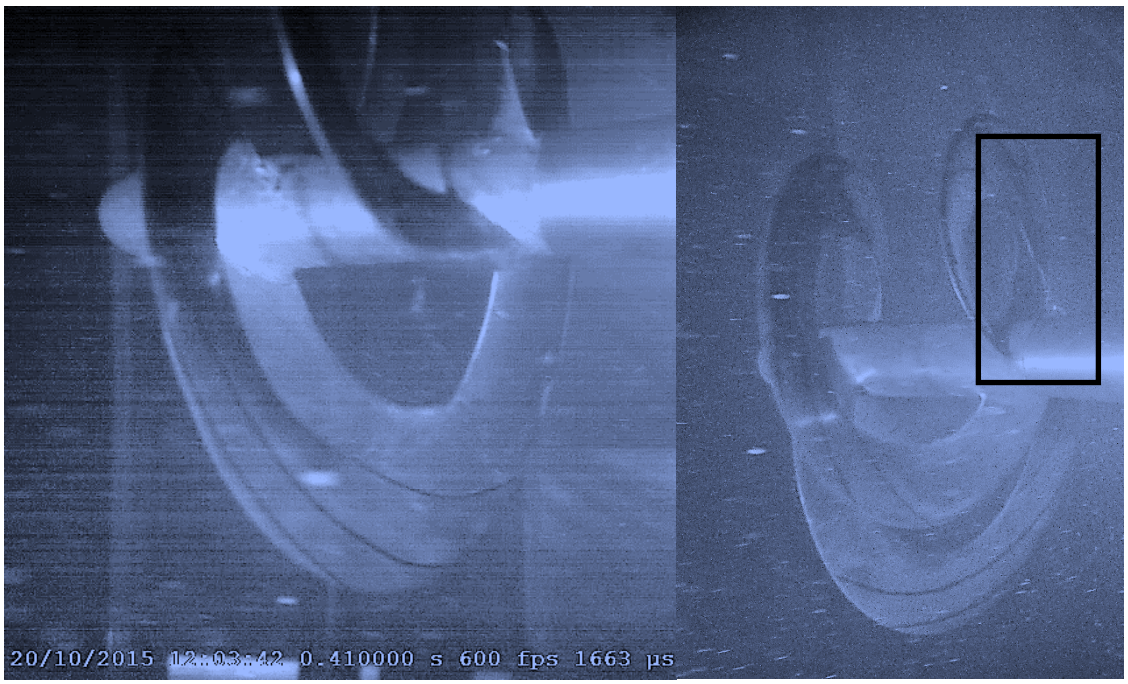

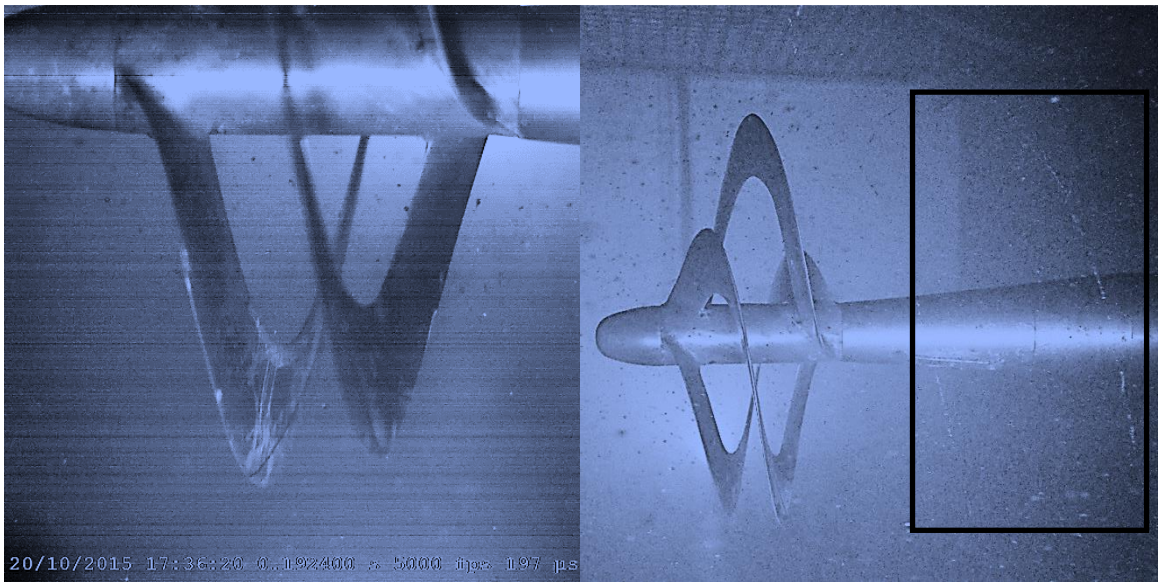

Tunnel Pressure: 450 mm Hg, *TSR* = 3

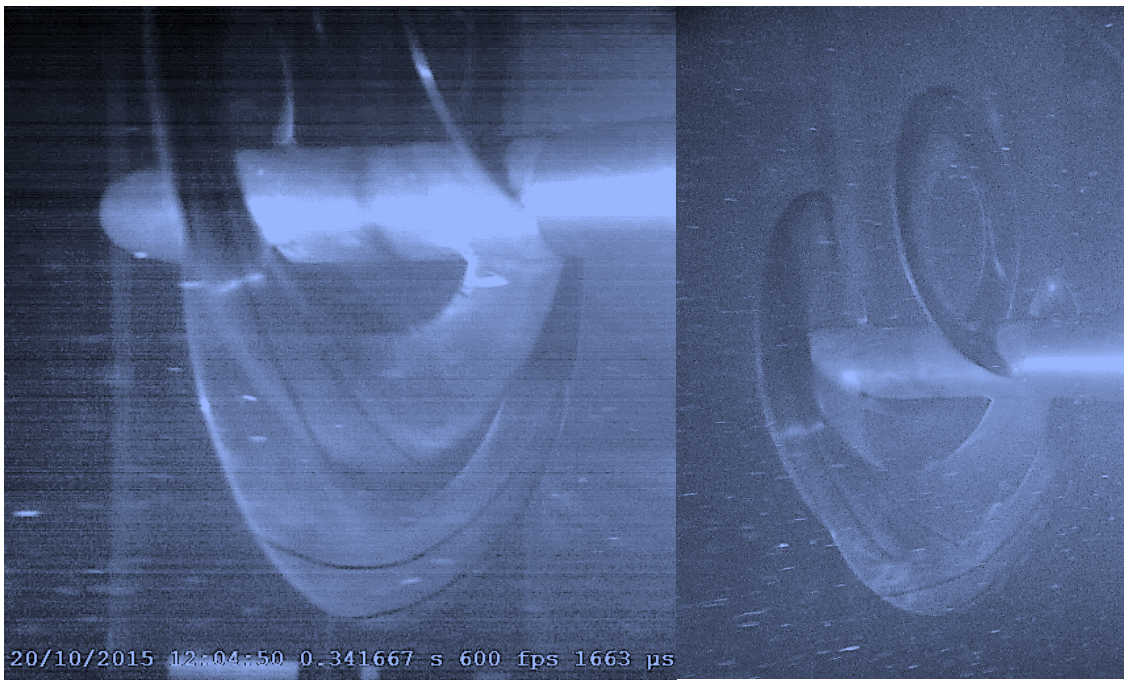

Tunnel Pressure: 450 mm Hg, *TSR* = 4

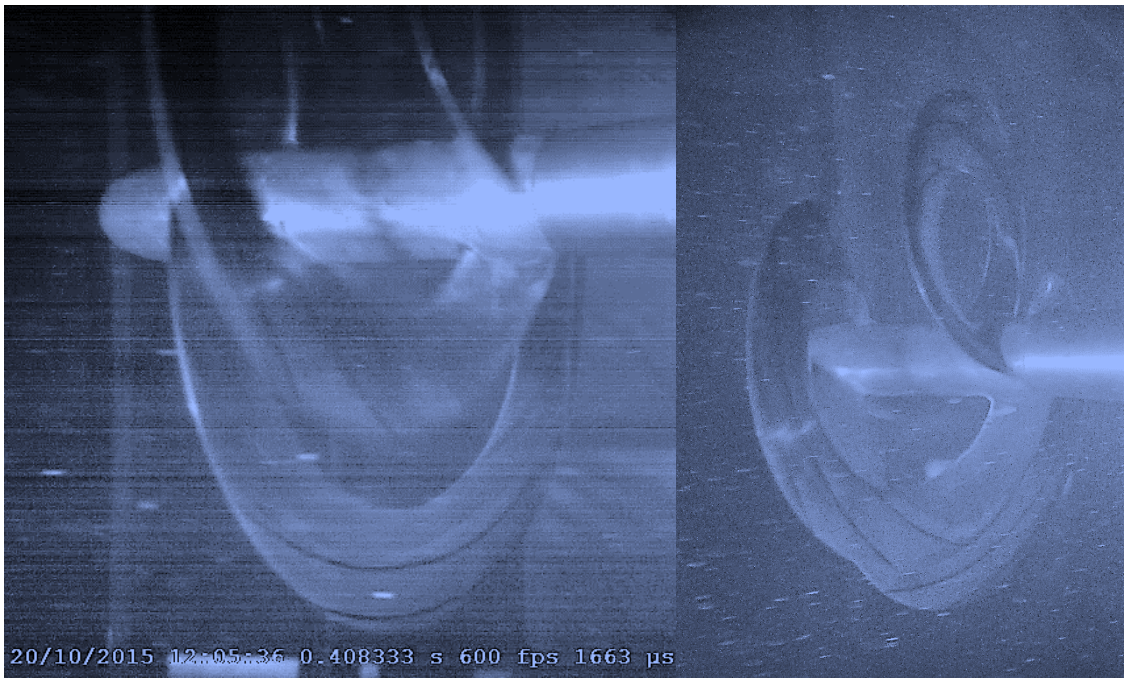

Tunnel Pressure: 450 mm Hg, *TSR* = 5

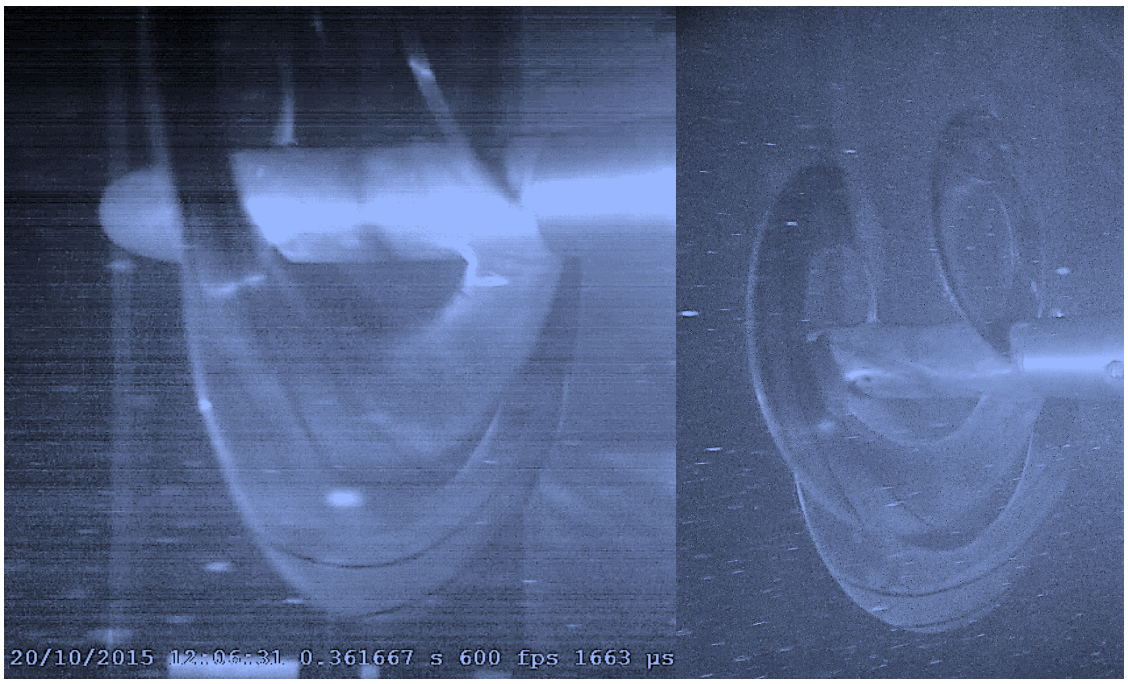

Tunnel Pressure: 350 mm Hg, *TSR* = 0

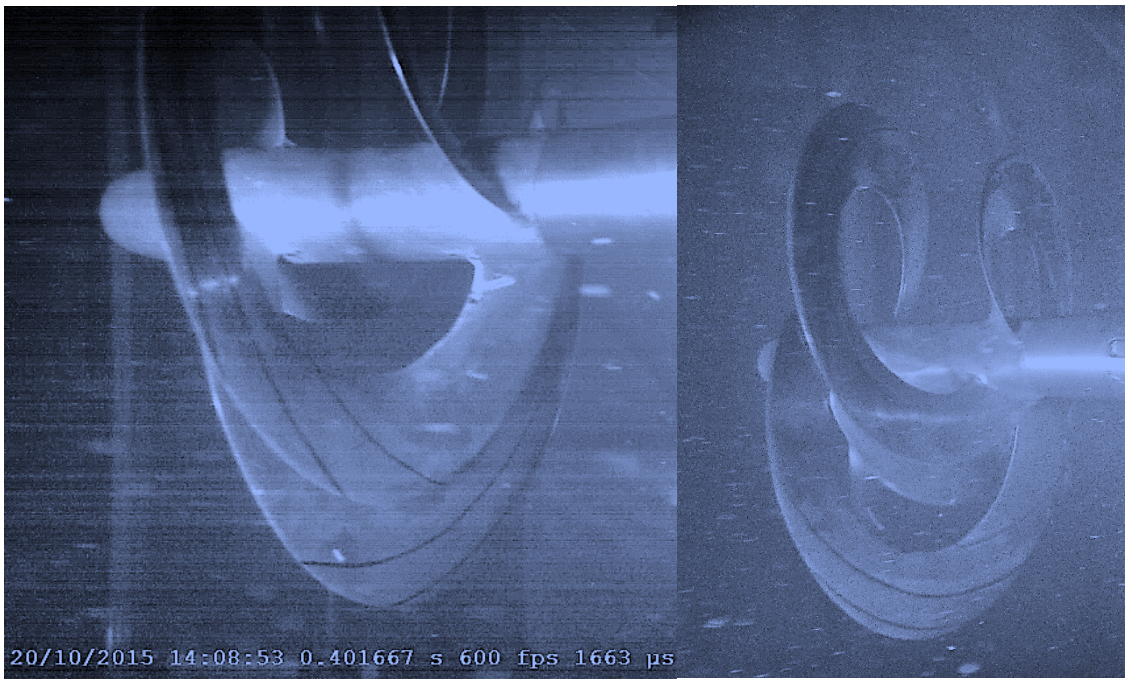

Tunnel Pressure: 350 mm Hg, *TSR* = 1

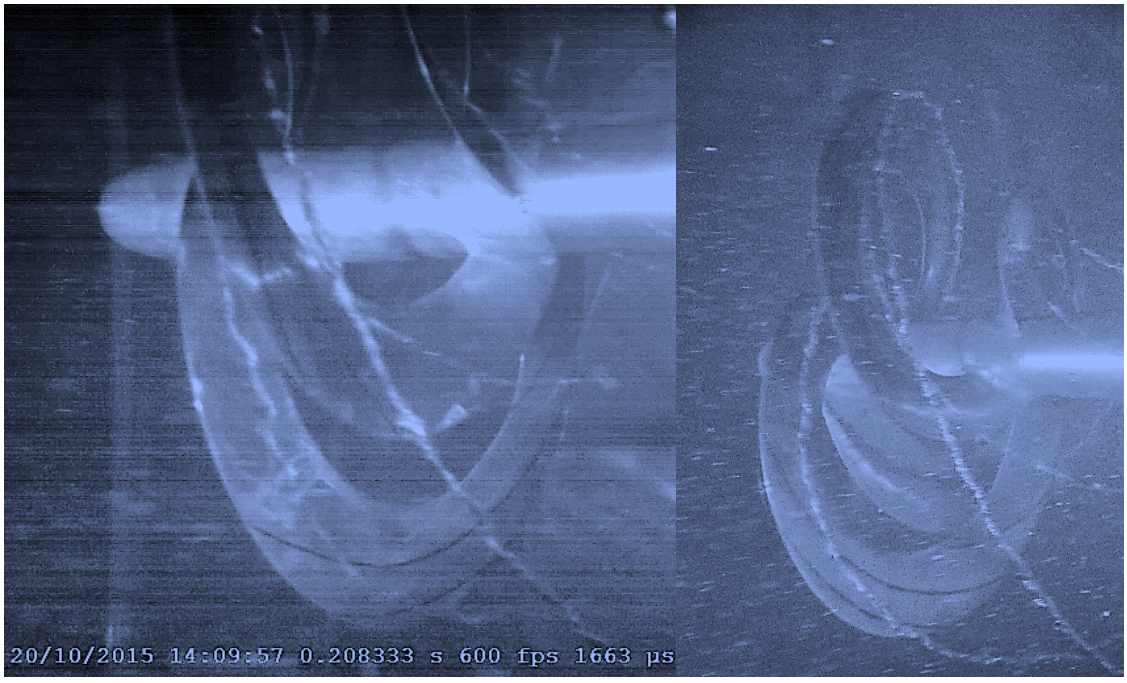

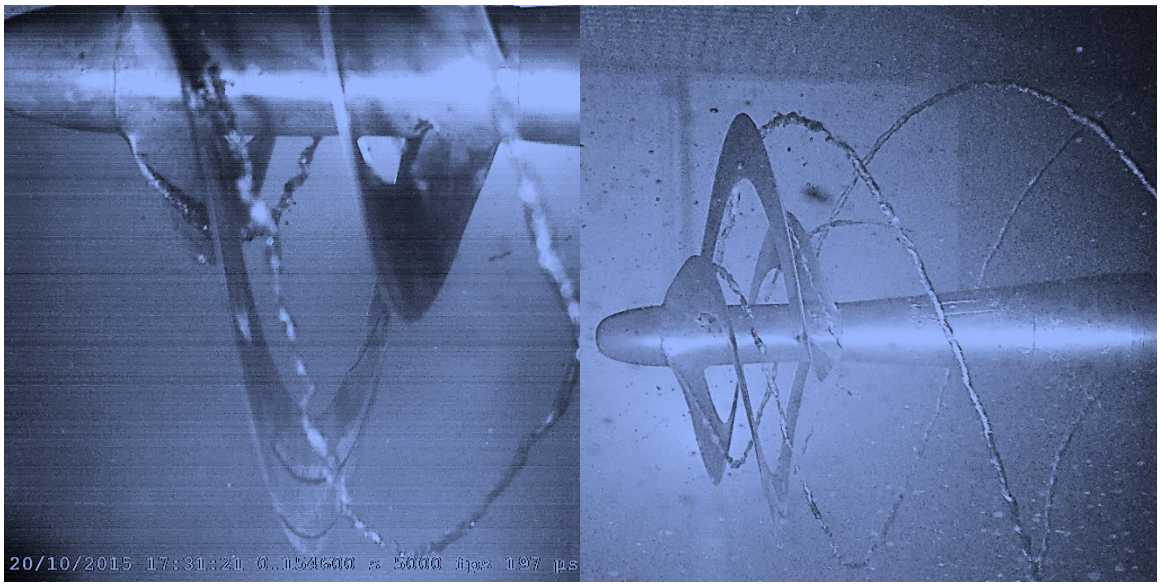

Tunnel Pressure: 350 mm Hg, *TSR* = 2

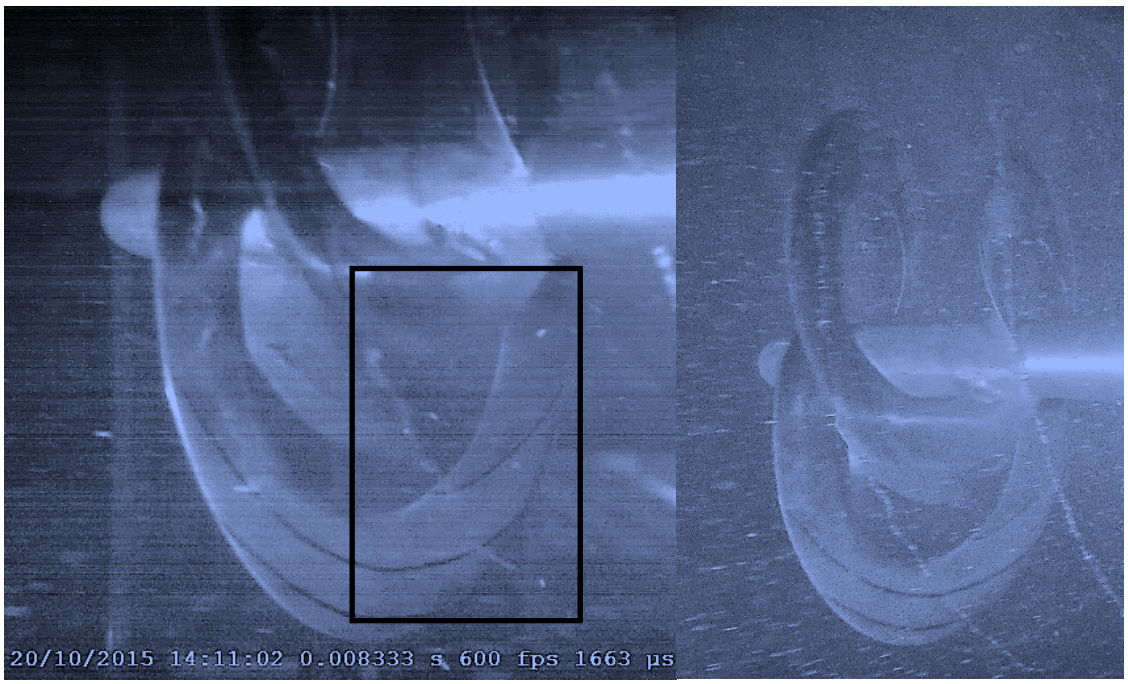

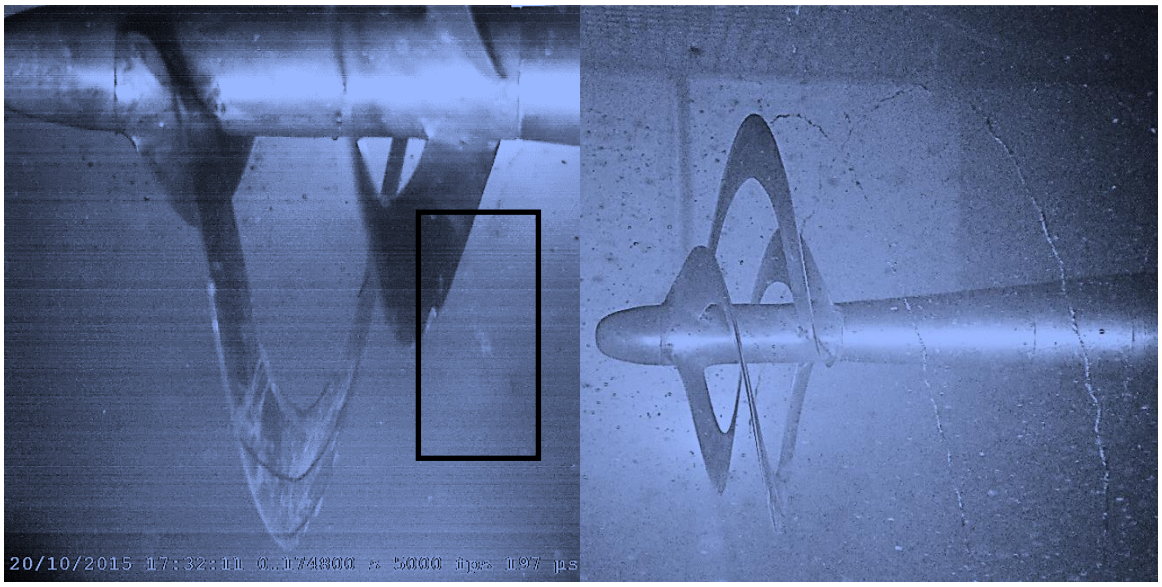

Tunnel Pressure: 350 mm Hg, *TSR* = 3

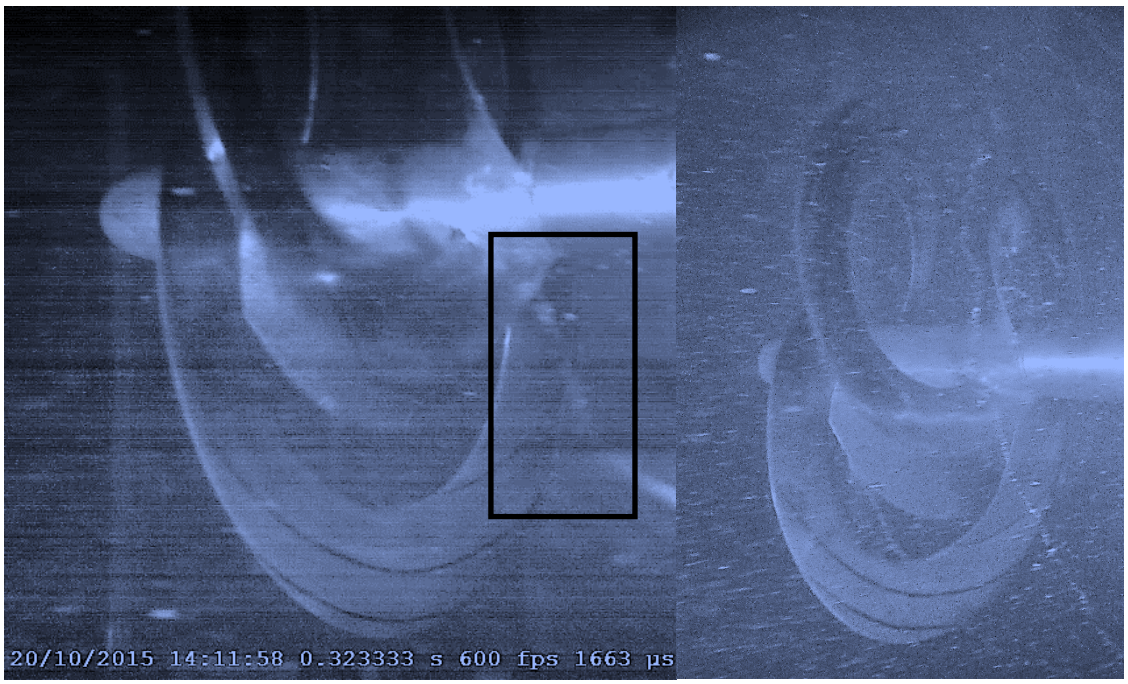

Tunnel Pressure: 350 mm Hg, *TSR* = 4

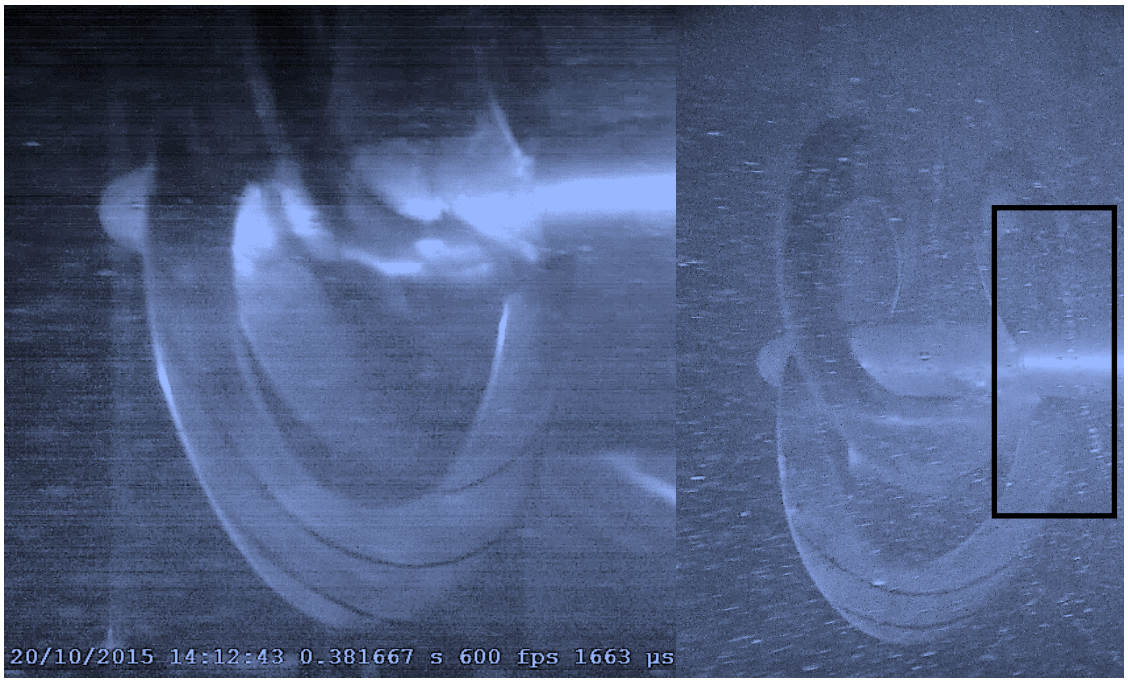

Tunnel Pressure: 350 mm Hg, *TSR* = 5

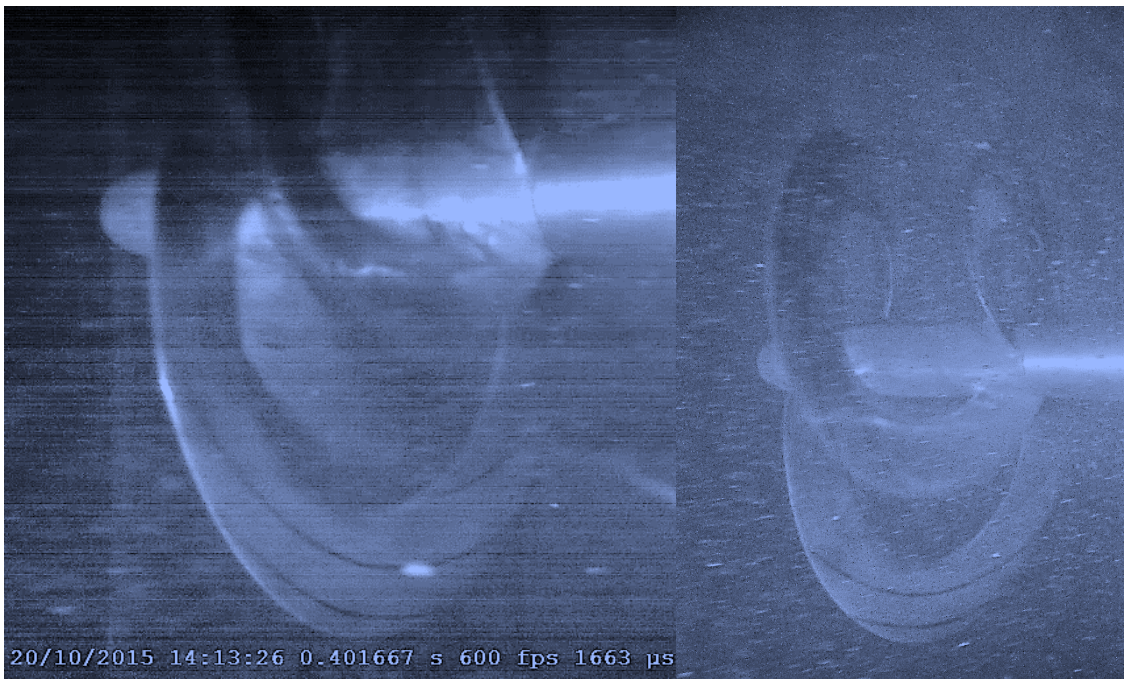

Tunnel Pressure: 250 mm Hg, *TSR* = 0

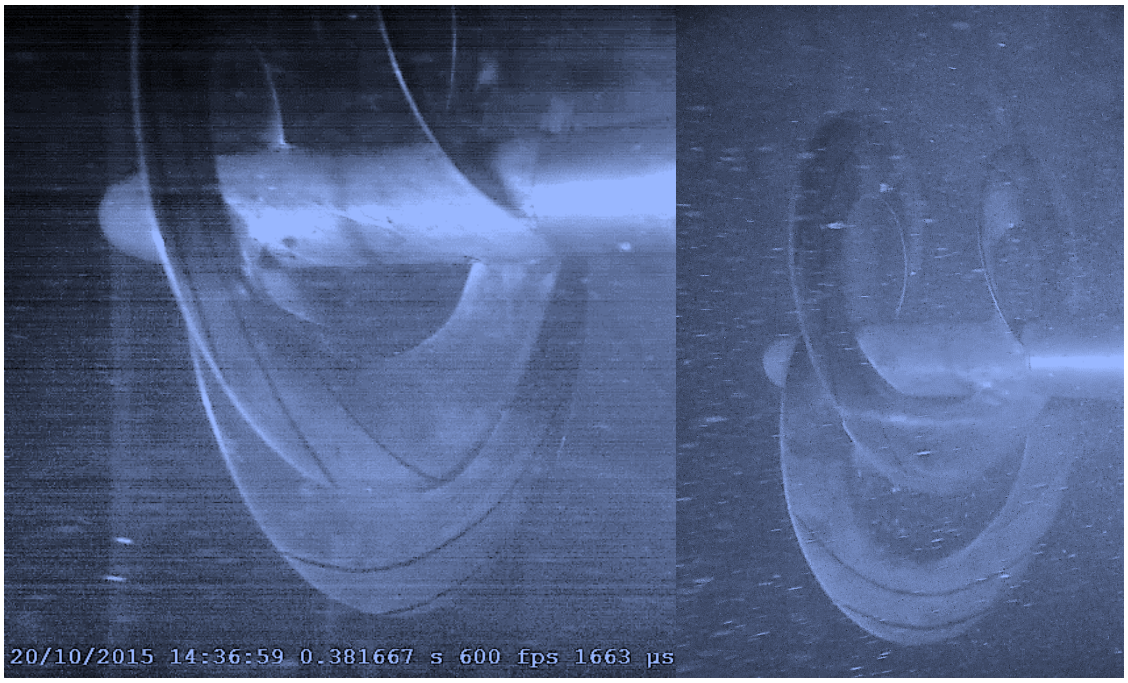

Tunnel Pressure: 250 mm Hg, *TSR* = 1

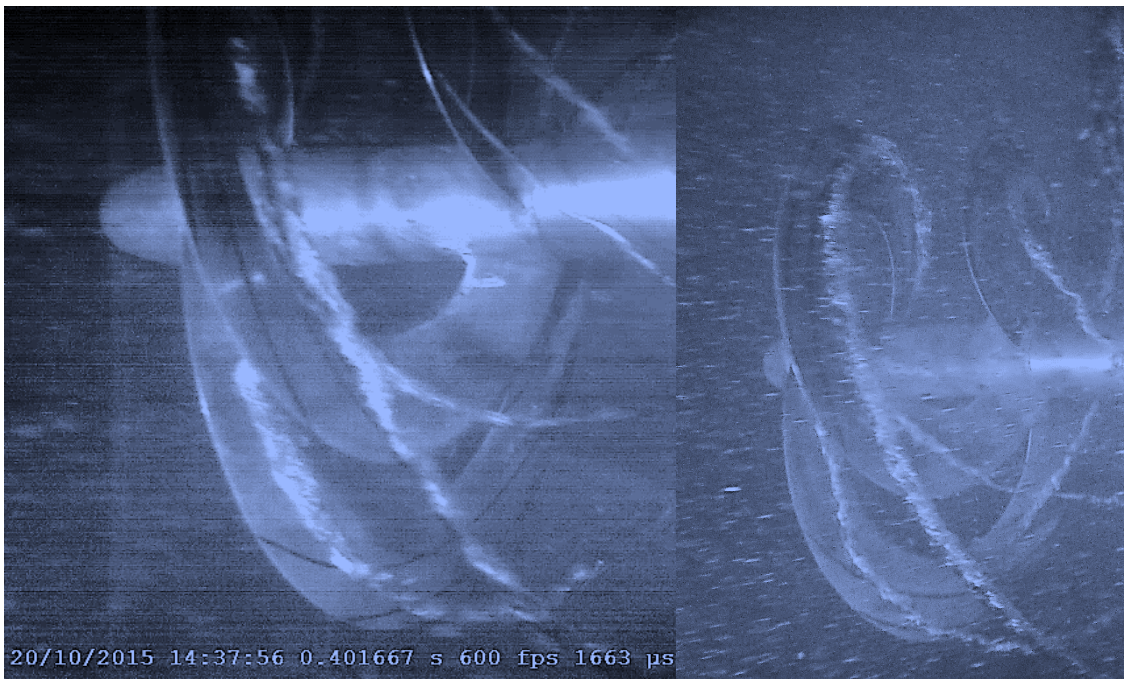

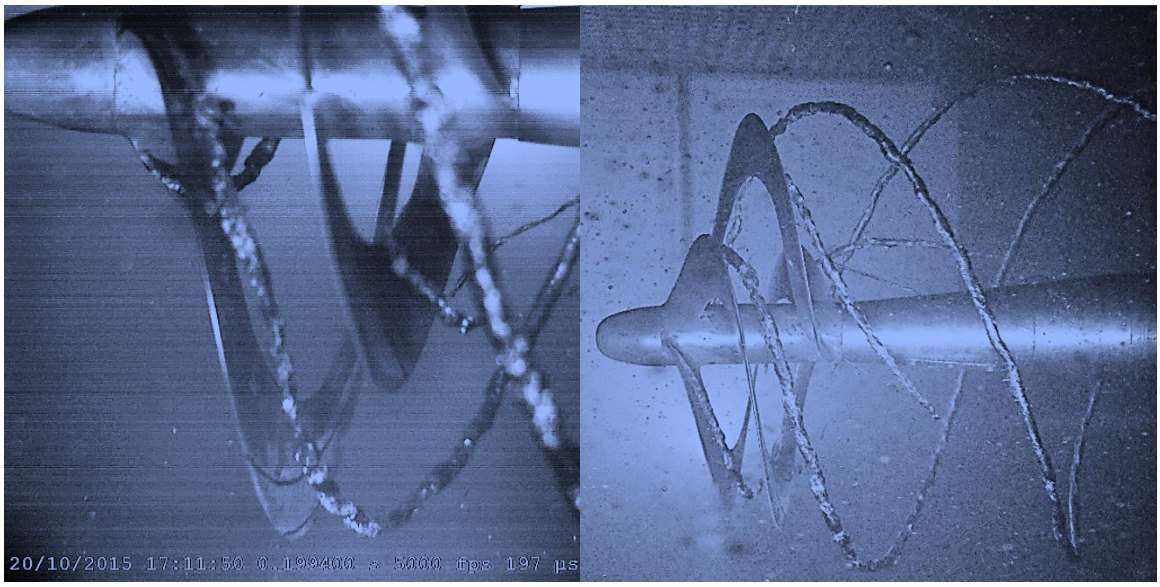

Tunnel Pressure: 250 mm Hg, *TSR* = 2

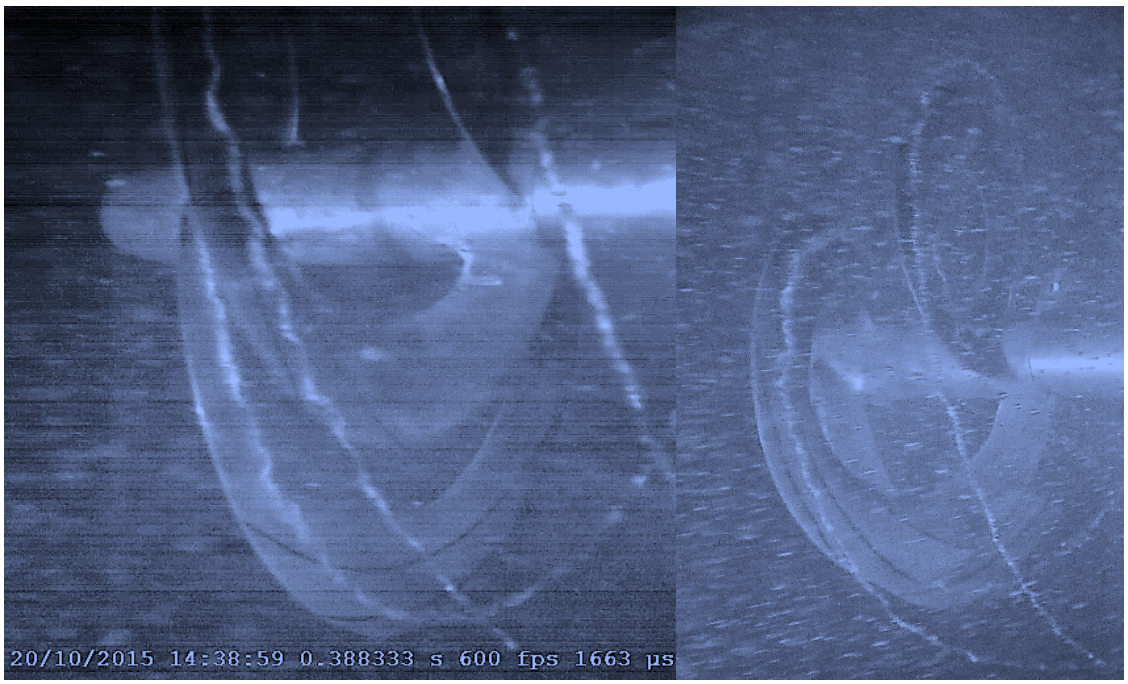

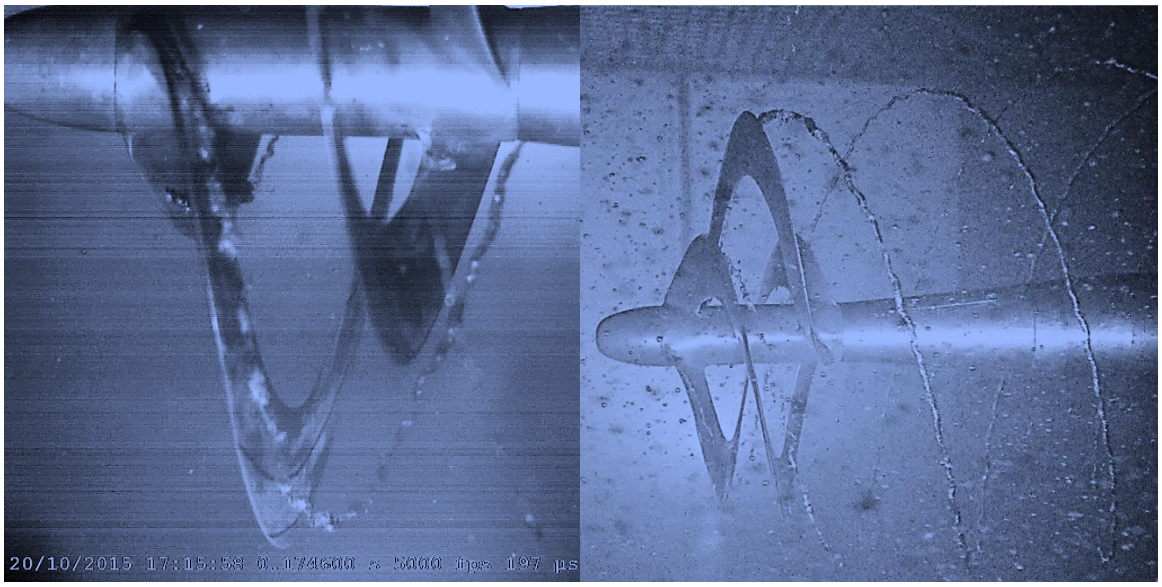

Tunnel Pressure: 250 mm Hg, *TSR* = 3

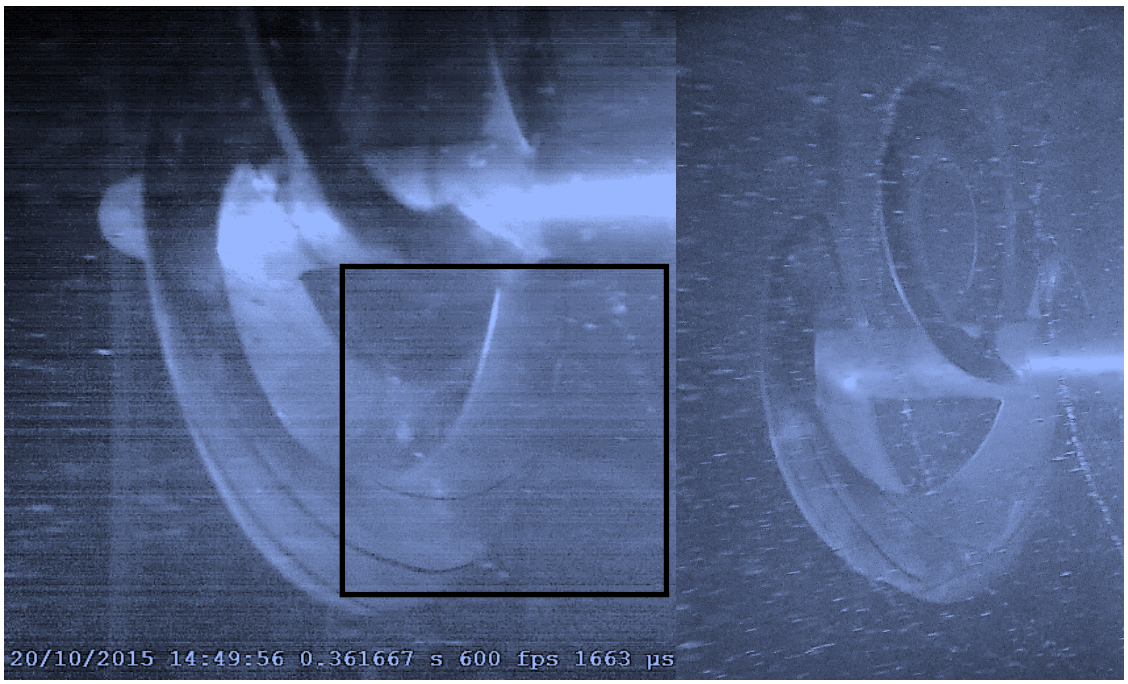

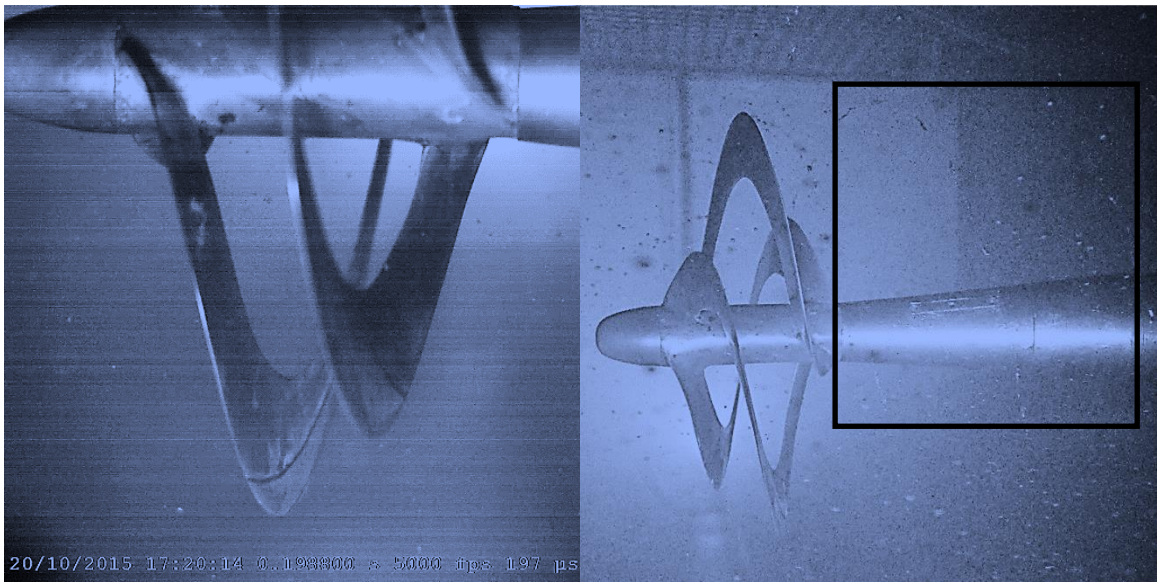

Tunnel Pressure: 250 mm Hg, *TSR* = 4

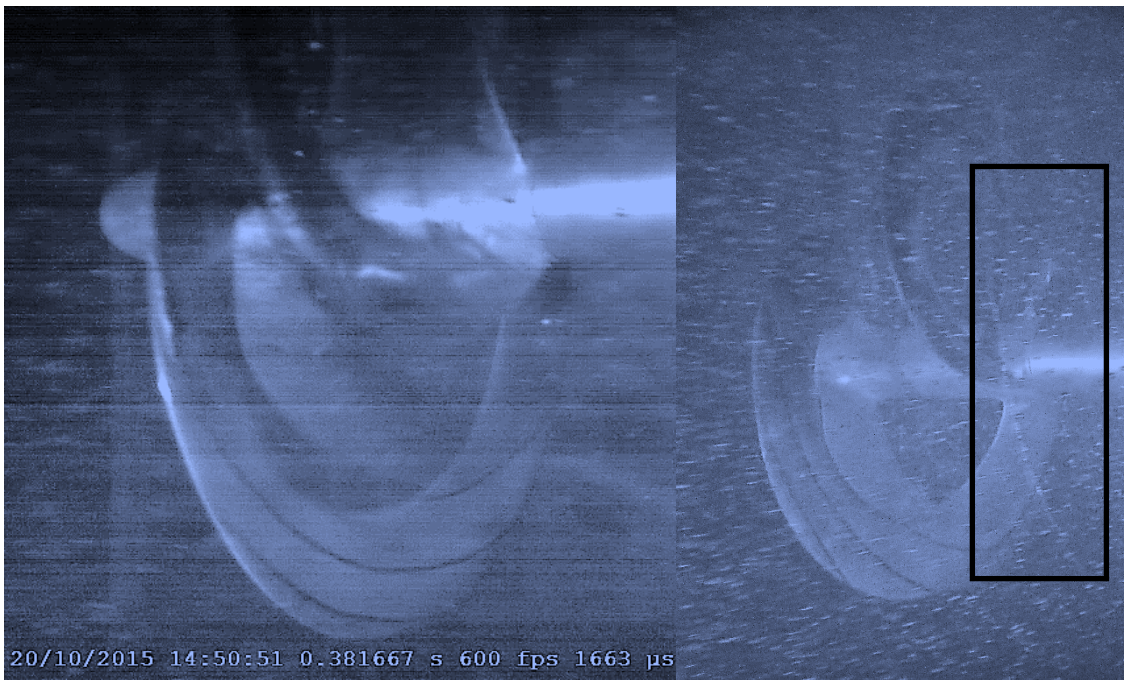

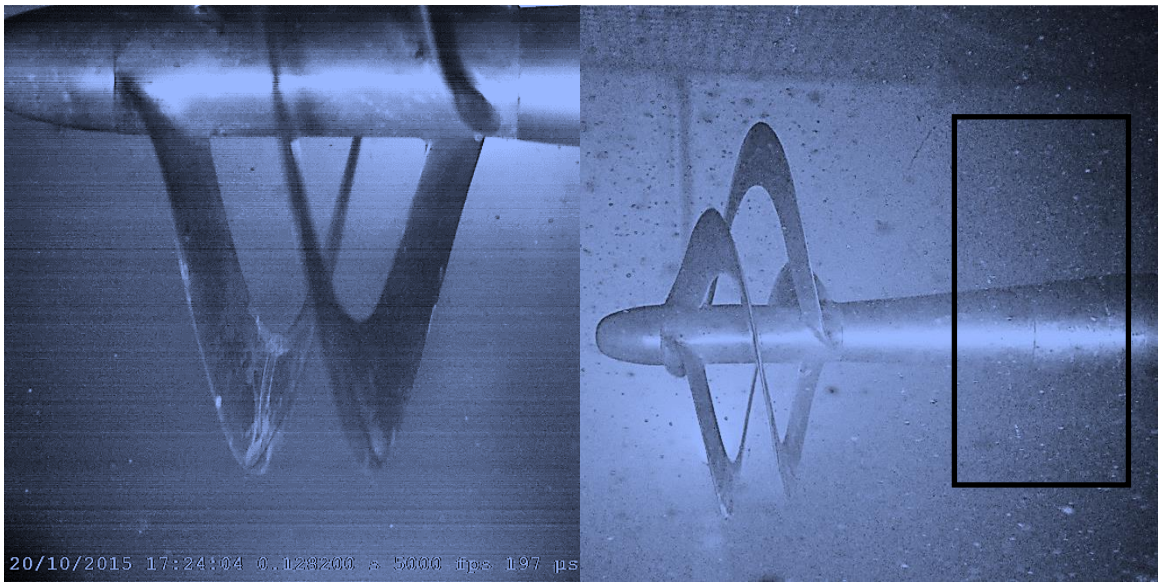

Tunnel Pressure: 250 mm Hg, *TSR* = 5

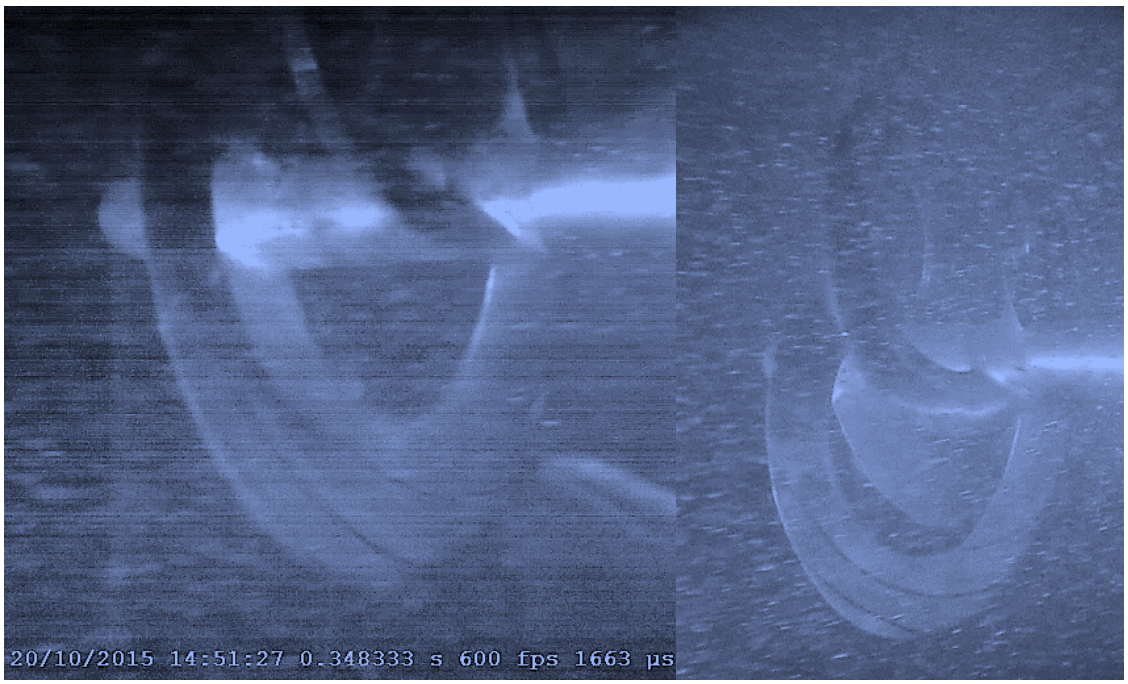

Appendix F: 1 Hz Band Level

1 Hz Band Level at each pressure condition

850 mm Hg

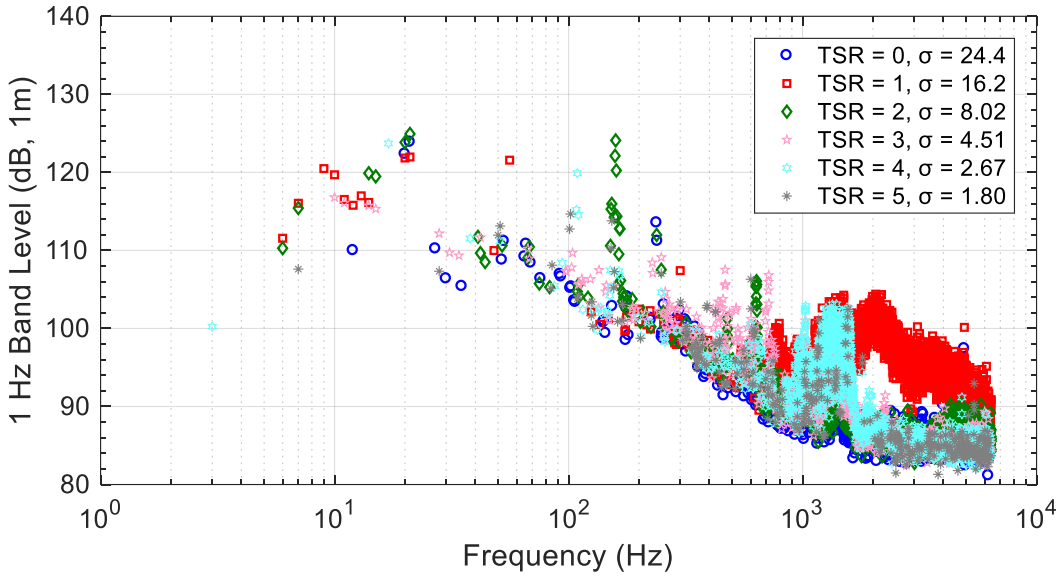

750 mm Hg

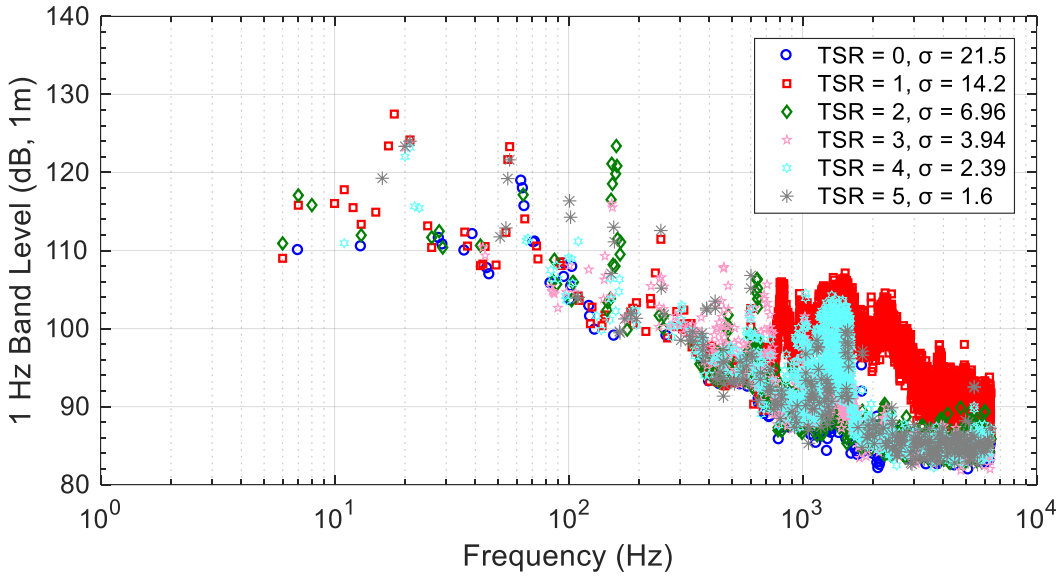

650 mm Hg

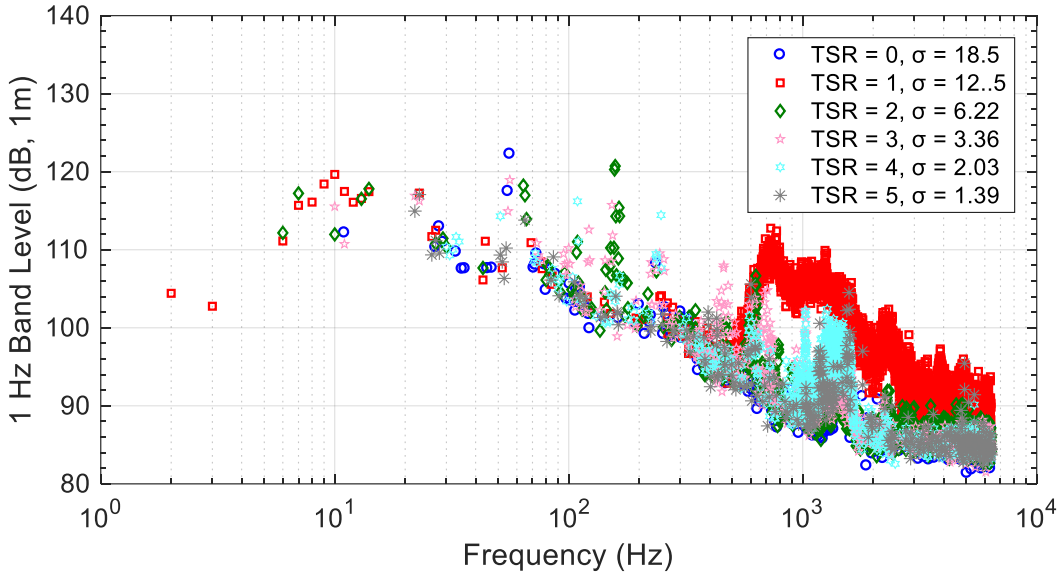

550 mm Hg

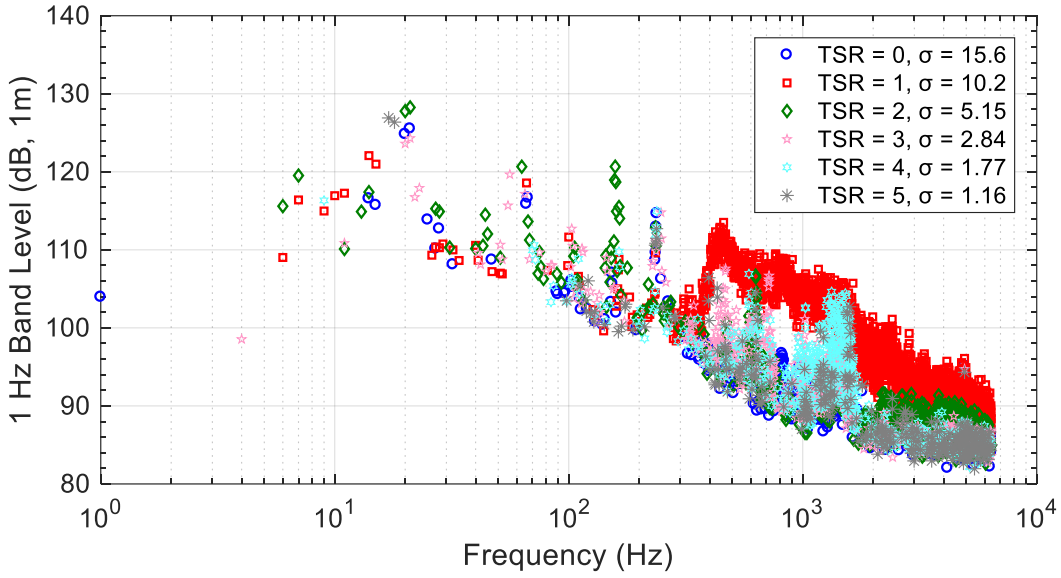

450 mm Hg

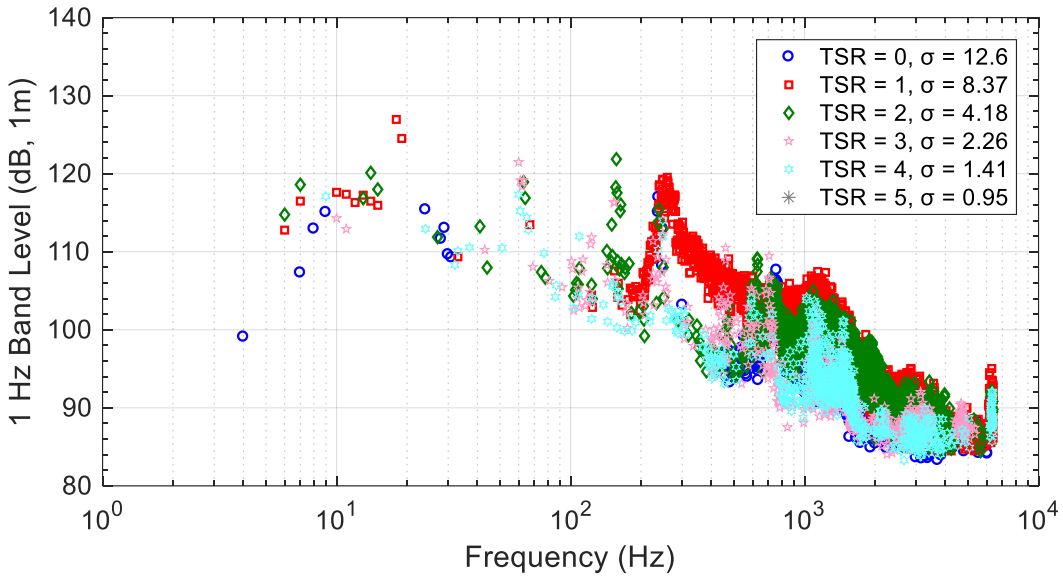

350 mm Hg

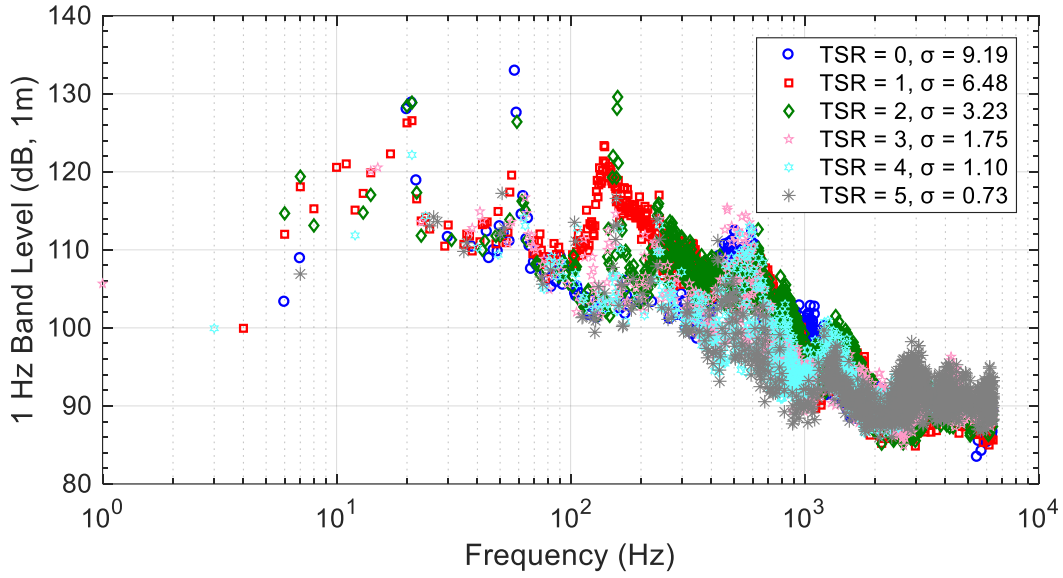

250 mm Hg

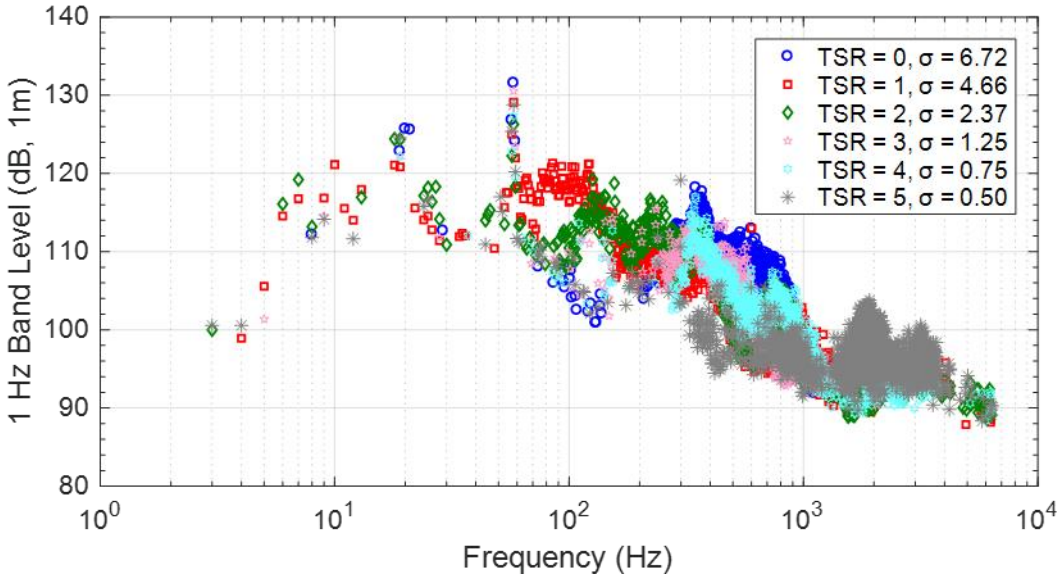
1 Hz Band Level (dB, 1m)
Frequency (Hz)
TSR = 0, σ = 6.72
TSR = 1, σ = 4.66
TSR = 2, σ = 2.37
TSR = 3, σ = 1.25
TSR = 4, σ = 0.75
TSR = 5, σ = 0.50

Appendix G: 1/3 Octave Band Level

1/3 Octave band level at each pressure condition

850 mm Hg

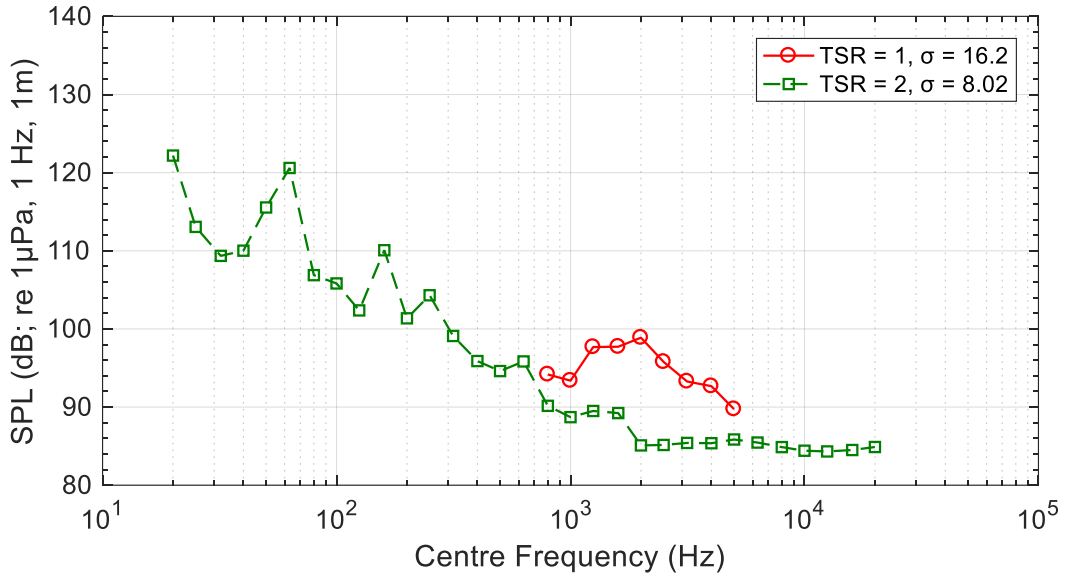

750 mm Hg

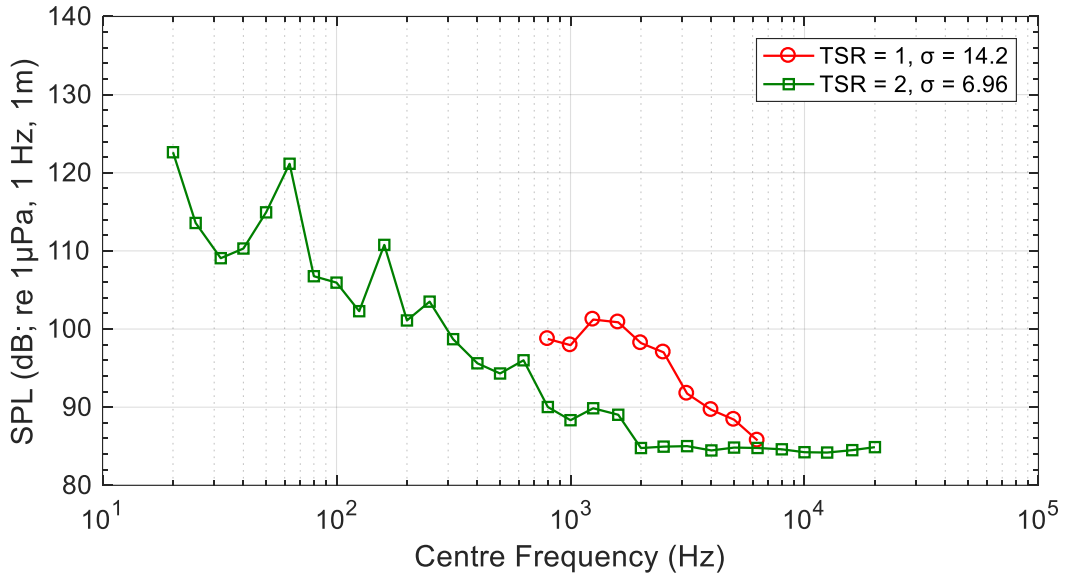

650 mm Hg

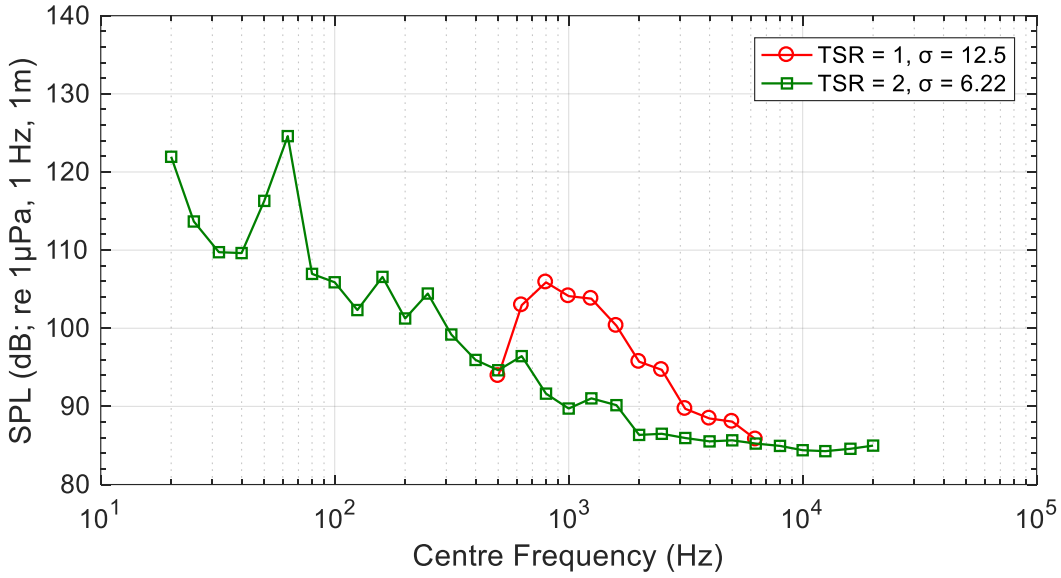

550 mm Hg

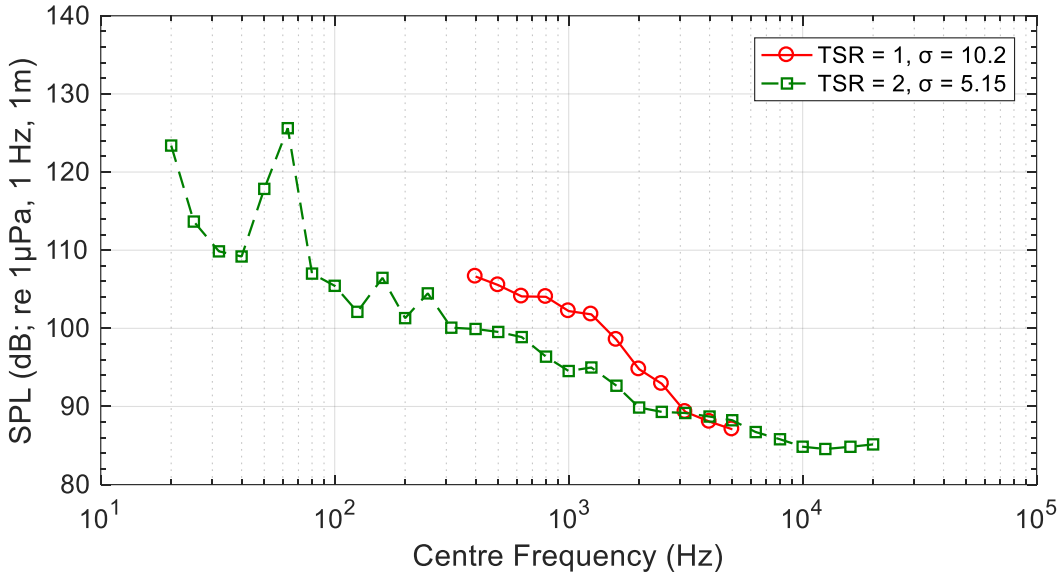

450 mm Hg

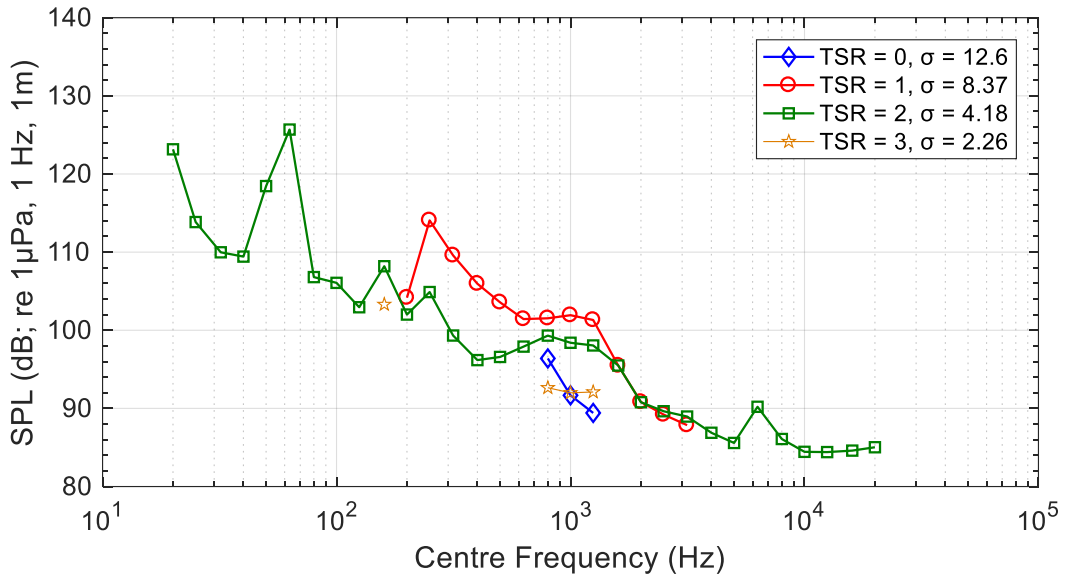

350 mm Hg

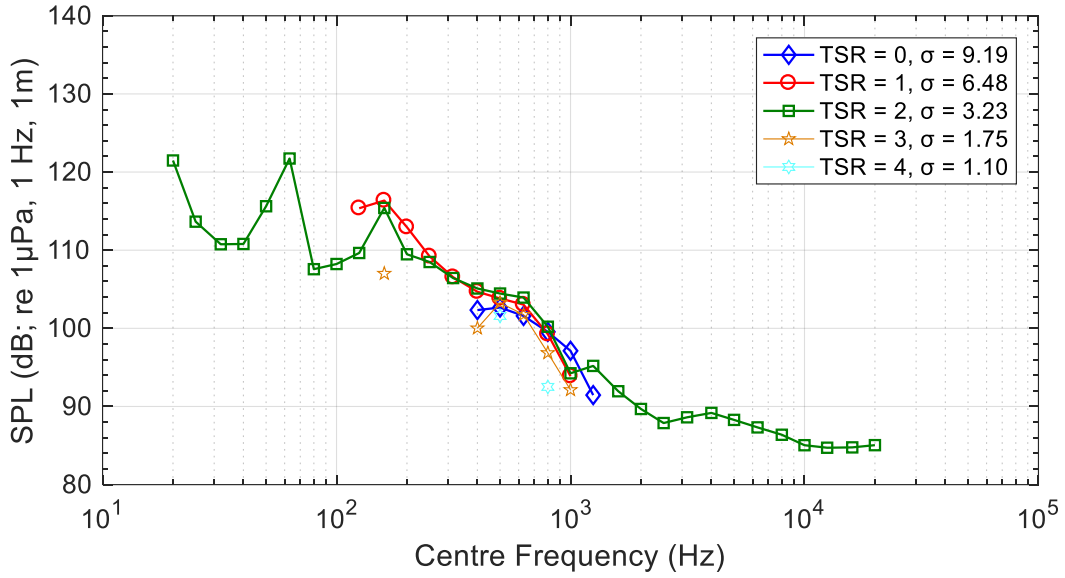

250 mm Hg

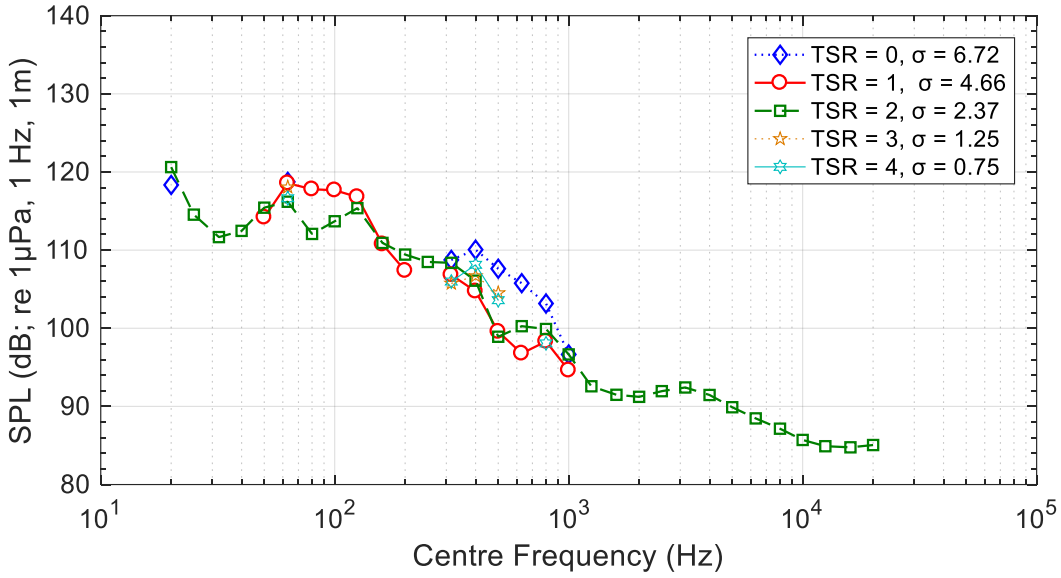
SPL (dB; re 1µPa, 1 Hz, 1m)
Centre Frequency (Hz)
TSR = 0, σ = 6.72
TSR = 1, σ = 4.66
TSR = 2, σ = 2.37
TSR = 3, σ = 1.25
TSR = 4, σ = 0.75

Appendix H: Procedure for Estimation of Discretization Error (Celik *et al.*, 2008)

Step 1: Define a representative mesh cell size, *h*, for three dimensional calculations

$$h = \left[\frac{1}{N}\sum_{i=1}^{N}(\Delta V_i)\right]^{1/3}$$

where ΔV_i is the volume of the *i*th cell, and N is the total number of cells used in the computations.

Step 2: Select three significantly different sets of grids and run simulations to determine the value of the solutions for the study i.e. in this case power and thrust coefficients which is denoted as variable ϕ. It is recommended that the refinement factor $r = h_{coarse}/h_{fine}$ be greater than 1.3.

Step 3: Let $h_1 < h_2 < h_3$ and $r_{21} = h_2/h_1$, $r_{32} = h_3/h_2$ and calculate the apparent order *p* of the method using the expression.

$$p = \frac{1}{ln(r_{21})}|ln|\varepsilon_{32}/\varepsilon_{21}| + q(p)|$$

$$q(p) = ln\left(\frac{r_{21}^{p} - s}{r_{32}^{p} - s}\right)$$

$$s = 1.sgn(\varepsilon_{32}/\varepsilon_{21})$$

where $\varepsilon_{32} = \emptyset_3 - \emptyset_2$, $\varepsilon_{21} = \emptyset_2 - \emptyset_1$ and $\emptyset_k$ represents the solution on the *k*th grid.

Step 4: Calculate the extrapolated values along with the apparent order *p*.

In approximate relative error,

$$e_a^{21} = \left|\frac{\emptyset_1 - \emptyset_2}{\emptyset_1}\right|$$

In extrapolated relative error

$$e_{ext}^{21} = \left|\frac{\emptyset_{ext}^{12} - \emptyset_1}{\emptyset_{ext}^{12}}\right|$$

In the fine-grid convergence index

$$\mathrm{GCI}_{fine}^{21} = \frac{1.25e_a^{21}}{r_{21}^p - 1}$$